The Dynamics of a Changing Arctic Ocean

Peter E. D. Davis

St. Edmund Hall

Thesis submitted to the University of Oxford

for the degree of Doctor of Philosophy

in

Earth Sciences

Department of Earth Sciences

University of Oxford

Trinity Term, 2015

Supervised by Helen Johnson and Camille Lique

"It is evident that the oceanographical conditions of the North Polar Basin have much influence upon the climate, and it is equally evident that changes in its conditions or circulation would greatly change the climatic conditions"

Fridtjof Nansen, 1902

Declaration

The contents of this thesis are all my own work, except where otherwise stated. The views and opinions expressed herein are mine and not necessarily those of any other person or body unless so attributed.

Citation: Davis, P. E. D. (2015), The Dynamics of a Changing Arctic Ocean, D.Phil. Thesis, University of Oxford, Department of Earth Sciences, Oxford, UK.

This thesis has been typeset using LaTeX 2_ε, and the references were compiled using BibTeX.

Printed in the United Kingdom.

Abstract

The Dynamics of a Changing Arctic Ocean

Peter Davis
St. Edmund Hall, Oxford
Doctor of Philosophy in Earth Sciences

Trinity Term, 2015

The Arctic Ocean is undergoing a period of rapid transition, and many different aspects of its environment (ocean, sea ice, and atmosphere) are changing faster than has ever previously been observed. Motivated by the role that the Arctic plays in the global climate and ocean circulation, the aim of this thesis is to investigate how the changing environment is affecting the dynamics and circulation of the Arctic Ocean.

Observations show that freshwater accumulation in the Beaufort Gyre of the western Arctic Ocean has accelerated over the past decade. First, a simple process model and idealised perturbations to the annual cycle in ocean surface stress are used to show that the decline in Arctic sea ice cover and an increase in the annual mean momentum flux can explain this accelerated accumulation. The adjustment timescale and quantity of freshwater accumulated are determined by a balance between Ekman pumping and an eddy-induced volume flux, highlighting the importance of eddies in the changing Arctic.

Sea ice decline may also drive periodic increases in vertical mixing. Using a 1D model of the Arctic Ocean water column, the competing effects of elevated vertical mixing and enhanced freshwater input on the stratification, the stability of the cold halocline, and the sea ice cover at the surface are explored. An elevated diffusive heat flux driven by stronger vertical mixing has little effect on the sea ice. Instead, the erosion of the cold halocline, which isolates the sea ice from the warm Atlantic water, represents the most important feedback for ongoing sea ice melt.

The changing Arctic Ocean will further affect the freshwater export to either side of Greenland; however, local dynamics will also be important. In this chapter, the vertical structure of the tides in Nares Strait in the Canadian Arctic Archipelago are explored, as tidal turbulence may represent an important frictional constraint for the freshwater flow in this region. The tides propagate as either standing or progressive waves, and the vertical structure is set by the proximity of the semi-diurnal critical latitude, the requirement of no normal flow through the coast, and the strong stratification at the surface. There is little temporal variability in the vertical structure, and tidal dissipation is comparable in magnitude to that over the highly dissipative region of the northwest European Shelf.

Extended Abstract

The Dynamics of a Changing Arctic Ocean

Peter Davis
St. Edmund Hall, Oxford
Doctor of Philosophy in Earth Sciences

Trinity Term, 2015

The Arctic Ocean is a semi-enclosed mediterranean sea that covers 2.6% of the world's total oceanic surface. In the vertical, it is characterised by a cold and fresh wind-driven surface layer, separated by the cold halocline from the warm and salty Atlantic layer, and the cold and salty bottom waters. The cold halocline is a unique feature of the Arctic Ocean, and is generally identified by the coincidence of a strong salinity gradient with near freezing temperatures. As salinity dominates density in the Arctic, the cold halocline represents a significant density gradient that isolates the sea ice cover at the surface from the heat contained within the Atlantic layer.

The Arctic Ocean plays a critical role in the global climate through its effect on the large-scale atmospheric energy budget, the global ocean circulation, and the global freshwater cycle. Specifically, excess freshwater that has been evaporated at lower latitudes is delivered to the Arctic Ocean through river run-off, excess precipitation, and an inflow of Pacific water through Bering Strait, and is subsequently exported to the North Atlantic, closing the northern hemisphere freshwater loop. This freshwater is exported directly into the regions of dense water formation, which are critical in maintaining the Atlantic Meridional Overturning Circulation (AMOC), and hence a change in the Arctic freshwater budget may impact the climate of northwestern Europe. Sea ice in the Arctic reflects 80-90% of incoming shortwave solar radiation back into space due to its high albedo surface, and it limits the turbulent exchange of heat and momentum between the

atmosphere and the ocean. Consequently, it helps maintain the low temperature environment of the high latitude regions and thus the equator-to-pole temperature difference, which is crucial in driving the global atmospheric and oceanic circulation. Furthermore, carbon uptake by biological and physical processes in the Arctic accounts for 10-12% of the total global oceanic carbon uptake, and therefore compared to its surface area, the region plays a disproportionately important role in the global carbon cycle.

Over the past few decades, the Arctic has been undergoing a period of rapid transformation, and many different aspects of its environment have been changing at their fastest rate on record. One of the clearest indicators of change is the rapid decline that has been observed in the Arctic sea ice cover. Since 1979 the monthly mean sea ice extent has declined at -3.8 $\pm$ 0.3% per decade, and the sea ice cover reached a record minimum extent in 2007, and again in 2012. Sea ice thickness has also been declining, and the Pan-Arctic Ice Ocean Modelling Assimilation System (PIOMAS) suggests that sea ice volume has decreased by -2.8 $\times$ 10^3 km^3 per decade since 1979, in agreement with shorter observational records. Overall, it is expected that the Arctic will become ice-free in summer sometime between the middle and the end of the century. At the same time, the sources, sinks, and distribution of freshwater in the Arctic Ocean have been fundamentally changing. Runoff from Eurasian rivers has increased by 7% between 1936 and 1999, and the rate of freshwater accumulation in the western Arctic Ocean has been accelerating. Freshwater input from sea ice melt has noticeably increased, and between 1992 and 2012, the freshwater content of the entire Arctic increased at a rate of 600 $\pm$ 300 km^3 yr^{-1} (approximately 7% of the annual input). In the future, freshwater accumulation in the Arctic is expected to continue, as a warming climate drives an enhanced hydrological cycle with increased moisture transport towards the polar regions.

The impacts of these changes, along with many others, will be felt both locally and globally. Within the Arctic itself, sea ice decline will affect the transfer of wind momentum into the upper ocean, and over the coming decades, is expected to lead to an overall spin-up of the Arctic Ocean, with implications for the freshwater budget and the export of

freshwater to the North Atlantic. In addition, stronger wind forcing may fundamentally change the levels of turbulence and vertical mixing within the Arctic Ocean, by generating strong inertial motions over open water. Elevated vertical mixing may erode the cold halocline or drive an enhanced vertical diffusive heat flux, fundamentally altering the extent to which the sea ice cover at the surface is isolated from the warm Atlantic water. On the other hand, the projected increase in the freshwater input may act to offset the effect of elevated vertical mixing by increasing the strength of the stratification. On more global scales, sea ice decline is affecting the stability of the Arctic atmosphere, increasing the baroclinicity and changing storm activity. It has been hypothesised (although the physics remain highly contentious) that "Arctic Amplification" (whereby the ice-albedo feedback effect has caused the mean atmospheric temperature over the Arctic to rise at almost twice the rate of the global average) has already modified the midlatitude jet stream, with implications for northern hemisphere weather patterns. Observations and modelling studies have shown that increased Arctic freshwater export can impact dense water formation, with implications for the AMOC, the climate of nothwestern Europe, and the dynamics of the global atmospheric circulation.

Motivated by the dramatic changes occurring in the Arctic environment, and the wide-ranging and significant impacts that these changes may have at both local and global scales, the aim of this thesis is to explore and understand how the changing environment is affecting the Arctic Ocean's circulation and dynamics using both simple numerical models and observations. In Chapter 2, the physical processes behind the accelerated accumulation of freshwater in the western Arctic Ocean and its link with Arctic sea ice decline are considered, whilst in Chapter 3, the effects of elevated vertical mixing and enhanced freshwater input on the stratification, the strength of the cold halocline, and the sea ice cover at the surface are examined. In Chapters 4 and 5 the local dynamical processes that set the vertical structure of the tides in Nares Strait are explored, as turbulence generated by tides may represent an important frictional constraint on the Arctic freshwater export through this region. Implications of the work in this thesis are discussed in Chapter 6.

The Beaufort Gyre in the Canadian Basin of the western Arctic Ocean is a permanent anticyclonic circulatory feature driven by the winds associated with the atmospheric Beaufort High. It accumulates freshwater through Ekman convergence and the mechanical deformation of the salinity field, and contains approximately 25% of the total Arctic Ocean freshwater content. Recent satellite and hydrographic observations have shown that the rate of freshwater accumulation in the Beaufort Gyre has accelerated over the past decade, coinciding with the dramatic decline in Arctic sea ice cover. It has been proposed that this accelerated accumulation is a dynamical adjustment in response to the changing efficiency by which wind energy is transferred through a thinner and weaker sea ice cover, and if the period of time over which the Arctic Ocean adjusts to a change in forcing is close to seasonal, the emergence of an asymmetrical annual cycle in ocean surface stress (i.e. the integrated stress felt by the ocean from the wind blowing over a partly ice-covered Arctic) may also be responsible for driving multiyear trends in the freshwater content. By idealistically perturbing the annual cycle in ocean surface stress in a simple reduced gravity model of the Canadian Basin, a linear relationship is found between the annual mean momentum flux and the accumulation of freshwater in the Beaufort Gyre: as sea ice is becoming thinner and more broken up, the ocean surface stress is increasing for the same wind speed, resulting in an accelerated linear accumulation of freshwater in the Beaufort Gyre. In the model, both the adjustment timescale and the quantity of freshwater accumulated are determined by a balance between Ekman pumping and an eddy-induced volume flux towards the boundary, highlighting the importance of eddies in the adjustment of the Arctic Ocean to a change in forcing. On the other hand, when the seasonal cycle in ocean surface stress is modified (but the annual mean is held constant), there is no change in the net freshwater content of the Beaufort Gyre, as the adjustment timescale is considerably longer than seasonal (14 years). Nevertheless, it does impact the timing and amplitude of the annual cycle in Beaufort Gyre freshwater content, which may have implications for the magnitude and seasonality of the freshwater export to the North Atlantic.

If it were to reach the surface, there is enough heat contained within the Atlantic layer of the Arctic Ocean to melt all sea ice in the Arctic within a few years. This heat, however, is currently isolated from the surface by the strong stratification associated with the cold halocline (which limits the depth to which surface-generated mixing can penetrate), and internal wave mixing in the Arctic is presently too weak to drive a significant diffusive heat flux. Over the coming decades, however, freshwater input to the Arctic is expected to increase, and the decline in Arctic sea ice cover is likely to drive periodic increases in internal wave mixing during ice-free periods. Using a 1D model of the Arctic Ocean water column, the effect of these competing processes on the stratification and the stability of the cold halocline are explored, and their role in the ongoing melting of Arctic sea ice is quantified. Elevated vertical mixing initially warms the mixed layer due to an enhanced diffusive heat flux, however, the change in mixed layer temperature is too small to adversely affect the sea ice cover at the surface. In the Eurasian Basin, the elevated vertical mixing also strengthens the stratification over the Atlantic layer; after about a decade, this effect dominates, and the mixed layer begins to cool. The sea ice cover can be significantly affected if the elevated vertical mixing is strong enough to completely erode the cold halocline, and allow the heat contained within the Atlantic layer to be directly entrained into the mixed layer. This occurs within as little as 10 years in the Eurasian Basin, but in the Canadian Basin the stronger stratification ensures that the cold halocline always remains stable. Overall, the results suggest that until the cold halocline is eroded, the sea ice cover at the surface will remain largely immune to the heat contained within the Atlantic layer.

The changing dynamics of the surface freshwater layer, as well as the projected increase in the freshwater content of the Arctic Ocean will further affect the export of freshwater to either side of Greenland. However, local dynamics in these export regions are also likely to play an important role. The day-to-day variability in the flow through Nares Strait to the west of Greenland, through which approximately 30-50% of the total Canadian Arctic Archipelago freshwater export passes, is dominated by the tides. Consequently, tidally-generated turbulence may represent an important frictional constraint

on the subtidal flow. Using observations collected in Nares Strait between 2003 and 2006, and output from Version 8 of the Oregon State University TOPEX/Poseidon Global Inverse Solution (TPXO8) barotropic tidal model, the dynamical processes responsible for setting the vertical structure of the tides in Nares Strait are investigated in detail, providing the first steps towards a full understanding of the role they may play in controlling the export of freshwater through this region. The analysis shows that the semi-diurnal tides propagate with standing wave characteristics, explaining the unusually strong tidal currents that are observed in Nares Strait, whilst the diurnal tides propagate with a more progressive nature. There is significant variability in the vertical structure of the tides, and fitting simple boundary layer models to the observed vertical structure suggests that the important dynamical processes behind the vertical variability are the proximity of the strait to the semi-diurnal critical latitude, the requirement of no normal flow through the coastlines, and the strong stratification in the upper water column. In contrast, there is little temporal variability associated with the quasi-annual cycle in ice conditions and the presence of a second under-ice no slip boundary layer (although it must be noted that the observations do not extend above a depth of 30 m). Estimates of depth-integrated tidal dissipation calculated from the simple boundary layer models are consistent with the TPXO8 tidal model, and are comparable in magnitude to that over the highly dissipative region of the northwest European Shelf.

The work in this thesis has a number of implications for the the wider Arctic and scientific community. Individually, the work in each of the chapters provides new insight into the physical processes that will be important for the changing Arctic Ocean, and highlight not only how a reduction in sea ice cover will affect the ocean, but also how the ocean will affect the sea ice. However, none of these dynamical processes will operate in isolation, and the complex feedbacks that arise between them will define the overall response of the Arctic Ocean to the changing environment. In terms of modelling the changing Arctic, future studies should work to incorporate the physics associated with sea ice decline and the changing momentum transfer through sea ice into state-of-the-art coupled atmosphere-ice-ocean models, and more attention should be given to the

parameterisations of turbulent mixing in the Arctic Ocean. In addition, eddies are likely to play an immensely important role in the adjustment of the Arctic Ocean to a change in forcing, and future modelling and observational studies should investigate their dynamics in more detail. Overall, in light of the rate at which the Arctic is changing, and the many feedback processes that are likely to continue to drive further environmental change over the coming decades, future studies that aim to make progress in understanding the dynamics of the changing Arctic Ocean should be a priority.

Acknowledgements

The research in this thesis has been funded by the Natural Environment Research Council (NERC) through the "Ocean and sea-ice dynamics in Nares Strait and the Canadian Arctic Archipelago" research grant.

First and foremost, I would like to thank my supervisors Helen Johnson and Camille Lique for all their support, inspiration, and tireless encouragement throughout my DPhil. You have both kept me motivated when the going got tough, you have always listened to my problems and questions no matter how inane they may have been, and your expertise and advice during the research, writing, and proof reading of this thesis have been incredibly helpful. I would also like to say a particular thank you to Humfrey Melling from the Institute of Ocean Sciences (IOS). Your time and expertise during my research trip to the IOS helped prodigiously with my research, and you inspired me to keep working when all seemed lost. A special thank you must also go to Jeff Polton from the National Oceanography Centre, Liverpool. Our discussions throughout my DPhil, and your thoughts on tidal dissipation have helped enormously with the work in this thesis. I would also like to thank Michel Tsamados, Daniel Feltham and David Marshall for their useful discussions regarding the work in Chapter 2.

The upward looking sonar data used in Figure 2.8 were collected and made available by the Beaufort Gyre Exploration Program based at the Woods Hole Oceanographic Institution (http://www.whoi.edu/beaufortgyre) in collaboration with researchers from Fisheries and Oceans Canada at the Institute of Ocean Sciences. I'm also grateful to Ilker Fer, John Guthrie, and Camille Lique for providing access to the diffusivity observations in Figures 3.2 and 3.12.

I would like to thank all past and current members of my office, as well as the members

of the wider Physical Oceanography group at the University of Oxford. Your advice on computing and Matlab issues has saved many a frustrating hour, and the discussions of my work have always been enlightening. Our sometimes never-ending office discussions of the wider world have always provided a welcomed distraction, and the group punting, walking, and croquet tournaments on the Magdalen College lawns have provided good laughs and good memories in equal measure.

I'd also like to thank my family for all their continued love and support, and for always being interested in what I am doing (even if it does go over your heads!).

Finally, and most of all, I would like to thank Charlotte for always being there when I needed her. Our many mini adventures in and around Oxford have kept me sane throughout the writing up process, and our bigger expeditions throughout the UK have always reminded me that there is more to life than work. You have constantly encouraged and supported me, and your tireless proof-reading skills towards the end of my DPhil have been invaluable. Thank you!

Contents

List of Figures

List of Tables

Chapter 1

Introduction: The Arctic Ocean

Despite only covering 2.6% of the world's total oceanic surface (*Rey*, 1982), and containing only 1% of the total ocean volume (*Haine et al.*, 2015), the Arctic Ocean forms a pivotal part of the climate system through the role it plays in the global freshwater cycle, the global ocean circulation, and the large-scale atmospheric energy budget. Many different components of the Arctic environment, however, (including the atmosphere, ocean, and sea ice) are currently experiencing a period of rapid change, and these changes are expected to have significant impacts both within the Arctic itself, but also at lower latitudes. The aim of this thesis is to investigate how this changing environment may impact a number of different aspects of the Arctic Ocean's circulation and dynamics in order to better understand how the region may operate in the future.

1.1 Geography and Bathymetry

The Arctic Ocean is a semi enclosed mediterranean sea (Figure 1.1), bounded by Greenland, Canada, Alaska, Siberia, Russia, and Scandinavia. It is characterised by the existence of a deep central basin surrounded by extensive shallow shelf seas, which cover 53% of the total Arctic area (9.7×10^6 km^2; *Haine et al.*, 2015). The deep central basin is split by the Lomonosov Ridge at a depth of 1600 m into the Eurasian Basin and the Canadian Basin, which reach depths of 4500 m and 4000 m, respectively (*Rudels*, 2015). The Eurasian Basin is further divided into the southern Nansen Basin and northern Amundsen Basin by the Gakkel Ridge, and the Canadian Basin into the Canada Basin

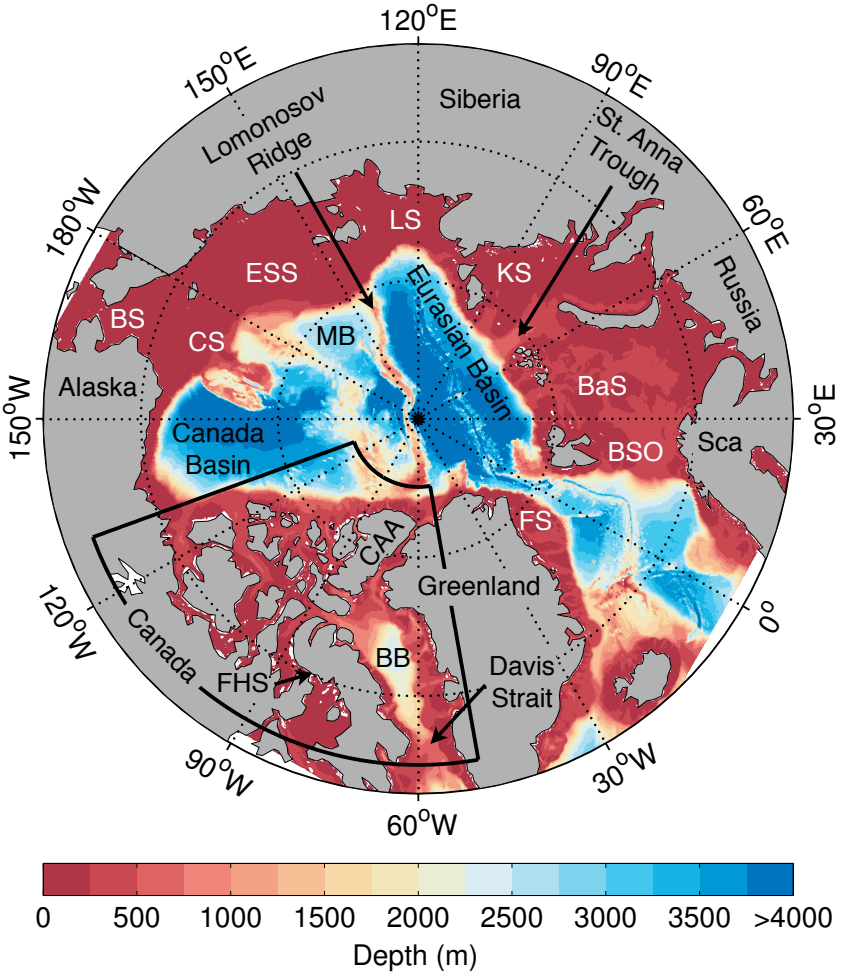

Figure 1.1: Bathymetry of the Arctic Ocean from the International Bathymetric Chart of the Arctic Ocean (*Jakobsson et al.*, 2012). BS stands for Bering Strait, CS for the Chukchi Sea, ESS for the East Siberian Sea, MB for the Makarov Basin, LS for the Laptev Sea, KS for the Kara Sea, BaS for the Barents Sea, BSO for the Barents Sea Opening, FS for Fram Strait, Sca for Scandinavia, CAA for the Canadian Arctic Archipelago, BB for Baffin Bay, and FHS for Fury and Hecla straits. The black box highlights the location of the Canadian Arctic Archipelago which will be discussed in more detail in Chapter 4.

and the Makarov Basin (Figure 1.1) by the Alpha and Mendeleev Ridges (*Rudels*, 2015). The Russian and Siberian periphery of the Arctic Ocean is composed of 5 epicontinental seas: the Chukchi Sea, the East Siberian Sea, the Laptev Sea, the Kara Sea, and the Barents Sea (CS, ESS, LS, KS, and BaS, respectively in Figure 1.1). They cover 48% of the total area, but due to their shallow average depth of only 100 m, make up no more than approximately 4% of the total volume (*Jakobsson et al.*, 2004). In contrast, against the coasts of Greenland, Canada, and Alaska, the continental shelf is only 50-90 km wide, with an average depth of 200 m (*Tomczak and Godfrey*, 2003).

The Arctic Ocean has four major connections to the surrounding oceans: Fram Strait,

Bering Strait, the Barents Sea Opening, and the convoluted channels and passageways of the Canadian Arctic Archipelago (FS, BS, BSO, and CAA, respectively in Figure 1.1). Fram Strait is the only deep connection that allows for two-way exchange (2600 m deep, 580 km wide; *Rudels*, 2015), and the latter three act more as sills than passageways in terms of the dynamics that affect the exchange of water between the Arctic, Pacific, and Atlantic (*Rey*, 1982). Bering Strait is 85 km wide and 50 m deep, the Barents Sea Opening is 480 m deep and 820 km wide, and the convoluted channels of the Canadian Arctic Archipelago (CAA) range in width from 1.9 km to >50 km and in depth from 65 m to 600 m (although the sill depths are considerably less; *Rudels*, 2015).

1.2 Role in Global Climate

The role that the Arctic Ocean plays in the global climate spans many different aspects of its hydrosphere, cryosphere, biosphere, and atmosphere; a number of its more important roles are summarised here.

The Arctic Ocean forms a critical part of the global hydrological cycle by closing the northern hemisphere freshwater loop. Through both meridional distillation, whereby freshwater is evaporated in the warm tropics and precipitated over the cold polar regions, and zonal distillation, by which westward atmospheric moisture transport over the Isthmus of Panama results in the Pacific being fresher than the Atlantic, the Arctic Ocean receives a net supply of freshwater that is then returned to the north Atlantic through the export of ice and low salinity water to either side of Greenland (*Carmack and McLaughlin*, 2011). This excess freshwater is exported directly into the regions of dense water formation (e.g. the Greenland and Labrador seas), which are critical in maintaining the Atlantic Meridional Overturning Circulation (AMOC; e.g. *Dickson et al.*, 2002). Consequently, as the AMOC is responsible for approximately 1 petawatt (10^{15} W) of northward heat transport at 25°N (e.g. *Johns et al.*, 2011), changes to the dynamics underlying the export of freshwater from the Arctic Ocean may affect the climate of northwestern Europe by altering the rate of dense water formation (e.g. *Jahn and Holland*, 2013; *Jackson et al.*, 2015).

The surface of the Arctic Ocean is characterised by the existence of a floating sea ice

cover, which is composed of thin (30 cm to 2 m) first-year ice that does not survive the summer season, and thick (2 m to 4 m) multiyear ice that has survived at least one melt season. The sea ice is in constant motion with individual ice floes, which range in size from a few meters to many kilometres across, constantly colliding with each other to create ice ridges and keels, and drifting apart to create areas of open water know as leads. Sea ice in the Arctic plays a crucial role in the atmospheric energy budget. By creating a high albedo surface that reflects 80-90% of incoming shortwave solar radiation back into space (*Perovich et al.*, 2002), and by modulating the turbulent exchange of heat and momentum between the atmosphere and ocean (e.g. *Barry et al.*, 1993; *Serreze et al.*, 2007), it helps maintain the low temperature environment of the high latitude regions and hence the equator-to-pole temperature difference. This temperature gradient is essential in driving the general atmospheric and oceanic circulation, as well as the polewards transport of heat that is required to close the Earth's energy budget (e.g. *Wunsch*, 2005). Sea ice cover in the Arctic is declining rapidly, and this is expected to have knock-on effects for atmosphere and ocean dynamics both within the Arctic itself, but also at lower latitudes.

In addition, the physical and biological uptake of carbon in the Arctic Ocean accounts for 10-12% of the total present-day global oceanic carbon uptake (*MacGilchrist et al.*, 2014), and therefore given its size, the region also plays a disproportionately important role in the global carbon cycle. Furthermore, Arctic soils, permafrosts, wetlands, and ocean sediments contain more organic carbon than any other region on the planet (1650 Gt; *Tamocai et al.*, 2009), as well as large quantities of methane hydrates (400 Gt; *Gornitz and Fung*, 1994). Consequently, future changes in ocean temperature (*Takahashi et al.*, 2002), sea ice extent (*Bates et al.*, 2006), ocean ecosystems (*Arrigo et al.*, 2008), permafrost stability, and thawing soils (*Schuur et al.*, 2009) are all poised to affect the Arctic carbon cycle, with potentially catastrophic impacts for the remainder of the planet (*Kerr*, 2010; *Whiteman et al.*, 2013).

1.3 Water Masses and Circulation

The water mass structure of the Arctic Ocean can be broadly split into three distinct layers (*Jones*, 2001; Figure 1.2). As salinity dominates density at low temperatures, the

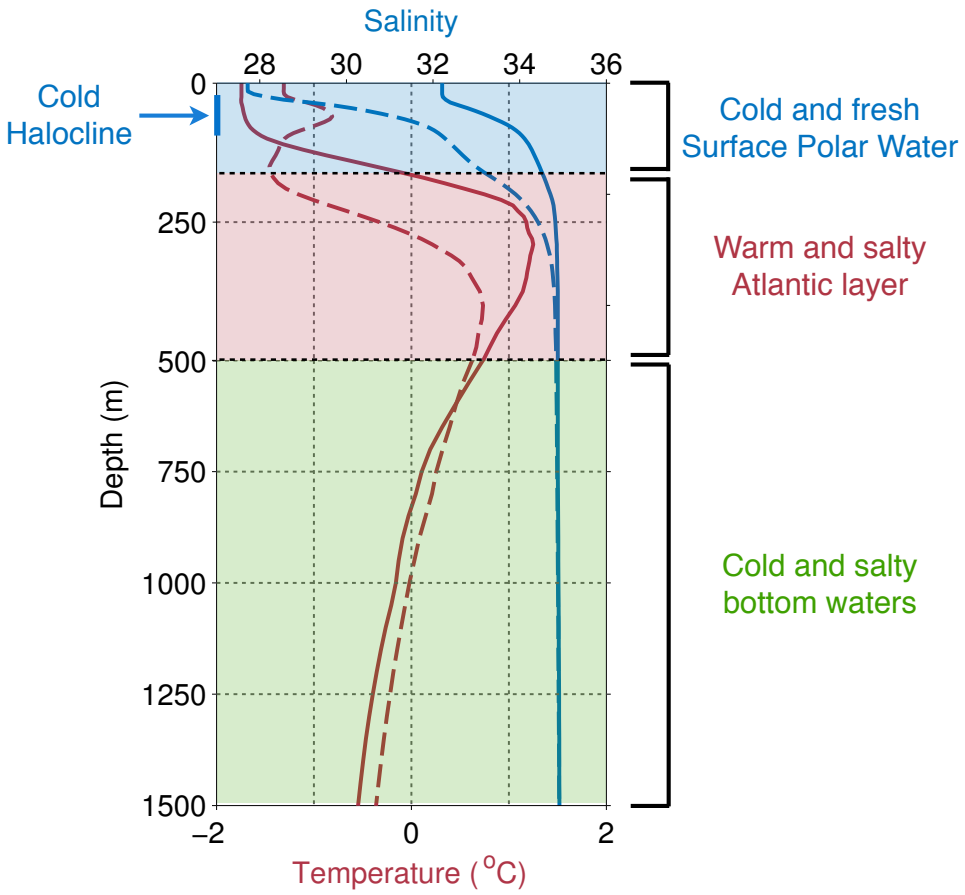

Figure 1.2: Schematic of the Arctic Ocean water mass structure in terms of climatological temperature (red) and salinity (blue) profiles from the Monthly Isopycnal / Mixed Layer Ocean Climatology (MIMOC; *Schmidtko et al.*, 2013) in the Eurasian Basin (solid lines) and the Canadian Basin (dashed lines). The delineations between the different water masses are for illustrative purposes only, and the approximate region of the water column covered by the cold halocline is indicated on the depth axes. For a higher resolution schematic of this region see Figure 3.1. Note the change in vertical scale below a depth of 500 m.

surface layer is characterised by the cold and fresh Surface Polar Water (Figure 1.3a), which consists of the Polar Mixed Layer (*Peralta-Ferriz and Woodgate*, 2015b) and the cold halocline (*Aagaard et al.*, 1981). Beneath this lies the warm (T>0°C) and salty Atlantic layer (*Rudels et al.*, 2004), and the deeper cold and salty bottom waters found in the different basins (*Aagaard*, 1981).

The cold halocline (highlighted by the blue bar in Figure 1.2) is a unique feature of the Arctic Ocean water column, and is characterised by the coincidence of a strong salinity gradient with near freezing temperatures (although in the Canadian Basin the inflow of Pacific waters through Bering Strait creates a local temperature maximum within the halocline; *Aagaard et al.*, 1981; *Timmermans et al.*, 2014). The dynamics behind the formation of the cold halocline are generally thought to be both advective and convective

in nature, and whilst the exact mechanisms remain uncertain, the cold halocline is likely created from waters formed during sea ice formation, brine rejection, and haline convection over the shallow shelf seas or within the deep Arctic basins themselves (*Rudels et al.*, 1996; *Steele and Boyd*, 1998; *Rudels et al.*, 2004). By limiting the depth to which surface-generated mixing can penetrate, the strong salinity gradient associated with the cold halocline is essential in isolating the sea ice cover at the surface from the heat contained within the Atlantic layer, and in the Eurasian Basin, the near freezing temperatures ensure that any pycnocline water that is mixed up to the surface is devoid of any excess heat (*Steele and Boyd*, 1998).

1.3.1 Surface Freshwater Layer

The surface layer of the Arctic Ocean is a vast reservoir of freshwater (Figure 1.3b). Freshwater is defined as the volume of water with zero salinity that must be added to a seawater sample in order to reach the observed salinity from a specified reference salinity (*Haine et al.*, 2015). In the Arctic, the reference salinity is generally taken to be 34.8 psu, which represents the mean salinity of the Arctic Ocean (*Aagaard and Carmack*, 1989), although different values are used (e.g. *Rabe et al.*, 2011 use a reference salinity of 35.0 psu). In this sense, the liquid freshwater content in meters (FW_c; Figure 1.3b) can be calculated from

$$FW_c = \int_D^{\eta} \frac{S_{ref} - S}{S_{ref}}\, dz, \tag{1.1}$$

where S is the in-situ salinity, S_{ref} is the reference salinity, η is the sea surface height, and D is the depth of integration, which is usually taken as the depth of the S_{ref} isohaline. Similarly, the flux of freshwater through a section refers to the equivalent flux of zero salinity water through that section in $m^3\ s^{-1}$ or $km^3\ yr^{-1}$, and the total volume of freshwater in km^3 for a specific region is given by the area integral of Equation 1.1 over that region. The first complete freshwater budget of the Arctic Ocean was constructed by *Aagaard and Carmack* (1989), however, due to the uncertainties in the data, the budget was not fully constrained. As the Arctic system has slowly evolved over time and more robust data have been collected throughout the region, this initial freshwater budget has been updated many times (e.g. *Lewis et al.*, 2000, *Serreze et al.*, 2006, *White et al.*, 2007,

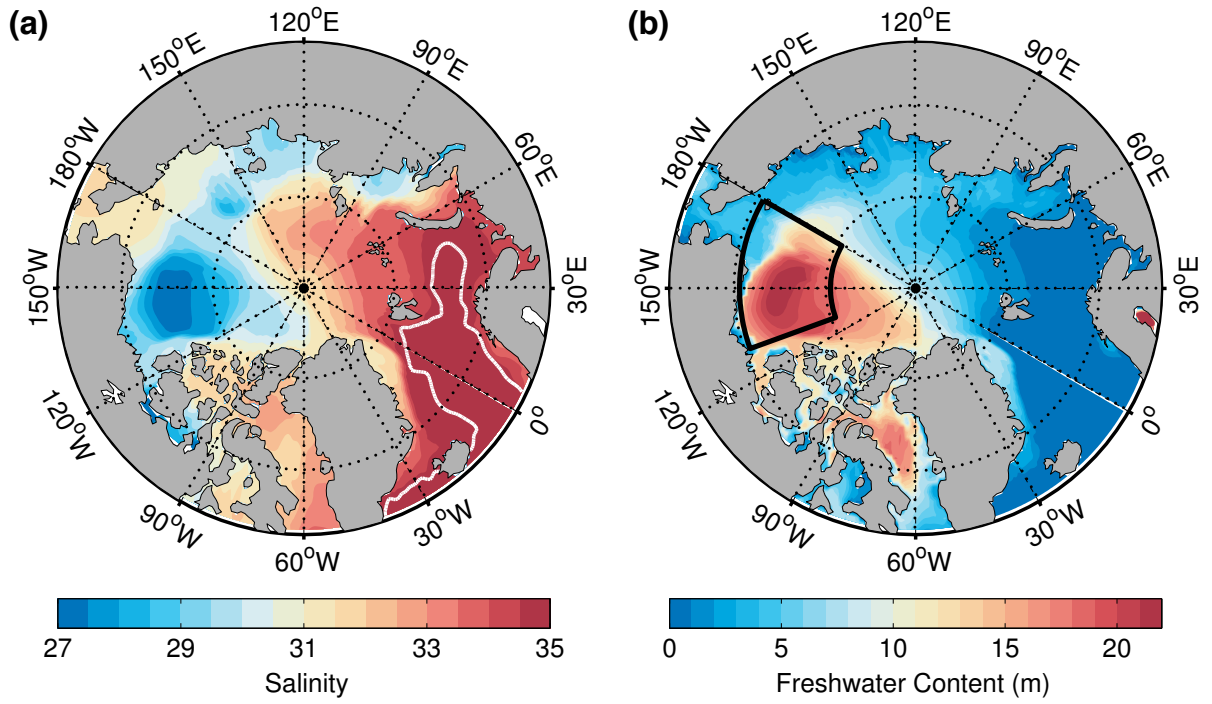

Figure 1.3: (a) Sea surface salinity and (b) liquid freshwater content (FW_c) from MIMOC. The freshwater content is calculated by vertically integrating the salinity anomaly (Equation 1.1) from the surface to the depth of the 34.8 psu isohaline. The black box in (b) marks the location of the Beaufort Gyre as defined by *Proshutinsky et al.* (2009) and *Giles et al.* (2012). It is the single largest region of freshwater storage in the Arctic and will be discussed in more detail in Chapter 2. The white contour in (a) marks the location of the 34.8 psu isohaline.

Dickson et al., 2007, and *Rawlins et al.*, 2010), with the most recent budget constructed by *Haine et al.* (2015). It must be noted, however, that whether the budget is now fully constrained, and whether any surplus/deficit in the supply/export of freshwater to/from the Arctic is significant is still a matter of debate, especially given that the observations of the different components of the freshwater budget vary considerably both in quality and in the period of time over which they were taken. Here, an average freshwater budget is presented based on the most robust and up-to-date observations of each component.

In order of importance, freshwater in the Arctic is sourced from river runoff, inflow through Bering Strait (Figure 1.4), and excess precipitation over evaporation. Based on the observations of *Shiklomanov* (2010) and the ERA-Interim reanalysis product (*Dee et al.*, 2011), river runoff accounts for an average input of 3900 ± 390 km^3 yr^{-1}. This represents approximately 11% of the total global continental river runoff (*Fichot et al.*, 2013), and is driven by the net precipitation that occurs over the Arctic catchment area due to the convergence of water vapour in the atmosphere above 50°N (*Serreze et al.*, 2006).

The inflow of freshwater through Bering Strait equals 2500 ± 300 km^3 yr^{-1} (*Woodgate and Aagaard*, 2005; *Woodgate et al.*, 2006), and is driven by the sea level difference that exists between the Pacific, Arctic, and Atlantic Oceans due to the net atmospheric flux of freshwater from the Atlantic to the Pacific (*Steele and Ermold*, 2007). The interannual variability in the flow through Bering Strait is ≈1000 km^3 yr^{-1}, and exceeds that of all other freshwater sources in the Arctic (*Woodgate et al.*, 2012). The variability is highly correlated with volume flux changes, which are in turn related to changes in the local wind field (about one-third of the volume flux variability) and changes in the Pacific-Arctic sea level difference (about two-thirds of the variability; *Woodgate et al.*, 2012). The flux of ice through the Bering Strait is small compared to the liquid component, and in 2007, for example, it added only another 140 ± 40 km^3 of freshwater into the Arctic (*Travers*, 2012). Finally, excess precipitation over evaporation (i.e. positive P-E) delivers 2000 ± 200 km^3 yr^{-1} of freshwater directly into the Arctic Ocean itself (*Haine et al.*, 2015). With the addition of a small amount of freshwater from icebergs and glacial melt water (330 ± 20 km^3 yr^{-1}; *Bamber et al.*, 2012), the total freshwater input to the Arctic is ≈8900 ± 530 km^3 yr^{-1} (Table 1.1).

Freshwater is exported from the Arctic in both liquid and solid (ice) forms to either side of Greenland through Fram Strait and the CAA (Figure 1.4). The flux through the CAA as measured at Davis Strait is dominated by the liquid component (2900 ± 190 km^3 yr^{-1}; *Curry et al.*, 2014), as the presence of land-fast ice (immobile ice that is attached to coastlines) upstream in the CAA results in a relatively small ice flux (331 ± 45 km^3 yr^{-1}; *Melling*, 2002; *Curry et al.*, 2014). In contrast, the flux through Fram Strait in the East Greenland Current and the West Spitsbergen Current (Figure 1.4) is split approximately equally between an ice flux of 2000 ± 400 km^3 yr^{-1} (*Spreen et al.*, 2009; *Haine et al.*, 2015) and a liquid flux of 2800 ± 420 km^3 yr^{-1} (*Serreze et al.*, 2006; *de Steur et al.*, 2009, 2014). It must be noted that although the West Spitsbergen Current flows into the Arctic Ocean, it counts as a sink of freshwater as its mean salinity is above 34.8 psu. With the addition of the relatively insignificant fluxes through Fury and Hecla straits and the Barents Sea Opening (Figure 1.4) of 200 km^3 yr^{-1} (*Straneo and Saucier*, 2008) and 90 ± 90 km^3 yr^{-1} (*Haine et al.*, 2015), respectively (at the Barents Sea Opening the

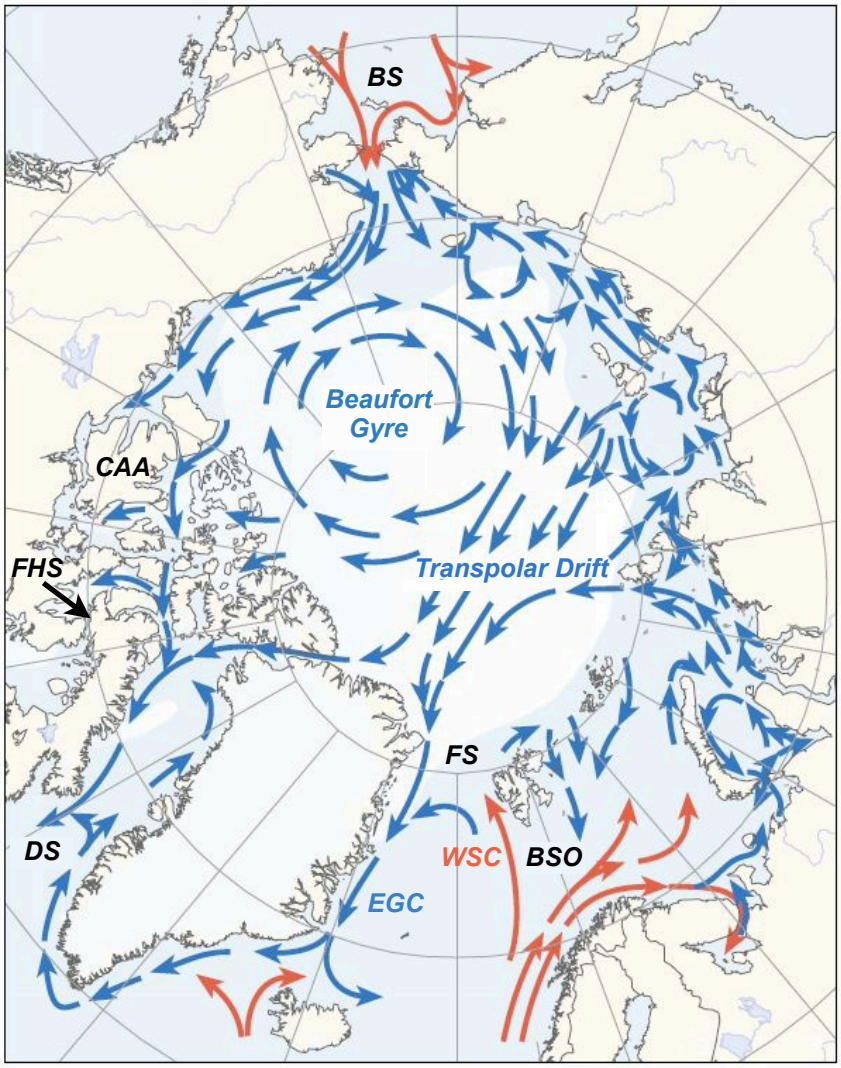

Figure 1.4: Schematic showing the idealised circulation of warm (red) and cold (blue) water in the surface layer of the Arctic Ocean and Nordic Seas, along with the names of the key currents and openings referred to in Section 1.3.1. BS stands for Bering Strait, BSO for the Barents Sea Opening, WSC for the West Spitsbergen Current, EGC for the East Greenland Current, FS for Fram Strait, DS for Davis Strait, FHS for Fury and Hecla straits, and CAA for the Canadian Arctic Archipelago. The figure is adapted from *Huntington* (2001)

inflow of salty Atlantic water compensates for the inflow of the fresh Norwegian Coastal Current), the total freshwater export from the Arctic is ≈8300 ± 600 km^3 yr^{-1} (Table 1.1). Although based on these estimates, there is a residual between the sources and sinks of freshwater in the Arctic Ocean, it is insignificant in light of the large uncertainties in the individual terms, and is likely due to differences in the period of time over which the observations were taken, rather than any systematic surplus in the supply of freshwater to the Arctic.

Within the Arctic Ocean itself (including the CAA and Baffin Bay), a total of more than 110,000 km^3 of freshwater (*Haine et al.*, 2015) is stored in liquid (93,000 km^3) and

ice forms (17,800 km^3; Table 1.1). The distribution of this freshwater is unequal, with the majority stored in the western Arctic and the Beaufort Gyre (Figures 1.3 and 1.4; discussed later). It is clear that the freshwater content of the Arctic Ocean is significantly greater than the magnitude of the fluxes to either side of Greenland, and thus only a small change in the freshwater content may have significant impacts downstream (*Proshutinsky et al.*, 2002). In addition, the large freshwater storage means that the freshwater budget does not have to be balanced at any given time.

The dynamics that determine the magnitude of the freshwater export to either side of Greenland vary, and whilst the volume fluxes at Davis Strait and Fram Strait are strongly anti-correlated, the freshwater fluxes are not (*Lique et al.*, 2009). At Davis Strait, variability in the liquid freshwater flux is generally determined entirely by variability in the volume transport (*Lique et al.*, 2009), whereas at Fram Strait, the correlation is weak (*Lique et al.*, 2009; *Jahn et al.*, 2012). Instead, the liquid freshwater export at Fram Strait depends more strongly on variability in the outflow salinity (*Jahn et al.*, 2012), which varies strongly due to sea ice formation/melt north of Greenland (*Lique et al.*, 2009). In addition, the ice flux through Fram Strait is correlated with the across-strait atmospheric pressure difference (*Tsukernik et al.*, 2010), which drives southward winds through the strait.

The origin of the freshwater exported to either side of Greenland also varies, and can be determined through the analysis of long-term hydrographic records (*Rudels et al.*, 2004), nutrient data (e.g. nitrate and phosphate; *Jones et al.*, 1998), oxygen isotopes (*Dodd et al.*, 2012), and the use of Lagrangian particle trackers in models of the Arctic Ocean circulation (*Lique et al.*, 2010). The export through the CAA is composed primarily of Pacific and Atlantic derived water that has entered the Arctic through Bering Strait and the Barents Sea, respectively. The Pacific water, which, due to denitrification in the productive regions of the Bering and Chukchi seas, is identified by an elevated phosphate concentration for a given nitrate concentration compared to Atlantic water (*Jones et al.*, 2003), is generally found at the surface, whereas the Atlantic water is found both at depth and at the surface through mixing with Pacific-derived waters. Lagrangian particle tracking (*Lique et al.*, 2010) shows that the Pacific water is advected towards the CAA

Freshwater Sources	**Annual Flux (km^3 yr^{-1})**	**Reference**
River runoff	3900 ± 390	*Shiklomanov*, 2010; *Dee et al.*, 2011
Bering Strait (liquid)	2500 ± 300	*Woodgate and Aagaard*, 2005; *Woodgate et al.*, 2006
Bering Strait (ice)	140 ± 40	*Travers*, 2012
P-E	2000 ± 200	*Haine et al.*, 2015
Greenland (icebergs + melt water)	330 ± 20	*Bamber et al.*, 2012
Total	≈ 8900 ± 530	

Freshwater Sinks	**Annual Flux (km^3 yr^{-1})**	**Reference**
CAA (liquid)	-2900 ± 190	*Curry et al.*, 2014
CAA (ice)	-331 ± 45	*Curry et al.*, 2014
Fram Strait (liquid)	-2800 ± 420	*Serreze et al.*, 2006; *de Steur et al.*, 2009, 2014
Fram Strait (ice)	-2000 ± 400	*Spreen et al.*, 2009; *Haine et al.*, 2015
Fury and Hecla straits	-200	*Straneo and Saucier*, 2008
Barents Sea Opening	-90 ± 90	*Haine et al.*, 2015
Total	≈ -8300 ± 600	

Freshwater Reservoirs	**Volume (km^3)**	**Reference**
Liquid	93,000	*Haine et al.*, 2015
Ice	17,800	*Haine et al.*, 2015
Total	110,800	

Table 1.1: State-of-the-art estimate of the Arctic freshwater fluxes and reservoir volumes. Positive fluxes freshen the Arctic, whilst negative fluxes remove freshwater from the Arctic.

through the surface layers of the Canadian Basin with a transit time of ≈10 years, whilst *Rudels et al.* (2004) trace the Atlantic water to the Barents Sea winter mixed layer. In contrast, by analysing concurrent measurements of salinity, $\delta^{18}O$, nitrate, and phosphate, and by constructing a 4-end-member mass balance, *Dodd et al.* (2012) show that the export through Fram Strait is composed almost entirely of Atlantic-derived water and meteoric water (in agreement with modelling studies; *Lique et al.*, 2010), and the Pacific component is small but highly variable (e.g. *de Steur et al.*, 2015).

The circulation within the surface layer is primarily wind-driven, and consequently varies with the prevailing atmospheric conditions over the Arctic. The main mode of atmospheric variability in the Arctic is that associated with the Arctic Oscillation, which reflects the strength of the pressure gradient between the polar and midlatitudes, and is defined as the first empirical orthogonal function of the sea level pressure poleward of 20° latitude (*Thompson and Wallace*, 1998). The negative phase of the Arctic Oscillation brings relatively high (low) sea-level pressures to the Arctic (midlatitudes), and vice-versa for the positive phase. During average conditions (Figures 1.4 and 1.5a), wind-driven flow in the eastern Arctic (including the Laptev Sea, Kara Sea, and Barents Sea) is generally to the north and/or west, moving liquid freshwater and sea ice out into the deep Makarov and Eurasian basins and forming the Transpolar Drift (Figure 1.4). In the western Arctic, the anticyclonic winds associated with the atmospheric Beaufort High drive an anticyclonic circulation at the surface known as the Beaufort Gyre (Figure 1.5). Freshwater accumulates in the centre of the gyre due to Ekman convergence, and hence it contains around 25% of the total freshwater stored in the Arctic (Figure 1.3b; *Proshutinsky et al.*, 2009). When the Arctic enters a positive phase of the Arctic Oscillation (such as during the summer of 1989; Figure 1.5b), the sea-level pressure over the entire Arctic is generally lower than average, and a weaker Beaufort High/Beaufort Gyre tends to release freshwater to the shelves over a number of years (*Proshutinsky and Johnson*, 1997). Eurasian river runoff flows further east into the East Siberian Sea (*Steele and Boyd*, 1998), before leaving the shelf and penetrating into the central Arctic and Canadian Basin (*Morison et al.*, 2012). Consequently, the Transpolar Drift shifts eastward, directing some fraction of the freshwater that may have been released from the weaker Beaufort

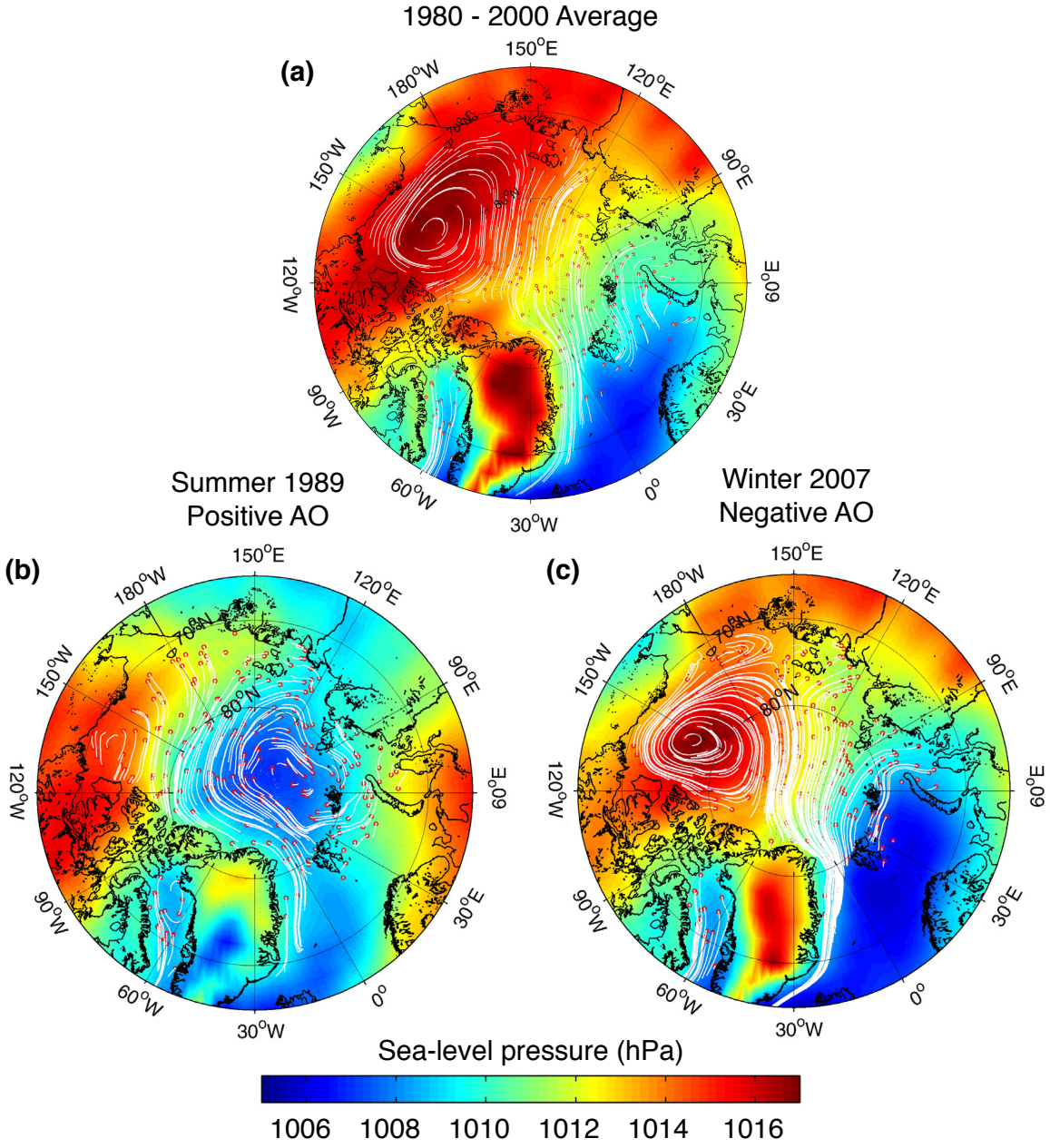

Figure 1.5: Figure from *Haine et al.* (2015) showing sea-level pressure (coloured contours) and surface flow derived from the average sea ice velocity (based on the Polar Pathfinder Sea Ice Motion dataset; *Fowler et al.*, 2013) during (a) average conditions, (b) a positive phase of the Arctic Oscillation, and (c) a negative phase of the Arctic Oscillation. The red dots indicate the starting point of each ice drift trajectory which lasts two years.

Gyre towards Fram Strait, where it can be exported into the North Atlantic (e.g. *Condron et al.*, 2009; *Stewart and Haine*, 2013), and the thick multiyear ice found against the coast of Greenland and the CAA is generally advected out of the Arctic, decreasing the overall thickness of ice (*Rigor and Wallace*, 2004). In contrast, during the negative phase of the Arctic Oscillation (e.g. during the winter of 2007; Figure 1.5c), the winds associated with the atmospheric Beaufort High are stronger, and over several years freshwater accumulates

within the Beaufort Gyre and the Canadian Basin (*Proshutinsky et al.*, 2009). Eurasian river runoff is exported directly into the Transpolar Drift (*Dmitrenko et al.*, 2008), and is advected towards Fram Strait, whilst the thick multiyear ice against Greenland is generally retained within the Arctic, as it recirculates within the stronger Beaufort Gyre (*Rigor and Wallace*, 2004).

Despite a significant increase in our knowledge regarding the Arctic's surface freshwater layer since the International Polar Year (for example see *McPhee et al.*, 2009), a large number of open questions still remain regarding the dynamical processes that determine its circulation and the Arctic freshwater budget. For example, state-of-the-art Intergovernmental Panel on Climate Change (IPCC)–class climate models still exhibit significant variability (ca. 100%) in the magnitude of the ice and freshwater export to either side of Greenland (despite their relatively consistent freshwater budgets; *Holland et al.*, 2007), and models evaluated as part of the Arctic Ocean Model Intercomparison Project (AOMIP) show significant deficiencies in their ability to simulate the cold halocline (*Holloway et al.*, 2007), sea ice velocities (*Martin and Gerdes*, 2007), sea ice fractions (*Johnson et al.*, 2007), and Arctic freshwater export (*Jahn et al.*, 2012). In addition, although observations consistently show that the freshwater content of the Arctic, and in particular the western Arctic, has been increasing rapidly over the past decade (e.g. *Giles et al.*, 2012; *Rabe et al.*, 2014), there is significant disagreement over the mechanisms responsible. Whilst *Morison et al.* (2012) argue that between 2005-2008 the trend towards more positive Arctic Oscillation atmospheric conditions and the diversion of Eurasian river runoff into the western Arctic Ocean can explain the dominant freshwater content changes, *Giles et al.* (2012) suggest that it is the strength of the Beaufort High, coupled with an increase in the efficiency of momentum transfer through the declining sea ice cover, that is responsible for the accumulation of freshwater. Given the importance of the surface freshwater layer and the cold halocline in controlling the vertical exchange of heat and momentum between the atmosphere and ocean, in isolating the sea ice cover at the surface from the heat contained within the Atlantic layer, and in linking the Arctic to the lower latitudes through the export of freshwater to either side of Greenland, more work must be done to understand the circulation of this layer. This is the aim of the work

presented in Chapter 2 of this thesis, which explores the dynamics behind the accelerated accumulation of freshwater in the Beaufort Gyre.

1.3.2 The Atlantic Layer

Atlantic water in the Arctic Ocean is sourced from the warm and saline waters that originate in the Gulf Stream and flow across the Greenland-Scotland Ridge into the Nordic Seas (*Hansen et al.*, 2008). As this water flows northward in the Norwegian Atlantic Current (*Beszczynska-Möller et al.*, 2011), the flow bifurcates at the Barents Sea Opening, with one branch continuing north to Fram Strait as the West Spitsbergen Current, and one flowing into the Barents Sea (Figure 1.6; *Lien et al.*, 2013).

The flow of Atlantic water through the Barents Sea consists of multiple narrow currents that follow the shallow bottom topography (*Beszczynska-Möller et al.*, 2011). During its transit through the region, the density of the Atlantic water inflow is heavily modified due to atmospheric cooling, ice formation, precipitation, sea ice melt, and mixing with fresh surface and coastal waters; as a result, a number of distinct water masses are created (*Beszczynska-Möller et al.*, 2011). Lighter (i.e. fresher) variants feed the surface waters of the Eurasian and Canadian basins (forming a front over the Alpha-Mendeleev ridge between the Atlantic-derived and Pacific-derived surface waters; *Karcher and Oberhuber*, 2002), and are generally recirculated to the Fram Strait through the Transpolar Drift. In contrast, heavier variants enter the Arctic Ocean as Barents Sea Branch Water through the St. Anna Trough (Figures 1.1 and 1.6), and circulate at mid-depth in the Atlantic layer (Figure 1.2; *Karcher et al.*, 2012). The inflow of Atlantic water into the Barents Sea ensures that a significant proportion of the region remains relatively ice-free all year-round, and thus the majority of heat contained within this branch of the Atlantic water inflow is generally lost to the atmosphere before it reaches the central Arctic Ocean. Indeed, *Smedsrud et al.* (2010) show that the Atlantic water loses up to 92% of its heat within the southern Barents Sea, and as it enters the Arctic, it has often been cooled to below 0°C (*Schauer et al.*, 2002b). Overall, the mean volume flux of Atlantic water that enters the Arctic Ocean through the Barents Sea is 1.5 Sv (1 Sv = 10^6 m^3 s^{-1} = 31,500 km^3 yr^{-1}; *Schauer et al.*, 2002a).

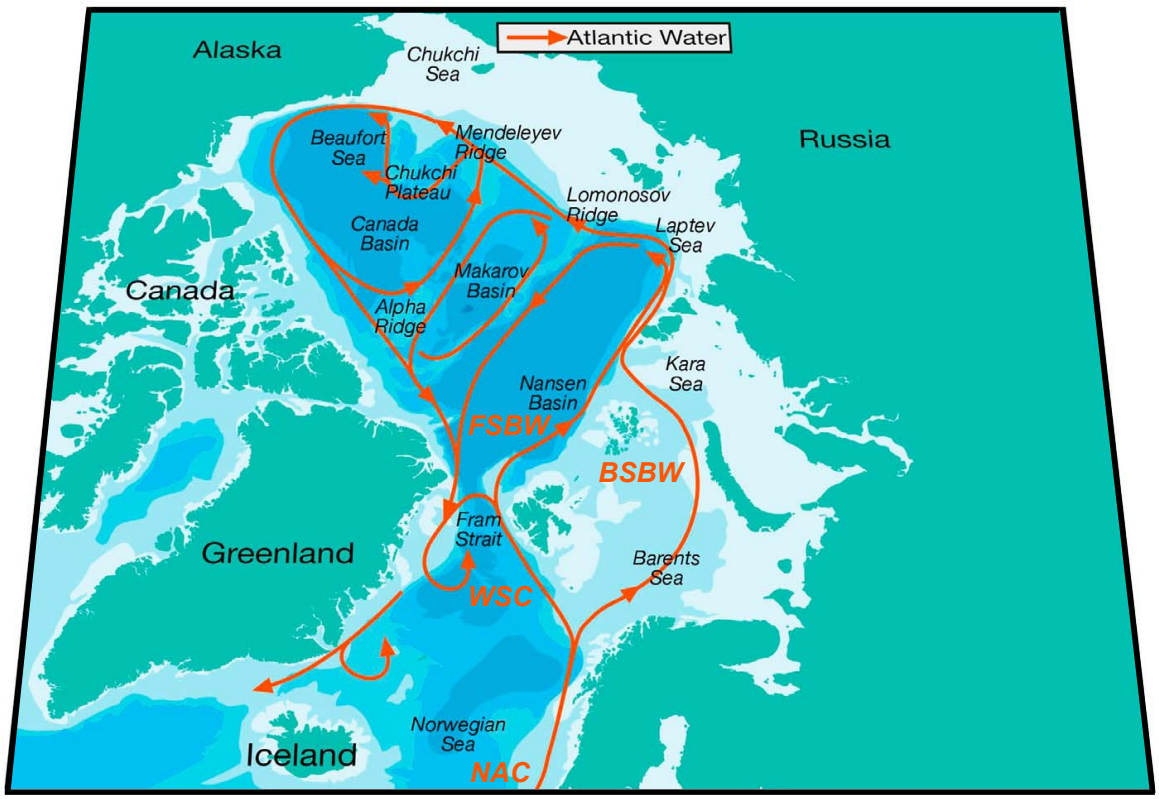

Figure 1.6: Schematic of the circulation in the Atlantic layer from its source in the Nordic Seas and its bifurcation at the Barents Sea Opening, through to its basin-wide circulation in the mid-depth pan-Arctic boundary current and eventual export through Fram Strait and the CAA (not shown on the schematic). NAC stands for the Norwegian Atlantic Current, WSC for the West Spitsbergen Current, FSBW for Fram Strait Branch Water, and BSBW for Barents Sea Branch Water. The figure is adapted from *Karcher et al.* (2007).

For the Atlantic water that continues northward from the Barents Sea Opening and that enters the Arctic Ocean through Fram Strait in the West Spitsbergen Current (Figure 1.6), the upper layers are gradually transformed into a colder and less saline water mass through the effects of sea ice melt and mixing with fresh surface waters of Arctic origin (*Rudels et al.*, 1996, 2004). This surface transformation creates a layer of strong stratification that essentially isolates the bulk of the Atlantic water in this branch from surface convection and the cooling effects of the atmosphere, and thus in contrast to the Barents Sea inflow, the Atlantic water that enters the Arctic through Fram Strait maintains its warm core signature (2-3°C; *Beszczynska-Möller et al.*, 2012). This signature has historically been used to trace the pathway and transformation of Atlantic water throughout the Arctic Ocean (*Coachman and Barnes*, 1963). North of Fram Strait, the Atlantic water inflow turns to the east and continues as Fram Strait Branch Water in a warm and saline boundary current along the southern margin of the Nansen Basin (Figure 1.6;

Rudels, 2015). The long-term mean volume flux of Atlantic water through Fram Strait (excluding Atlantic water that is immediately returned to the south due to the complex recirculations in the strait; *Rudels et al.*, 2000) is 3.7 ± 1.6 Sv (*Fahrbach et al.*, 2001; *Schauer et al.*, 2004).

Fram Strait Branch Water meets the Barents Sea Branch Water at the St. Anna Trough, where mixing between the two branches creates interleaving layers that are observed in the interior of the Eurasian Basin (*Rudels*, 2015). The two water masses continue to circulate around the central deep Arctic Basins in a cyclonic topographically steered pan-Arctic boundary current (Figure 1.6; *Aksenov et al.*, 2011), with Fram Strait Branch Water generally lying above or being displaced off the slope by the denser Barents Sea Branch Water (*Schauer et al.*, 2002b; *McLaughlin et al.*, 2002). The large-scale submarine ridges that stretch across the deep central basins (Figure 1.1) impose topographic constraints on this boundary current, causing the flow to be diverted into the interior of the Arctic Ocean. This creates a complex system of basin-wide cyclonic gyres (Figure 1.6), and results in the ventilation of the interior basins through processes such as double diffusion and thermohaline intrusions (*McLaughlin et al.*, 2009). During its transit along the Arctic boundary, the Atlantic water undergoes significant freshening and cooling, and after a period of time that depends upon the specific pathway taken (15-30 years), it is exported to the North Atlantic in surface and intermediate water masses (*Karcher and Oberhuber*, 2002; *Karcher et al.*, 2007).

The cooling of the Atlantic water as it circulates around the Arctic Ocean (the maximum core temperature decreases from the 2-3°C seen in the Nansen Basin to the 0.5°C seen in the Canadian Basin) implies that heat is lost to the overlying freshwater layer (e.g. *Lique et al.*, 2014), and thus the heat contained within the Atlantic layer plays a role in the sea ice budget at the surface. Although this role is currently small (*Polyakov et al.*, 2010 suggest that the present-day vertical heat flux from the Atlantic layer accounts for only 5% of the current net sea ice melt), if this heat flux were to increase in the future due to stratification changes in the cold halocline, or increased turbulent mixing due to stronger wind forcing, the heat contained within the Atlantic layer may contribute more significantly to the ongoing melting of Arctic sea ice. The dynamics of these future

changes are explored in more detail in Chapter 3.

There is still significant uncertainty regarding which mechanisms are responsible for controlling the pan-Arctic boundary current of Atlantic water, and different simulations of the Atlantic water circulation in many state-of-the-art climate models (including those that are identically forced) can be wildly different in terms of intensity, direction and pathway (*Steiner et al.*, 2004; *Karcher et al.*, 2007; *Holloway et al.*, 2007). A number of different forcing mechanisms have been proposed, with the majority implying that the strength and variability of the Atlantic water circulation are set by remote, rather than local, forcing. For example, *Yang* (2005) and *Karcher et al.* (2007) suggest that the circulation of Atlantic water in the Eurasian Basin is highly sensitive to the net flux of potential vorticity through St. Anna Trough, which constrains the flow in the pan-Arctic boundary current to be cyclonic in order to maintain a balance between the potential vorticity flux and dissipation. In addition, *Peralta-Ferriz et al.* (2011, 2014) suggest that northward winds over the Nordic Seas can enhance the northward geostrophic flow into the Arctic Ocean through Fram Strait, and *Aksenov et al.* (2011) propose that non-local wind forcing over the Barents Sea can also play an important role in determining the circulation. It has further been suggested by *Holloway* (1992) and *Nazarenko et al.* (1998) that eddy-topography interactions may result in a cyclonic along slope boundary current, and direct interactions between the surface layer and the Atlantic layer may be important in the Canadian Basin (*Lique et al.*, 2015). Overall, it is likely that each of these different mechanisms will play a role in setting the circulation in the Atlantic layer, and assessing their relative importance remains a key outstanding question in Arctic oceanography.

1.4 The Changing Arctic Ocean

As stated earlier, the Arctic Ocean plays a leading role in the global climate despite its limited areal extent. However, the region is currently undergoing a period of rapid change, and many different aspects of the Arctic environment are evolving at a rate never previously observed. For example, mean atmospheric temperatures over the Arctic have been rising at twice the rate of the global average (*Hassol*, 2004), sea ice thickness and extent has been rapidly declining (*Cavalieri and Parkinson*, 2012), a substantial warming

in many different layers of the Arctic Ocean has been observed (e.g. *Polyakov et al.*, 2005; *Woodgate et al.*, 2006; *Steele et al.*, 2008; *Timmermans et al.*, 2014), the Arctic hydrological cycle is becoming intensified (*Held and Soden*, 2006), and discernible changes to the Arctic marine ecosystem are occurring (*Wassmann et al.*, 2011). These changes are likely to drastically alter the circulation and the dynamics of the Arctic Ocean, and may have far-reaching consequences. As a result, it is critical to understand and quantify not only the dynamics of the present-day Arctic Ocean, but to also understand how these dynamics may be affected by the rapidly changing Arctic environment. In this section, some of the more significant environmental changes which motivate the work in this thesis are examined, and the effects that these changes may have within the Arctic itself as well as on the global climate are considered.

1.4.1 Rapid Sea Ice Decline

One of the clearest indicators of change in the Arctic is the rapid decline that has been observed in the sea ice cover (Figure 1.7). At the start of the satellite era (i.e. 1979), the maximum sea ice extent in early March covered an area of between 14 and 16 million km^2, decreasing to an annual minimum in September of between 5 and 7.5 million km^2 (Figure 1.7a; *Deser and Teng*, 2008). However, over the past 33 years (1979 to 2012), monthly mean sea ice extent has decreased at a rate of -3.8 $\pm$ 0.3% per decade (which increases to -7.0 $\pm$ 1.5% per decade if just autumn months are considered), and over recent years, it appears as if this trend may have accelerated (*Stroeve et al.*, 2012b; *Vaughan et al.*, 2013). In 2007 the September sea ice extent reached a record minimum of 4.3 million km^2, but this was surpassed in 2012 with a minimum extent of only 3.6 million km^2 (Figure 1.7b; *Haine et al.*, 2015). Sea ice thickness and volume are also declining: using submarine and satellite observations *Kwok and Rothrock* (2009) show that sea ice thickness at the end of summer has decreased from 3.02 m between 1958-1976 to 1.43 m between 2003-2007, and the Polar Science Centre Pan-Arctic Ice Ocean Modelling and Assimilation System (PIOMAS; *Zhang and Rothrock*, 2003) suggests that sea ice volume has declined by -2.8 $\times$ 10^3 km^3 per decade between 1979 and 2010 (*Schweiger et al.*, 2011), in general agreement with the shorter observational trends from ICESat (*Kwok et al.*, 2009) and

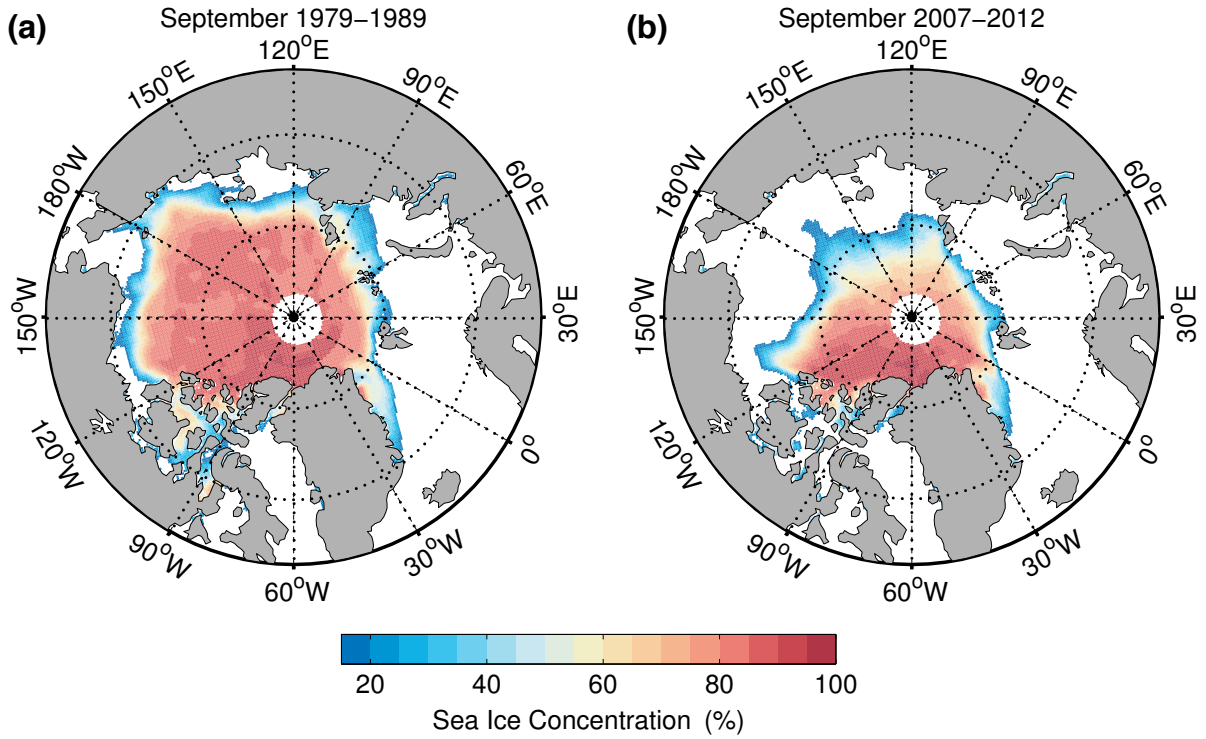

Figure 1.7: Mean September sea ice concentration between (a) 1979-1989, and (b) 2007-2012 from the Special Sensor Microwave/Imager (SSM/I) and Special Sensor Microwave Imager/Sounder (SSMIS) satellite instruments (*Maslanik and Stroeve*, 1999). Sea ice concentrations below 15% are assumed to represent open water and have been set to zero.

CryoSat-2 (*Laxon et al.*, 2013). The decrease in the average thickness and volume of sea ice has been driven by the preferential loss of thick multiyear ice over thin single year ice, such that the 16% per decade decline in areal extent of multiyear ice between 1981 and 2011 (*Comiso*, 2012) is greater than the rate of decline of the sea ice cover as a whole, and the Arctic is shifting towards a more seasonal first year ice regime (*Maslanik et al.*, 2011). Overall, analysis of the suite of global climate models which make up the Climate Model Intercomparison Project, Phase 5, suggests that the Arctic could become ice-free in summer sometime between the middle and the end of the century (*Stroeve et al.*, 2012a), whilst using different statistical methods, *Wang and Overland* (2009) suggest it could be as early as 2037.

To date, sea ice decline in the Arctic appears to have been primarily forced by temporal and spatial changes in atmospheric conditions and circulation (*Stroeve et al.*, 2012b; *Vihma*, 2014). The mean atmospheric temperature over the Arctic has risen by more than 3.5°C between 1948 and 2003 (*Lindsay and Zhang*, 2005), leading to a reduced equilibrium ice thickness and more open water in September (*Stroeve et al.*, 2012b). The

corresponding existence of thinner ice the following spring and the earlier onset of melting (*Markus et al.*, 2009) promotes the formation of more open water in summer, enhancing the ice-albedo feedback effect (whereby the lower albedo of open water causes more heat to be absorbed in the upper few meters of the ocean and therefore more ice to melt; *Curry et al.*, 1995) and leading to even more sea ice loss and open water. The trend towards a thinner and younger sea ice in the spring (*Maslanik et al.*, 2007) has also preconditioned the sea ice cover to be more susceptible to the patterns of atmospheric circulation that lead to sea ice loss (e.g. positive phases of the Arctic Oscillation and the Arctic atmospheric Dipole Anomaly; *Wang et al.*, 2009). Indeed, *Lindsay and Zhang* (2005) conclude that after preconditioning by warmer atmospheric temperatures, the shift to the positive phase of the Arctic Oscillation in 1989 increased the fraction of open water in summer, and along with the subsequent role played by the ice albedo feedback effect, was responsible for the significant decrease in the thickness of ice that occurred over the following decade. Similarly, *Zhang et al.* (2008) conclude that the record minimum sea ice extent in 2007 was triggered by a change in the atmospheric circulation that considerably strengthened the ice motion and the Transpolar Drift, leading to the formation of large open water areas in the western Arctic Ocean and enhanced melting through the ice-albedo feedback effect. In addition, an intense cyclonic storm that formed over the central Arctic in August 2012 may have been partly responsible for the the record minimum sea ice extent that occurred later in that year (*Simmonds and Rudeva*, 2012; *Parkinson and Comiso*, 2013).

Whilst atmospheric forcing may dominate, it has also been suggested that the ocean itself may be playing a role in the ongoing melting of Arctic sea ice (*Polyakov et al.*, 2012). Indeed, *Woodgate et al.* (2010) suggest that the inflow of warm Pacific water through Bering Strait may have affected the 2007 record minimum sea ice extent, and *Zhang et al.* (2013) propose that enhanced storm-driven mixing in 2012 increased the bottom melting of ice by a factor of four. In addition, the increasing fraction of open water in summer is allowing significantly more sunlight to be absorbed into the upper ocean (*Perovich et al.*, 2008), raising the heat content of the near surface layers (*Jackson et al.*, 2010) and affecting the formation of ice the following winter (*Steele et al.*, 2011;

Timmermans, 2015).

The impacts of the declining Arctic sea ice cover are significant and far ranging. Historically, the thick and extensive sea ice cover has shielded the upper Arctic Ocean from direct wind forcing, dampening its response to atmospheric forcing and leading to isolated water masses and slow redistribution of properties (*Rainville et al.*, 2011). However, as the sea ice cover thins and retreats, and more of the ocean becomes directly forced by the winds, an increase in the efficiency of momentum transfer may lead to a spin-up of the Arctic Ocean by increasing the annual mean ocean surface stress (i.e. the integrated stress at the ocean surface arising from the wind blowing over the partly ice-covered Arctic). Furthermore, if the period of time over which the Arctic Ocean adjusts to a change in forcing is close to seasonal, then the emergence of an asymmetrical annual cycle in ocean surface stress, or differences between spin-up and spin-down timescales, may cause multiyear trends in the circulation of the wind-driven surface layer. Indeed, *Giles et al.* (2012) have already hypothesised that freshwater accumulation in the Beaufort Gyre is accelerating in response to the enhanced momentum transfer, and *Yang* (2009) conclude that the ice velocity in the Beaufort Sea accelerated between 1979-1986 and 1997-2004 due to a change in the ice dynamics rather than a shift in the geostrophic winds. Changes such as these may have significant impacts on the Arctic Ocean freshwater budget and the export of freshwater to either side of Greenland, and hence Chapter 2 of this thesis explores the dynamical link between sea ice decline and the accelerated accumulation of freshwater in the Beaufort Gyre.

At the same time, by generating strong inertial motions at the base of the mixed layer, winds blowing over a largely ice-free Arctic may fundamentally change the levels of turbulence found within the Arctic Ocean water column (*Rainville et al.*, 2011). At present, the magnitude of internal wave mixing in the Arctic is one to two orders of magnitude smaller than that observed at lower latitudes (e.g. *Levine et al.*, 1985), and consequently the vertical diffusive heat flux from the Atlantic layer negligible (e.g. *Polyakov et al.*, 2010). In the future, however, an increase in the magnitude of internal wave mixing may drive an elevated vertical heat flux and erode the stratification associated with the cold halocline, decreasing the extent to which the sea ice cover is isolated from the heat contained within

the Atlantic water. As there is enough heat in the Atlantic layer to melt all sea ice in the Arctic within a few years (*Turner*, 2010), elevated internal wave mixing may represent a strong positive feedback for the ongoing melting of Arctic sea ice. Therefore, in Chapter 3 of this thesis the effects of elevated internal wave mixing and enhanced freshwater input (discussed in more detail in Section 1.4.2) on the stratification and the vertical heat flux are investigated in more detail in a 1D model of the Arctic Ocean water column. In addition, by affecting the levels of turbulence in the water column, the decrease in Arctic sea ice cover may affect the magnitude of vertical nutrient fluxes (*Nishino et al.*, 2015) and thus the timing and extent of phytoplankton blooms in the Arctic (*Ardyna et al.*, 2014), both of which will alter the dynamics of the Arctic Ocean ecosystem and carbon cycle.

Furthermore, the declining Arctic sea ice cover is also fundamentally changing the distribution of the Sun's energy over the Earth's surface, and hence it has the potential to impact both local and remote aspects of the global climate (*Aagaard and Carmack*, 1994; *Budikova*, 2009). Locally, the ice-albedo feedback effect has caused the mean atmospheric temperature over the Arctic to rise at almost twice the rate of the global average (a process known as "Arctic Amplification"; *Serreze et al.*, 2009; *Screen and Simmonds*, 2010), and the increase in the heat flux from the ocean to the atmosphere due to the large open water fractions in September has reduced the atmospheric static stability (*Overland and Wang*, 2010), increased baroclinicity (*Jaiser et al.*, 2012) and changed storm activity (*Simmonds and Keay*, 2009). Beyond the Arctic, *Francis and Vavrus* (2012) have suggested that by weakening the equator-to-pole temperature difference, Arctic Amplification is modifying the midlatitude jet stream by decreasing the strength of the west-to-east zonal winds and increasing the Rossby wave amplitude (i.e. creating a more sinuous jet stream). A slower and more sinuous jet stream may result in the slower propagation of weather patterns in midlatitudes, increasing the probability of extreme weather events such as the anomalously cold conditions and large snow falls that have been observed over North America, Europe and east Asia between 2007 and 2011 (*Liu et al.*, 2012). It must be noted, however, that more recent work by *Barnes* (2013) has questioned the physics behind the response of the midlatitude jet stream to Arctic sea ice decline, and conclude that the dynamical link proposed by *Francis and Vavrus* (2012) is an artefact of their methodology.

Instead, *Screen et al.* (2014b) suggest that future sea ice loss will in fact reduce the risk of cold extremes over North America by amplifying atmospheric warming over the Arctic. Despite these contradictions, sea ice in the Arctic is changing rapidly, and the climate of the northern hemisphere is likely to be strongly affected (*Barnes*, 2013). Although the relationship between Arctic Amplification and midlatitude weather appears complex, and other processes/internal variability may be important (*Screen et al.*, 2014a; *Barnes and Screen*, 2015), the ramifications of more extreme weather events over Europe and North America motivates significant effort into understanding the role that the changing Arctic will play in Atlantic sector weather.

1.4.2 The Changing Freshwater Budget

Over the last few decades, observations have shown that the freshwater budget of the Arctic Ocean has been changing significantly. Between 1936 and 1999 Eurasian river runoff increased by 7% (*Peterson et al.*, 2002), which is consistent with an increase in precipitation over the Arctic (e.g. *Deser et al.*, 2015), and *Haine et al.* (2015) estimate that between 2000 and 2010 the annual freshwater input to the Arctic increased to 9400 $\pm$ 490 km^3 yr^{-1}. By 2003-2007 the freshwater content of the Beaufort Gyre had increased by 1000 km^3 compared to pre-1990s climatology (*Proshutinsky et al.*, 2009), and by 2008 had perhaps reached 8500 km^3 (*McPhee et al.*, 2009), reflecting the accelerated freshwater accumulation that has been observed by *Giles et al.* (2012) since 2002. Over the entire Arctic, *Rabe et al.* (2011) suggest that between 1992-1999 and 2006-2008 the freshwater content increased by 8400 $\pm$ 2000 km^3, and between 2000 and 2012, *Alkire et al.* (2015) observed a mean annual increase in freshwater input from sea ice melt of 292 $\pm$ 97 km^3 yr^{-1}, associated with the observed decline in sea ice volume. Overall, between 1992 and 2012 the freshwater content of the Arctic Ocean has been increasing at a rate of 600 $\pm$ 300 km^3 yr^{-1} (*Rabe et al.*, 2014).

In the future, accumulation of freshwater in the Arctic is expected to continue, as a warming climate drives an enhanced hydrological cycle with greater atmospheric moisture transport to the polar regions (*Held and Soden*, 2006). Consequently, coupled climate models indicate that precipitation and river runoff is likely to increase over the twenty-

first century (e.g. *Kattsov et al.*, 2007), with the Community Climate System Model, Version 4 (CCSM4) predicting that precipitation will increase by ≈40% polewards of 70°N by 2100 (*Vavrus et al.*, 2012). It must be noted, however, that in CCSM4 the increase in precipitation is largely driven by an increase in local evaporation during winter rather than increased atmospheric moisture transport, suggesting that the hydrological cycle is also enhanced within the Arctic itself due to winter sea ice retreat (*Bintanja and Selten*, 2014). By 2100 the total freshwater input to the Arctic (i.e. Bering Strait inflow, river runoff and excess precipitation over evaporation) is expected to have increased to $\geq$ 11,000 km^3 yr^{-1}, whilst the total freshwater export (i.e. liquid and ice fluxes through Fram Strait and the CAA) is expected to have increased to 10,000 km^3 yr^{-1} (*Haine et al.*, 2015). These estimates suggest that by 2100 the Arctic freshwater budget will be unbalanced, and freshwater will continue to accumulate in the region despite the elevated export.

Within the Arctic Ocean itself, enhanced freshwater input is likely to affect a number of different aspects of its circulation and dynamics. By increasing the strength of the stratification at the surface, it will act to offset the effects of the elevated internal wave mixing (as discussed in Section 1.4.1), and may reduce the overall probability that an enhanced diffusive heat flux from the Atlantic layer will melt a significant quantity of sea ice in the future (see Chapter 3). Moreover, by altering the levels of turbulence in the water column, stronger stratification may also reduce the turbulent exchange of heat and momentum between the atmosphere, ice, and ocean, and thus is perhaps poised to affect the dynamics and stability of the atmosphere, the circulation in the surface freshwater layer, and the state of the sea ice cover at the surface (indeed, the freezing point of freshwater is higher than that of seawater, and enhanced freshwater input to the Arctic may aid sea ice formation). In addition, primary productivity in the Arctic has been shown to be sensitive to both the levels of turbulence in the water column (as it determines the vertical nutrient flux), and the availability of light (*Popova et al.*, 2010). Whilst elevated internal wave mixing would tend to amplify the nutrient flux and decrease the light availability by mixing phytoplankton deeper into the water column, stronger stratification at the surface will tend to have the opposite effect, decreasing the

vertical nutrient flux but holding the phytoplankton near the surface for longer. Hence, the complex interplay between elevated freshwater input and enhanced internal wave mixing may be important in determining the future evolution of Arctic primary productivity, with implications for the Arctic carbon cycle.

The impacts of elevated Arctic freshwater export are also likely to be significant. Freshwater is exported from the Arctic into the regions of dense water formation (i.e. the Greenland and Labrador seas), and therefore by decreasing the surface salinity and preventing the formation of new dense waters even in the presence of severe winter cooling, elevated freshwater export may cause the AMOC to slow. Indeed, *Jahn and Holland* (2013) show that under the most extreme CO_2 emission scenario (RCP8.5), the AMOC in the CCSM4 model decreases in strength by up to 72% in the future due to elevated Arctic freshwater export and a shutdown of North Atlantic deep convection, whilst the idealised freshwater hosing experiments of, for example, *Stouffer et al.* (2006), show that the AMOC slows by 30% after 100 years in response to a 0.1 Sv increase in the supply of freshwater to the North Atlantic. Similarly, during the Great Salinity Anomalies of the late 1960's and early 1980's during which elevated freshwater export from the Arctic caused the Labrador and Nordic seas to undergo decadal periods of freshening (e.g. *Dickson et al.*, 1988; *Belkin et al.*, 1998; *Belkin*, 2004), it is believed that deep convection was interrupted (e.g. *Schlosser et al.*, 1991), and may have even entered a feedback loop that made the re-initiation of deep convection in the early 1970s increasingly more difficult (*Gelderloos et al.*, 2012). Furthermore, evidence from palaeoclimatic records also suggests that the northern hemisphere-wide cooling that is thought to have occurred during the 8.2 kyr event was caused by the sudden emptying into the North Atlantic of a large proglacial lake formed by the retreating Laurentide Ice Sheet (Lake Agassiz), and the subsequent slowing/shutdown of the AMOC (*Teller et al.*, 2002; *Alley and Ágústsdóttir*, 2005).

The effects of a weakened AMOC will be felt globally, and are likely to have significant societal impacts. Coupled climate models suggest that a weakening of the AMOC will decrease the northward heat transport throughout the Atlantic Ocean, cooling the North Atlantic (or partly compensating for the greenhouse induced warming in this region), and warming the South Atlantic (e.g. *Vellinga and Wood*, 2002, 2008). Such a cooling in the

North Atlantic may impact the strength of the trade winds and the position of the Inter Tropical Convergence Zone over the equator (*Dong and Sutton*, 2002; *Zhang and Delworth*, 2005), which in turn could modify both the El Nino Southern Oscillation (*Timmermann et al.*, 2007), and the Indian and African monsoons (*Zhang and Delworth*, 2006). In addition, a weakening of the AMOC has been shown to affect Atlantic hurricane activity (e.g. *Goldenberg et al.*, 2001), as well as the strength and trajectory of the midlatitude jet stream (*Woollings et al.*, 2012), directly impacting weather patterns over North America and northern Europe

In light of these significant impacts, as well as observations that show that the deep North Atlantic Ocean has already undergone a period of widespread freshening over the past four decades due to changes in the overflows from the subarctic seas (*Dickson et al.*, 2002), it is critically important to understand how the dynamics of freshwater export to either side of Greenland might be affected by the changing Arctic. Not only will the dynamics be affected by changes within the Arctic itself (e.g. the accelerated accumulation of freshwater in the Beaufort Gyre or the changing stratification in the surface layers associated with elevated vertical mixing), but local dynamics in Fram Strait and the CAA will also be important. For example, the shallow sills found in the narrow channels of the CAA (discussed in more detail in Chapter 4) and a change in the local wind field in Fram Strait, are both likely to play important roles in determining the magnitude of any future increase in the liquid and ice freshwater fluxes through these regions. The flow of freshwater through Nares Strait to the west of Greenland currently accounts for 30-50% of the total freshwater flux through the CAA (*Beszczynska-Möller et al.*, 2011), and therefore represents a major pathway through which freshwater is exported from the Arctic Ocean into the North Atlantic. Consequently, the work in Chapters 4 and 5 of this thesis will examine the local dynamics within Nares Strait, and in particular will focus on the unusually strong tidal currents which dominate the day-to-day variability in the flow (e.g. *Münchow and Melling*, 2008), and may impose an important frictional constraint on the subtidal flow.

1.5 Thesis Aims and Layout

Motivated by the rate at which the Arctic environment is changing, and the consequences that these changes may have for the climate, ocean circulation, and ecosystems both locally within the Arctic itself but also remotely at lower latitudes, the overall aim of this thesis is to explore and understand how these changes are affecting different aspects of the Arctic Ocean's circulation and dynamics using both simple numerical models and observations.

In Chapter 2, a simple reduced gravity model of the Canadian Basin will be used to explore how recent sea ice decline may be affecting the accumulation of freshwater in the Beaufort Gyre. In particular, by idealistically perturbing the annual cycle in ocean surface stress, the chapter will examine whether the observed acceleration in the accumulation of freshwater is a dynamical response associated with the decline in Arctic sea ice cover and the increased efficiency of momentum transfer through sea ice. The timescales over which the Arctic Ocean adjusts to a change in forcing will also be considered, as well as whether an asymmetrical annual cycle in ocean surface stress associated with the changing annual cycle in sea ice cover can lead to a spin-up of the Arctic Ocean.

In Chapter 3, a 1D model of the Arctic Ocean water column will be used to explore how the competing processes of elevated freshwater input and periodic increases in internal wave mixing during ice-free periods may affect the stratification, the strength of the cold halocline, and the sea ice cover at the surface over the coming decades. The evolution of the diffusive heat flux from the Atlantic layer will be considered, along with the time taken for the cold halocline to be fully eroded and the mixed layer to be in direct contact with the Atlantic layer. The effect of these two processes on the sea ice cover at the surface will be quantified, and the role that they might play in the ongoing melting of Arctic sea ice will be discussed.

In Chapters 4 and 5, observations collected in Nares Strait in the Canadian Arctic Archipelago will be used to examine the dynamics behind the vertical and temporal variability of the tides, which dominate the flow in this region. In Chapter 4, an introduction to the Canadian Arctic Archipelago and the tides in Nares Strait will be presented, and the data sources and data analysis methods used in both Chapters 4 and 5 will be dis-

cussed. In addition, the along-strait propagation of the tidal wave associated with each of the major tidal constituents in Nares Strait will be examined. In Chapter 5, the vertical structure of the different tidal constituents in Nares Strait will be determined, along with the structure of the across-strait flow. Simple point eddy viscosity boundary layer models will be used to explore the key dynamics behind what sets the vertical structure of the different tidal constituents, and the output of these simple models will be used to make broad estimates of the rate of tidal dissipation. In addition, the effect of the quasi-annual cycle in ice conditions on the vertical structure of the tides will be considered. The overall aim of these chapters is to take a first step towards understanding the important dynamics that affect the tides in Nares Strait, such that the role they may play in limiting the freshwater flux through this region, both presently and into the future, can be investigated in more detail.

Finally, a summary of the key findings from the work in this thesis will be presented in Chapter 6, and the implications of the work for Arctic science as a whole will be discussed.

Chapter 2

Sea Ice Decline and the Accelerated Accumulation of Freshwater in the Beaufort Gyre

The work in this chapter is published as:

Davis, P.E.D., C. Lique, and H.L. Johnson (2014), On the Link between Arctic Sea Ice Decline and the Freshwater Content of the Beaufort Gyre: Insights from a Simple Process Model, *Journal of Climate*, **27**, 8170–8184, doi:10.1175/JCLI-D-14-00090.1

The Beaufort Gyre in the Canadian Basin of the western Arctic Ocean is the single largest region of freshwater storage in the Arctic. Over the past two decades, hydrographic observations (e.g. *Proshutinsky et al.*, 2009, *McPhee et al.*, 2009 and *Krishfield et al.*, 2014) have shown that the freshwater content of the Beaufort Gyre is increasing, and it is possible that if this excess freshwater were to be released into the North Atlantic (e.g. *Stewart and Haine*, 2013), it may significantly disrupt the AMOC (e.g. *Jahn and Holland*, 2013). It is therefore critical to understand the dynamics behind the changing freshwater content of the Arctic Ocean. Since 2002, *Giles et al.* (2012) have suggested that the rate of freshening in the Beaufort Gyre is accelerating, and have proposed that a dynamical adjustment in response to the declining Arctic sea ice cover may be the cause. Understanding the dynamical adjustment is the focus of this chapter.

2.1 Introduction

The Beaufort Gyre is a permanent anticyclonic circulation driven by the winds associated with the atmospheric Beaufort High (*Proshutinsky et al.*, 2009). These clockwise winds cause water to converge in the centre of the gyre, and the resulting downwelling (Ekman pumping) leads to an accumulation of freshwater through the mechanical deformation of the salinity field (*Proshutinsky et al.*, 2002; *Yang*, 2009; *Proshutinsky et al.*, 2009). The strength of the atmospheric Beaufort High projects onto a number of different modes of atmospheric variability (most importantly the Arctic Oscillation, but also the Pacific-North American pattern, the Arctic atmospheric Dipole Anomaly and the Pacific Decadal Oscillation; *Serreze and Barrett*, 2011), and therefore the Beaufort Gyre exhibits strong annual and interannual variability. On annual timescales, stronger anticyclonic winds in winter associated with higher atmospheric pressures (Figure 2.3a Winter) result in an accumulation of freshwater, whereas lower atmospheric pressures and weaker (or possibly cyclonic) winds in summer (Figure 2.3a Summer) relax the salinity gradient resulting in a release of freshwater (*Proshutinsky et al.*, 2002). In addition, ice growth in winter and melt in summer will decrease or increase the freshwater content of the Beaufort Gyre, respectively, and any changes in the advection of surface, Pacific and Atlantic waters are also likely to have an impact (*Proshutinsky et al.*, 2009). Consequently, the mean annual cycle in freshwater content reflects the complex interplay between these different forcings.

On interannual timescales, *Proshutinsky and Johnson* (1997) and *Proshutinsky et al.* (2002) have suggested that in response to the changing modes of atmospheric variability, two different wind regimes exist within the Arctic: cyclonic and anticyclonic. During the anticyclonic regime, freshwater is accumulated within the Beaufort Gyre over several years due to a strengthened atmospheric Beaufort High (i.e. a negative phase of the Arctic Oscillation; Figure 1.5c). In contrast, during the cyclonic regime the atmospheric Beaufort High weakens (i.e. a positive phase of the Arctic Oscillation; Figure 1.5b), and freshwater is released to the shelves where it may be exported into the North Atlantic. As a result, there is a strong linear relationship between the freshwater content of the Beaufort Gyre and the wind stress curl on interannual timescales (*Proshutinsky et al.*, 2002, 2009).

Since 1997, the Arctic has been in the longest anticyclonic regime on record, leading to a large excess accumulation of freshwater within the Beaufort Gyre. For example, using data from aerial hydrographic surveys in spring 2008, *McPhee et al.* (2009) have shown that the Beaufort Gyre has gained 8500 km^3 of freshwater compared to the winter Polar Science Center Hydrographic Climatology (PHC; *Steele et al.*, 2001), whilst *Giles et al.* (2012) used satellite observations of sea surface height between 1995 and 2010 to infer a similar increase of 8000 $\pm$ 2000 km^3.

The results of *Giles et al.* (2012) show a clear spatial correlation between the positive trend in the sea surface height associated with the Beaufort Gyre (Figure 2.1a,b), and the negative trend in the curl of the wind field (i.e. a trend towards more anticyclonic winds; Figure 2.1c). However, despite this clear spatial correlation, the temporal correlation is less clear. Whilst the trend in the curl of the wind field remained constant over the whole period, the trend in the sea surface height changed sign after 2002 (Figure 2.1d). Consequently, *Giles et al.* (2012) have suggested that since 2002 the winds may have become more effective at driving an accumulation of freshwater within the Beaufort Gyre, due to an increase in the efficiency of momentum transfer into the upper ocean. On the other hand, however, it must be noted that *Morison et al.* (2012) argue that a shift in the advection pathways of Eurasian river runoff, associated with a positive phase of the Arctic Oscillation during 2005-2008, can account for the increased accumulation of freshwater, with no role played by the Beaufort Gyre wind-driven circulation. In reality, it is likely that both processes are important (*Mauritzen*, 2012).

In the absence of sea ice, the magnitude of the momentum transfer into the upper ocean (i.e. the ocean surface stress) is determined simply by the surface wind stress. However, in the partly ice-covered Arctic, the magnitude of the momentum transfer is determined by both the surface wind stress ($\boldsymbol{\tau}_{Air-Water}$) and an ice-water stress component ($\boldsymbol{\tau}_{Ice-Water}$), with their relative magnitudes scaled by the ice concentration (α; *Yang*, 2009):

$$\boldsymbol{\tau}_{OceanSurface} = \alpha\boldsymbol{\tau}_{Ice-Water} + (1-\alpha)\boldsymbol{\tau}_{Air-Water} \tag{2.1}$$

In the past, the thick and extensive Arctic sea ice cover has acted to reduced the momentum transfer, due to the large internal ice stresses reducing the ice-water stress component,

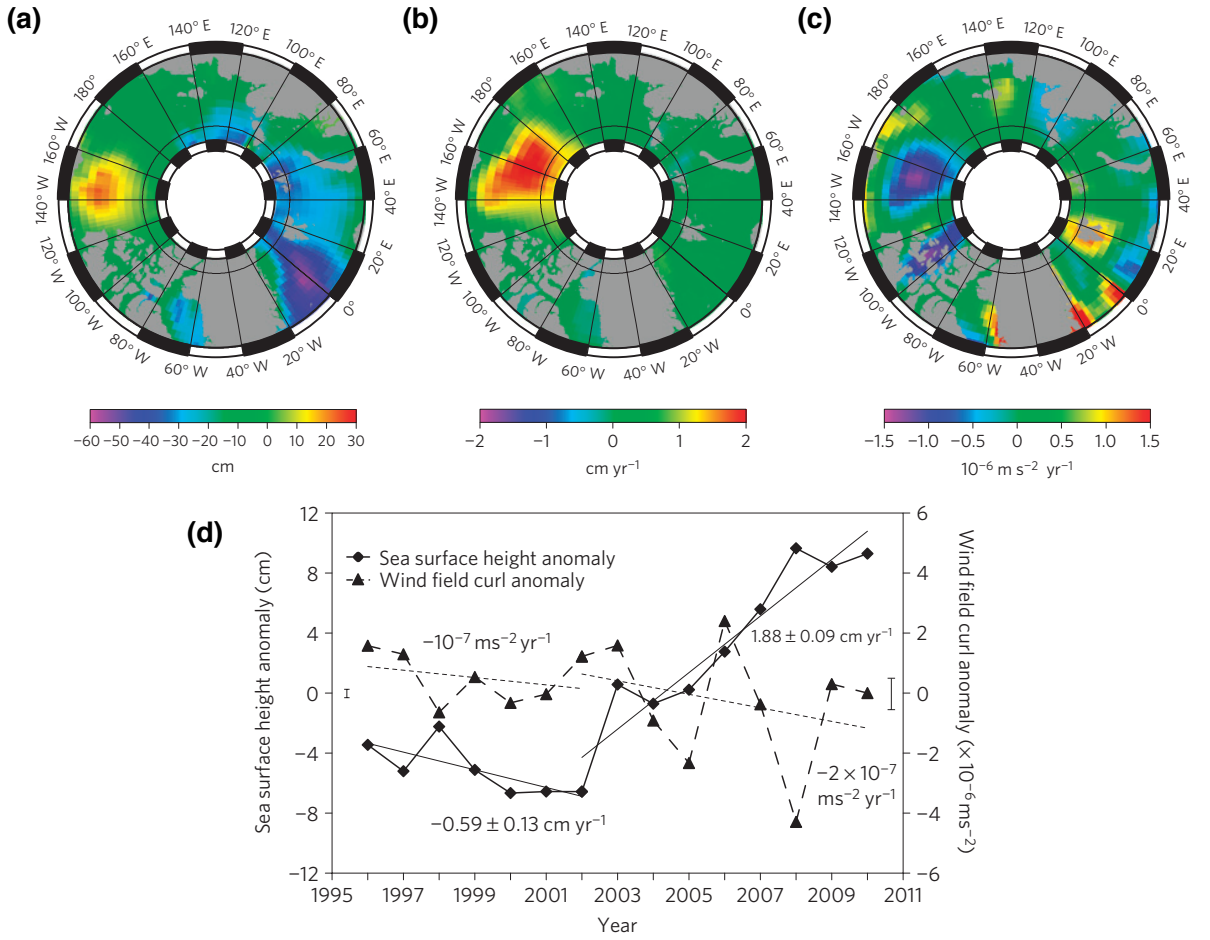

Figure 2.1: Figure from *Giles et al.* (2012) showing (a) the Arctic Ocean mean sea surface height calculated from 15 years of satellite data (1995-2010) with reference to the EGM08 geoid, (b) the trend in Arctic Ocean sea surface height, (c) the trend in the wind field curl calculated from NCEP/NCAR reanalysis data, and (d) the temporal correlation between the trend in the sea surface height anomaly over the Beaufort Gyre and the trend in the wind field curl.

and shielding of the ocean from direct wind forcing. However, as the sea ice cover has begun to break up and retreat farther and for longer each year (*Stroeve et al.*, 2007; *Maslanik et al.*, 2007; *Cavalieri and Parkinson*, 2012), it has become both weaker and thinner (*Kwok and Rothrock*, 2009; *Zhang et al.*, 2012; *Laxon et al.*, 2013), and the number of leads, melt ponds and ice floe edges has increased, changing the shape of the ice pack (*Flocco et al.*, 2012; *Tsamados et al.*, 2014). Consequently, the efficiency of momentum transfer into the upper ocean has increased, as a thinner and weaker sea ice cover is more easily forced by the winds, and the changing shape of the ice pack is providing more and more near-vertical faces for the wind to push against (*Andreas et al.*, 2010). As a result, not only is the annual mean ocean surface stress ($\boldsymbol{\tau}_{OceanSurface}$) increasing (i.e. the net forcing), but its seasonality is also changing. For example, *Martin et al.* (2014) have

shown using the Polar Science Centre Pan-Arctic Ice Ocean Modelling and Assimilation System (PIOMAS) that the Arctic-wide annual mean ocean surface stress has increased by 0.006 N m^{-2} per decade between 2000 and 2012, corresponding to an increase of approximately 9% per decade based on the long-term mean stress of 0.064 N m^{-2}. Furthermore, using the Los Alamos sea ice model (CICE) and a new parametrisation for form drag, *Tsamados et al.* (2014) have shown that the drag coefficient (which can be taken as a measure of the efficiency of momentum transfer into the upper ocean), exhibits a small positive trend over the Beaufort Gyre in summer between 1990 and 2012.

The accelerated accumulation of freshwater in the Beaufort Gyre has coincided with the dramatic decline observed in Arctic sea ice cover. Has the corresponding increase in the annual mean ocean surface stress, or its changing seasonality, contributed to the accelerated accumulation, and thus modified the linear relationship observed between the freshwater content and the wind stress curl (*Proshutinsky et al.*, 2002, 2009)? The changing seasonality may have important implications for the adjustment of the Arctic Ocean to a change in forcing. If the dominant adjustment timescale is on the order of a season, modifications to the length of each season, or an asymmetry between spin-up and spin-down timescales over the annual cycle, may result in a multi-year trend in freshwater accumulation.

The dynamical response of the Beaufort Gyre to the thinning, weakening and changing shape of the Arctic sea ice cover will depend upon exactly how much more stress is transferred from the surface of the ice pack to the ocean below (i.e. the change to the annual mean ocean surface stress), and how the seasonal distribution of this transfer may change (i.e. the change to the seasonality in the ocean surface stress). However, both remain poorly constrained and understood, and many different processes such as stratification, atmospheric boundary layer stability, ocean circulation and sea ice conditions are important in determining the transfer of momentum through sea ice (*McPhee*, 2012). Indeed, two state-of-the-art studies by *Martin et al.* (2014) and *Tsamados et al.* (2014), that were designed to investigate how the magnitude and seasonality of the ocean surface stress has changed with the recent decline in Arctic sea ice cover, show seasonal cycles in ocean surface stress which are 180 degrees out of phase. Here the simplest possible

approach is adopted, and an idealised process model is used to investigate the dynamical response of the Beaufort Gyre to the changing efficiency of momentum transfer (and its link to the accelerated accumulation of freshwater) by idealistically perturbing the annual cycle in ocean surface stress through a wide parameter space. Sea ice is not represented explicitly in the model, but rather the effect of its decline is accounted for via perturbations made to the magnitude and seasonality of the ocean surface stress. In Section 2.2 the model setup is described, and the results of a control run are discussed in Section 2.3. Sections 2.4 and 2.5 present the setup and results of two different sets of idealised experiments designed to investigate the response of the Beaufort Gyre to the decline in Arctic sea ice cover, with a discussion of the results and their implications in Section 2.6. The conclusions of the work in this chapter and are presented in Section 2.7.

2.2 Model Setup

A non-linear 1.5-layer reduced gravity model (e.g. *Johnson and Marshall*, 2002; *Allison et al.*, 2011), is used to simulate the surface freshwater layer of the Canadian Basin in the Arctic Ocean. The model is governed by the standard non-linear shallow water equations:

$$\frac{\partial \mathbf{u}}{\partial t} + (f + \xi)\mathbf{k} \times \mathbf{u} + \nabla B = A\nabla^2 \mathbf{u} + \frac{\boldsymbol{\tau}}{\rho_0 h} \tag{2.2}$$

$$\frac{\partial h}{\partial t} + \nabla \cdot (h\mathbf{u}) = \nabla \cdot (\kappa \nabla h), \tag{2.3}$$

where ξ is the relative vorticity:

$$\xi = \frac{\partial v}{\partial x} - \frac{\partial u}{\partial y}, \tag{2.4}$$

and B is the Bernoulli potential:

$$B = g'h + \left(\frac{u^2 + v^2}{2}\right). \tag{2.5}$$

$\mathbf{u}$ is the velocity, t is time, f is the Coriolis parameter equal to 2Ω, where Ω is the angular velocity of the Earth (i.e. the model is an f-plane centred on the pole), g' is the reduced gravity of 0.02 m s^{-2}, A is the lateral friction coefficient of 150 m^2 s^{-1} (there is no bottom friction as per the definition of a 1.5-layer reduced gravity model), $\boldsymbol{\tau}$ is the ocean surface stress (i.e. $\boldsymbol{\tau}_{OceanSurface}$ in Equation 2.1), ρ_0 is the average density of 1026 kg m^{-3}, h is the surface layer thickness, $\nabla \cdot (\kappa \nabla h)$ is an advective term arising from the Gent-McWilliams (GM) eddy parametrisation (*Gent*, 2011), and κ is the eddy diffusivity. The equations are discretised on a C-grid with a resolution of 15 km x 15 km. No slip and no normal flow boundary conditions are applied at the domain boundaries:

$$\mathbf{u}_{\perp} = 0 \qquad \text{and} \qquad \mathbf{u}_{\parallel} = 0, \tag{2.6}$$

where the subscripts indicate the components perpendicular and parallel to the boundaries.

Following the idealised approach of *Spall* (2003, 2004, 2013), the Canadian Basin is represented as a circular domain approximately 1500 km in diameter, connected to a sponge region by a channel approximately 150 km wide (Figure 2.2). It is appropriate to use an idealised circular domain that does not represent the realistic topography of the Arctic Ocean, as it allows the response of the Beaufort Gyre to the changing ocean surface stress to be investigated in the cleanest possible manner, and ensures that the results are not affected by more complex topographic interactions which are most likely dependent on physical processes not included in the simple process model. In the vertical, the model consists of an active surface freshwater layer overlying a stationary Atlantic layer. This approach is similar to that of *Proshutinsky and Johnson* (1997), who used a barotropic model to investigate the wind-driven dynamics of the upper layer of the Arctic Ocean. The surface freshwater layer is initialised with a thickness of 400 m, matching the average depth of the 34.8 psu isohaline outside of the Beaufort Gyre in the PHC. The reduced gravity of 0.02 m s^{-2} is based on an average salinity of 32.3 psu in the surface freshwater layer and 35.0 psu in the Atlantic layer from the PHC, resulting in an internal Rossby deformation radius of approximately 20 km.

The sponge region is approximately 600 km wide, and is designed to absorb any

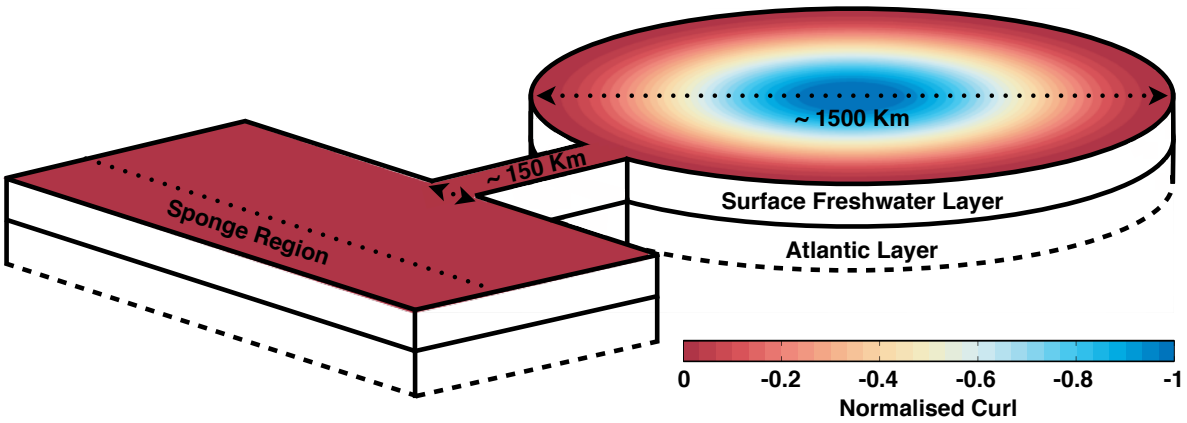

Figure 2.2: The reduced gravity model of the Canadian Basin, with an active surface freshwater layer of density $\rho - \Delta\rho$ initialised to be 400 m thick, overlying a stationary ($\mathbf{u} = 0$) Atlantic layer of density ρ. The model domain is ≈1500 km in diameter and is connected to a sponge region by a channel ≈150 km wide. The sponge region is designed to absorb any waves propagating out of the domain, and to allow an inflow or outflow transport to develop in response to changes in layer thickness within the domain. The model is forced with an anticyclonic ocean surface stress centred over the domain. The magnitude of the curl of the stress field (which is proportional to the strength of the Ekman pumping) is at a maximum in the center of the domain, and is zero at the boundaries and in the outflow.

waves propagating out of the domain, as well as allow an inflow or outflow transport to develop through the channel in response to changes in layer thickness inside the domain. Within this region the same equations as those in the remainder of the domain are solved, except that absorbing boundary conditions are implemented by constantly restoring the layer thickness to the initial layer thickness with a timescale of 1 day (i.e. this restoring acts as an extra dissipation term). The magnitude of the restoring is ramped up from zero to its maximum value over a region approximately 450 km wide using a hyperbolic tangent function, and this ensures that the sponge region does not act as a wall to waves propagating out of the domain. Visual examination and the analysis of the transport across the channel in a suite of different model simulations with widely different relaxation timescales in the sponge region provides strong evidence that the sponge region is not sending waves back into the domain (the deformation radius in the model is sufficiently small that any waves propagating back into the domain will be clearly visible hugging the right hand side of the channel). The results are not sensitive to the relaxation timescale in the sponge, unless the timescale is insufficient to fully absorb all waves propagating out of the domain.

The model is forced with an anticyclonic ocean surface stress ($\boldsymbol{\tau}_{OceanSurface}$ in Equation

2.1) centred over the domain (Figure 2.2). Along any diameter within the domain, the ocean surface stress in the x and y direction is described by

$$\tau^{(x)} = \sin(\theta)\left(\frac{1}{r}\int r\cos^2(r)\ \ dr\right), \tag{2.7}$$

and

$$\tau^{(y)} = -\cos(\theta)\left(\frac{1}{r}\int r\cos^2(r)\ \ dr\right) \tag{2.8}$$

respectively, where θ is the angle that lines connecting each grid point with the centre of the domain make with the positive x axis, and r is the radial distance between each grid point and the centre of the domain (i.e. $r^2 = x^2 + y^2$). Within the channel and sponge region, the stresses are described by

$$\tau^{(x)} = C\left(\frac{y}{r^2}\right), \tag{2.9}$$

and

$$\tau^{(y)} = C\left(\frac{-x}{r^2}\right), \tag{2.10}$$

where x and y are the distances to each grid point from the centre of the domain along the x and y axes respectively, and C is a scale factor to ensure that the curl of the stress field is continuous at the domain/channel boundary. The curl of the stress field must be continuous at the domain/channel boundary to ensure that an unrealistic step in the layer thickness is not created due to an abrupt change in the rate of Ekman pumping between the domain and the channel. The stress fields are normalised between 0 and 1, and during each model run are multiplied by an idealised annual cycle in ocean surface stress to set the magnitude of the forcing. This stress formulation ensures that the curl of the ocean stress field reaches a maximum in the centre of the domain, and decreases to zero at the boundaries and in the outflow region (Figure 2.2).

To balance the input of vorticity from the winds (thus allowing the model to reach a steady state, or to spin-down if the forcing is reduced to zero), the effect of eddies and diapycnal mixing have been incorporated into the model using the Gent-McWilliams parametrisation (e.g. *Gent*, 2011). Following the approach of *Allison et al.* (2011), the

magnitude of the eddy diffusivity (κ) can be determined by considering the total transport T across any closed layer thickness contour around the domain. Ekman transport driven by the anticyclonic ocean surface stress will cause water to accumulate in the centre of the domain, steepening the pressure gradient and driving an anticyclonic geostrophic current. Baroclinic instability associated with this current will result in an eddy-induced bolus transport towards the boundary of the domain. Consequently, the total transport across any closed thickness contour is the residual between the Ekman and eddy-induced transport velocities:

$$T = T_{Ek} - T_{Eddies}, \tag{2.11}$$

and can be obtained by integrating the cross-contour components of the eddy (hv_{Eddies}) and Ekman (hv_{Ek}) transport velocities along the entire thickness contour:

$$T \approx \oint h(v_{Ek} + v_{Eddies}) \; d\lambda \approx - \oint \frac{\tau^{(\lambda)}}{\rho_0 f} \; d\lambda - \oint \kappa \frac{\partial h}{\partial r} \; d\lambda, \tag{2.12}$$

where λ is the distance in the azimuthal direction, $\tau^{(\lambda)}$ is the ocean surface stress aligned parallel to the thickness contour, r is the radial direction, and it has been assumed that the thickness contours form concentric circles inside the domain. Integrating Equation 2.12 between the boundary and the centre of the domain and dividing by the radius of the domain, r, gives

$$T \approx -\frac{1}{r} \int \int \frac{\tau^{(\lambda)}}{\rho_0 f} \; dA - \frac{1}{r} \oint \kappa (h_c - h_b) \; d\lambda, \tag{2.13}$$

where h_c and h_b are the layer thickness in the centre and at the boundary of the domain respectively. If it is assumed that at steady state $T = 0$, $\tau^{(\lambda)} = 0.02$ N m^{-2} (discussed in more detail below), and $h_c - h_b = 60$ m based on the deepening of the 34.8 psu isohaline across the Beaufort Gyre in the PHC, then the eddy diffusivity (κ) must equal approximately 1300 m^2 s^{-1}.

Whilst eddies are likely to be the first order process responsible for balancing the Ekman pumping (*Marshall et al.*, 2002), other processes such as lateral friction against the Chukchi Cap may also play a role, and in the model their effect has been incorporated

into the strength of the eddy flux. Consequently, it must be noted that the strength of the eddy flux may be an over estimate.

2.3 Control Run

Initially the model is run for 40 years from rest in order to reach an idealised equilibrium state. The magnitude of the annual cycle in ocean surface stress used to force this control run (Figure 2.3c), is based on the average conditions that existed between 1979 and 1990 (i.e. before the dramatic decline in Arctic sea ice cover; *Stroeve et al.*, 2012b). Figures 2.3a and 2.3b show the summer (4 months: July - October) and winter (8 months: November - June) averages of the mean sea level pressure from the monthly ERA-Interim reanalysis (*Dee et al.*, 2011) and sea ice concentration from the Special Sensor Microwave/Imager (SSM/I) satellite (*Maslanik and Stroeve*, 1999) over this period. The winds associated with the atmospheric Beaufort High are stronger and more anticyclonic during winter than during summer, and there is a decline in the sea ice concentration over the Beaufort Gyre during the four months of summer (although this seasonal change is much smaller than that seen in more recent observations). The results of *Yang* (2009) suggest that between 1979 and 1990, variability in the ocean surface stress is dominated by atmospheric forcing rather than by the sea ice concentration, and consequently the annual cycle in ocean surface stress used to force the control run reflects only the changing wind conditions, with 8 months of strong anticyclonic winds or high stress (0.02375 N m^{-2}) followed by 4 months of weak anticyclonic winds or low stress (0.01250 N m^{-2}; Figure 2.3c). Due to the difficulties in estimating the ocean surface stress directly from wind speed in the ice-covered Arctic, the values of the ocean surface stress are taken from the Nucleus for European Modelling of the Ocean (NEMO)–Louvain-la-Neuve Sea Ice Model (LIM) global coupled sea ice-ocean model, which has been used in previous Arctic studies (*Lique et al.*, 2009, 2010; *Lique and Steele*, 2012). Using a drag coefficient of 2.25×10^{-3} (*Timmermann et al.*, 2005), the model annual mean ice-ocean stress of 0.018 N m^{-2} between 1979 and 1990 corresponds to an 'effective' wind speed of 2.0 m s^{-1}. This is lower than the ERA-Interim annual mean of 2.5 m s^{-1} over the same period, due to the sea ice cover reducing the transfer of momentum into the upper ocean.

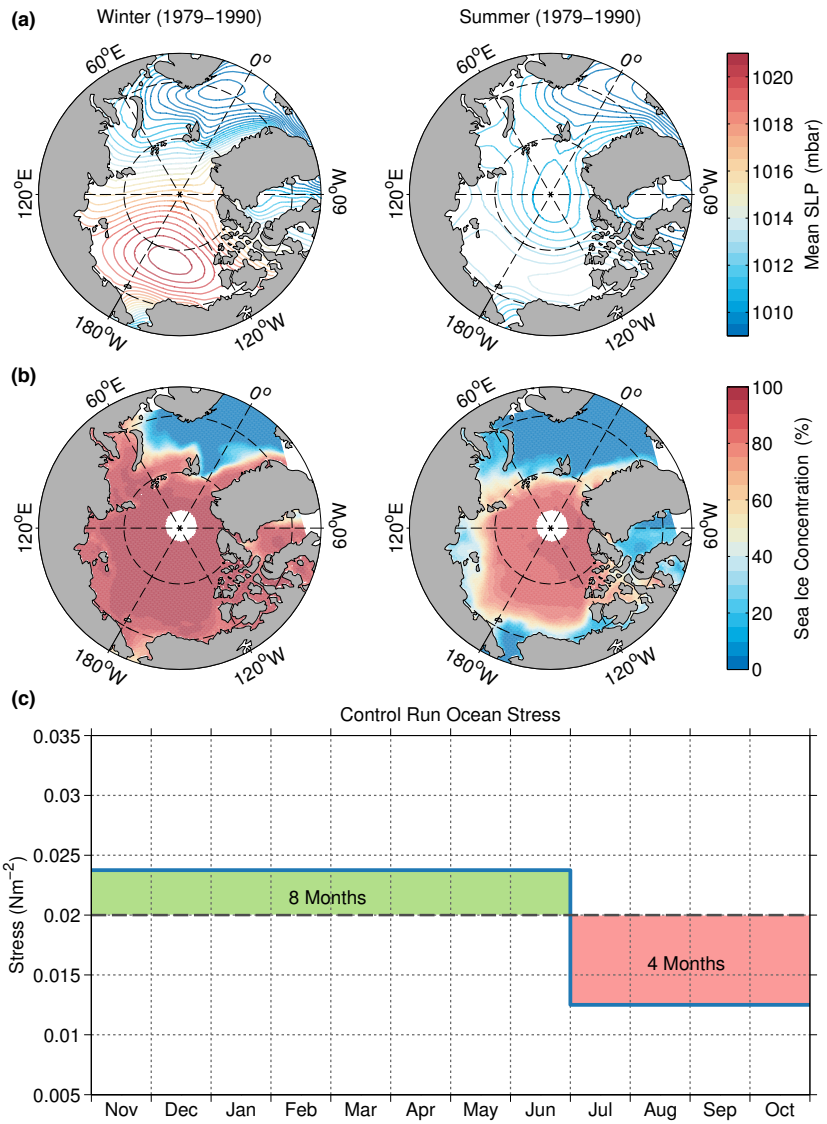

Figure 2.3: Summer (July - October) and winter (November - June) averages of (a) mean sea level pressure from the ERA-Interim reanalysis, and (b) sea ice concentration from the Special Sensor Microwave/Imager (SSM/I) satellite over the Arctic Ocean between 1979 and 1990. The annual cycle in ocean surface stress used to force the control run (c) is based on the occurrence of stronger and more anticyclonic winds over the Beaufort Gyre during the 8 months of winter (green) compared to the 4 months of summer (red). The reduction in sea ice cover between July and October defines the summer period.

Figure 2.4a shows the mean layer thickness and velocity fields over the last 5 years of the 40 year control run, whilst Figure 2.4b shows a cross section of the mean layer thickness through the centre of the domain. As expected from the scaling of the eddy diffusivity, the surface freshwater layer has thickened on average by 60 m across the domain, with the maximum thickening in the centre. Around the boundaries and in the outflow region little thickening has occurred, confidently suggesting that any forcing in the outflow region is not affecting the response within the circular domain. Associated

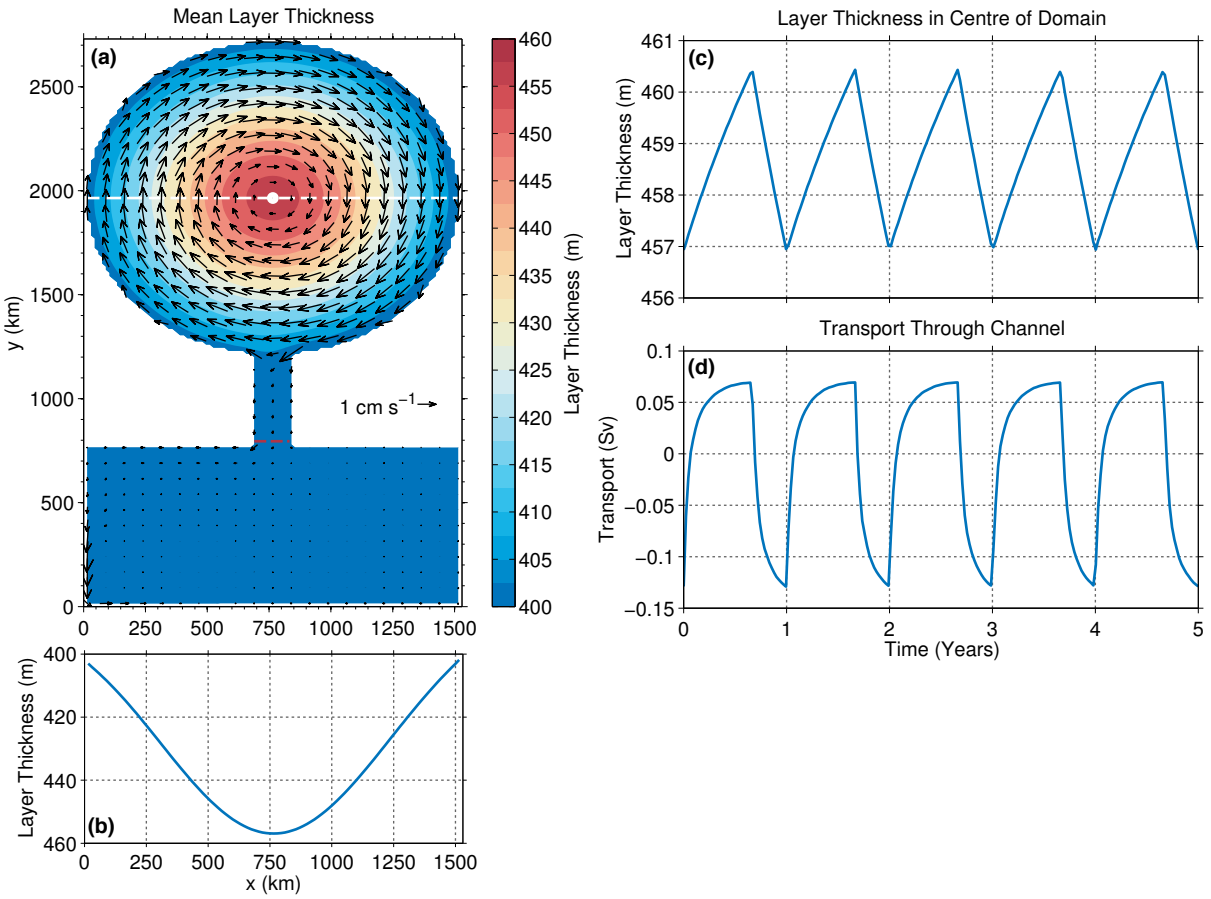

Figure 2.4: (a) Mean layer thickness (colours) and velocity field (vectors); (b) cross section of the mean layer thickness through the centre of the domain (i.e. along the white line); (c) the annual cycle in layer thickness in the centre of the domain (i.e. at the white dot); and (d) the annual cycle in transport through the channel (i.e. across the red line) all calculated over the last 5 years of the control run. Positive transports indicate an inflow, whilst negative transports indicate an outflow. Integer year numbers correspond to the end of the summer period.

with the deepening of the surface freshwater layer is an anticyclonic geostrophic circulation centred over the domain. The time-averaged maximum velocity of approximately 2 cm s^{-1} is consistent with the climatological values reported in *McPhee et al.* (2009) and *McPhee* (2013). Figures 2.4c and 2.4d show the annual cycles in layer thickness in the centre of the domain, and the transport through the channel over the last 5 years of the control run. The annual cycle in layer thickness, which can be interpreted as a proxy for the annual cycle in freshwater storage, oscillates around a mean of 458.7 m, and has a peak to peak amplitude of 3.4 m consistent with the results of *Proshutinsky et al.* (2009). The annual cycle in transport through the channel has a peak to peak amplitude of 0.2 Sv (1 Sv = 10^6 m^3 s^{-1}), with a mean of zero. The maximum freshwater storage and maximum inflow into the domain occurs at the end of the winter period, whilst the

minimum freshwater storage and maximum outflow occurs at the end of the summer period, reflecting the integrated forcing throughout the year.

Note that sensitivity analysis has shown that the results in the following sections are not dependent upon the exact magnitude of the annual cycle in ocean surface stress used to force the control run, nor on the realism of the steady state.

2.4 Experiment 1: Modified Seasonality

Because the Arctic sea ice cover has begun to break up and retreat farther and for longer each year, both the annual mean ocean surface stress (i.e. the net forcing) is increasing, and its seasonal cycle (i.e. the seasonality) is changing. Each may have an affect on the accumulation of freshwater in the Beaufort Gyre by triggering a different dynamical response, and therefore two sets of experiments were designed in order to investigate their effects separately.

In the first set of experiments, the effect of modifying the seasonality in ocean surface stress whilst holding the net forcing constant was investigated. Figures 2.5a and 2.5b show the idealised modifications made to the annual cycle in ocean surface stress. Over a number of model runs, the ocean surface stress during the 4 months of summer was incrementally increased with respect to the control run (Figure 2.5a), idealistically representing an increased efficiency of momentum transfer into the ocean. For high levels of ocean stress in summer, the period over which this stress was applied was then incrementally increased from 4 months to 6 months (Figure 2.5b), representing a longer melt season and therefore a longer period of enhanced momentum transfer. At the same time, however, the ocean surface stress in winter for each model run was reduced, to ensure that the net forcing remained constant at 0.02 N m^{-2} (black dashed line in Figures 2.5a and 2.5b). Each model run was initialised from the layer thickness and velocity fields at the end of the control run, and run for a further 40 years. It is important to note that whilst the terminology of "summer" and "winter" has been used, the seasons are defined solely as periods of different ocean surface stress and need not relate to specific times of the year.

Figure 2.6 shows the results of these experiments in terms of both the annual cycle in

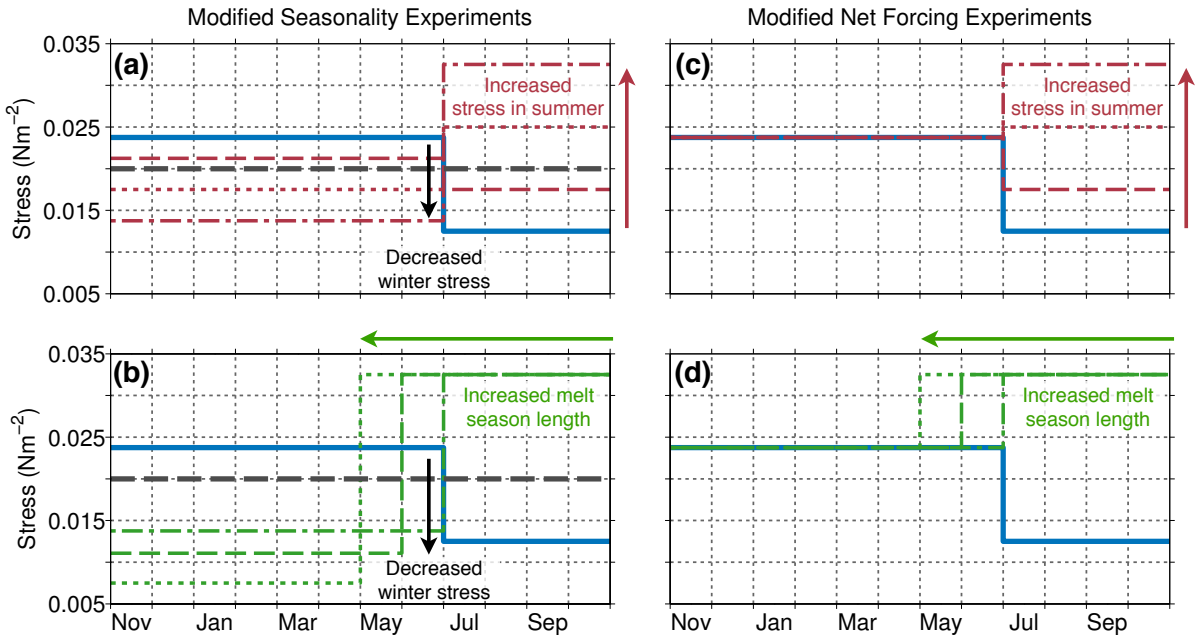

Figure 2.5: Modifications made to the annual cycle in ocean surface stress with respect to the control run (thick blue line) for (a) and (b) the modified seasonality experiments, and (c) and (d) the modified net forcing experiments. In (a) and (c) the ocean surface stress is incrementally increased in summer, representing the increased efficiency of momentum transfer. In (b) and (d), the period over which high values of summer stress is applied is then incrementally increased, representing a longer melt season. For the modified seasonality experiments (a) and (b), the stress in winter in each model run is reduced, to ensure that when integrated over the entire year the net forcing remains constant at 0.02 N m^{-2} (grey dashed line).

layer thickness in the centre of the domain, and the transport through the channel over the last 5 years of each model run. The key result is that if the net forcing is held constant, the changing seasonality in ocean surface stress has no effect on the annual mean or net freshwater content of the Beaufort Gyre. The annual cycle in layer thickness (and thus the freshwater content) from each of the model experiments oscillates around the control run mean of 458.7 m (Figures 2.6b and 2.6e), and when the annual cycle in transport through the channel is integrated over the full 40 years of each model run, it is clear that there is no net inflow into the domain (Figures 2.6c and 2.6f).

Nevertheless, by changing the seasonality in ocean surface stress, the shape of the annual cycle in both the layer thickness in the centre of the domain and the transport through the channel are significantly altered. With respect to the control run, as the ocean surface stress is steadily increased in summer (compare the blue line with the dashed, dotted and dot-dashed red lines in Figure 2.6a), the phase of the annual cycle in both the layer thickness and the transport through the channel eventually reverses, as the

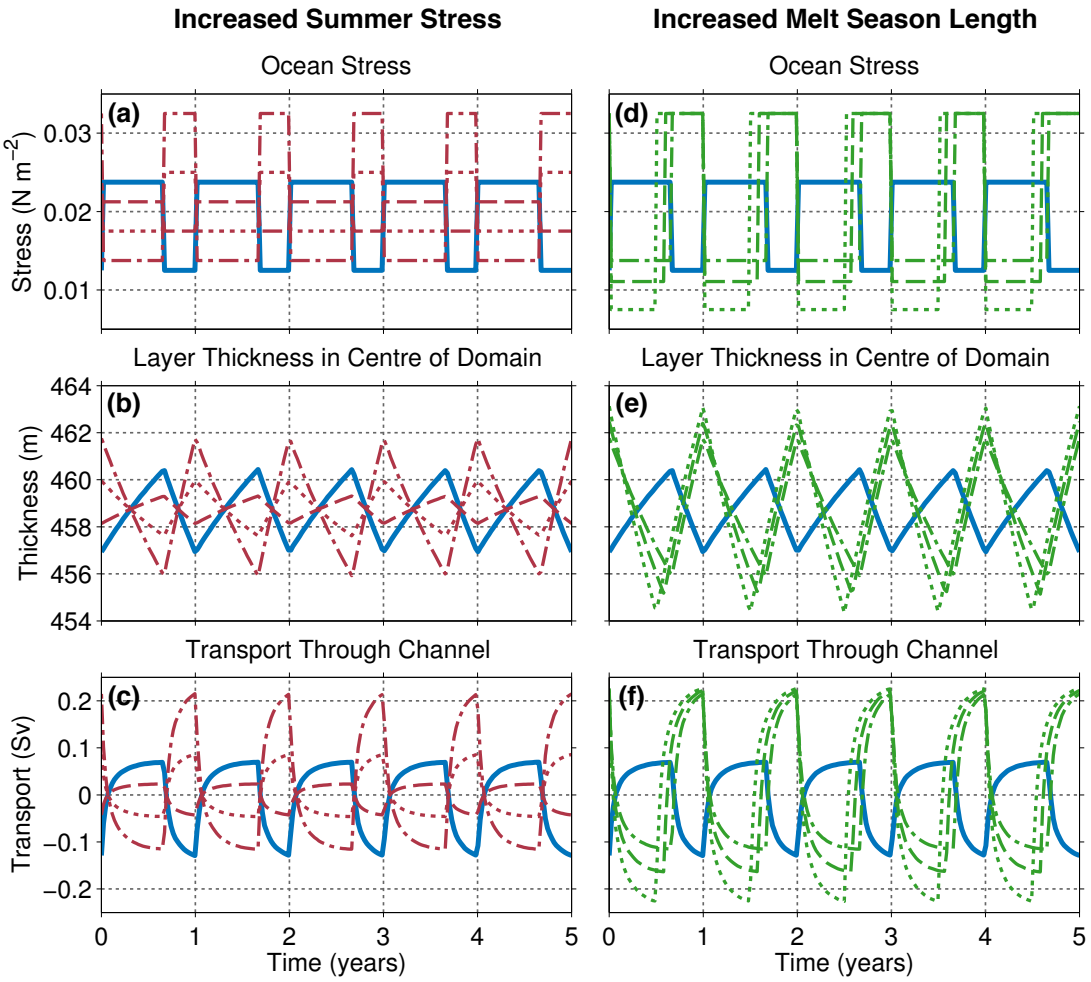

Figure 2.6: The annual cycle in (a) and (d) ocean surface stress, (b) and (e) the layer thickness in the centre of the domain (white dot in Figure 2.4a), and (c) and (f) the transport through the channel (red line in Figure 2.4a) from the last 5 years of each of the modified seasonality experiments. Positive transports indicate an inflow, whilst negative transports indicate an outflow. (a), (b) and (c) are for model runs where the ocean surface stress in summer has been increased, whilst (d), (e) and (f) are for model runs where the melt season length has been increased. Line styles and colours correspond to those used in Figures 2.5a and 2.5b. The thick blue line represents the control run. Integer year numbers correspond to the end of the summer period.

stress in summer becomes greater than the stress in winter, and the amplitude increases, reflecting the increased amplitude of the annual cycle in ocean surface stress. The peak to peak amplitudes increase from 3.4 m and 0.2 Sv, to a maximum (over these experiments) of 5.7 m and 0.3 Sv for the layer thickness in the centre of the domain (dot-dashed red line in Figure 2.6b) and the transport through the channel (dot-dashed red line in Figure 2.6c), respectively.

When the length of the melt season is increased for high values of ocean surface stress in summer (compare the blue line with the dot-dashed, dashed and dotted green lines

in Figure 2.6d), the amplitudes of the annual cycle in layer thickness and the transport through the channel increase further to 8.6 m and 0.5 Sv, respectively (dotted lines in Figures 2.6e and 2.6f). The timing of the minimum freshwater storage also occurs earlier due to the shorter winter period, whilst the timing of maximum freshwater storage remains unchanged.

2.5 Experiment 2: Modified Net Forcing

To explore the dynamical response of the Beaufort Gyre to an increased net forcing, and its effect on the freshwater content, a second set of experiments were performed. The same modifications to the annual cycle in ocean surface stress as seen in the modified seasonality experiments were applied (Figures 2.5a and 2.5b) but, in this case, the ocean surface stress in winter was not reduced to offset the increase in summer (Figures 2.5c and 2.5d). Consequently, the net forcing increased from the control run value of 0.02 N m^{-2} to a maximum of 0.028 N m^{-2}. Each model run was again initialised from the layer thickness and velocity fields at the end of the control run, and integrated for a further 40 years.

Figure 2.7a shows that the mean layer thickness in the centre of the domain, averaged over the last 5 years of each model run, increases linearly with respect to the increased ocean surface stress. The linear relationship is described by the equation

$$\Delta\bar{h} = 2937.5\Delta\bar{\tau}, \tag{2.14}$$

where $\Delta\bar{h}$ and $\Delta\bar{\tau}$ are the increase in mean layer thickness and net forcing, respectively, from the control run. To estimate the magnitude of the corresponding freshwater accumulation, the annual cycle in transport through the channel can be integrated in time to produce a cumulative volume transport into the domain over the full 40 years of each model run. This cumulative volume transport can then be multiplied by a salinity anomaly:

$$S_{Anomaly} = \frac{S_{ref} - S}{S_{ref}}, \tag{2.15}$$

where S_{ref} is the reference freshwater salinity and S is the in-situ salinity, to calculate

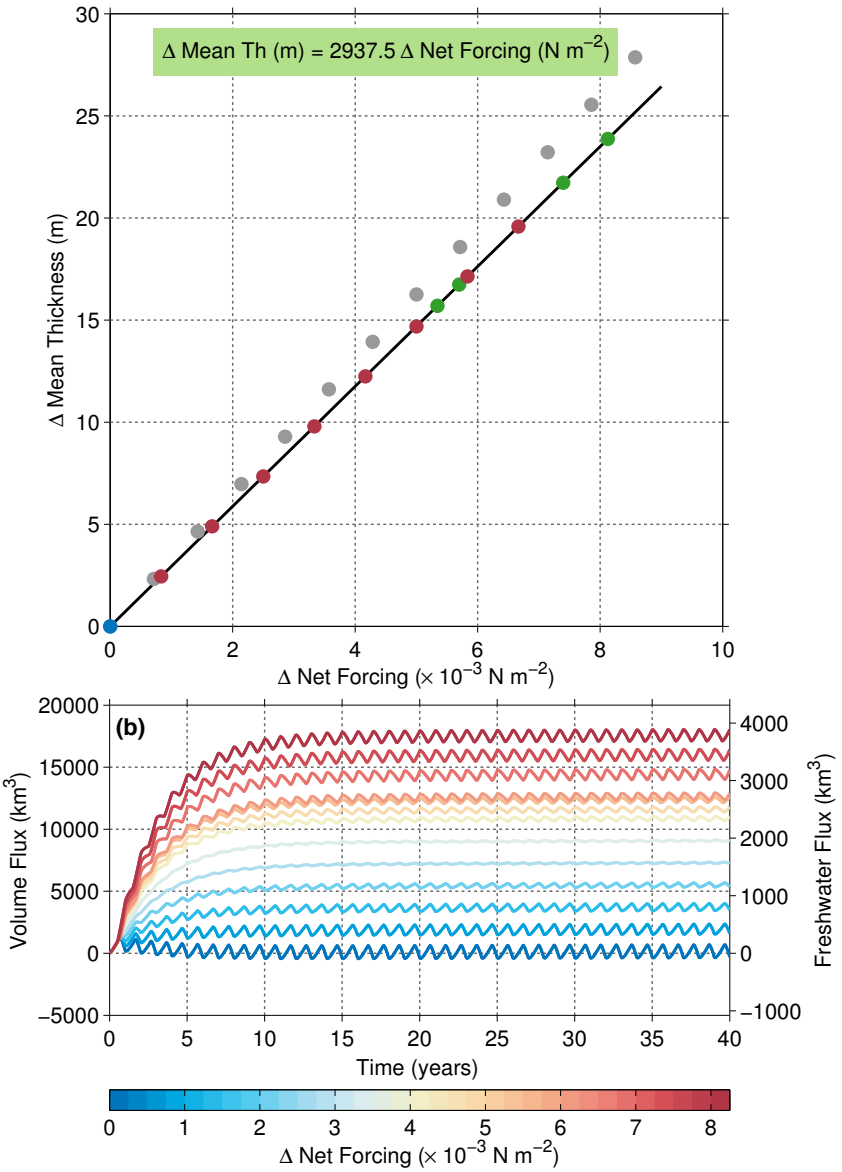

Figure 2.7: Results of the modified net forcing experiments. (a) The increase in mean layer thickness in the centre of the domain plotted as a function of the increase in net forcing. The blue dot represents the control run, whilst the red dots represent model runs with an increased ocean surface stress in summer and the green dots represent model runs with a longer melt season (as per the colors in Figures 2.5c and 2.5d). For comparison, the grey dots show the change in layer thickness for a given change in the ocean surface stress calculated using Equation 2.13. (b) The cumulative volume and freshwater transports into the domain over the full 40 years of each model run plotted as a function of the increase in net forcing.

the total freshwater accumulation. As the model only solves the dynamical equations and thus there is no salinity variable, S has been set to a salinity of 27.7 psu in accordance with *Giles et al.* (2012). This value is based on the salinity measured in the mixed layer by an Ice Tethered Profiler deployed in the Canadian Basin during April 2007 (*Toole et al.*, 2010), and as such the freshwater anomaly estimate that results must be viewed as an upper bound. The reference value (S_{ref}) equals 34.7 psu (again in accordance with *Giles*

et al., 2012). Figure 2.7b shows the cumulative volume and freshwater transports into the domain as a function of both time and the increase in net forcing. All model runs show a net flux of freshwater into the domain with respect to the control run. The lack of seasonal variation when $\Delta\bar{\tau}$ is approximately 4×10^{-3} N m^{-2} is due to the lack of seasonal variability in the forcing (i.e. the ocean surface stress in summer has been increased to a point where it equals the ocean surface stress in winter). Fitting an asymptotic exponential growth model to each of the model runs

$$V_{(t)}^{FW} = V_{Tot}^{FW}(1 - e^{-kt}), \tag{2.16}$$

where $V_{(t)}^{FW}$ is the cumulative freshwater transport into the domain as a function of time t, V_{Tot}^{FW} is the total freshwater accumulated in the domain for each model run and k is the growth constant, reveals an e-folding timescale of approximately 3.3 years for the accumulation of freshwater in the domain. This is slightly longer than the e-folding timescale of approximately 2.7 years for the increase in the mean layer thickness in the centre of the domain. As with the mean layer thickness in the centre of the domain, the total accumulation of freshwater depends linearly on the increase in net forcing, and for the greatest increase in net forcing in the suite of experiments (0.008 N m^{-2}), the total freshwater accumulated in the domain is approximately 4000 km^3. The results of *Martin et al.* (2014) suggest that between 2000 and 2012, the Arctic-wide annual mean ocean surface stress has increased by 0.007 N m^{-2}, which corresponds to an accumulation of freshwater in the model of approximately 3500 km^3. This is around 50% of the increase observed by *Giles et al.* (2012) over broadly the same period.

2.6 Discussion and Implications

Using a simple process model and idealised perturbations to the annual cycle in ocean surface stress, it has been demonstrated that the dynamical response of the Beaufort Gyre to the decline in Arctic sea ice cover and the related increase in the efficiency of momentum transfer into the upper ocean, is a plausible mechanism behind the accelerated accumulation of freshwater inferred by *Giles et al.* (2012). Despite the simple nature of

the process model used here, the broader implications of the results and their relevance to the wider Arctic system are discussed in the following section.

2.6.1 Adjustment Timescales

The results of both the modified seasonality experiments and the modified net forcing experiments shed some light on the timescales over which the Arctic Ocean adjusts to a change in forcing, as well as on which adjustment processes are responsible. Figures 2.6b and 2.6e show that over each season the layer thickness in the centre of the domain continues to increase or decrease in response to the change in ocean surface stress, and never fully adjusts to a new equilibrium state. In contrast, Figures 2.6c and 2.6f suggest that the magnitude of the transport through the channel adjusts more quickly to the seasonal changes in ocean surface stress, asymptoting towards a new equilibrium value over the period of each season. Consequently, it appears that the processes which dominate the adjustment to a change in forcing around the boundary of the domain are very different to those which determine the adjustment in the centre. The response timescale (e-folding timescale) of the transport through the channel is approximately 1 month. As the propagation speed of a boundary trapped kelvin wave in the model is:

$$c = \sqrt{g'h} \approx 2.8 \text{ m s}^{-1} \tag{2.17}$$

and the circumference of the model is approximately 4712 km, this suggests that fast boundary waves travelling around the domain within a period of (t_{bw}):

$$t_{bw} = \frac{4712 \times 10^3}{c} \approx 20 \text{ days} \tag{2.18}$$

are the dominant process behind the quick adjustment on the boundary, with waves propagating out of the sponge region (where a strong restoring to the initial layer thickness of 400 m is applied) effectively fixing the layer thickness around the boundary in the model on timescales longer than 1 month.

Away from the boundaries, however, Kelvin waves have little effect. Here, the layer thickness as a function of time is determined by the balance between wind-induced Ekman

pumping and the eddy-induced volume flux towards the boundary (i.e. Equation 2.12):

$$\frac{\partial}{\partial t}\int\int h \;\; dA = -\frac{1}{r}\int\int \frac{\tau^{(\lambda)}}{\rho_0 f} \;\; dA - \frac{1}{r}\oint \kappa(h_c - h_b) \;\; d\lambda, \tag{2.19}$$

where the first term on the right hand side represents wind-induced Ekman pumping, and the second term represents the relaxation effect of the eddy flux. Scale analysis suggests that the relaxation timescale due to the eddy term is given by

$$\frac{rA_{BG}}{\kappa\lambda_{BG}}, \tag{2.20}$$

where A_{BG} and λ_{BG} are the area and circumference of the Beaufort Gyre, respectively, and is approximately equal to 14 years. As a result, it can be concluded that eddies play a limited role in balancing Ekman pumping on the seasonal timescale. Consequently, the layer thickness in the centre of the domain continually adjusts to the change in ocean surface stress over each season, and does not tend towards a new equilibrium state. Furthermore, this long adjustment timescale ensures that the annual cycle in layer thickness in the centre of the domain (e.g. 3.4 m in the control run) is only a small fraction of the change in mean layer thickness across the Beaufort Gyre (60 m), as the annual cycle represents only the very beginning of a much longer term adjustment to the changing ocean surface stress. Indeed, when the model is run from rest to a fully-adjusted equilibrium state (the e-folding timescale is 2.5 years) with a constant ocean surface stress of either 0.02375 N m^{-2} or 0.0125 N m^{-2} (i.e. the winter or summer value of ocean surface stress from the control run, respectively), the difference in equilibrium layer thickness between the two runs is approximately 33 m.

In the modified net forcing experiments, however, the eddy relaxation term eventually balances the wind-induced Ekman pumping, and it is the eddy relaxation timescale that determines the total quantity of freshwater that is accumulated in the domain (see Figure 2.7b). This highlights the importance of eddies in the Arctic Ocean's adjustment to a change in forcing, and provides a strong motivation to use eddy resolving models when investigating the transient response of the Arctic Ocean to future changes in the forcing. Indeed, although the use of the GM eddy parameterisation is consistent with the approach

used by many simple process models that do not resolve eddies directly, it is possible that the linear nature of GM and the use of a constant eddy diffusivity in a changing Arctic is not appropriate, especially if the circulation associated with the Beaufort Gyre exhibits either eddy saturated or eddy compensated behaviour (i.e. similar to the Antarctic Circumpolar Current; *Morrison and Hogg*, 2013). The impact this behaviour may have on the results in discussed later in Section 6.2.1. In addition, an analysis of the spatial scales, growth rate, and structure of the eddy field in the Arctic using the Eady model (*Eady*, 1949) may shed some important light on why the growth rate of eddies in the Arctic appears to be slow.

2.6.2 Effect of Sea Ice Concentration

Using the Polar Science Center Pan-Arctic Ice Ocean Modelling and Assimilation System (PIOMAS) and the Los Alamos sea ice model (CICE) with a new parameterisation for form drag, the results of both *Martin et al.* (2014) and *Tsamados et al.* (2014) show a long-term positive trend in the annually averaged momentum flux into the upper ocean in response to the decline in Arctic sea ice. However, *Martin et al.* (2014) find that in PIOMAS the trend is not positive over all seasons. Instead, their model suggests that the efficiency of momentum transfer into the upper ocean is at an optimum when the sea ice concentration is approximately 80% (i.e. in fall and spring). Above this point, a thick and extensive sea ice cover dampens the transfer of momentum due to the large internal ice stresses and shielding of the ocean from direct wind forcing. Below this point, the momentum transfer into the upper ocean decreases, as the drag associated with drifting sea ice is greater than that of open water. Consequently, between the 1980s and 2000s the ocean surface stress in summer decreases by 7% in their model, reflecting the increasing length of time that the sea ice concentration is below 80%. It contrast, this negative trend in summer is not observed in the results of *Tsamados et al.* (2014). It is possible that the form drag parametrisation used by *Tsamados et al.*, which was not implemented in the model used by *Martin et al.*, allows the ice concentration to decline further before the efficiency of momentum transfer decreases due to the fraction of open water. For example, the observations of *Andreas et al.* (2010) show that over summer sea ice and the marginal

ice zone (where form drag is important), the drag coefficient peaks at an ice concentration of ≈50%.

Irrespective of the exact details, the Arctic is currently undergoing a transition from the presence of a thick and extensive sea ice cover year-round to a seasonally ice-free state. If the concept of an optimal ice concentration for the efficiency of momentum transfer into the upper ocean holds, then the current positive trend in the momentum flux will begin to slow and eventually reverse, as the length of time when the sea ice concentration is below the optimum value increases (*Martin et al.*, 2014). At this point, the accelerated accumulation of freshwater in the Beaufort Gyre will stop, and the excess freshwater that has built-up will no longer be supported by Ekman pumping. It is unclear how long it will take for the positive trend in the momentum flux to reverse, and this may have important implications for the future evolution of the Arctic's freshwater budget and for freshwater release into the North Atlantic.

Throughout this chapter, it has been assumed in the construction of the idealised annual cycles that the momentum transfer will increase during summer. It should be noted, however, that the seasons have been arbitrarily defined, and the increased momentum transfer in summer could equally be interpreted as an increased momentum transfer in winter. Furthermore, given the results of the modified seasonality experiments, it is clear that whether the momentum transfer is increased in winter or summer is not important for the accelerated accumulation of freshwater in the Beaufort Gyre, as all that matters is the integrated net forcing over the entire year.

2.6.3 Relevance of the Simple Model

Despite having no effect on the net freshwater content of the Beaufort Gyre, modifications made to the seasonality in ocean surface stress whilst the net forcing is held constant *do* impact the annual cycle in freshwater storage and transport through the channel in the model (see Figures 2.6b,c,e,f). Given the limitations of the simple process model (including, but not limited to, the parametrised effects of eddies and diapycnal mixing, and the lack of vertical resolution and a sea ice component), it is possible that there are processes missing from the model which may be important in determining the response

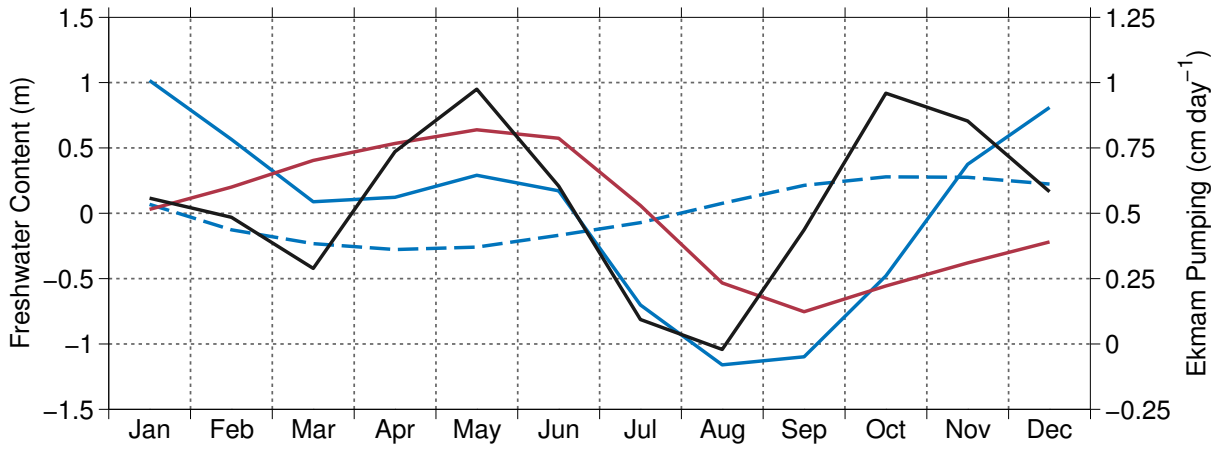

Figure 2.8: The blue lines show the mean annual cycle in the liquid freshwater content (FW_c; Equation 1.1) anomaly integrated between the surface and 25 m (dotted line) and between the surface and the depth of the 34.8 psu isohaline (solid line) over the Beaufort Gyre region from the MIMOC climatology. The red line shows the mean annual cycle in the solid (ice) freshwater content anomaly from upward looking sonar deployed as part of the Beaufort Gyre Exploration Project. The black line is the mean annual cycle in Ekman pumping velocity at the base of the Ekman layer over the Beaufort Gyre region, calculated from the wind stress curl. Positive velocities indicate a downwelling.

of the Beaufort Gyre to a change in the seasonality in ocean surface stress. To explore this further, the driving mechanisms behind the annual cycle of freshwater content in the Beaufort Gyre are examined using Arctic climatological datasets and data collected in the Beaufort Gyre.

Averaged over the Beaufort Gyre region, Figure 2.8 shows the annual cycle in liquid freshwater content (FW_c; Equation 1.1) anomaly integrated between both the surface and the 34.8 psu isohaline (blue solid line), and between the surface and 25 m (blue dashed line) from the Monthly Isopycnal / Mixed-layer Ocean Climatology (MIMOC; *Schmidtko et al.*, 2013), the annual cycle in solid (ice) freshwater content anomaly (red line) from upward-looking sonar deployed as part of the Beaufort Gyre Exploration Project, and the magnitude of the annual cycle in Ekman pumping (black line) from the ERA-Interim reanalysis. MIMOC has been used instead of the PHC as it resolves the annual cycle, and has been updated with the most recent surface data collected by Ice-Tethered Profilers. In the upper 25 meters of the water column, the annual cycle in liquid freshwater content (blue dashed line) is dominated by thermal forcing (sea ice formation and melt; red line). It reaches a minimum in April-May due to brine rejection from sea ice formation, and a maximum in October-November due to sea ice melt. On the other hand, over the full depth

range of the Beaufort Gyre (i.e. from the surface to the depth of the 34.8 psu isohaline), the annual variation in Ekman pumping (black line) appears to be the dominant forcing behind the annual cycle in total liquid freshwater content (solid blue line), with thermal forcing having little effect. The liquid freshwater content peaks in December-January due to stronger Ekman pumping during winter (although there appears to be a short time lag), and is at a minimum during August-September due to weaker Ekman pumping and a relaxation of the salinity field. An intermediary peak is observed in May, which is most likely associated with a seasonal re-intensification of the atmospheric Beaufort High (*Yang*, 2006, 2009).

Together, these results suggest that Ekman pumping is the dominant process in setting the annual cycle in liquid freshwater content within the Beaufort Gyre (although locally the balance may be different; *Proshutinsky et al.*, 2009). Consequently, it can be concluded that the simple process model does resolve the important dynamical processes behind the response of the Beaufort Gyre to a change in forcing, and that the decline in Arctic sea ice cover will affect the seasonality of the Beaufort Gyre and its freshwater content in a manner similar to the results of the model. The amplitude of the annual cycle in freshwater content (blue line in Figure 2.8) would be expected to increase as the amplitude of the annual cycle in ocean surface stress increases, and the timing of the peaks in the annual cycle will change as the efficiency of momentum transfer increases and decreases at different times throughout the year.

2.6.4 Implications for the Arctic Freshwater Budget

In the modified seasonality experiments, the amplitude of the annual cycle in transport through the channel averages 0.3 to 0.4 Sv. In comparison with the studies of *de Steur et al.* (2009) and *Curry et al.* (2014), this is smaller than the amplitude of the annual cycle in the volume transport of surface layer waters through both Fram Strait (≈4 Sv) and Davis Strait (≈0.6-0.8 Sv). The small amplitude in the model directly reflects the limited annual variability seen in the layer thickness, which is both consistent with observational data (e.g. *Proshutinsky et al.*, 2009) and is a direct consequence of the long timescale over which the model adjusts to the change in forcing. Consequently, whilst having some

impact, the annual variability in the export of freshwater from the Beaufort Gyre cannot be the main driver behind the annual variability seen in the exports to either side of Greenland, and variability driven by local conditions is likely to be more important. For example, *Lique et al.* (2009) have shown that the variability in the liquid freshwater flux through Fram Strait depends upon variability in both the volume flux and the in-situ salinity, which varies strongly due to ice formation and melt north of Greenland. Given the far-reaching consequences that changes in the export of freshwater to either side of Greenland may have on the circulation of the Atlantic Ocean, future studies should aim to quantify the contribution that the seasonal release of freshwater from the Beaufort Gyre has on the total freshwater export from the Arctic Ocean.

Independent of any accumulation of freshwater due to sea ice decline, the freshwater content of the Beaufort Gyre has been steadily increasing since the mid 1990s due to the large-scale anticyclonic wind regime (*Proshutinsky et al.*, 2009). If, in the future, the wind regime becomes cyclonic, then the excess freshwater stored in the Beaufort Gyre will be released to the shelves (*Häkkinen and Proshutinsky*, 2004; *Condron et al.*, 2009; *Jahn et al.*, 2010), where it may be exported into the North Atlantic (*Stewart and Haine*, 2013). Such a release of freshwater has been proposed as a mechanism to explain some of the "Great Salinity Anomaly" events, during which the subpolar North Atlantic and Nordic seas underwent decadal periods of freshening (e.g. *Dickson et al.*, 1988; *Belkin et al.*, 1998; *Belkin*, 2004), with associated effects on the formation of North Atlantic Deep Water (*Dickson et al.*, 2000; *Jahn et al.*, 2010). Consequently, the accelerated accumulation of freshwater in the Beaufort Gyre may exacerbate the effects of a switch to a cyclonic wind regime, by making the Arctic even more anomalously fresh beforehand, and thus increasing the quantity of freshwater that may be exported into the North Atlantic. It must be noted, however, that local dynamics in Fram Strait and the Canadian Arctic Archipelago will also play a major role in determining the quantity of freshwater that can be exported from the Arctic Ocean in the future, and understanding these dynamics motivates the work in Chapters 4 and 5.

2.6.5 Effect of Changing Meteorological Conditions

Throughout this chapter, the focus has been on the effect that changing sea ice conditions will have on the freshwater content of the Beaufort Gyre, without considering the potential impacts of changes in the wind field. However, as the strength of the atmospheric Beaufort High projects onto several different modes of atmospheric variability (*Serreze and Barrett*, 2011; *Mauritzen*, 2012), large-scale changes in atmospheric conditions may lead to a further accumulation or release of freshwater from the Beaufort Gyre that has not been accounted for in the model. For example, since the mid 1990s a negative trend in the phase of the Arctic Oscillation has strengthened the atmospheric Beaufort High in winter (i.e. the anticyclonic wind regime), and more recently, a positive trend in the strength of the Arctic Dipole Anomaly between 2007 and 2012 may have acted to strengthen the Beaufort High in summer (*Overland et al.*, 2012; *Ogi and Wallace*, 2012). Furthermore, the study of *Simmonds and Keay* (2009) has shown that the strength of Arctic summer cyclones over the Eurasian Arctic has been increasing over the past 30 years, and if this were to continue, then the momentum flux into the ocean during summer may be reinforced by an enhanced wind forcing over the Beaufort Gyre region.

2.7 Conclusions

The overall aim of this chapter was to investigate the dynamical response of the Beaufort Gyre to the changing efficiency of momentum transfer associated with the decline in Arctic sea ice cover, and its link to the accelerated accumulation of freshwater observed by *Giles et al.* (2012). From two sets of experiments where the annual cycle in ocean surface stress was idealistically perturbed to reflect the effect of diminishing Arctic sea ice, it has been shown that when the annual mean ocean surface stress (i.e. the net forcing) is held constant, changes to its seasonal cycle (i.e. the seasonality) have no net effect on the annual mean freshwater content of the Beaufort Gyre in the model. Instead, the Beaufort Gyre continually adjusts to the seasonal changes in ocean surface stress since the adjustment timescale, which is set by eddies, is considerably longer than seasonal.

On the other hand, a linear relationship is found between the increase in the annual

mean ocean surface stress and the amount of freshwater accumulated in the Beaufort Gyre, regardless of the seasonal cycle in the forcing. This linear relationship is similar to that found by *Proshutinsky et al.* (2002, 2009) between the freshwater content of the Beaufort Gyre and the wind stress curl over the region, and it suggests that as the Arctic sea ice cover continues to decline, the linear accumulation of freshwater in the Beaufort Gyre for a given wind stress curl will increase (e.g. *Giles et al.*, 2012), due to the enhancement in the magnitude of the stress that is transferred from the surface of the ice pack to the ocean below. This confirms that the increased efficiency of momentum transfer into the upper ocean associated with the decline in Arctic sea ice cover is a plausible mechanism to explain the accelerated accumulation of freshwater in the Beaufort Gyre. The total quantity of freshwater accumulated for a given change in ocean surface stress depends on the eddy diffusivity, i.e. on the length of time it takes for the eddy field to balance the change in Ekman pumping. The key dynamical process at play is as follows: as Arctic sea ice is becoming weaker, thinner and more broken up, the annually averaged momentum flux into the upper ocean is increasing for the same wind speed, resulting in an accelerated linear accumulation of freshwater through an enhanced mechanical deformation of the salinity field.

The results have implications for both the net amount of freshwater stored in the Beaufort Gyre and the annual cycle in its freshwater content. This may have an effect on the annual cycle in freshwater export from the Arctic Ocean, and future observational studies aimed at detecting changes in the seasonality of the Beaufort Gyre freshwater content would be worthwhile. At the same time, the results have highlighted the importance of eddies in the transient response of the Arctic to a change in forcing, and more should be done to investigate the role they play using eddy resolving models.

Chapter 3

Effects of Elevated Vertical Mixing and Freshwater Input on Arctic Stratification and Sea Ice Cover

The work in this chapter has been submitted for publication as:
Davis, P.E.D., C. Lique, H.L. Johnson, and J.D. Guthrie (2015), Competing Effects of Elevated Vertical Mixing and Increased Freshwater Input on the Stratification and Sea Ice Cover in a Changing Arctic Ocean, *Journal of Physical Oceanography*.

The previous chapter focused on understanding the effect that Arctic sea ice decline, and the changing efficiency by which wind energy is transferred into the upper ocean, is having on the freshwater content of the Beaufort Gyre. Stronger wind forcing, however, will also affect the magnitude of internal wave mixing in the Arctic (e.g *Rainville et al.*, 2011), and may positively feedback on to the sea ice decline by increasing the diffusive heat flux from the Atlantic layer. At the same time, however, the accumulation of freshwater in the Arctic (e.g. *Vavrus et al.*, 2012) may act to offset the effects of elevated internal wave mixing by increasing the strength of the stratification associated with the cold halocline. Motivated by the impacts of Arctic sea ice decline, this chapter focuses on understanding how these two competing processes may affect the strength of the stratification and the stability of the cold halocline, and thus the role they may play in the ongoing melting of Arctic sea ice, in a 1D model of the Arctic Ocean water column.

3.1 Introduction

The vertical structure in the upper water column of the Eurasian Basin is characterised by the cold and fresh surface mixed layer overlying the deeper warm (T>0°C) and salty Atlantic layer (Figure 3.1). The heat contained within the Atlantic layer is sufficient to melt all sea ice in the Arctic within a few years (*Turner*, 2010). However, this heat is isolated from the mixed layer by the cold halocline, in which near-freezing temperatures coincide with a strong salinity gradient (Figure 3.1; *Aagaard et al.*, 1981; *Rudels et al.*, 1996; *Toole et al.*, 2010). As salinity dominates density at low temperatures, the cold halocline creates a layer of strong stratification which limits the depth to which surface-generated mixing can penetrate, and the near-freezing temperatures ensure that any pycnocline water that is mixed up to the surface is devoid of excess heat. As a result,

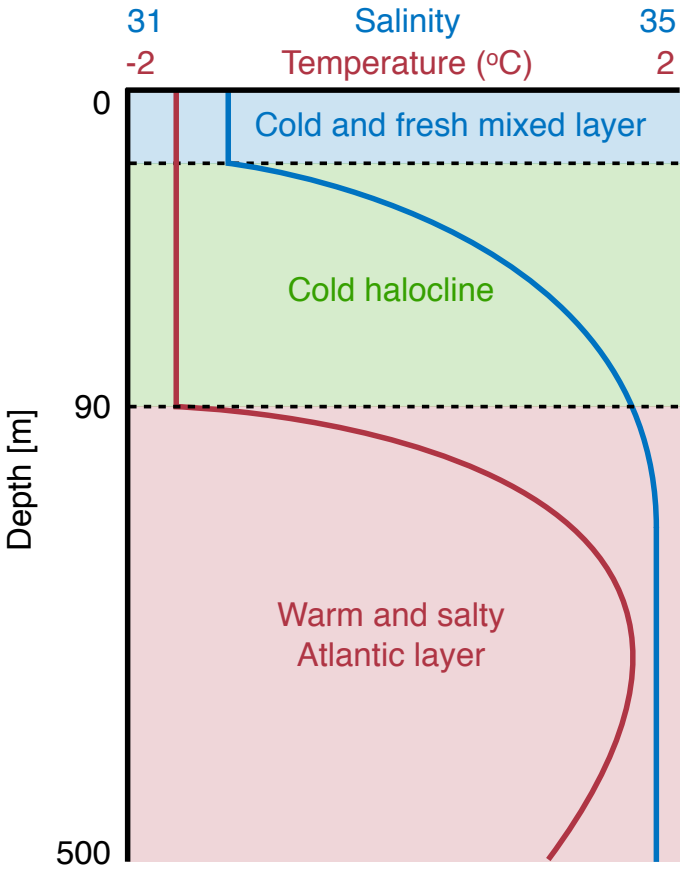

Figure 3.1: Schematic of the vertical temperature (red line) and salinity (blue line) structure in the upper 500 m of the Eurasian Basin in the Arctic Ocean. The cold halocline (green layer) is characterised by the coincidence of near-freezing temperatures with a strong salinity gradient, and acts to isolate the cold and fresh surface mixed layer (blue) from the heat contained within the warm and salty Atlantic layer (red).

the only process by which the heat contained within the Atlantic layer can be transferred to the surface is through diffusion, such as that associated with the breaking of internal waves or double diffusive processes.

Scattered observations throughout the Arctic Ocean have shown, however, that the energy associated with the internal wave field is one to two orders of magnitude smaller than that observed at lower latitudes (*Levine et al.*, 1985, 1987; *Plueddemann*, 1992; *D'Asaro and Morison*, 1992; *Guthrie et al.*, 2013). This is due to the limited generation of internal wave energy through the interaction of the barotropic tide with topography (*Simmons et al.*, 2004; the majority of the Arctic basin is north of the M_2 critical latitude), shielding of the ocean from direct wind forcing due to the sea ice cover (*Rainville et al.*, 2011), and the dissipation of internal wave energy in oscillating under-ice boundary layers (*Morison et al.*, 1985; *Pinkel*, 2005). Consequently, the rate of vertical mixing across the cold halocline from the breaking of internal waves is only slightly larger than molecular levels, and the vertical heat flux to the surface is close to zero. For example, *Shaw and Stanton* (2014) show that the vertical diffusivity (K_z) in the deep central Canadian Basin averages near molecular levels between 2.2×10^{-7} and 3.4×10^{-7} m^2 s^{-1}, leading to a heat flux of 0.1 W m^{-2}, and *Rainville and Winsor* (2008) found that K_z averaged 10^{-6} m^2 s^{-1} in the deep interior basins, increasing to 10^{-5} m^2 s^{-1} in the upper ocean. In the Eurasian Basin, *Fer* (2009) inferred from microstructure observations that the heat flux across the cold halocline was not significantly different from zero, and *Sirevaag and Fer* (2012) observed a heat flux due to double diffusion of 0.6 W m^{-2}. Similarly, in the Canadian Basin, *Timmermans et al.* (2008) observed a heat flux of 0.05-0.3 W m^{-2}. These estimates are only an order of magnitude larger than molecular diffusion alone, and are significantly smaller than the value required to adversely affect the sea ice cover at the surface (*Maykut and Untersteiner*, 1971).

The Arctic region is, however, changing rapidly. As discussed in Chapter 1, climate model projections suggest that sea ice cover at the surface will decline at such a rate that the ocean will be ice-free in summer sometime around the middle of the century (*Wang and Overland*, 2009; *Stroeve et al.*, 2012a), and freshwater input from enhanced river runoff and excess precipitation over evaporation will increase by ≈30% by 2050

(*Vavrus et al.*, 2012; *Bintanja and Selten*, 2014; *Haine et al.*, 2015). Although increased freshwater input should strengthen the cold halocline by increasing the magnitude of the salinity gradient, the decline in Arctic sea ice cover may lead to periodic increases in vertical mixing, through the enhancement of wind-driven near-inertial motions during ice-free periods (*Pinkel*, 2005; *Rainville and Woodgate*, 2009; *Rainville et al.*, 2011). Although a substantial amount of this excess near-inertial energy will be lost to directly mixing the surface layer, a portion may propagate deeper where it can erode the cold halocline and enhance the vertical heat flux from the Atlantic layer (*Fer*, 2014). Consequently, the interplay between enhanced freshwater input and elevated vertical mixing may play a significant role in determining how the vertical heat flux to the underside of the sea ice will change over the coming decades. As even a small change in the vertical heat flux may have irreversible impacts on sea ice cover at the surface (*Maykut and Untersteiner*, 1971; *Polyakov et al.*, 2012), which itself might affect both local and remote climates (see Section 1.4.1), understanding these processes is critical.

Observations already show that the freshwater content of the Arctic Ocean is increasing (see Section 1.4.2). On the other hand, despite the average decrease of $14 \pm 3\%$ per decade in the September sea ice extent between 1979 and 2012 (*Overland and Wang*, 2013), and the average increase in the Arctic-wide melt season length of 6 days per decade over the same period (*Markus et al.*, 2009), it is not yet clear whether vertical mixing is increasing. The analysis of expendable current profiler (XCP) data collected in the 1980s and late 2000s by *Guthrie et al.* (2013) shows that there has been no temporal trend in vertical mixing over the thermocline, and the pan-Arctic microstructure measurements reported in *Rippeth et al.* (2015) suggest that vertical mixing over the Atlantic layer thermocline shows no dependence on sea ice cover. In contrast, *Rainville and Woodgate* (2009) observed a dramatic increase in the strength of vertical mixing in the upper 100 m during ice-free periods in the Chukchi Sea, with the average diffusivity increasing from molecular levels during winter to 2×10^{-4} m^2 s^{-1} during summer. Similarly, *Dosser et al.* (2014) observed a seasonal cycle in the amplitude of wind-driven near-inertial waves in the upper 200 m of the Canadian Basin in response to the annual cycle in sea ice cover. During summer, the average amplitude increased by 0.45 m over the winter value, despite the weaker winds,

suggesting a strong coupling between sea ice conditions and the inertial wave field. In addition, the appearance of a second autumn phytoplankton bloom in the Arctic, which is correlated with delayed freeze up and increased exposure of the ocean to direct wind forcing, provides indirect evidence that elevated vertical mixing is driving a supply of nutrients into the mixed layer during these periods (*Ardyna et al.*, 2014); in the ice-free Chukchi Sea, *Nishino et al.* (2015) also observed a peak in nutrient fluxes and primary productivity associated with gale force winds and enhanced turbulent mixing (*Kawaguchi et al.*, 2015).

Despite the lack of a consistent pan-Arctic signal, which might still be too small to detect, the decline in Arctic sea ice cover is very likely to result in periodic increases in vertical mixing during ice-free periods, as the ocean is more easily forced by the wind (*Tsamados et al.*, 2014; *Martin et al.*, 2014), and the magnitude of under-ice dissipation is reduced. The aim of this chapter is to explore how the competing effects of elevated vertical mixing and freshwater input will affect the stratification, the stability of the cold halocline and the sea ice cover at the surface, using a 1D model of the Arctic Ocean water column. Specifically, the focus will be on the following questions:

1. How do periodic increases in vertical mixing affect the diffusive heat flux through the cold halocline and therefore the sea ice cover at the surface? To what extent can freshwater input at the surface offset the effect of elevated vertical mixing?

2. In what mixing/freshwater regimes does the cold halocline remain stable and how long might it take for the cold halocline to be completely eroded? What effect will this have on the sea ice cover at the surface?

The approach used in this chapter is similar to that of *Killworth and Smith* (1984) and *Bjork* (1989), who use 1D models to investigate the Arctic Ocean halocline and upper ocean stratification. By using a model that contains only the essential physics needed to represent the competing effects of elevated vertical mixing and freshwater input, it is possible to explore a wide parameter space that is applicable to the future Arctic, and isolate the role that the changing Arctic Ocean will play in the ongoing melting of Arctic sea ice.

In Section 3.2 the setup of the 1D model is described, with the design of the model experiments detailed in Section 3.3. In Section 3.4 the results of the different model experiments are presented, with a discussion of their implications in Section 3.5. The conclusions of the work in this chapter are presented in Section 3.6.

3.2 Model Setup

The 1D General Ocean Turbulence Model (*Burchard et al.*, 1999) is used to simulate the upper 500 metres of the Arctic Ocean, which is sufficient to cover the region of the water column in which this chapter is interested (i.e. to the core of the AWL). The model is governed by the following temperature and salinity diffusion equations:

$$\begin{aligned} \frac{\partial \theta}{\partial t} &= \frac{\partial}{\partial z}\left(K_z \frac{\partial \theta}{\partial z}\right) - R^{\theta} \\ \frac{\partial S}{\partial t} &= \frac{\partial}{\partial z}\left(K_z \frac{\partial S}{\partial z}\right) - R^{S}, \end{aligned} \tag{3.1}$$

where θ is potential temperature (henceforth all temperatures are assumed to be potential temperature) , S is salinity, t is time, z is depth, K_z is vertical diffusivity, and $R^{\theta}(z)$ and $R^{S}(z)$ represent all other processes not explicitly resolved here that maintain the temperature and salinity stratification. The equations are discretised on a vertical grid with a resolution of 1 meter, and the nonlocal K-Profile Parameterisation (KPP) scheme of *Large et al.* (1994) is used to ensure continuity between the interior and mixed layer diffusivities (discussed later).

The model is initialised with winter (DJF) climatological temperature and salinity profiles from the central Eurasian Basin (Figure 3.2a), averaged between 85^{o}N-90^{o}N and 0^{o}E-120^{o}E from the Monthly Isopycnal / Mixed Layer Ocean Climatology (MIMOC; *Schmidtko et al.*, 2013). The profiles are interpolated from their climatological levels onto a regular 1 metre grid, and smoothed with a 9 metre running mean to minimise sharp gradients. The results of this study are not sensitive to small changes in these initial profiles. Due to the lack of a sea ice model at the surface, the ML temperature can cool below the local freezing point, and this cooling is taken to represent sea ice formation.

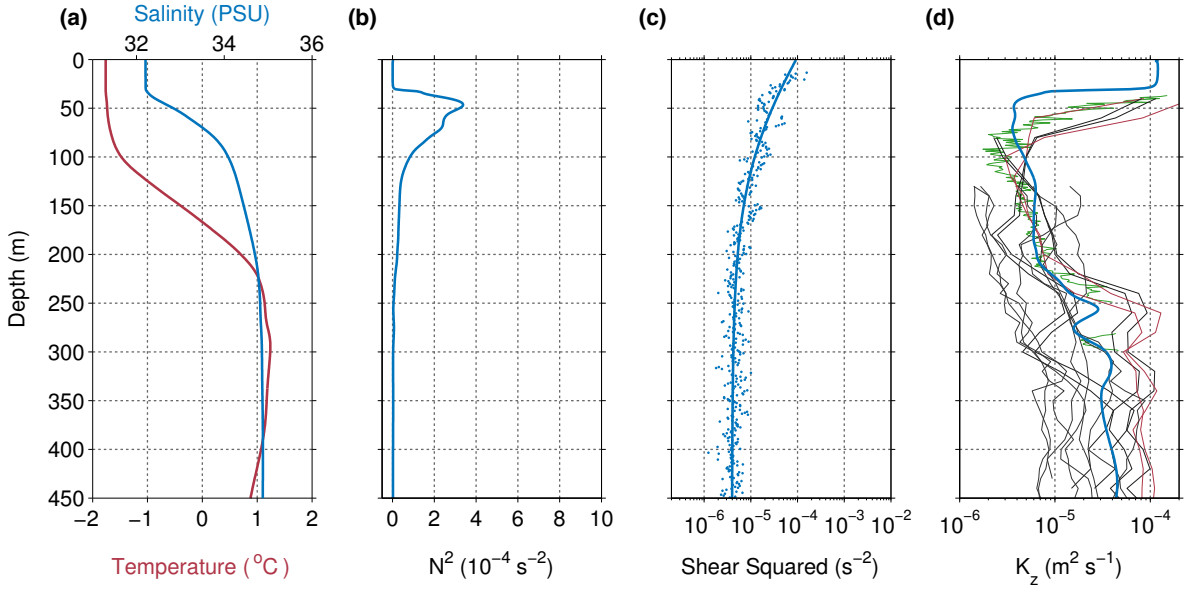

Figure 3.2: Initial profiles of (a) temperature and salinity averaged over the central Eurasian Basin region from the MIMOC climatology, (b) the corresponding buoyancy frequency, (c) the climatological shear squared, derived from XCP data collected during the North Pole Environmental Observatory surveys between 2008 and 2011, and (d) the corresponding vertical diffusivity due to shear instability associated with internal wave breaking (blue line), parameterised through Eq. 3.2. The thin black lines in (d) show the vertical diffusivity in the Eurasian Basin estimated by *Guthrie et al.* (2013), and the red and green lines show the vertical diffusivity derived from microstructure observations by *Guthrie et al.* (2013) and *Fer* (2009), respectively.

The model is forced solely by vertical mixing/diffusivity, freshwater input at the surface, and the prescribed, constant in time but depth-dependent terms $R^{\theta}(z)$ and $R^{S}(z)$. These represent the net effect of those processes (e.g. lateral advection, surface heat fluxes, and mean sea ice processes) which balance the vertical diffusivity and freshwater input at the surface in the long term mean, and are determined by restoring θ and S to the mean winter profiles in the control run to ensure a steady state is reached. They are then fixed for the remainder of the study. The details of these terms are described in more detail below.

In the interior, it is assumed that the vertical diffusivity in Equation 3.1 is a function of only the shear instability associated with internal wave breaking, and is parameterised in terms of the Richardson number (Ri; *Pacanowski and Philander*, 1981):

$$K_z = \frac{K_z^{max} + \nu_b(1+\alpha Ri)^n}{(1+\alpha Ri)^{n+1}} + K_z^b, \tag{3.2}$$

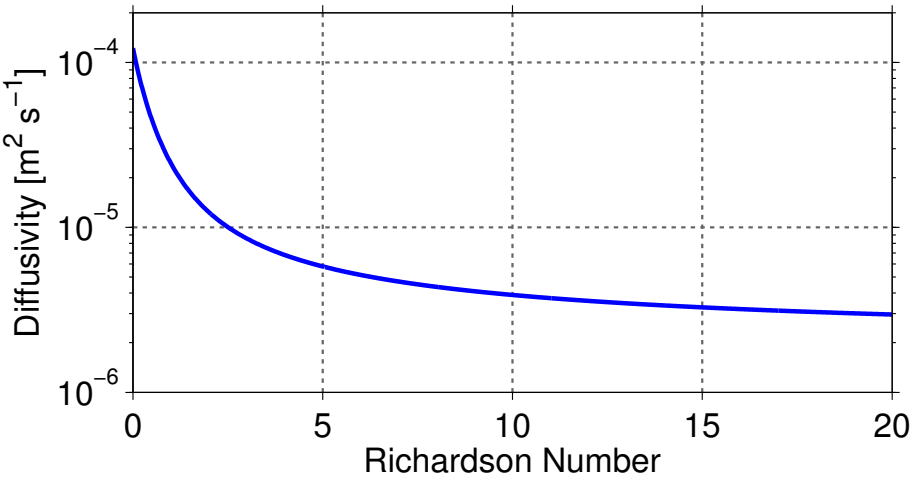

Figure 3.3: Vertical diffusivity plotted as a function of the Richardson number (i.e. Equation 3.2). Large Richardson numbers indicate the presence of strong stratification and therefore low mixing/diffusivity, whilst small Richardson numbers indicate the presence of strong shear and therefore high mixing/diffusivity.

where

$$Ri = \frac{N^2}{S^2} \tag{3.3}$$

is a function of the buoyancy frequency (N^2; Figure 3.2b) and the shear squared (Figure 3.2c)

$$S^2 = \left(\frac{\partial u}{\partial z}\right)^2 + \left(\frac{\partial v}{\partial z}\right)^2. \tag{3.4}$$

K_z^{max} is the maximum diffusivity, K_z^b is the background diffusivity, ν_b is the background viscosity, and α and n are tuning parameters. This parameterisation was specifically chosen as it allows the diffusivity to be sensitive both to changes in the freshwater input, and periodic increases in vertical mixing. Physically, if the stratification is strong (significant freshwater input, large N^2) and the shear is weak (small S^2), the Richardson number is large and the diffusivity is small, with K_z tending towards K_z^b (Figure 3.3). Conversely, if the stratification is weak and the shear is strong, the Richardson number is small and the diffusivity tends towards K_z^{max} (Figure 3.3).

Observations in the Arctic (e.g. *Halle and Pinkel*, 2003, *Pinkel*, 2005, and *Dosser et al.*, 2014) have shown that the internal wave field is highly episodic in nature, and the shear instability associated with internal wave breaking exhibits high frequency variability both in time and space. However, it is challenging to incorporate this variability directly into models due to the limitations associated with their much coarser space and time

resolutions. As *Lique et al.* (2014) have shown that these episodic mixing events act to increase the magnitude of the average background mixing, and as it is expected that the Arctic internal wave field will move closer to a more typical mid-latitude Garrett-Munk (*Garrett and Munk*, 1975) internal wave field during longer ice free periods (i.e. with stronger mean background shear and diffusivity), the classical approach used by models that don't resolve the relevant time and space scales is followed by defining the initial shear squared profile (Figure 3.2c) to be the average of 28 individual u and v velocity shear profiles collected during the North Pole Environmental Observatory airborne hydrographic surveys between 2008 and 2011 (*Guthrie et al.*, 2013). The u and v velocity data from each of the XCP casts are interpolated onto a regular 1 meter grid, and the corresponding u and v velocity shear profiles are calculated from overlapping 8 meter bins, with a resolution of 1 meter. The absolute values from each of the 28 u and v velocity shear profiles are then averaged to produce a single u and v velocity shear profile, to which curves of the form

$$\frac{\partial u}{\partial z} \quad \text{or} \quad \frac{\partial v}{\partial z} = ae^{bz} + ce^{dz}, \tag{3.5}$$

where z is depth and a, b, c, and d are constants, are fitted in order to smooth sharp gradients. These fitted velocity shear profiles are then integrated from the bottom boundary at 500 meters (where the velocity is set to zero) to the surface, to produce the corresponding idealised u and v velocity profiles with which the model is forced. It is important to note that although the shear should scale with the stratification, no empirical relationship between these two properties exists that can be implemented in the model. Therefore although the shape of the shear profile will likely change as the stratification evolves, this behaviour is not incorporated into the model on the assumption that any change in shear due to the evolving stratification will likely be significantly smaller than the change in shear which is implemented manually to enhance the vertical mixing (discussed in section 3.3).

To match the initial profile of K_z (Figure 3.2d) to observations of diffusivity from the Eurasian Basin (*Fer*, 2009; *Guthrie et al.*, 2013), K_z^b was set to the observed value of 2.0×10^{-6} m^2 s^{-1} (*Rainville and Winsor*, 2008), ν_b to 2.0×10^{-5} m^2 s^{-1} (*Large et al.*, 1994), α to 1 and n to 2. K_z^{max} was set to 10^{-4} m^2 s^{-1}, the maximum plausible value in

the ocean interior (*Munk*, 1966; *Munk and Wunsch*, 1998). Figure 3.2d shows the good agreement between the initial K_z profile and the observations. In the ML, K_z is large (approximately 10^{-4} m^2 s^{-1}) due to the weak stratification and strong shear (Figures 3.2b and 3.2c). Below the ML and into the cold halocline, the stratification increases and the shear decreases, reducing K_z to a minimum of 2.0×10^{-6} m^2 s^{-1}. Beneath the cold halocline, the weakening stratification drives a general trend towards higher K_z, despite the lower shear.

At present, freshwater input to the Arctic from rivers and excess precipitation over evaporation equals 6400 km^3 yr^{-1} (*Haine et al.*, 2015). When divided by the area of the Arctic (9.7×10^6 km^2), this corresponds to an average input of 2.12×10^{-8} m s^{-1} (based on a 360 day model year), which is applied at the surface of the model. Throughout this chapter it is assumed that the freshwater input from rivers is distributed evenly throughout the Arctic Ocean. To rapidly distribute this freshwater throughout the ML, an ocean stress of 0.044 N m^{-2} is applied at the surface which generates a region of highly elevated diffusivities due to the KPP mixed layer module. The magnitude of the ocean stress agrees well with the average winter ocean stress over the Eurasian Basin from the NEMO-LIM coupled ice-ocean model (*Lique and Steele*, 2012). In all model runs, the effect of the wind stress on the vertical diffusivity is restricted to the upper 31 m, which is the depth of the ML in the climatological profiles (the depth of the ML throughout this study is defined as the depth at which the density has increased by 0.01 kg m^{-3} from the surface value). This choice has been made to ensure that changes to the diffusivity and thus the vertical heat flux below this depth reflect only the interplay between the elevated diffusivity and the enhanced freshwater input. In all model experiments the the ML depth is free to evolve in response to the changing heat flux/FW input.

The lateral advection of "new" water masses into the 1D domain, as well as all other processes such as surface heat fluxes, and salt fluxes from sea ice formation and melt, that balance the vertical diffusivity and freshwater input at the surface in the long term mean, are taken into account through the depth dependent terms $R^\theta(z)$ and $R^S(z)$. The effect of seasonality and future changes in the strength of these processes (which likely depend on poorly understood processes such as the effect of sea ice retreat on shelf and

shelf edge processes, changes in the absorption of solar radiation into the upper ocean, variability and change in advective pathways, and shifts in the annual cycle of sea ice cover/thickness) has specifically been excluded, by fixing the magnitude of the terms in each model run to be equal to the relaxation required to reach a steady state in the control run, i.e.:

$$R^{\theta}(z) = \frac{1}{\tau}\overline{[\theta(t,z) - \theta(0,z)]}$$

and

$$R^{S}(z) = \frac{1}{\tau}\overline{[S(t,z) - S(0,z)]}, \tag{3.6}$$

where the overbar represents a time average over the control run, τ is the relaxation timescale (12 days), and $[\theta(t,z) - \theta(0,z)]$ and $[S(t,z) - S(0,z)]$ are the differences between the temperature and salinity profiles at time t, and the initial temperature and salinity profiles ($t = 0$). This choice allows us to isolate and understand the effect that only elevated vertical mixing and enhanced freshwater input will have on the Arctic stratification and thus the sea ice cover at the surface. Figure 3.4 shows the magnitude of $R^{\theta}(z)$ and $R^{S}(z)$. In general, they act to cool and remove freshwater from the ML, whilst warming and increasing the salinity of the AWL. Defining the boundary between the AWL and the upper cold halocline at 100 m, and calculating the integrated heating over these two layers as

$$Q = -\int R^{\theta}(z)\rho_0 C_p \, dz, \tag{3.7}$$

where ρ_0 is the density (1027 kg m^{-3}) and C_p is the ocean specific heat capacity (3985 J kg^{-1} K^{-1}), shows that temperature term $R^{\theta}(z)$ results in a warming over the AWL of 0.28 W m^{-2}, and a fully compensating cooling over the cold halocline. This compares well to the observational estimates of the vertical heat flux from the AWL of *Timmermans et al.* (2008), *Sirevaag and Fer* (2012), and *Shaw and Stanton* (2014). It should be noted that there is no flux of salt or heat through the bottom boundary at 500 meters.

Because a simple 1D representation of the Arctic Ocean is adopted, there are a number of important processes that cannot be directly resolved in the model. As $R^{\theta}(z)$ and $R^{S}(z)$ are fixed in time, the effect that any interplay between enhanced vertical mixing and seasonality in the Arctic ML depth (which is poorly constrained; *Peralta-Ferriz and*

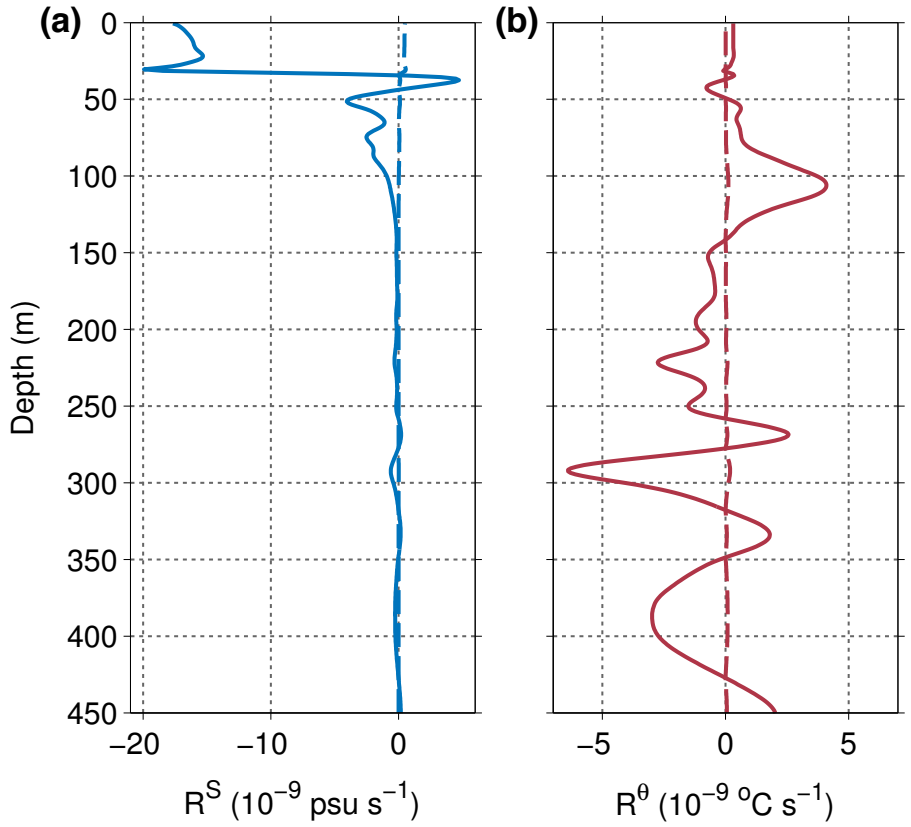

Figure 3.4: Magnitude of the depth-dependent relaxation constants for (a) salinity: R^S, and (b) temperature: R^θ, that are required to ensure that the initial temperature and salinity profiles do not diverge from their initial values in the control run. The magnitude of the relaxation in each perturbation run is fixed at these values.

Woodgate, 2015a), winter convection (due to surface heat fluxes and sea ice formation), and the processes that form the cold halocline may have on the sea ice cover at the surface cannot be considered, whilst the effects of long term changes in the advection of water masses around the Arctic are also ignored. In addition, despite the net effect of the surface heat flux being included within the $R^\theta(z)$ and $R^S(z)$ terms, the effect of changes in surface heating are not considered. Although the surface heat flux is likely to play a major role in the future sea ice budget of the Arctic by heating the upper ocean during ice-free periods (e.g. *Timmermans*, 2015), this study is primarily interested in isolating the role that elevated vertical mixing and deeper changes to the Arctic Ocean water column will play in the ongoing melting of Arctic sea ice. Finally, the effects of ice-ocean interactions at the surface are not included; *Barthélemy et al.* (2015) show that the parameters required for brine rejection parameterisations are poorly observed and constrained. Possible implications of these missing processes for the results will be discussed in Section 3.5.

3.3 Experimental Design

Over the coming decades, freshwater input to the Arctic Ocean is expected to increase (e.g. *Haine et al.*, 2015), and the decline in Arctic sea ice cover is likely to drive periodic increases in vertical mixing during ice-free periods. To explore how these competing processes will affect the stratification and sea ice cover, four parameters were perturbed in the model. These are: (1) the magnitude of the velocity shear during ice-free periods, (2) the depth to which this elevated velocity shear penetrates, (3) the length of the ice-free period, and (4) the magnitude of the freshwater input. Since the future trends in the magnitude of these parameters are unknown, they are perturbed idealistically through a wide parameter space that is broadly applicable to the future Arctic. For each unique set of parameters, the model is initialised from the profiles in Figure 3.2 and run for 50 years, which represents the period of time over which CMIP3/CMIP5 (Coupled Model Intercomparison Project Phase 3/5) models predict that the Arctic will have become predominantly ice-free in summer (*Wang and Overland*, 2009, 2012; *Stroeve et al.*, 2012a).

The magnitude of velocity shear during ice-free periods is perturbed by multiplying the initial velocity shear profiles by a factor of 1 through 6 (referred to as the shear factor or *SFac*), matching the change in the velocity shear observed by *Rainville and Woodgate* (2009) during ice-free periods in the Chukchi Sea. The shear factor is not constant throughout the water column, but is at its maximum at the surface and decreases smoothly to 1 at the depth to which the elevated velocity shear penetrates (referred to as *ZMax*). Based on the initial profiles, *ZMax* is defined as either 90 m (the base of the cold halocline), 300 m (the core of the Atlantic layer) or 195 m (midway between the base of the cold halocline and the core of the Atlantic layer). An example of the effect that these perturbations have on the shear squared and diffusivity profiles can be seen in Figures 3.5a and 3.5b. Although the perturbations to K_z in Figure 3.5b are small (with a shear factor of 6 extending to a *ZMax* of 300 m, K_z increases to only 7-8$\times 10^{-6}$ m^2 s^{-1} across the cold halocline), the cumulative effect over a model run is much more significant. For example, Figure 3.5c shows the effect on K_z after 50 years, when the same perturbations have been applied for 6 months of each year, with no change in the freshwater input. In this case, K_z has increased by nearly two orders of magnitude, as the stratification has

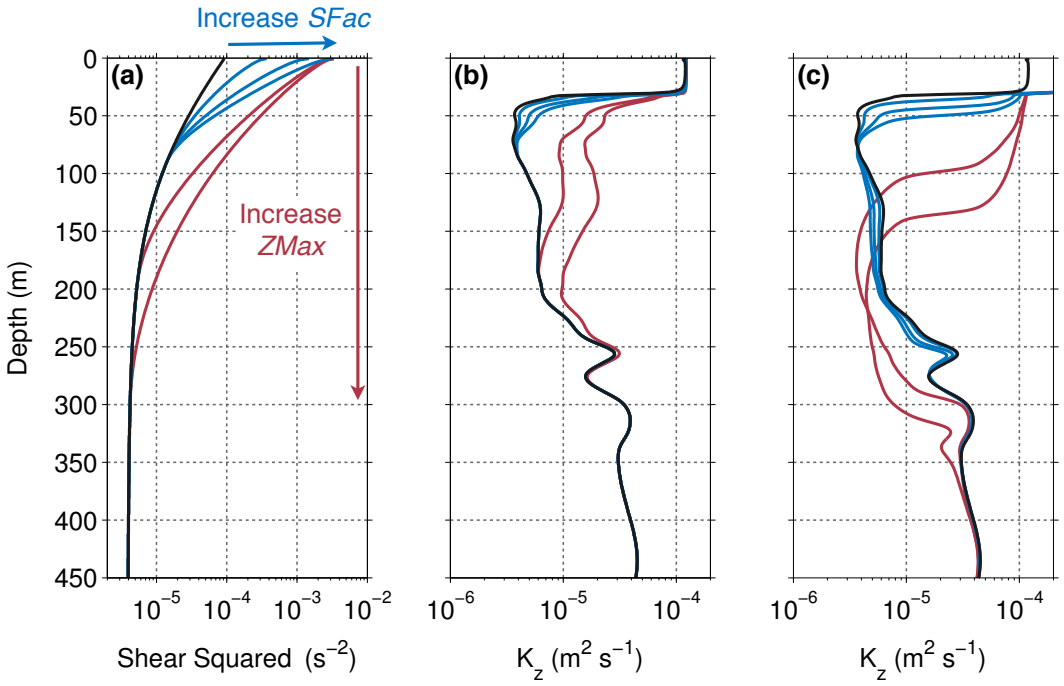

Figure 3.5: The effect on (a) the shear squared profile, and (b) the parameterised diffusivity profile when the control velocity shear profiles are multiplied by a shear factor of 2, 4 or 6 down to a *ZMax* of 90 m (blue lines), and by a shear factor of 6 down to a *ZMax* of 195 m or 300 m (red lines). (c) shows the effect that the same perturbations made to the velocity shear in (a) have on the diffusivity after 50 years of a model run in which they have been applied for 6 months of each year with no change in the freshwater input. Note that the very high diffusivities seen in the mixed layer in (c) are due to the ocean stress applied at the surface.

weakened throughout the 50 years.

The length of the ice-free period is either 2 months, 4 months, or 6 months, reflecting the general trend towards a thinner and less extensive sea ice cover, with the earlier occurrence of melt onset and later freeze-up (*Markus et al.*, 2009; *Overland and Wang*, 2013; *Pinker et al.*, 2014; *Wang and Overland*, 2015). During these ice-free periods the model is forced with the perturbed velocity shear profiles (i.e. Figure 3.5a), and over the remainder of the year the model is forced with the control velocity shear profiles (i.e. Figure 3.2c). It should be noted that these "ice-free periods" can also be interpreted as periods during which a less extensive but still present sea ice cover is acting to enhance the transfer of wind momentum into the upper ocean (as discussed in Chapter 2).

The freshwater input from river runoff and excess precipitation over evaporation is perturbed by applying annual anomalies at the surface which represent a 0% to 30% increase from present-day values, spanning the change projected by the state-of-the-art CMIP5 climate models in the Arctic freshwater input over the next 50 years (*Vavrus et al.*,

2012; *Bintanja and Selten*, 2014; *Haine et al.*, 2015). The annual anomaly is distributed equally throughout the year, and is applied at the surface grid cell.

3.4 Results

Arctic sea ice is sensitive to changes in the diffusive heat flux, and the extent to which the mixed layer is isolated from the heat contained within the Atlantic layer. How and why these parameters will likely evolve over the coming decades is explored in this section.

3.4.1 Mixed Layer Temperature and the Diffusive Heat Flux

Figure 3.6 shows the change in average mixed layer temperature from the control value, for model runs in which the velocity shear has been elevated for 6 months of each year, down to a depth of 90 m (Figure 3.6a), 195 m (Figure 3.6b), and 300 m (Figure 3.6c). The results from only the longest ice-free period are shown, as the mechanisms that control the mixed layer temperature are independent of the length of the ice-free period, and are equally applicable to the remainder of the parameter space. For all model runs in which the velocity shear is elevated (i.e. excluding a shear factor of one), there is an initial increase in mixed layer temperature, the magnitude of which depends predominantly on the shear factor, and the depth of *ZMax*. For example, when *ZMax* is 300 m (Figure 3.6c), the maximum change in mixed layer temperature for model runs with a shear factor of 6 is 0.25°C (purple dot-dashed line), compared to a maximum of only 0.03°C for model runs with a shear factor of 2 (light blue dot-dashed line). In contrast, when *ZMax* is 90 m (Figure 3.6a), the maximum change in mixed layer temperature does not exceed 0.01°C.

After a number of years, however, the mixed layer begins to cool. The point in time at which this occurs in each model run is marked with a coloured dot, and is determined by the magnitude of the freshwater input and the depth of *ZMax*. For example, for model runs with a *ZMax* of 300 m (Figure 3.6c) and no change in the freshwater input (blue dots), the maximum mixed layer temperature occurs after 15-20 years. In comparison, with a freshwater input anomaly of 30% (black dots), the maximum mixed layer temperature is reached between 11-14 years. When *ZMax* is only 90 m (Figure 3.6a), the maximum

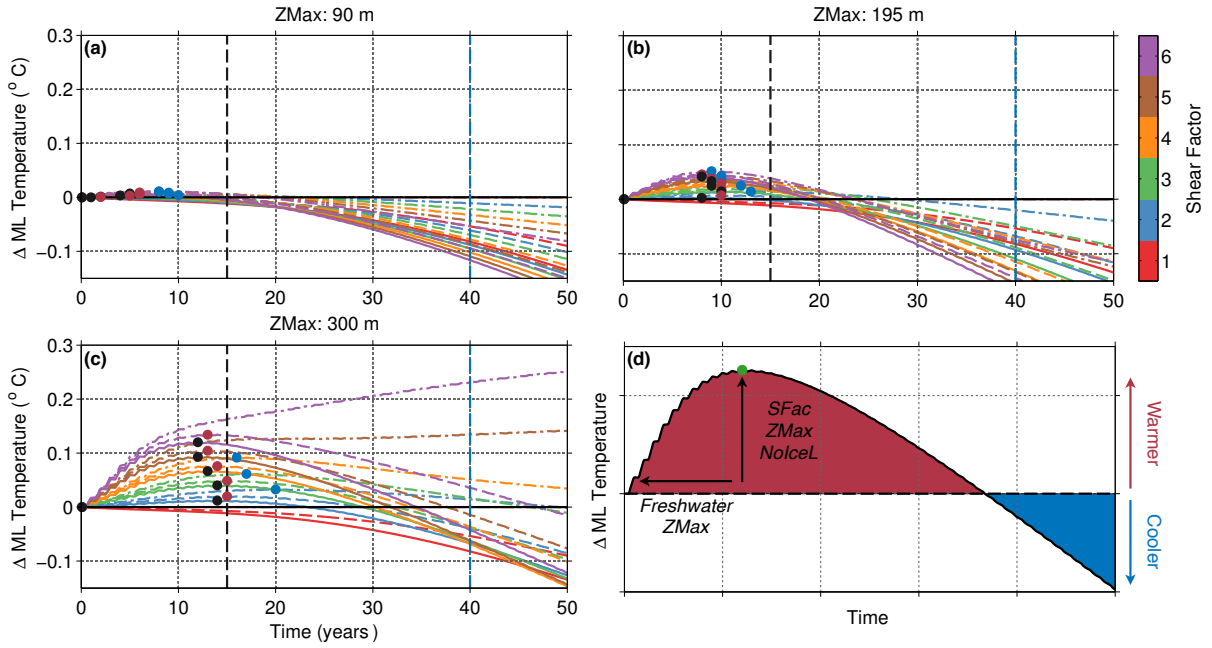

Figure 3.6: Time series of the change in the mixed layer temperature from the control value, for model runs in which the velocity shear profiles have been perturbed for 6 months of each year, down to a *ZMax* of (a) 90 m, (b) 195 m, and (c) 300 m. The color of each line in (a,b,c) represents the shear factor, and the solid, dashed and dot-dashed lines represent a 30%, 15% and 0% increase in the freshwater input, respectively. The coloured dots mark the maximum change in the mixed layer temperature, with the black, red and blue dots corresponding to a 30%, 15% and 0% increase in the freshwater input, respectively. If a symbol is not present for a specific model run, it indicates that the mixed layer temperature has not reached a maximum within 50 years. The black and blue dashed vertical lines mark 15 and 40 years of each model simulation, respectively. (d) Schematic showing the mechanisms that control the timing and magnitude of the maximum change in the mixed layer temperature (green dot). *SFac* refers to the shear factor, *ZMax* refers to the depth to which the elevated shear penetrates, *NoIceL* refers to the length of the ice-free season, and *Freshwater* refers to the magnitude of the freshwater input anomaly.

mixed layer temperature occurs within the first 10 years, irrespective of the freshwater input. For the two model runs in Figure 3.6c with an *SFac* of 5 and 6 and a 0% increase in the freshwater input (i.e. the brown and purple dot-dashed lines, respectively), the positive trend in mixed layer temperature does not reverse for at least another 50 years. At this point, it must be noted that due to the lack of a sea ice model at the surface, the mixed layer temperature can cool below the local freezing point. If this occurs it is assumed that sea ice is forming at the surface, and this can be see in more detail in Figure 3.9.

Following *de Boisséson et al.* (2010), the mixed layer heat budget for the model can be written as

$$h\left\langle\frac{\partial\theta}{\partial t}\right\rangle = -h\langle\mathbf{u}\rangle.\nabla\langle\theta\rangle + K_z\frac{\partial\theta}{\partial z}_{(z=-h)}, \tag{3.8}$$

where h is the depth of the mixed layer, $\langle\rangle$ indicates a depth average over the mixed layer, the first term on the right-hand side represents the change in mixed layer temperature due to advection, and the second term the change in mixed layer temperature due to the diffusive heat flux at the base of the mixed layer. As the rate of advection is constant in the model, variability in mixed layer temperature depends solely on changes in the diffusive heat flux. Therefore it can be deduced from Figure 3.6 that during the initial phase of each model run, the diffusive heat flux is enhanced compared to the control run, whereas later in each run, the diffusive heat flux must decrease with respect to the control run.

To understand the changes in the diffusive heat flux across parameter space, a number of individual model runs are examined. Figure 3.7 shows the water column structure after 15 and 40 years (black and blue dashed line in Figure 3.6, respectively), for four model runs that span the full range of trajectories in mixed layer temperature, whilst Figure 3.8 shows Hövmoller plots of the change in temperature and salinity from the control run for the same four model runs. The initial increase in mixed layer temperature (top inset in Figure 3.7a, and, for example, Figure 3.8c,g) in all model runs in which the velocity shear is perturbed is due to larger diffusivities in the upper 100 m (Figure 3.7d) driving an enhanced diffusive heat flux. In contrast, when only the freshwater input is increased (Figure 3.8a), the mixed layer cools as the stronger stratification decreases the diffusivity and reduces the magnitude of the diffusive heat flux (blue profile in Figure 3.7a). The initial increase in mixed layer temperature depends strongly on the depth to which the elevated shear penetrates, as the diffusive heat flux depends upon both the diffusivity and the strength of the temperature gradient. Deeper mixing can interact with the much stronger Atlantic layer temperature gradient below ≈100 m, and can thus drive significantly more heat into the mixed layer. For example, for two model runs with the same shear factor and freshwater input, the change in mixed layer temperature after 15 years is 0.16°C when *ZMax* is 300 m (orange profile in Figure 3.7a and Hövmuller plot 3.8g), compared to only 6×10^{-3} °C when *ZMax* is 90 m (purple profile in Figure 3.7a and Hövmuller plot 3.8e). In contrast to *ZMax*, the elevated freshwater input has little effect, with a 30% increase reducing the maximum change in mixed layer temperature by only

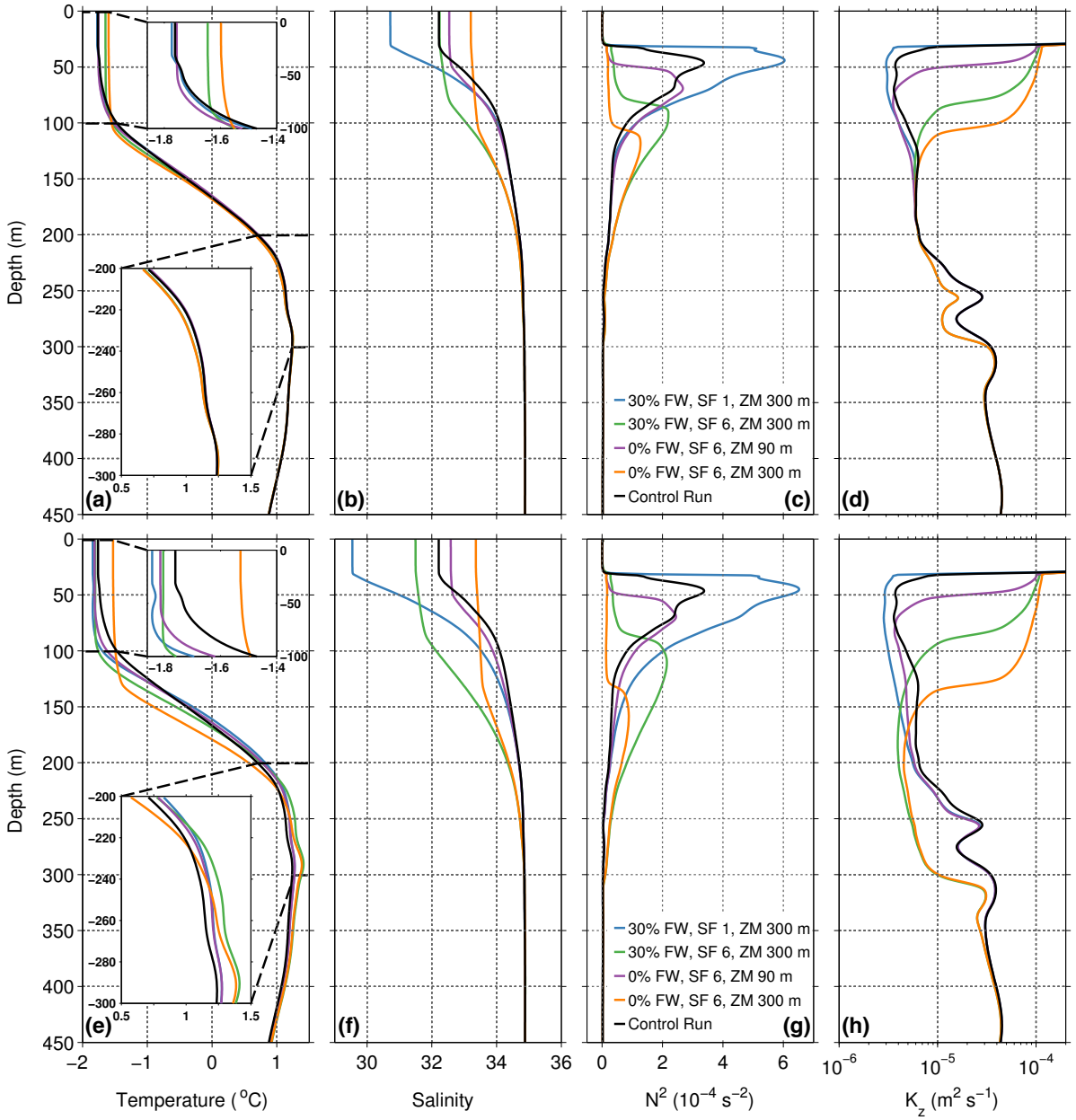

Figure 3.7: Profiles of (a,e) temperature, (b,f) salinity, (c,g) buoyancy frequency and (d,h) diffusivity for a number of individual model runs. Profiles (a,b,c,d) show the water column structure after 15 years of each model run (black dashed line in Figure 3.6), and profiles (e,f,g,h) show the water column structure after 40 years (blue dashed line in Figure 3.6). In the legend, FW refers to the magnitude of the freshwater input anomaly, SF refers to the magnitude of the shear factor, and ZM refers to the depth of *ZMax*.

0.04°C (compare the orange and green profiles in Figure 3.7a). Overall, in comparison with the current annual change in mixed layer temperature driven by the absorption of solar radiation (>1°C; *Perovich et al.*, 2008; *Steele et al.*, 2011), and the projected future increase from CMIP5 models in the annual cycle of sea surface temperature due to sea ice retreat (*Carton et al.*, 2015), the change in mixed layer temperature after 15 years is insignificant.

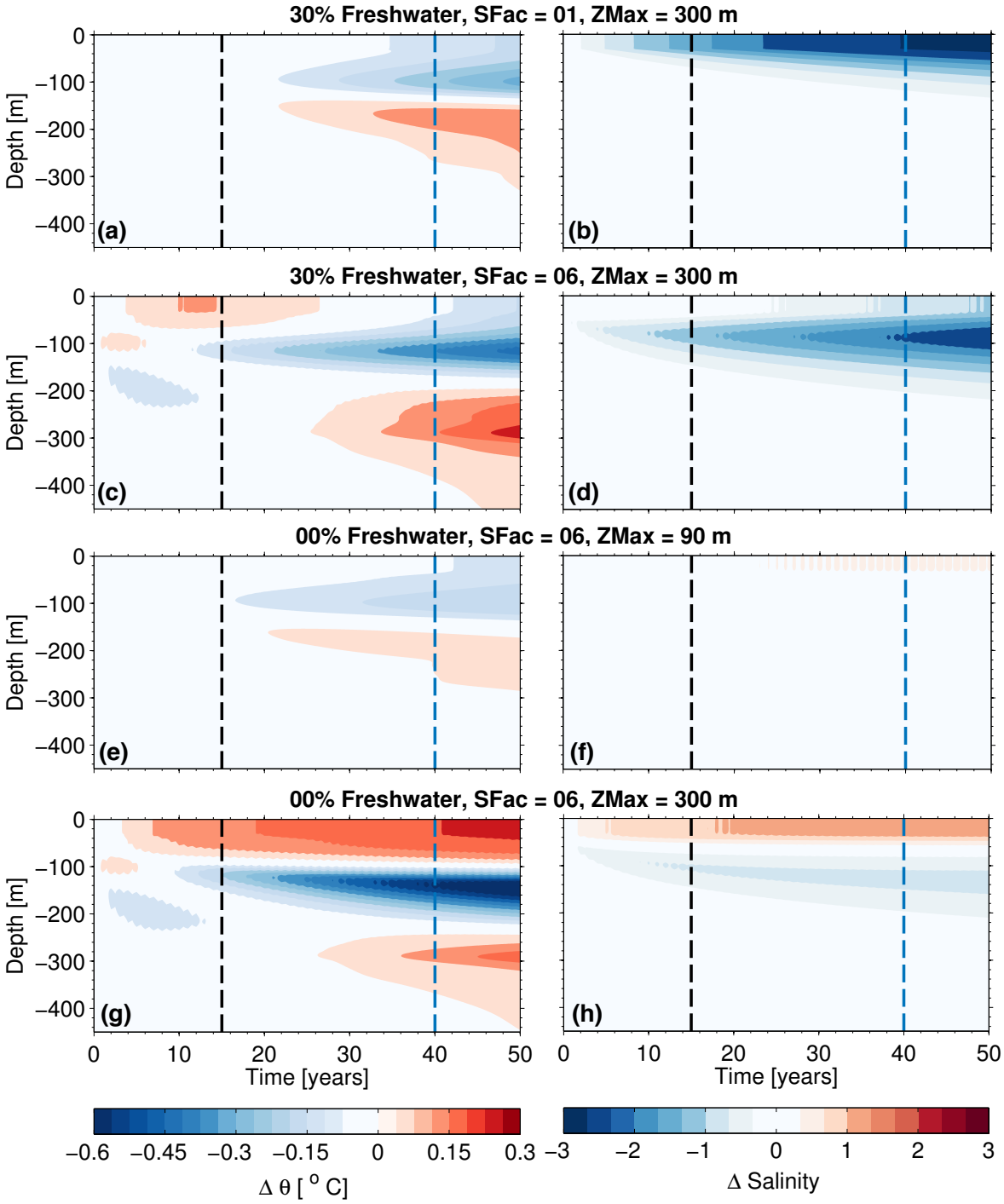

Figure 3.8: Hövmoller plots of the change in (a,c,e,g) temperature and (b,d,f,h) salinity from the control run for the same individual model runs as plotted in Figure 3.7. The black and blue dashed vertical lines mark 15 and 40 years of each model simulation, respectively.

The elevated diffusivity also affects the stratification throughout the water column. As evident in Figure 3.7c, the strength of the stratification has decreased to zero over the cold halocline (associated with a weakening of the salinity gradient), whilst deeper in the water column, the stratification has increased due to a strengthening of the salinity gradient. Consequently, the depth of maximum stratification has increased from 44 m

in the control run, to a maximum of 118 m, and the diffusivity has decreased between 200-300 m.

After 40 years, Figures 3.7e and Hömuller plots 3.8a,c,e show that the mixed layer has cooled in all model runs with respect to the control run (except when $ZMax$ is 300 m and there is no increase in the freshwater input (orange profile in Figure 3.7a and Hövmuller plot 3.8g). In this case the diffusivity has continued to increase in the upper water column, maintaining the flux of heat into the mixed layer). The mixed layer has cooled due to the continued strengthening of the stratification over the Atlantic layer (i.e. between ≈100 m and 300 m) decreasing the diffusivity and thus the magnitude of the diffusive heat flux. The stratification has strengthened because of both the freshwater input at the surface freshening the water column (Figures 3.8b,d), and the continued deepening of the maximum salinity gradient. In addition to cooling the mixed layer, the reduced diffusive heat flux also causes the Atlantic layer to warm (bottom inset Figure 3.7e), which is similar to the results of *Nummelin et al.* (2015).

To summarise the results thus far, the schematic presented in Figure 3.6d highlights the dominant processes responsible for determining the evolution of the diffusive heat flux and mixed layer temperature. Elevated shear drives an initial increase in mixed layer temperature, due to larger diffusivities enhancing the diffusive heat flux across the base of the mixed layer. As the diffusive heat flux depends upon both the diffusivity and the magnitude of the temperature gradient, the change in mixed layer temperature is greater for higher shear factors, and when the elevated shear penetrates deep into the Atlantic layer. It must be noted, however, that over the entire parameter space, the diffusive heat flux at the base of the mixed layer does not exceed 0.2 W m^{-2}. This is significantly smaller than the ocean/ice to atmosphere heat flux during winter (25 W m^{-2}; *Overland et al.*, 1997) and the input of solar radiation into the upper ocean during summer (25-75 W m^{-2}), which has been shown to have a significant impact on the sea ice cover at the surface (*Timmermans*, 2015). The increase in the mixed layer temperature is also greater for longer ice-free seasons, as the integrated heat flux over the year is larger. After a period of time, however, strengthening of the stratification over the Atlantic layer weakens the diffusivity, and a decrease in the upward diffusive heat flux causes the mixed layer to cool.

The time it takes for this to occur is shorter when the freshwater input is greater and when *ZMax* is shallower (shallower mixing drives only a small increase in the diffusive heat flux due to the near zero temperature gradient, but is able to readily deepen the maximum stratification because of the stronger salinity gradient near the surface).

Following *Steele et al.* (2008, 2011), the effect of the elevated diffusive heat flux on the sea ice cover was quantified by calculating the change in the mixed layer heat content from the initial profile ($t = 0$) after $t = 15$ and $t = 40$ years of each model run:

$$H_c = \rho_0 C_p \left[\int_{z=-h}^{z=0} (\theta(t) - \theta_f(t))\, dz \; - \; \int_{z=-h}^{z=0} (\theta(0) - \theta_f(0))\, dz \right], \tag{3.9}$$

where ρ_0 is the density (1027 kg m^{-3}), θ_f is the in-situ freezing point based on the average mixed layer salinity at time t, and C_p is the ocean specific heat capacity (3985 J kg^{-1} K^{-1}). The equivalent net quantity of sea ice that can be melted/formed due to this change in heat content is

$$\Delta h_I = \frac{H_c}{\rho_I L_I}, \tag{3.10}$$

where ρ_I is the density of sea ice (900 kg m^{-3}) and L_I is the latent heat of fusion of sea ice ($3{\times}10^5$ J kg^{-1}).

Figure 3.9 shows that after 15 years, the effect of the elevated diffusive heat flux is limited (similar to the results of *Nummelin et al.*, 2015), with a maximum equivalent net sea ice loss of only 12 cm (bottom right in Figure 3.9c). When the elevated shear extends to a depth of either 195 m or 300 m, the contour lines showing the change in mixed layer temperature are aligned parallel to the freshwater axes, highlighting the limited role played by freshwater input in determining the initial increase in mixed layer temperature. In contrast, when *ZMax* is 90 m, or the freshwater input is significant, the decrease in mixed layer heat content is equivalent to the net formation of 4 cm of sea ice. This formation is driven by the combination of cooler mixed layer temperatures compared to the control run, and an increase in the local freezing point due to the input of freshwater. This second process is particularly important for the equivalent net sea ice formation seen to the right of the magenta line in Figures 3.9a,b,c, where the input of freshwater has raised the local freezing point faster than the rate at which the mixed layer temperature

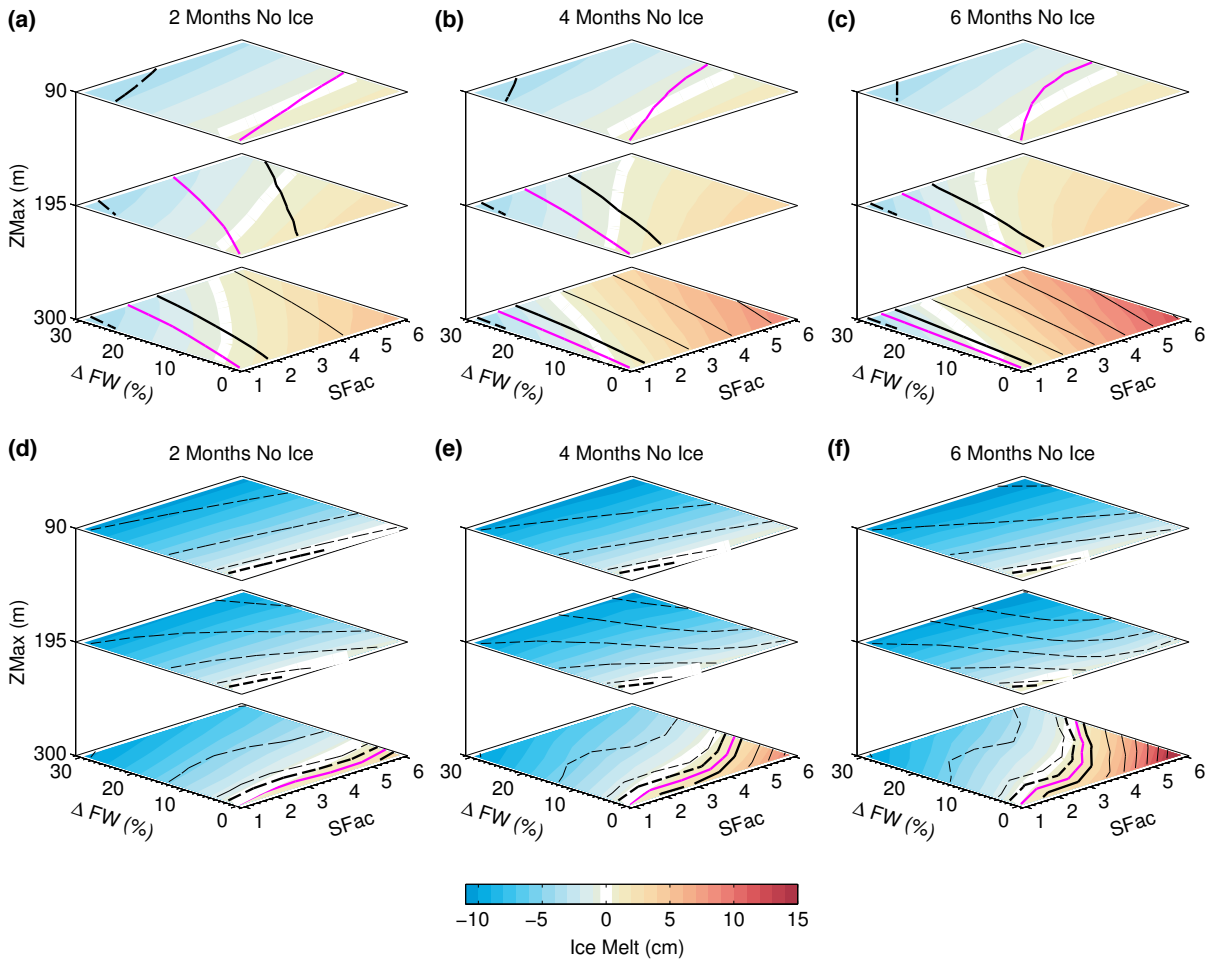

Figure 3.9: Thickness of ice (colour contours) that could be melted/formed due to the change in the mixed layer heat content after (a,b,c) 15 years and (d,e,f) 40 years of each model run, plotted as a function of the shear factor (*SFac*) and the freshwater anomaly at the surface (Δ FW). The individual columns represent the different lengths of the ice-free season, and the individual layers in each column represent the three different depths to which the elevated shear penetrates (i.e. *ZMax*). Negative ice melt indicates ice formation. Overlain are contours showing the change in the mixed layer temperature from the control run. Solid contours indicate an increase in the mixed layer temperature, and dashed contours indicate a decrease in the mixed layer temperature. The contour interval is 0.03°C, with the zero contour marked in magenta, and the first contour (i.e. ±0.03°C) marked in bold.

has increased. It must be noted that a snapshot taken at 15 years is after the maximum mixed layer temperature has been reached for model runs with a *ZMax* of either 90 m or 195 m (Figure 3.6). However, at the point of maximum mixed layer temperature for each *ZMax* (8 years and 9 years for 90 m and 195 m, respectively), the equivalent net loss of ice is only 2 cm and 5 cm, respectively.

After 40 years, Figure 3.9 shows that the parameter space is dominated by net sea ice formation, with ongoing sea ice melt limited to model runs in which strongly elevated shear extends to the Atlantic layer and there is little change in the freshwater input. In

this case, the maximum equivalent net sea ice loss is ≈16 cm (bottom right Figure 3.9f). The magnitude of the equivalent net sea ice formation seen throughout the remainder of the parameter space is determined by the magnitude of the freshwater input (the coloured contours lie parallel to the *SFac* axes), and reaches a maximum of 11 cm. It is interesting to note that for a *ZMax* of 90 m or 195 m, runs with higher shear factors tend to exhibit a greater decrease in mixed layer temperature from the control run for a given freshwater input, but this is not reflected in the sea ice formation. This is due to these runs exhibiting a smaller decrease in the mixed layer salinity compared to those with a lower shear factor, such that the ability to form more sea ice due to the cooler mixed layer temperatures is offset by a lower freezing point. As will be discussed later, the quantity of sea ice that can be melted by the elevated diffusive heat flux is significantly less than the current annual cycle of sea ice melt and formation, and in the long term is considerably weaker than the effects of the other major processes responsible for ongoing melting of Arctic sea ice.

3.4.2 Cold Halocline Strength and Heat Entrainment

In the presence of a cold halocline, heat from the Atlantic layer cannot be directly entrained into the mixed layer, and the vertical heat flux is dominated by diffusive fluxes. In the following section, the focus will be on how the competing effects of elevated vertical mixing and enhanced freshwater input may affect the stability of the cold halocline, and whether it weakens sufficiently to allow warm Atlantic water to be directly entrained into the mixed layer.

Similar to the approach of *Bourgain and Gascard* (2011), the strength of the cold halocline is represented by the magnitude of the associated density gradient (N^2 in s^{-2}), calculated as

$$N^2 = \frac{g}{\rho_0} \frac{\rho_2 - \rho_1}{z_2 - z_1}, \tag{3.11}$$

where g is the acceleration due to gravity (9.81 m s^{-2}), and ρ_2 and ρ_1 are the densities at the base of the cold halocline (z_2) and the base of the mixed layer (z_1), respectively. The base of the cold halocline is defined as the depth at which the temperature gradient first exceeds 8.5×10^{-3} °C m^{-1}. After 40 years, Figure 3.10 shows that for large increases in the shear that extend deep into the water column, the strength of the cold halocline

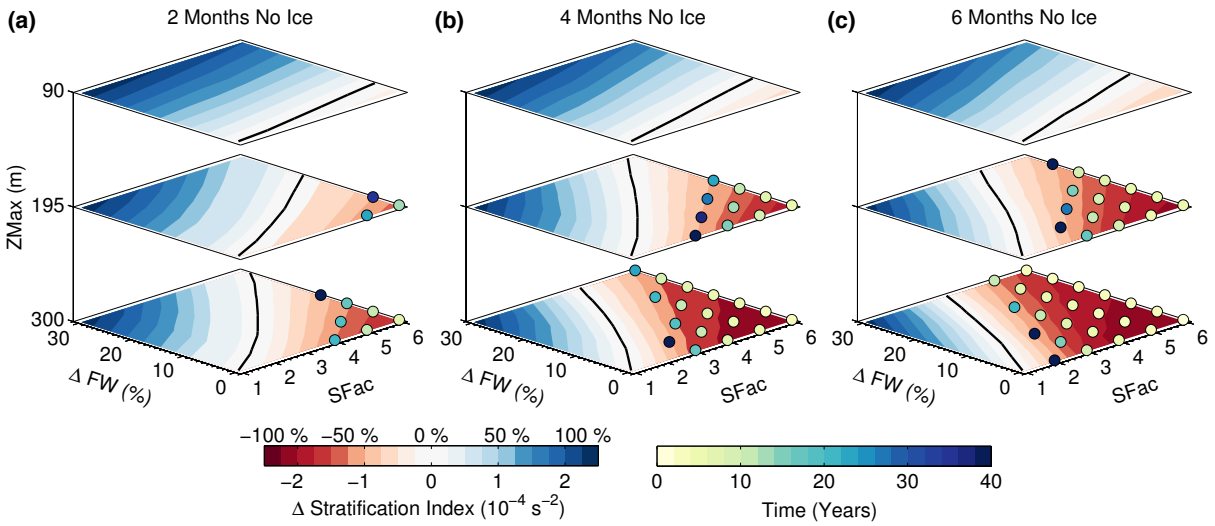

Figure 3.10: Change from the control run in the strength of the stratification associated with the cold halocline after 40 years of each model run, plotted in the same format as Figure 3.9. The solid black line indicates the zero contour for the change in the stratification index. Each model run in which the cold halocline is no longer present after 40 years is indicated with a dot. The color of the dot indicates how long it takes for the cold halocline to be fully eroded.

decreases, with the density gradient weakening by up to 94% from the control run. In contrast, when the freshwater input is large, or the elevated shear does not penetrate below 90 m, the strength of the cold halocline increases. Although it is challenging to define a theoretical cut-off in θ-S space below which the halocline is no longer present, a visual examination of individual θ and S profiles suggests that the cold halocline has been fully eroded once the stratification index has decreased by ≈40%. Each model run in Figure 3.10 in which the cold halocline is no longer present after 40 years is marked with a dot, with the color indicating the time taken for the cold halocline to be eroded. When *ZMax* is only 90 m, the cold halocline remains present, irrespective of the shear factor. In contrast, when the shear is strongly elevated, and extends to a depth of 300 m for up to 6 months of each year, the cold halocline can be fully eroded within 5-10 years.

Once the cold halocline has been fully eroded, the stratification barrier that isolates the mixed layer from the Atlantic layer is no longer present, and the sea ice cover at the surface is sensitive to the effects of wind-generated overturning, storm-driven mixing and static instability. For example, sea ice formation in the Arctic releases salt into the mixed layer, increasing the density and triggering haline convection (*Martinson and Steele*, 2001). In the absence of a cold halocline, this convection entrains water from the Atlantic layer that is above the freezing point, and can thus impact the sea ice at the surface. To quantify

the impact of this entrainment heat flux, the parameterisation developed by *Martinson* (1990) and *Martinson and Iannuzzi* (1998) is used. The parameterisation assumes that the thermal forcing for ice growth (F_L) is given by the difference between the ice to atmosphere heat flux (F_A) and the ocean to ice heat flux (F_H), which is parameterised as the average diffusive heat flux over the halocline (Figure 3.11)

$$\begin{aligned} F_L &= F_A - F_H, \\ F_L &= F_A - \rho C_p K_z \frac{\partial \theta}{\partial z}. \end{aligned} \tag{3.12}$$

F_A is taken as 25 Wm^{-2} from *Overland et al.* (1997). It should be noted that F_L does not include lateral sources of ocean heat, and consequently this parameterisation may overestimate the entrainment heat flux if vertical processes do not dominate. The thermal forcing drives an initial ice growth which, through brine rejection and haline convection, results in an entrainment heat flux from the Atlantic layer (F_E), with a magnitude given by

$$F_E = F_L \frac{\lambda_{TB}}{(\lambda_{SD} + \lambda_{TB})}. \tag{3.13}$$

λ_{SD} represents the stabilising freshwater content, relative to the salinity at the base of the halocline, that must be eroded by brine rejection in order to overturn the water column and drive deep convection. λ_{TB} represents the available heat relative to the freezing point that can be entrained into the mixed layer from the Atlantic layer (Figure 3.11; *Martinson and Iannuzzi*, 1998). λ_{SD} and λ_{TB} are calculated through vertical integration between the base of the halocline ($z = -h2$; defined as the depth at which the salinity gradient becomes less than 10^{-3} psu m^{-1}, see Figure 3.11) and the surface ($z = 0$), and are presented in terms of ice thickness (i.e. how much ice would need to form to fully erode the stabilising freshwater content, and how much ice could be melted by the heat

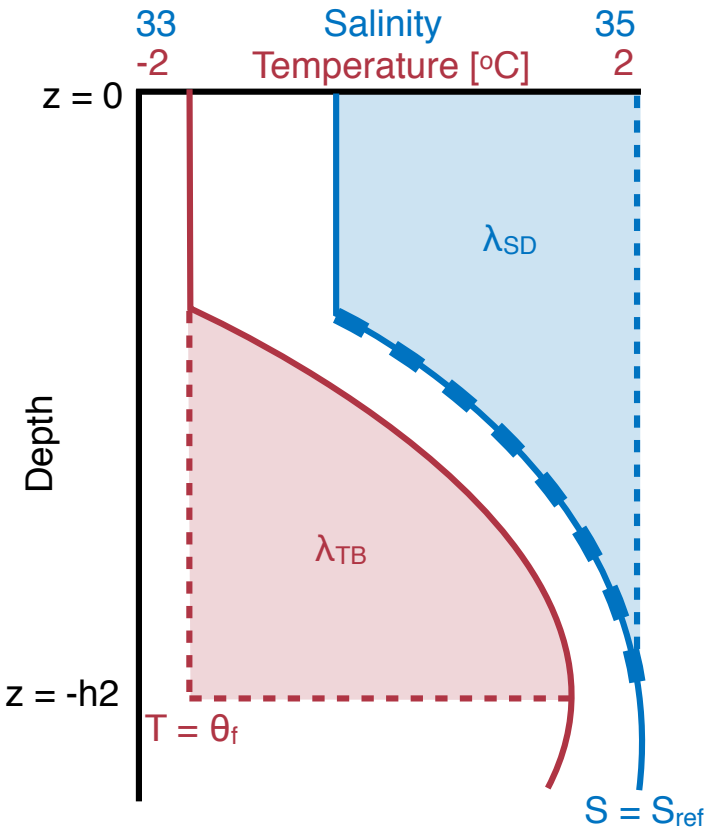

Figure 3.11: Schematic showing an idealised temperature and salinity profile in the absence of a cold halocline (i.e. there is no significant salinity gradient over the region of constant near-freezing temperatures), and the regions of the water column that are integrated through Eq. 3.14 to determine the magnitude of λ_{SD} (blue), and λ_{TB} (red). λ_{SD} represents the stabilising freshwater content relative to S_{ref} that must be eroded by brine rejection in order to overturn the water column and drive deep convection. λ_{TB} represents the available heat relative to θ_f that can be entrained into the mixed layer from the Atlantic layer. The thick dashed blue line represents the region of the water column referred to as the halocline in this parameterisation, and indicates the depth range over which the average diffusive heat flux is calculated.

contained within the Atlantic layer):

$$\lambda_{TB} = \int_{z=-h2}^{z=0} (\theta - \theta_f) \frac{\rho C_p}{\rho_I L_I} \, dz,$$

$$\lambda_{SD} = \int_{z=-h2}^{z=0} (S_{ref} - S)\sigma^{-1} \, dz. \tag{3.14}$$

S_{ref} is the reference salinity at the base of the halocline, and $\sigma^{-1} = 0.03$ is a factor used to convert λ_{SD} into units of ice thickness, based on an ice salinity of 5 psu (*Martinson and Iannuzzi*, 1998; *Vancoppenolle et al.*, 2009a,b). The thickness of ice that can be melted

by this entrainment heat flux over a 6-month period is given by

$$\Delta h_{Ice} = \left(\frac{F_E}{\rho_I L_I} \right) \Delta t, \tag{3.15}$$

where Δt is 180 days. Applying this parameterisation to the final temperature and salinity profiles from each model run in which the cold halocline has been fully eroded, shows that the entrainment heat flux is capable of melting/preventing from growing an average of 57 cm of sea ice over 6 months, with a range of 41 cm to 64 cm depending on the exact details of the stratification. This is significantly greater than the effect of the elevated diffusive heat flux, and represents a 40% reduction in the thickness of sea ice compared to that which could have been formed if a cold halocline were present. If Δt is changed to 4 months, the average thickness of ice that can be melted/prevented from growing decreases to 38 cm. The results are similar to those of *Linders and Björk* (2013), who used a 1D model to show that sea ice growth could be reduced by up to 60 cm over a single year compared to if a cold halocline was present, representing a 22% fractional reduction. The absence of the cold halocline resulted in the formation of a significantly deeper mixed layer, which drove a maximum ocean-ice heat flux of approximately 12 W m^{-2} at the end of winter (compared to a near-zero ocean-ice heat flux when the cold halocline was present). Furthermore, the study of *Steele and Boyd* (1998) suggests that during the mid 1990s, the annual average heat flux to the underside of the sea ice increased by 30-40% due to the erosion of the cold halocline in the Eurasian Basin.

The thickness of sea ice that can be melted by this entrainment heat flux is sensitive to the choice of parameters, and should not be directly compared to the estimates of equivalent net sea ice loss driven by the elevated diffusive heat flux. However, the difference in the magnitude of the two estimates suggests that the erosion of the cold halocline is the dominant of the two processes.

3.5 Discussion

Using a simple 1D model of the Arctic Ocean, it has been shown that elevated velocity shear in the Eurasian Basin initially causes the mixed layer to warm (first 10-20 years),

due to higher diffusivities and an enhanced diffusive heat flux. However, after this initial period, the mixed layer cools across much of the parameter space due to a strengthening of the stratification and a reduction in the diffusivity over the Atlantic layer. At the same time, strongly elevated diffusivity can erode the cold halocline within 10 years. In this section, the relevance of the results in a wider Arctic context are discussed, along with the timescales over which the different processes that lead to sea ice melt are important, and the effect of the different stratification found in the Canadian Basin compared to the Eurasian Basin. The section finishes with a discussion of the model limitations.

3.5.1 Timescales

Both the elevated diffusive heat flux and the erosion of the cold halocline can affect sea ice thickness in the Eurasian Basin. However, the magnitude of their effect, and the timescales over which they operate are fundamentally different. For any increase in the shear, the elevated diffusive heat flux immediately leads to sea ice melt at the surface by driving heat into the mixed layer (Figure 3.6), and can melt up to 16 cm of sea ice after 40 years. In contrast, it takes time (at least 10 years) for elevated mixing to fully erode the cold halocline (Figure 3.10) and for the mixed layer to be in direct contact with the Atlantic layer. Once the two layers are able to directly interact, however, a simple parameterisation suggests that the heat entrainment driven by haline convection can melt half a meter of sea ice in 6 months. Therefore, although direct heat entrainment from the Atlantic layer represents the most important process for the on-going melting of sea ice at the surface, it is the elevated diffusive heat flux that dominates initially, and it is only after the cold halocline has been fully eroded that heat entrainment becomes important (and the elevated diffusive heat flux becomes irrelevant).

3.5.2 Canadian Basin

Up to this point, the work in this chapter has focused on the Eurasian Basin, where constant near-freezing temperatures are found throughout the halocline. In contrast, in the Canadian Basin, a temperature maximum exists in the upper 150 m of the water column, due to the inflow of summer Pacific water (sPw) through Bering Strait (Figure

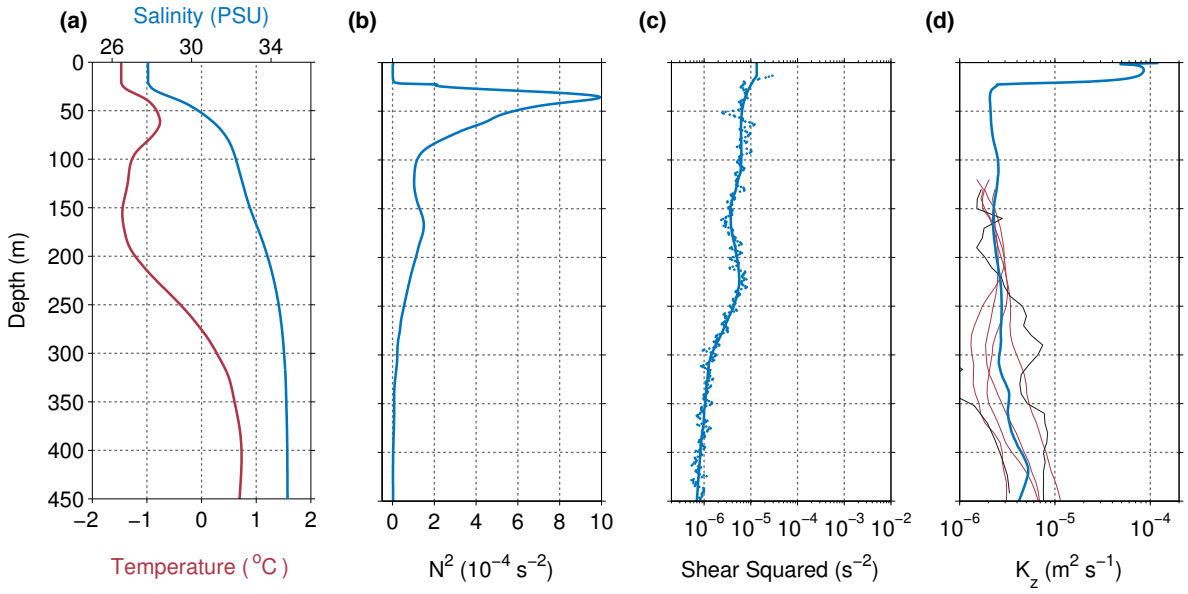

Figure 3.12: Initial profiles of (a) temperature and salinity averaged over the central Canadian Basin from the MIMOC climatology, (b) the corresponding buoyancy frequency, (c) the climatological shear squared, derived from XCP data collected during the 1985 Arctic Internal Wave Experiment, and (d) the corresponding vertical diffusivity due to shear instability associated with internal wave breaking (blue line), parameterised through Eq. 3.2. The thin black lines in (d) show the vertical diffusivity in the Canadian Basin estimated by *Guthrie et al.* (2013), and the red lines show the vertical diffusivity profiles parameterised from profiling moorings deployed in the Canadian Basin from *Lique et al.* (2014). Note the different range on the salinity and buoyancy frequency axes compared to Figure 3.2.

3.12a; *Steele et al.*, 2004; *Timmermans et al.*, 2014). sPw contains enough heat to melt ≈70 cm of sea ice (based on the heat content in the upper 155 m from an annual average profile taken from the MIMOC climatology), and thus elevated vertical mixing in the Canadian Basin may not need to penetrate so far into the water column before it can drive a significant heat flux to the surface. At the same time, however, the much stronger stratification in the central Canadian Basin due to the surface convergence of freshwater in the Beaufort Gyre (*Proshutinsky et al.*, 2009), may act to offset the effect of this shallower heat source.

To explore how the markedly different stratification in the Canadian Basin may respond to the competing effects of elevated vertical mixing and increased freshwater input, the model was re-run using initial profiles representative of the central Canadian Basin. The winter temperature and salinity profiles (Figure 3.12a) were extracted from the MIMOC climatology between 72^{o}N-80^{o}N and 130^{o}W-160^{o}W, and the shear squared profile (Figure 3.12c) is based on the average of 37 XCP casts collected during the 1985 Arctic Internal Wave Experiment (*D'Asaro and Morehead*, 1991). Rather than using double ex-

ponential curves to smooth the velocity shear profiles as in the Eurasian Basin, the shear profiles were smoothed with a 4^{th} order Savitzky-Golay filter that removed the sharp gradients but ensured the overall shape was maintained. To ensure that a shallower mixed layer depth was maintained (21 m compared to 31 m in the Eurasian Basin; consistent with the observations of *Peralta-Ferriz and Woodgate*, 2015b), the ocean stress applied at the surface was reduced to 0.02 N m^{-2}. Through Equation 3.2, the diffusivity profile (Figure 3.12d) was matched to the observations of *Guthrie et al.* (2013) and *Lique et al.* (2014) by using the same choice of parameters as those used in the Eurasian Basin, except for the value of α, which was increased to 2 to better match the observations below 250 m. The advection terms in Equation 3.1 were recalculated to match the changed θ, S, and diffusivity profiles in the Canadian Basin. Furthermore, the depths of $ZMax$ were changed to 155 m (the core of summer Pacific water; *Steele et al.*, 2004), 410 m (the core of the Atlantic layer), and 282 m (midway between the core of the summer Pacific water and the core of the Atlantic layer).

As in the Eurasian Basin, the mixed layer temperature increases in all model runs in which the shear is elevated (Figure 3.13). The magnitude of the warming depends strongly on the strength of the shear (as higher diffusivities drive a larger diffusive heat flux), but is significantly less sensitive to the depth to which it penetrates. Indeed, when $ZMax$ is 410 m, the maximum increase in the mixed layer temperature after 40 years is 0.11°C, reducing only slightly to 0.10°C and 0.09°C when $ZMax$ is 282 m and 155 m, respectively. This lack of dependence on $ZMax$ is due to the much stronger stratification found in the Canadian Basin than in the Eurasian Basin (compare Figure 3.12b with Figure 3.2b). Even when the elevated velocity shear extends to the depth of the Atlantic layer for 6 months of each year, the overall increase in the diffusivity is sufficiently small (the diffusivity does not exceed 10^{-5} m^2 s^{-1} anywhere in the water column), that there is effectively no change in the diffusive heat flux from the Atlantic layer. Consequently, the only heat available to be fluxed into the mixed layer is that contained in the sPw, which is accessible to even the shallowest increases in diffusivity. As a result, shallower mixing in the Canadian Basin can transfer significantly more heat into the mixed layer than in the Eurasian Basin (compare Figures 3.13a,b with Figures 3.6a,b), but the opposite

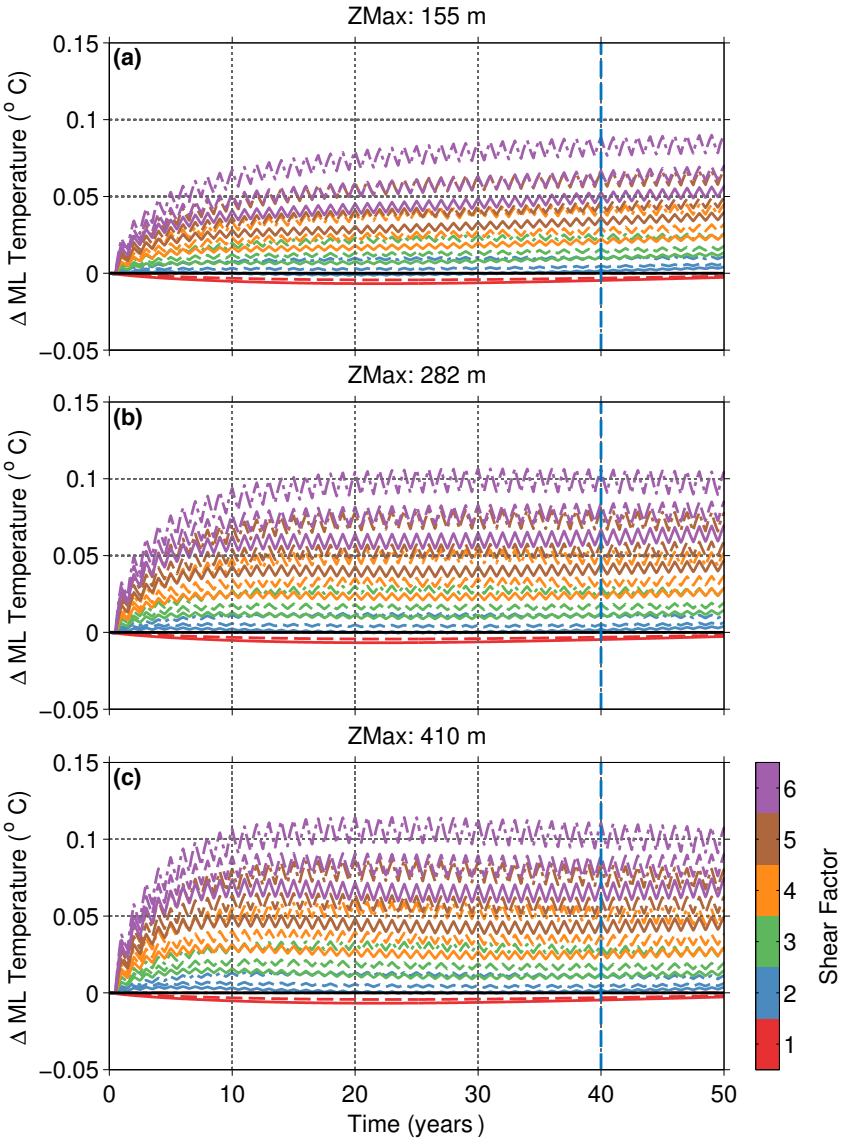

Figure 3.13: Time series of the change in the mixed layer temperature from the control value in the Canadian Basin, for model runs in which the velocity shear profiles have been perturbed for 6 months of each year, down to a *ZMax* of (a) 155 m, (b) 282 m, and (c) 410 m. The color of each line represents the shear factor, and the solid, dashed and dot-dashed lines represent a 30%, 15% and 0% increase in the freshwater input, respectively.

is true for deeper mixing as it cannot release the heat held within the Atlantic layer. Furthermore, Figure 3.13 shows that the positive trend in the mixed layer temperature does not reverse as in the Eurasian Basin, as the stratification does not strengthen over the Atlantic layer. Instead, a pseudo-steady state is reached where the flux of heat into the mixed layer during ice-free periods is balanced by advective cooling during ice-covered periods, as evident from the seasonal cycle in Figure 3.13.

Despite the increase in mixed layer temperature from the control run, Figure 3.14 shows that after 40 years (blue line in Figure 3.13), the parameter space is dominated

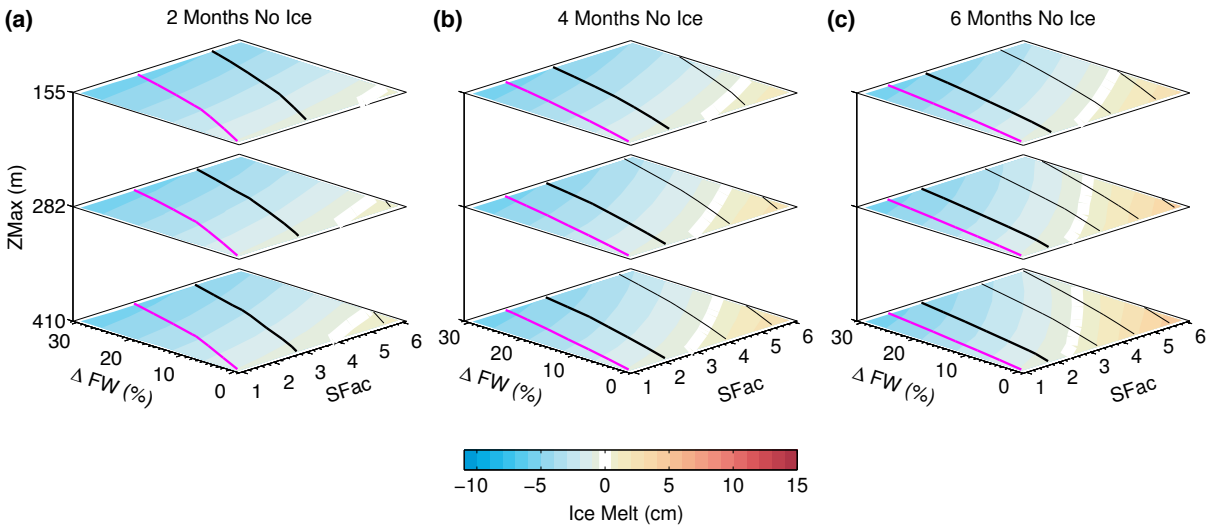

Figure 3.14: Thickness of ice (colour contours) that could be melted/formed due to the change in mixed layer heat content after 40 years of each model run in the Canadian Basin, plotted in the same format as Figure 3.9. Negative ice melt indicates ice formation. Overlain are contours showing the change in the mixed layer temperature from the control run. Solid contours indicate an increase in the mixed layer temperature, and dashed contours indicate a decrease in the mixed layer temperature. The contour interval is 0.03°C, with the zero contour marked in magenta, and the first contour (i.e. ±0.03°C) marked in bold.

by net sea ice formation. The ice melt contours lie perpendicular to the change in mixed layer temperature contours, indicating that freshening of the mixed layer and the corresponding increase in the local freezing point is out-competing the increase in mixed layer temperature. The maximum equivalent net sea ice growth is 6 cm. Sea ice melt is restricted to regions of parameter space with strongly elevated shear and little or no increase in the freshwater input. The maximum equivalent net sea ice melt is only 5 cm (compared to 16 cm in the Eurasian Basin), due to the cooler and shallower mixed layer in the Canadian Basin.

In contrast to the Eurasian Basin, a visual examination of the θ and S profiles suggests that the Canadian Basin halocline remains stable throughout the parameter space, and that the heat contained with the Atlantic layer can never be directly entrained into the mixed layer. On the other hand, as the sPw lies directly beneath the mixed layer, weakening of the stratification over the sPw may allow the heat in this region to be entrained into the mixed layer. However, if the parameterisation discussed in Section 3.4.2 is applied to all Canadian Basin model runs after 40 years, the change in the sea ice thickness due to heat entrainment from the sPw is negligible, and is similar to the results of *Toole et al.* (2010), which concluded that the mixed layer in the Canadian Basin is insensitive to the

heat contained within the sPw.

3.5.3 Relevance for Future Sea Ice Melt

As upper bound estimates, the results show that an elevated diffusive heat flux could increase the mixed layer heat content sufficiently after 40 years to melt an equivalent of 5 cm of sea ice in the Canadian Basin, and 4 cm of sea ice in the Eurasian Basin before the cold halocline has been fully eroded. Once this has taken place, a simple parameterisation of the entrainment heat flux driven by haline convection suggests it could melt half a meter of sea ice in 6 months. How relevant are these processes compared to the other mechanisms responsible for sea ice melt within the Arctic?

The near-surface temperature maximum (NSTM) has recently become a persistent feature of the Canadian Basin water column due to the decline in summer sea ice extent (*Jackson et al.*, 2010, 2011). This decrease has caused the amount of solar radiation absorbed into the upper ocean to increase from 200 MJ m^{-2} yr^{-1} to 400 MJ m^{-2} yr^{-1} between 1979-1992 and 1992-2005 (*Perovich et al.*, 2007), warming the mixed layer. Using a numerical model, *Steele et al.* (2011) showed that the heat content of the NSTM in autumn is sufficient to melt 1 m of sea ice over the following winter, and although some of this heat will be lost directly to the atmosphere, the remainder will reduce sea ice growth. Furthermore, *Steele et al.* (2008) show that between 1965 and 1995, the increase in the upper ocean temperature during summer in the southern Chukchi and western Beaufort Seas (driven by a positive trend in the Arctic Oscillation) was sufficient to reduce winter ice growth by 56-75 cm, and *Pinker et al.* (2014) suggest that over the entire Arctic, the anomalous solar heating of the ocean in 2007 (120 MJ m^{-2} increase over the 1984-2009 mean) could decrease winter ice growth by 44 cm. All these estimates are significantly greater than the effect of the elevated diffusive heat flux in both the Eurasian and Canadian Basins, but are comparable to the effect of the entrainment heat flux driven by sea ice formation.

The results therefore suggest that the erosion of the cold halocline represents the most important process considered here for the ongoing melting of Arctic sea ice, and an elevated diffusive heat flux driven by periodic increases in vertical mixing will play only a

very limited role. It will take at least a decade for the cold halocline to be eroded in the Eurasian Basin (whilst it is never eroded in the Canadian Basin), and in the meantime, elevated vertical mixing will not result in a significant loss of sea ice at the surface.

3.5.4 Choice of Mixing Parameterisation

In this chapter a choice was made to use the parameterisation of *Pacanowski and Philander* (1981) to link the magnitude of the vertical diffusivity to the strength of the shear and the stratification (i.e. Equation 3.2). It must be noted, however, that many different parameterisations for the relationship between the shear and stratification exist (for example *Henyey et al.*, 1986, *Gregg*, 1989, and *Polzin et al.*, 2014), and although the use of a different parameterisation will not fundamentally change the conclusions of this chapter, it may affect the details of the results.

Indeed, irrespective of the details of exactly how the vertical diffusivity is related to the shear, the perturbations made to the shear profile (i.e. *SFac*) will always ensure that the vertical diffusivity is perturbed right through its parameter space from the current background value appropriate for the Arctic of 2×10^{-6} m^2 s^{-1}, to the maximum plausible value of 1×10^{-4} m^2 s^{-1}. Consequently, it is not clear that a different parameterisation will fundamentally result in more or less heat being fluxed into the mixed layer than that seen in Figures 3.6 and 3.7, and therefore a different parameterisation is unlikely to change the conclusion that an elevated diffusive heat flux will play little role in the ongoing melting of Arctic sea ice. On the other hand, if the vertical diffusivity in a different parameterisation is more or less sensitive to changes in shear than in the parameterisation used in this chapter, then the details of the results will be different. If the vertical diffusivity is more sensitive to changes in the shear then the mixed layer may warm faster, as the vertical diffusivity and thus the diffusive heat flux increase at a greater rate, and if the vertical diffusivity is less sensitive to changes in the shear, then the mixed layer will warm more slowly. Similarly, as the rate at which the vertical diffusivity increases also affects the rate at which the stratification strengthens over the Atlantic layer, if the mixed layer temperature increases at a greater rate it is also likely that the maximum mixed layer temperature will be reached earlier. At the same time, it must also be noted that as the

rate at which the cold halocline is eroded may well be shorter or longer if the vertical diffusivity is more or less sensitive to changes in the shear, then the use of a different parameterisation may affect the period of time it takes for the mixed layer to be in direct contact with the Atlantic layer, and for the sea ice cover to be sensitive to surface driven heat entrainment.

3.5.5 Model Limitations

As discussed earlier, there are a number of processes that are not resolved in the 1D model that may also play a role in determining how Arctic sea ice and stratification will respond to the competing effects of elevated vertical mixing and enhanced freshwater input. For example, the effects of ice-ocean interactions (e.g. brine rejection) are likely to act in opposition to any melt/formation of sea ice driven by elevated vertical mixing. As excess heat is brought up to the surface by either a diffusive or entrainment heat flux (once the cold halocline has been fully eroded), sea ice melt will release freshwater, stabilising the water column and limiting the extent to which heat can continue to be brought to the surface. Conversely, sea ice formation will release brine, weakening the stratification and allowing more heat to be brought to the surface.

In addition, as the magnitude of $R^{\theta}(z)$ and $R^{S}(z)$ are fixed at that required to balance the effect of mixing in the control run, it has not been possible to consider the effect that any interplay between elevated vertical mixing and seasonal and long term changes in the processes that set the stratification of the Arctic Ocean may have on the flux of heat to the underside of the sea ice. In the real Arctic, however, the processes that set the stratification will undoubtedly change on the timescales considered, and despite the current knowledge of these changes being poorly constrained, they may have important implications for the results. For example, on seasonal timescales, a negative surface heat flux and brine rejection from sea ice formation at the end of summer will act to deepen the ML, entraining water from the pycnocline and thinning the cold halocline. Whilst this process may not deepen the ML sufficiently such that it entrains water that is above the freezing point (unlike when the cold halocline is absent), a seasonal thinning of the cold halocline and the weaker salinity stratification may allow the enhanced vertical mixing to

flux more heat into the ML. On longer timescales, *Davis et al.* (2014) suggest that over the coming decades, the possible change in momentum input at the ocean surface, linked with the change in sea ice conditions, might affect the rate of freshwater accumulation in the Beaufort Gyre and drive a long term positive trend in the stability of the water column. At the same time, *Lique et al.* (2015) show that strengthening of the Beaufort Gyre can strongly affect the circulation of the Atlantic water boundary current, and limit the penetration of heat into the Canadian Basin. These and other seasonal (e.g. the absorption of solar radiation during the ice free summer) and long term Arctic changes (e.g. variability in the mechanisms that form the cold halocline) will likely have significant impacts on the stratification throughout the water column and the temperature of the AWL, but an investigation of these impacts is deferred to future studies.

3.6 Conclusions

The aim of this chapter was to investigate how the competing effects of elevated vertical mixing and enhanced freshwater input at the surface may affect the stratification, the stability of the cold halocline, and the sea ice cover at the surface over the coming decades. Using a 1D model in which the diffusivity is assumed to be a function of the shear instability associated with internal wave breaking, the strength of the velocity shear, the depth to which this elevated shear penetrates, the length of the ice-free season, and the freshwater input at the surface were perturbed through a wide parameter space that is applicable for a future Arctic.

In the Eurasian Basin, elevated shear drives an initial increase in mixed layer temperature, due to an enhanced diffusive heat flux at the base of the mixed layer. The magnitude of the diffusive heat flux depends predominantly on the depth to which the elevated shear penetrates, as deeper mixing is able to interact with the strong Atlantic layer temperature gradient. After about a decade, however, the effect of changing stratification begins to dominate and the mixed layer cools, as a decrease in the diffusivity over the Atlantic layer reduces the supply of heat to the surface. After 40 years, the maximum increase in the mixed layer heat content driven by the elevated diffusive heat flux is equivalent to $\approx$15 cm of sea ice melt. In other regions of parameter space, the elevated freshwater

input, stronger stratification, and weaker vertical heat flux results in an equivalent net formation of ≈10 cm of sea ice.

The stability of the cold halocline in the Eurasian Basin is strongly affected by the elevated shear, and when it penetrates into the Atlantic layer, the cold halocline can be fully eroded within 10 years. Once the cold halocline has been fully eroded, the heat contained within the Atlantic layer can be directly entrained into the mixed layer, and a simple parameterisation suggests that a buoyancy-driven heat entrainment feedback could result in the loss of half a meter of sea ice over 6 months.

In the Canadian Basin, the much stronger stratification out-competes the elevated velocity shear, and the increase in the diffusivity is small. There is little increase in the diffusive heat flux from the Atlantic layer, and despite the heat contained within the shallower sPw, the parameter space is dominated by sea ice formation due to freshwater input at the surface (the maximum equivalent sea ice melt is only 5 cm). Due to the limited change in diffusivity, the halocline is never eroded in the Canadian Basin.

Comparing the results to other major processes responsible for sea ice melt in the Arctic suggests that the quantity of ice that can be melted by the elevated diffusive heat flux in both the Eurasian and Canadian Basins is insignificant, and instead it is the erosion of the cold halocline that represents the largest risk for ongoing melting of Arctic sea ice. Therefore, until, or indeed unless, the cold halocline is eroded, the results suggest that the sea ice cover in the Arctic will remain largely immune to the heat contained within the Atlantic layer, and the role of the ocean will be limited to the part it plays in the ice-albedo feedback effect and the bottom melting of sea ice through the absorption of solar radiation.

Chapter 4

Tides and Tidal Propagation in Nares Strait

The work in the previous two chapters has focused on understanding how the changing Arctic environment (namely sea ice retreat, increased momentum input into the upper ocean, elevated vertical mixing, and enhanced freshwater input) may affect the circulation and freshwater content of the Beaufort Gyre (Chapter 2) and the sea ice cover at the surface (Chapter 3). Whilst these changing dynamics will have significant local impacts by, for example, changing the baroclinicity of the Arctic atmosphere or affecting the ecology of Arctic phytoplankton, they will also have global impacts, partly by changing the magnitude of the export of ice and liquid freshwater through Fram Strait and the Canadian Arctic Archipelago (CAA). However, the local dynamics in both Fram Strait and the CAA will also be critical in determining the exact magnitude of any change in the export of ice and liquid freshwater from the Arctic Ocean. It is therefore critically important to understand and quantify what dynamical processes are responsible for limiting the flow through these regions. In Nares Strait, which accounts for between 30-50% of the present-day freshwater flux through the CAA (e.g. *Beszczynska-Möller et al.*, 2011), the kinetic energy associated with the tides is an order of magnitude greater than that associated with the subtidal flow (consequently the strait is dominated by tidal dynamics), and tidally-generated turbulence may represent an important frictional constraint on the flow. In this chapter, an introduction to the importance of tides and tidal propagation in Nares Strait

is presented, whilst in Chapter 5 the dynamical mechanisms which determine the depth and temporal variability of the tides are investigated in more detail, providing the first step towards developing a fuller understanding of the role that they may play in limiting the flow through the strait.

4.1 Introduction

4.1.1 The Canadian Arctic Archipelago

The Canadian Arctic Archipelago lies on the Canadian Polar Shelf, and covers an area of 2.5 million km^2 (Figure 4.1; *Melling*, 2000). It is made up of 94 major islands split by a myriad of straits and channels through which fresh surface waters and salty intermediate waters flow from the Arctic to the Atlantic via Baffin Bay. As seen in Chapter 1, the current annual flux of freshwater through the CAA in liquid and ice forms as measured at Davis Strait are 2900 $\pm$ 190 km^3 yr^{-1} and 331 $\pm$ 45 km^3 yr^{-1}, respectively. The entirety of this freshwater flux must pass through one of seven channels within the CAA (Figure 4.1), the details of which are given in Table 4.1. It is clear that in comparison to the cross-sectional area of Kennedy Channel and Barrow Strait, Bellot Strait is insignificant, and the flux through this region can be ignored (*Melling*, 2000). In addition, Fury and Hecla straits are often blocked with ice year-round, which significantly reduces the flux of freshwater due to friction. Consequently, nearly all the freshwater that is exported from the Arctic through the CAA must pass through either Barrow Strait, Cardigan Strait and Hell Gate, Wellington Channel, or Nares Strait (Figure 4.1). Whilst the the entire CAA acts as one large sill restricting the flow between the deep Arctic basins and Baffin Bay (depths >1000 m), it is the much shallower sills in Barrow Strait (125 m), Cardigan Strait (180 m), Wellington Channel (80 m), and Nares Strait (220 m), that represent the most important topographic constraints (*Prinsenberg and Hamilton*, 2005; *Münchow et al.*, 2007).

Although the observations at Davis Strait integrate the entire freshwater flux that passes through the CAA (e.g. *Curry et al.*, 2014), the mechanisms behind any variability or trend in the freshwater flux through this section are masked, as they cannot be

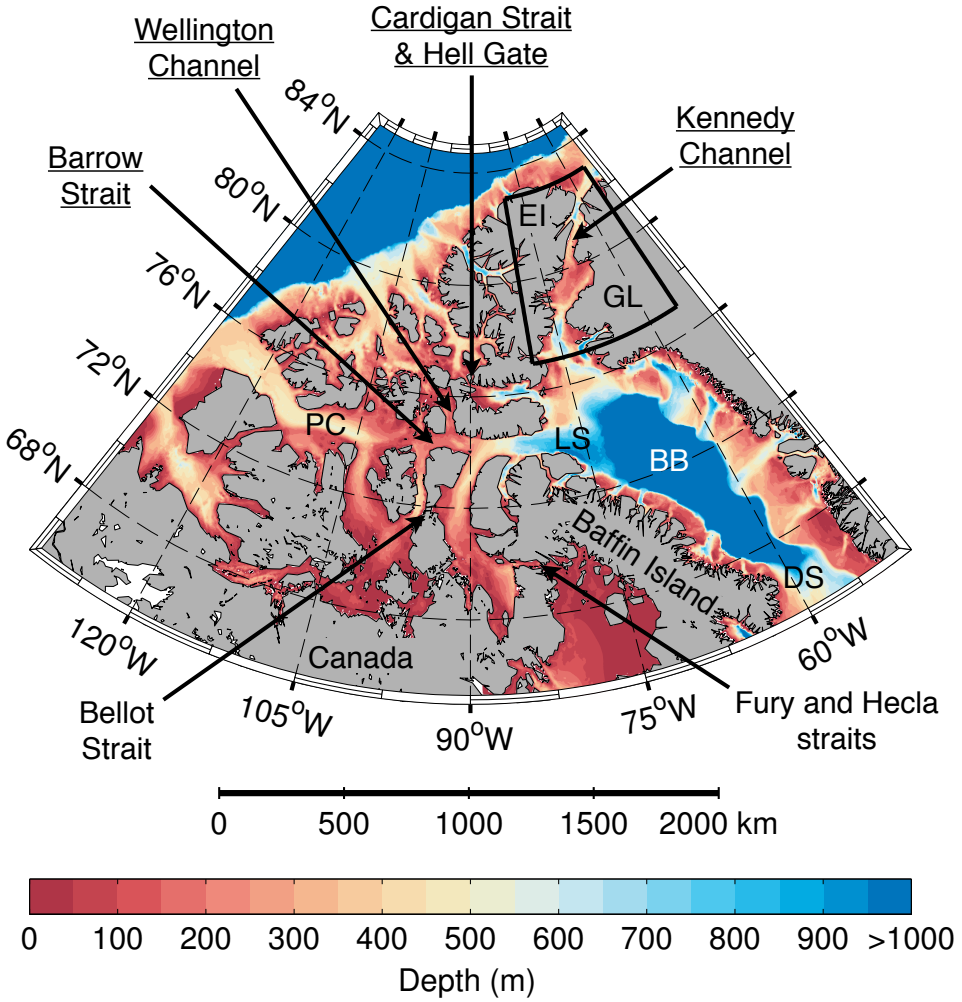

Figure 4.1: Bathymetry of the Canadian Arctic Archipelago from the International Bathymetric Chart of the Arctic Ocean. EI stands for Ellesmere Island, GL for Greenland, LS for Lancaster Sound, PC for Parry Channel, BB for Baffin Bay, and DS for Davis Strait. The seven passageways through which the entire freshwater flux through the CAA must pass are marked with black arrows, with the five most important underlined. The black box highlights the location of Nares Strait.

associated with a change in any specific channel, and could simply be related to variability in the complex circulation and counter-flows that exist within Baffin Bay itself. Currently, the total freshwater flux to either side of Greenland (i.e. both liquid and ice forms) is dominated by that through Fram Strait ($\approx$4800 $\pm$ 580 km^3 yr^{-1} compared to $\approx$3200 $\pm$ 200 km^3 yr^{-1} through the CAA; from Section 1.3.1). However, as the total freshwater export from the Arctic Ocean increases over the twenty-first century (see Section 1.4.2; *Vavrus et al.*, 2012; *Haine et al.*, 2015), the increase in the freshwater flux through the CAA is expected to be much greater than that through the Fram Strait (perhaps +48% compared to +3%; *Münchow et al.*, 2007), as the significant decrease in the ice flux through Fram Strait offsets to a large degree the increase in the Fram Strait liquid

Channel	Area (m^2)	Area Fraction	Width (km)	Width Fraction	Mean Depth (m)	Sill Depth (m)
Kennedy Channel	10,960,000	38.3%	38.2	24.6%	287	220
Hell Gate & Cardigan Strait	1,420,000	5.0%	12.4	8.1%	115	125, 180
Wellington Channel	4,550,000	15.9%	28.3	18.2%	160	80
Barrow Strait	7,930,000	27.6%	52.3	33.7%	152	125
Fury and Hecla straits	3,740,000	13.1%	22.0	14.2%	170	65
Bellot Strait	31,600	0.1%	1.9	1.2%	17	24
Sum of Sections	28,631,600	100%	155.1	100%	150	

Table 4.1: Area, Area Fraction, Width, Width Fraction, Mean Depth, and Sill Depth of the seven major constrictions within the CAA through which the entire flux of water from the Arctic to the Atlantic must pass. Details from *Godin and Candela* (1987), *Melling* (2004) and *Straneo and Saucier* (2008).

flux (*Koenigk et al.*, 2007; *Vavrus et al.*, 2012). Consequently, it is important to quantify the present-day magnitude of the freshwater flux through each of the major straits of the CAA, and to determine the dynamics behind what drives and what limits the flow through each of these regions.

Measuring the freshwater flux through the straits of the CAA is, however, technically very challenging. The presence of a thick, year-round sea ice cover makes access by ship very difficult, and the logistics are further hampered by the remote location and harsh climate. The proximity of the CAA to the magnetic north pole limits the use of the geomagnetic field in providing a reference for the flow direction (*Melling*, 2000), and the fast tidal currents along with the drifting sea ice and icebergs present significant "snagging" hazards to instruments deployed on moorings within the water column. Indeed, data from moorings deployed in Nares Strait between 2003 and 2006 suggests that some instruments

were forced down from their deployment depth of 30 m to 200 m by a passing iceberg (*Melling*, 2006). In addition, many of the channels within the CAA can be considered "dynamically wide". The internal Rossby deformation radius for the surface freshwater layer:

$$L_D = \frac{(g' D_0)^{1/2}}{f}, \tag{4.1}$$

where

$$g' = g\left(\frac{\Delta\rho}{\rho_0}\right) \tag{4.2}$$

is the reduced gravity, g is acceleration due to gravity, $\Delta\rho$ is a representative density difference, ρ_0 is the average density, D_0 is the vertical scale of motion, and f is the Coriolis parameter, determines the width of a baroclinic flow in geostrophic balance (*Gill*, 1982). In the CAA, the deformation radius is ≈10-15 km, and thus is significantly smaller than the width of many of the major straits (Table 4.1; *Münchow et al.*, 2006). Consequently, there can be significant variability in the baroclinic structure across each strait, such that the flow can be in opposite directions on either side (*Melling et al.*, 2008). As a result, in order to fully quantify the flow of freshwater through each of the major straits, the spatial resolution of both Conductivity, Temperature and Depth sections, and mooring arrays deployed across the straits must be less than the deformation radius.

Despite these difficulties, recent observational programs that include Arctic/Subarctic Ocean Fluxes (ASOF) and the Canadian Arctic Through-Flow Study have aimed to accurately measure the flux of freshwater through the major straits within the CAA. Since 1998, a 65 km wide mooring array has been deployed in Lancaster Sound which integrates the total freshwater flux that passes through Barrow Strait and Wellington Channel (LS in Figure 4.1; *Melling et al.*, 2008). The majority of the instruments on the array do not extend shallower than 30 m due to the risk of iceberg/ice keel snagging, and therefore the mooring array does not measure the region of the water column through which most of the freshwater flows. Indeed, the deployment of one ICYCLER instrument between 2003-2004, which used a buoyant profiler to periodically measure the temperature and salinity structure above 30 m, showed that during June to October, the freshwater inventory calculated using data from this region is 20% larger than that inferred from extrapolation

of the data at 30 m alone (*Melling et al.*, 2008). In addition, the spatial resolution of the mooring array is less than the internal Rossby deformation radius, and therefore a proportion of the across-strait variability is not measured. Nevertheless, *Prinsenberg and Hamilton* (2005) and *Prinsenberg et al.* (2009) estimate the mean volume flux between 1998-2006 to be 0.7 ± 0.3 Sv, with a corresponding freshwater flux of 48 ± 15 mSv (1 Sv = 10^3 mSv = 10^6 m^3 s^{-1}) or 1500 km^3 yr^{-1}, which represents approximately half of the total freshwater flux through the CAA. The annual cycle in the volume flux is at a maximum in June with a magnitude of 1.15 Sv, and at a minimum in December with a magnitude of 0.25 Sv. There is similar annual cycle in the freshwater flux, and this annual variability is most likely associated with the presence of landfast ice in winter (discussed later; *Melling et al.*, 2008; *Prinsenberg et al.*, 2009). The freshwater flux through Lancaster Sound is highly correlated with the volume flux (r^2 >0.96; *Prinsenberg et al.*, 2009; *McGeehan and Maslowski*, 2012; *Jahn et al.*, 2012), which on longer timescales is correlated with the wind conditions upstream in the Beaufort Sea, which modulate the sea level difference between the Arctic Ocean and Baffin Bay (*Melling et al.*, 2008; *Peterson et al.*, 2012).

Unlike Lancaster Sound, Hell Gate and Cardigan Strait are particularly narrow (4 km and 8 km, respectively), and therefore the deformation radius can be resolved with only a small number of instruments (*Melling et al.*, 2008). However, observations taken between 1998 and 2004 show that the strong currents in these narrow straits may change by up to 50% within 2.4 km (e.g. the current speed was ≈30 cm s^{-1} at the western edge of Cardigan Strait compared to ≈15 cm s^{-1} in the centre), and that the volume flux estimates based on this data of 0.2 Sv and 0.1 Sv through Cardigan Strait and Hell Gate, respectively, are biased by an unknown amount due to aliasing of the across-strait variability (*Melling et al.*, 2008). In addition, the significant drag associated with the strong currents means that it is not possible to use salinity recorders held at fixed depths on taut line moorings to determine the salinity field in these regions; to date, the freshwater flux through these straits remains unobserved (although it is likely to be significantly smaller than that through Lancaster Sound due to the smaller volume transport).

In contrast to Lancaster Sound, long-term observations in Nares Strait, which forms

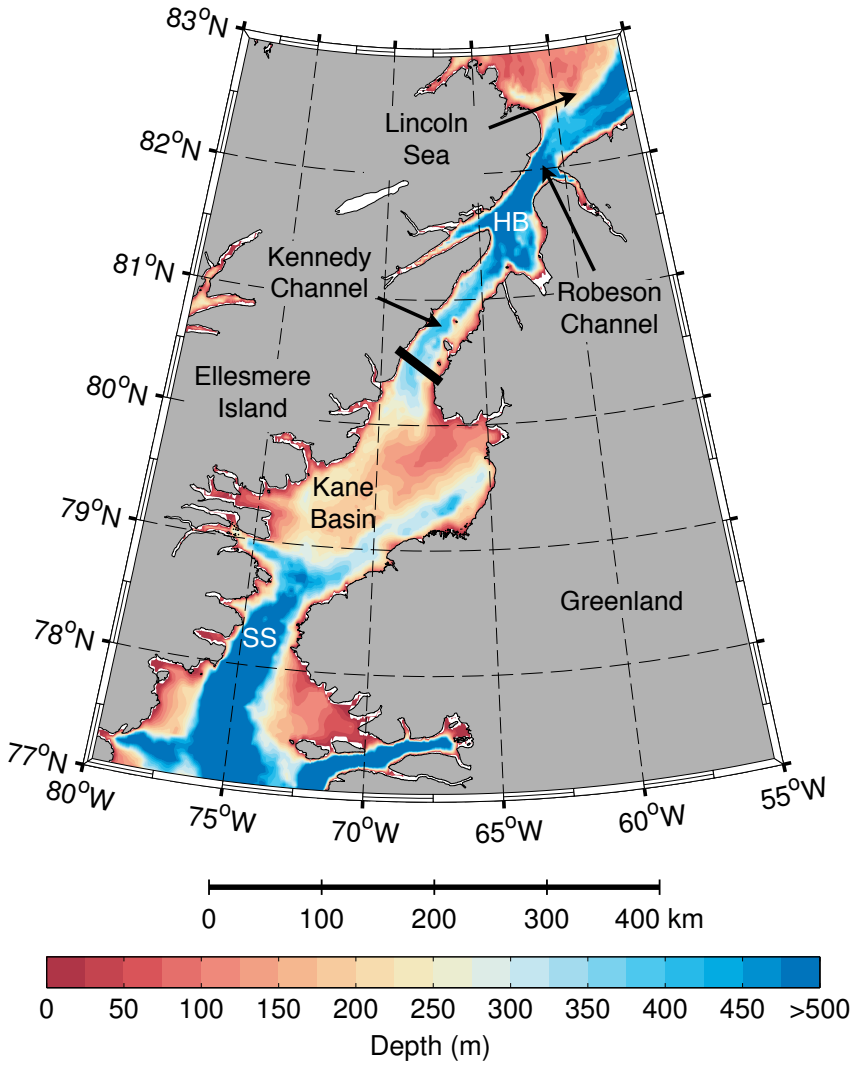

Figure 4.2: Bathymetry of Nares Strait from the International Bathymetric Chart of the Arctic Ocean. SS stands for Smith Sound, and HB for Hall Basin. The location of the mooring array deployed across Kennedy Channel between 2003 and 2006 is marked with a black line.

the focus of this present chapter and Chapter 5, have been harder to obtain and have not existed until more recently.

4.1.2 Nares Strait

Nares Strait, through which flows the remaining 30-50% of the total CAA freshwater flux (*Beszczynska-Möller et al.*, 2011), is located on the eastern boundary of the archipelago separating Ellesmere Island from Greenland (Figure 4.2). It stretches 530 km from Baffin Bay in the south to the Lincoln Sea in the north, and has a varying width from 21 km in Robeson Channel to 150 km in Kane Basin. Water depth varies considerably along the channel axis, decreasing from 600 m in Smith Sound to the 220 m sill

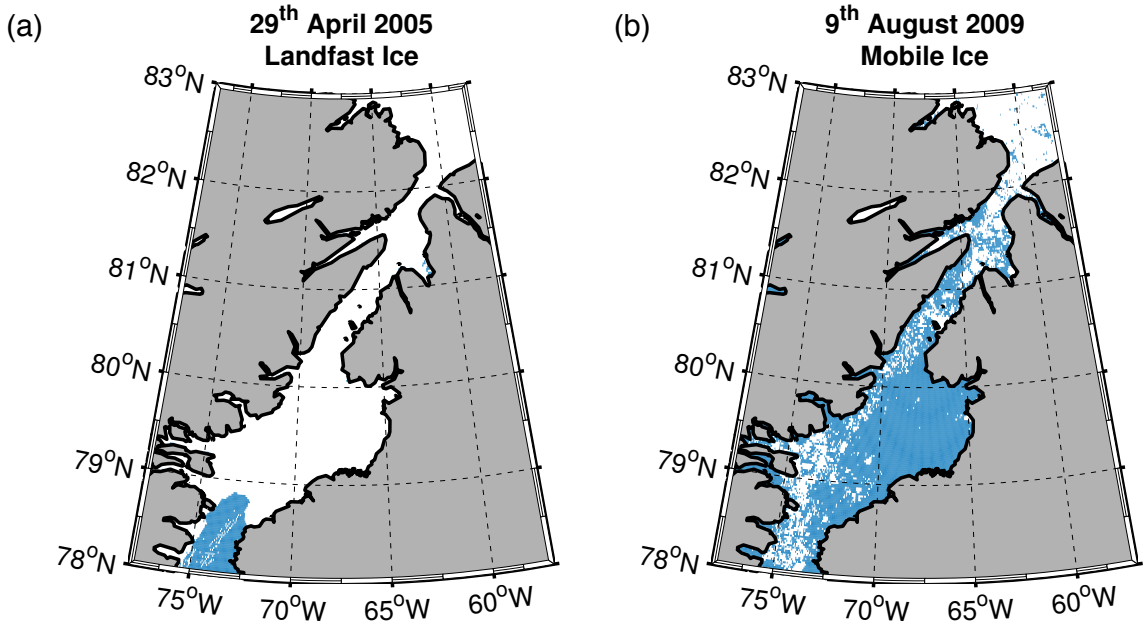

Figure 4.3: MODIS satellite images showing ice (white) conditions in Nares Strait during (a) landfast ice conditions and (b) mobile ice conditions after the ice bridge has collapsed to the north in the Lincoln Sea. The images are based on the surface reflectance data in the 654 nm band, with an ocean-ice threshold of 0.15 and 0.05 during landfast and mobile ice conditions, respectively (note that reflectance is affected by snow on ice and land, gasses, aerosols and thin cirrus clouds throughout the atmosphere, leading to the requirement of different ocean-ice thresholds for each image).

depth in western Kane Basin, before increasing again to 800 m in Hall Basin. North of Hall Basin, the depth decreases considerably to a maximum of 350-400 m in Robeson Channel, and decreases again to between 200-300 m in the Lincoln Sea (*Münchow and Melling*, 2008). The salinity field across the strait is characterised by the existence of cold and fresh surface waters of Pacific origin against the coast of Ellesmere Island, with warm and salty waters of Atlantic origin (up to 0°C and 34.5 psu) found at depth (below 100 m) and against the coast of Greenland (*Münchow et al.*, 2007; *Rabe et al.*, 2010).

The ice conditions in Nares Strait are generally characterised by stable first-year and multiyear landfast ice in winter, and rapidly drifting mobile multiyear ice in summer (Figure 4.3). The transition from mobile ice to landfast ice occurs between November and March, when an ice bridge that is strong enough to resist the forces of wind and tide forms in Smith Sound (*Melling*, 2000; *Samelson et al.*, 2006; *Dumont et al.*, 2009). The ice bridge generally collapses in late June/July, and the prevailing winds flush the ice south into Baffin Bay, creating much lighter ice conditions in the strait. However, by mid-August, the ice bridge that forms to the north across the Lincoln Sea breaks, allowing

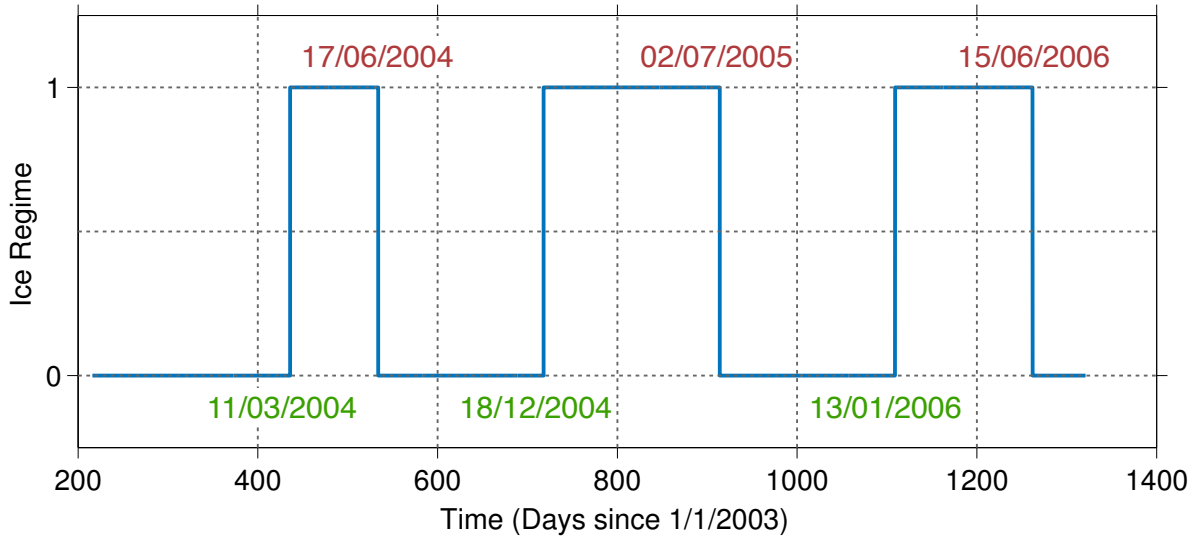

Figure 4.4: Time series of the ice regime in Nares Strait between 2003 and 2006. An ice regime of 0 indicates mobile ice, whilst an ice regime of 1 indicates landfast ice. Dates in green mark the transition from mobile ice to landfast ice, whilst dates in red mark the transition from landfast ice to mobile ice.

thick multiyear ice from the central Arctic to invade the strait (*Münchow et al.*, 2006, 2007). During the landfast ice regime, the motionless sea ice cover at the surface creates a second under-ice no-slip boundary layer, whilst during the mobile ice regime the upper boundary condition can either be open water, pack ice in free drift, or pack ice retarded by ice stress. Consequently, the transition between the different ice regimes can have a significant effect on the dynamics of the flow within Nares Strait. Figure 4.4 shows a time series of the different ice regimes in Nares Strait between 2003 and 2006 (i.e. the period of time over which the data analysed in Chapters 4 and 5 were collected; discussed in more detail later), along with the dates of the transitions between mobile and landfast ice. The transitions between the mobile and landfast ice regimes are determined by analysing the background noise levels detected by Acoustic Doppler Current Profilers moored on the seabed (the background noise during mobile ice regimes is orders of magnitude greater than that during landfast ice regimes).

On a day-to-day basis, the flow through Nares Strait is dominated by the motion associated with the diurnal and semi-diurnal tides (*Münchow et al.*, 2006; *Münchow and Melling*, 2008). However, at subtidal frequencies, a freshwater flux through the strait is facilitated by the existence of a persistently southward subtidal flow. Through the interpretation of a six week velocity time series from three current meters deployed in

Nares Strait in 1972, *Sadler* (1976) made the first estimation of the volume flux associated with this subtidal flow to be 0.7 Sv. However, despite this estimation being often cited, used as a boundary condition in numerical models, and employed to constrain pan-Arctic freshwater budgets (e.g. *Serreze et al.*, 2006), more than 50% of the reported volume flux is attributed to a single instrument deployed at a depth of 100 m, 5 km off the coast of Ellesmere Island (*Münchow and Melling*, 2008). Similarly, *Melling et al.* (2001) deployed current meters in Smith Sound for 10 months between 1997 and 1998 during the North Water project, but concluded that data from just two moorings across the 40 km wide section were insufficient to estimate the volume flux, as they do not resolve the deformation radius. In 2003, quasi-synoptic ship-based surveys of ocean current and salinity that resolved the deformation radius were carried out at four locations in Nares Strait during the deployment of a long-term monitoring array in Kennedy Channel (black line in Figure 4.2); from this data, *Münchow et al.* (2007) estimated a mean southward volume and freshwater flux of 0.91 ± 0.10 Sv and 31 ± 4 mSv (977 ± 127 km^3 yr^{-1}), respectively (see also *Münchow et al.*, 2006). More recently, using the velocity data collected between 2003 and 2006 at the 38 km wide long-term monitoring array, *Münchow and Melling* (2008) estimated the mean southward volume flux below 30 m to be 0.57 ± 0.09 Sv, whilst *Rabe et al.* (2011) used the long-term temperature and salinity data recorded at the same location to estimate a mean southward geostrophic volume and freshwater transport between 30-200 m of 0.47 ± 0.05 Sv and 20 ± 3 mSv, respectively. The geostrophic freshwater flux increases to no less than 28 mSv (880 km^3 yr^{-1}) if the data at 30 m is extrapolated to the surface.

In the three-year mean, the southward freshwater flux is primarily contained within a buoyant boundary jet hugging the coast of Ellesmere Island (0.20 m s^{-1}) and a secondary jet in the centre of the strait (0.14 m s^{-1}; *Rabe et al.*, 2010). However, there is significant variability in the structure of the flow between the different ice regimes, with the jet in the centre of the strait dominating during mobile ice periods and the jet against the coast of Ellesmere Island dominating during landfast ice periods (although between 2003 and 2006 a second core against the coast of Ellesmere Island developed during mobile ice periods; *Münchow et al.*, 2007; *Rabe et al.*, 2012). On average, the flux of freshwater through the

strait is 20% larger during the mobile ice regime than during the landfast ice regime, with a maximum difference of up to 40% (*Rabe et al.*, 2012).

The freshwater flux through the strait is highly correlated with the volume flux (*Rabe et al.*, 2012), which in turn is driven by a combination of the along-strait pressure difference, the across-strait density gradient, and, during mobile ice seasons, the local along-strait wind (*Münchow et al.*, 2006; *Münchow and Melling*, 2008; *McGeehan and Maslowski*, 2012). By examining the coherence between the freshwater flux and the along-strait pressure difference between 2003 and 2006, *Rabe et al.* (2012) found that during mobile ice regimes, variability in the pressure difference accounted for 35% of the total variance in the freshwater flux, whilst local winds (i.e. the part not correlated with the along-strait pressure difference), accounted for 45% of the total variance at weekly timescales. An examination of the phase difference between the freshwater flux and the winds suggests that variability in the local winds lead the freshwater flux by one day, with a 10 m s^{-1} southward wind generating a freshwater flux of 10 mSv (most likely associated with Ekman transport towards Ellesmere Island titling the isopycnal surfaces downwards and enhancing the freshwater jet). Variability in the along-strait pressure difference leads the freshwater flux by roughly a quarter of a day. In contrast, during landfast ice regimes, the coherence between the local winds and the freshwater flux was below the 95% confidence interval at all frequencies (i.e. the flow is uncoupled from atmospheric forcing by the rigid sea ice cover at the surface), and variability in the along-strait pressure difference dominates the variability in the freshwater flux (explaining around 40% of the variance at weekly timescales).

4.1.3 Aims and Long-term Goals

In order to understand to what extent the freshwater flux through Nares Strait might increase in the future, it is important to move beyond the dynamics responsible for driving the flow, and to consider the nature of the frictional processes that are responsible for limiting the flow of freshwater through the region. Here, and in Chapter 5, the focus is on the strong tidal currents, which are the dominant dynamic in Nares Strait.

The tides could have a number of important implications for the flow through Nares

Strait, and therefore the development of a full understanding of the tidal dynamics in this region is an important long-term goal. For example, if the magnitude of the turbulence generated by a flow is proportional to the flow speed, then the majority of the turbulence generated in Nares Strait will be associated with the tidal flow. However, the effect of the friction and the removal of energy that is associated with the generation of this turbulence will not be confined to act just upon the tidal flow, and thus by constraining the magnitude of the tidally-generated turbulence in Nares Strait, an understanding of how it may act to limit the flux of freshwater from the Arctic Ocean into Baffin Bay, and constrain the extent to which the flux might increase in the future, can be developed. In a similar vein, previous studies (for example *Campbell et al.*, 1998) have shown that the changing water depth over a tidal cycle and frictional effects at the sea bed can lead to a highly distorted along-channel flow, such that there can be a net transport of water through a strait over each tidal cycle. Developing a full understanding of whether and to what extent this occurs in Nares Strait will allow a quantification of how significant the tides are in generating a net flux of freshwater through the Strait. Beyond frictional effects, modelling work in the Indonesian Throughflow (for example *Koch-Larrouy et al.*, 2007 and *Sprintall et al.*, 2014) has also shown that the strong tidal currents and tidal mixing in this region play a key role in water mass transformations. Such processes may also be important in Nares Strait (which is an key pathway for the flow of Pacific and Atlantic derived waters out of the Arctic), and therefore it is important to develop an understanding of the magnitude of tidal mixing in Nares Strait and to combine this with numerical simulations to quantify the extent to which the tides may effect water mass transformations, stratification, and the flow through the region at present and into the future.

Consequently, to start building a full understanding of the tidal dynamics in the region, the overall aim of this chapter is to provide an introduction to the tides in Nares Strait, with a more detailed examination of the dynamics behind the temporal and vertical structure of the tides left to Chapter 5. Section 4.2 introduces the theory behind the tides in both the global ocean and Nares Strait, and discusses the existing knowledge of their structure in Nares Strait from the depth- and time-averaged analysis of *Münchow*

and Melling (2008). In Section 4.3 the datasets and data analysis methods used in both this chapter and in Chapter 5 are described, whilst in section 4.4, the propagation of the tidal wave associated with each of the major tidal constituents through Nares Strait is explored. The brief conclusions from the work in this chapter will be presented later at the end Chapter 5.

4.2 Tides in Nares Strait

Tides in the ocean arise due to the gravitational interaction between the Earth and the Moon and the Earth and the Sun. As they rotate around their common centres of gravity, a centrifugal force is generated that maintains the bodies within their orbits, and prevents each from flying off in a straight line or collapsing together. This centrifugal force is equal at all points over the Earth's surface, and is directed parallel to a line joining the centre of the Earth with the centre of the Moon or the centre of the Sun (blue arrows in Figure 4.5).

Conversely, although the total gravitational force between the Earth and the Moon and the Earth and the Sun must equal the total centrifugal force, the gravitational force varies over the Earth's surface as a function of distance from the Moon or the Sun. Consequently, points on the Earth's surface nearer the Moon or the Sun will experience a greater gravitational attraction than points on the Earth's surface further from the Moon or the Sun. The gravitational force acts in the direction of the centre of the Moon or the Sun, and is shown by the red arrows in Figure 4.5 (*Segar*, 2012).

The residual force that arises between the constant centrifugal force and the gravitational force at each point over the Earth's surface is known as the tide-generating force, and it can be directed parallel to, into, or away from the Earth's surface (green arrows in Figure 4.5). At the closest and furthest points to the Moon and the Sun on the Earth's surface, the tide-generating force is purely vertical, and consequently has little effect on the ocean due to the much stronger and opposing force of the Earth's gravity (which is approximately 9×10^6 times greater). At all other points on the Earth's surface, however, the direction between that point and the Moon or the Sun, and the direction between that point and the Earth's centre of mass form an angle with each other, and thus the

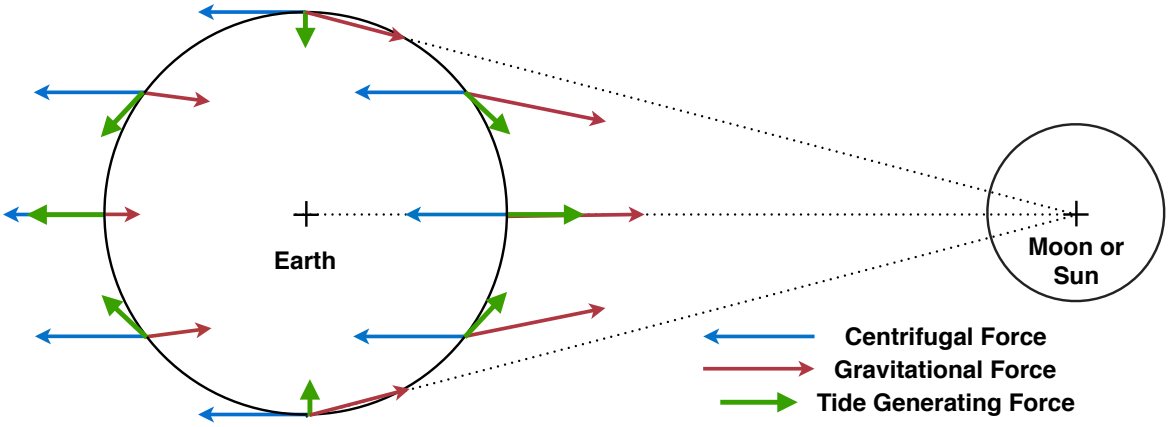

Figure 4.5: Schematic of the Earth-Moon or Earth-Sun system showing how the centrifugal force (blue arrows), the gravitational force (red arrows), and the tide-generating force (green arrows) vary over the Earth's surface. The centrifugal force is directed parallel to a line joining the centre of the Earth with the centre of the Moon or Sun, and is equal at all points over the Earth's Surface. The gravitational force acts in the direction of the centre of the Moon or Sun, and is greater for points closer to either of them. The tide-generating force is the residual force that arises between the constant centrifugal force and the gravitational force at each point over the Earth's surface. It has no effect at the points closest to and furthest from the Moon or Sun (due to the much stronger effect of the Earth's gravity), however, at all other points it has a component that is aligned parallel to the Earth's surface, and water accelerates in the direction of this force.

tide-generating force has a component that acts parallel to the Earth's surface (i.e. a tractive force). This component cannot be compensated by the Earth's gravity, and thus water accelerates in the direction of the force (*Segar*, 2012). As the magnitude of the tide-generating force is proportional to the mass of the attracting body (i.e. the Sun or the Moon), but inversely proportional to the cube of the distance between the Earth and the attracting body, the strength of the tide-generating force associated with the Sun is only 46% of that associated with the Moon.

As the Earth-Moon and Earth-Sun systems rotate, the response to the tide-generating force at each point over the Earth's surface takes the shape of a sinusoid, resulting in the ubiquitous rising and falling of sea levels and the waxing and waning of tidal currents that are observed throughout the world's oceans. If both the Earth-Moon and Earth-Sun system were perfectly aligned and all orbited in the same plane (as in the simple setup discussed above), the tidal response would reflect the interaction of only two "tidal constituents": the rotation of the Earth relative to the Moon (the M2 tidal constituent with a period of 12.42 hours) and the rotation of the Earth relative to the Sun (the S2 tidal constituent with a period of 12 hours). In reality, however, due to the complex orbits

of the Earth, the Moon and the Sun (their orbits are not circular and they do not orbit in the same plane), there are hundreds of different tidal constituents, each with a distinct period, and the response at the Earth's surface to the tide-generating force represents the integrated effect of each of these tidal constituents. Fortunately, many are weak enough to have no noticeable effect, and the ocean's response is often dominated by a combination of the major constituents listed in table 4.2.

Over the Arctic Ocean, the tide-generating force is generally weak as there is no component that acts parallel to the Earth's surface (Figure 4.5; *Kowalik and Proshutinsky*, 1994; *Segar*, 2012). Figure 4.6 shows the amplitude of the M2 and S2 tides in terms of sea level variation from Version 8 of the Oregon State University TOPEX/Poseidon Global Inverse Solution (TPXO8) barotropic tidal model (*Egbert and Erofeeva*, 2002) for (a,c), the Arctic Ocean and (b,d), the global ocean. TPXO8 is a global barotropic inverse tidal model which best fits the Laplace Tidal Equations to along track-averaged satellite altimeter data (i.e. TOPEX/Poseidon and more recently the Jason satellites), as well as coastal and benthic tide gauges. The model has a $1/6^o$ resolution in the open ocean, increasing to $1/30^o$ in the Arctic. Tidal energy is dissipated at the seabed through a quadratic drag law, and the significant loss of energy to the baroclinic tide over regions of steep topography is not accounted for (*Egbert and Erofeeva*, 2002). The bathymetry data used in the model is a blend of the global Smith and Sandwell (*Smith and Sandwell*, 1997), ETOPO (*Amante and Eakins*, 2009) and General Bathymetric Chart of the Oceans databases (*Becker et al.*, 2009), along with the regional International Bathymetric Chart of the Arctic Ocean (*Jakobsson et al.*, 2008, 2012).

In the deep central basins of the Arctic Ocean, Figure 4.6a shows that the amplitude of the M2 tide rarely exceeds 0.15 m: noticeably smaller than the open ocean range observed at lower latitudes (note that amplitude refers to the difference between the mean sea level and the maximum sea level; the total tidal range is twice the amplitude). In contrast, the amplitude in Nares Strait is significantly greater, reaching a maximum of ≈1.2-1.3 m which is comparable with the amplitude observed over the low latitude continental shelves (e.g. the northwest European Shelf). It is interesting to note that the amplification of the tide in Nares Strait is also reflected in the S2 tidal constituent (the amplitude is ≈0.4-0.5

Tidal Constituent	Name	Period (hrs)	Magnitude Ratio	Record Length (hrs)
Semi-Diurnal				
M2	Principal lunar semi-diurnal	12.42	1	13
S2	Principal solar semi-diurnal	12.00	0.465	355
N2	Larger lunar elliptic semi-diurnal	12.66	0.192	662
K2	Lunisolar semi-diurnal	11.97	0.029	4383
Diurnal				
K1	Lunar diurnal	23.93	0.584	24
O1	Lunar diurnal	25.82	0.415	328
P1	Solar diurnal	24.06	0.193	4383
Q1	Larger lunar elliptic diurnal	24.06	0.079	662
Higher Harmonics				
M4	Principal lunar overtide	6.21	-	25
M6	Principal lunar overtide	4.14	-	26
S4	Principal solar overtide	6.00	-	355
MN4	Quarter diurnal	6.27	-	662

Table 4.2: Details of the major tidal constituents, along with their respective periods, magnitude ratios compared to the strength of the tide-generating force associated with the M2 tide, and record lengths required to resolve each constituent (*Emery and Thomson*, 2004). The higher harmonics result from the non-linear combinations of the diurnal and semi-diurnal tides.

m in Nares Strait compared to maximum of ≈0.05 m over the deep central Arctic basins), but not in the K1 tidal constituent, the reasons for which will be discussed in Section 4.4.

Existing research into the strength and structure of the tides in Nares Strait by

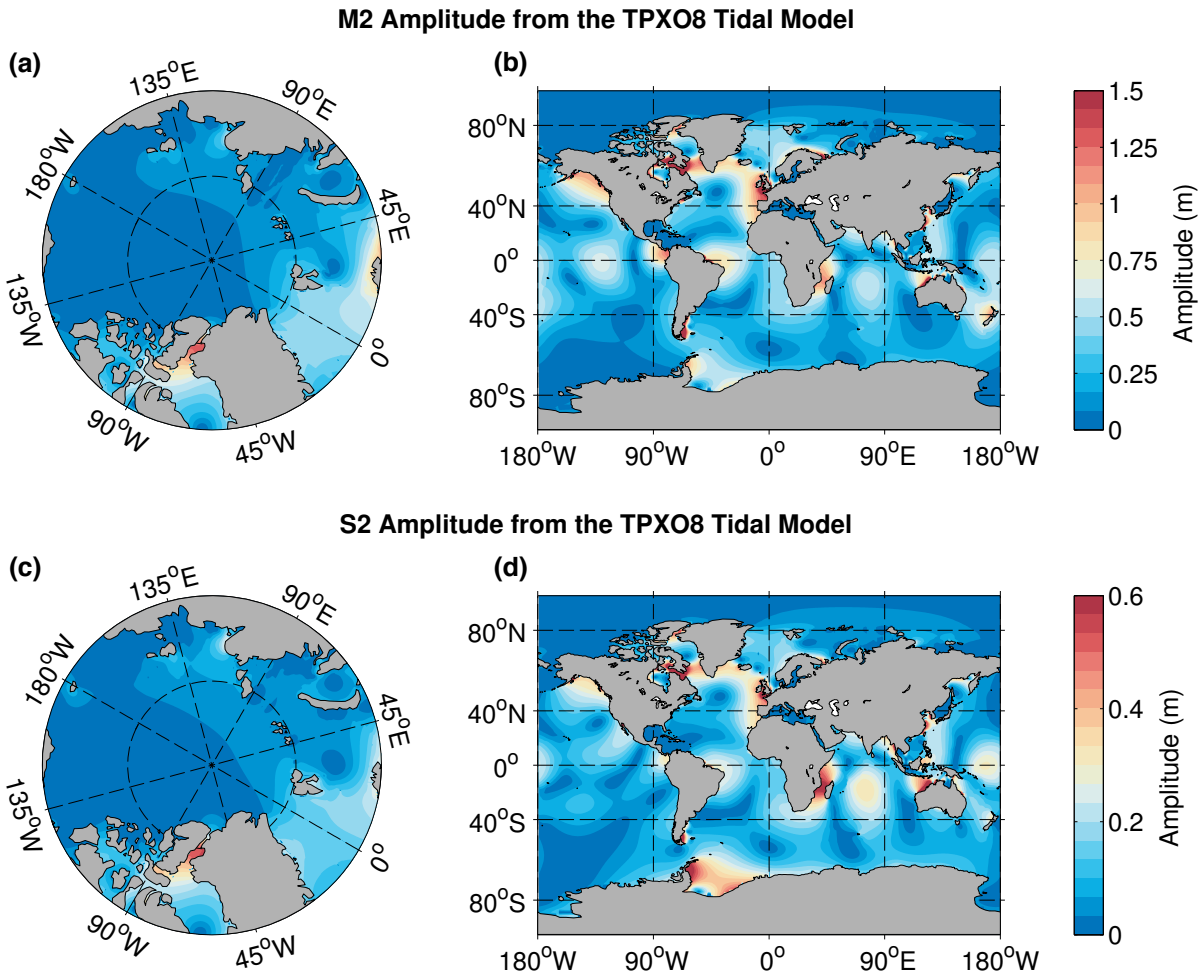

Figure 4.6: Amplitude of (a,b) the M2 and (c,d) the S2 tide in the TPXO8 tidal model (*Egbert and Erofeeva*, 2002) for (a,c) the Arctic Ocean, and (b,d) the global ocean. M2 and S2 tidal amplitudes in the central Arctic are generally lower than those observed at lower latitudes, except in Nares Strait where they are comparable in magnitude to those observed over the low latitude continental shelves (e.g. the northwest European Shelf). Note the different colour scales between the M2 and S2 tide.

Münchow and Melling (2008) has been limited to a depth- and time-averaged analysis (Figure 4.7). By harmonically analysing three-year-long records of the depth-averaged current velocity in Nares Strait, they found that the tidal flow was dominated by 7 major tidal constituents: M2, K1, S2, O1, N2, P1 and K2. The M2 tidal constituent was observed to be the most significant, containing between 55-57% of the total tidal energy, followed by the K1 and S2 tidal constituents which contain between 19-21% and 9-10% of the total tidal energy, respectively. Given that the TPXO8 model shows that the amplitude of the S2 tide is greater than that of the K1 tide in Nares Strait, it is perhaps counter-intuitive to observe a stronger depth-averaged current velocity associated with the K1 tidal constituent. The reasons for this observation will be discussed in Section

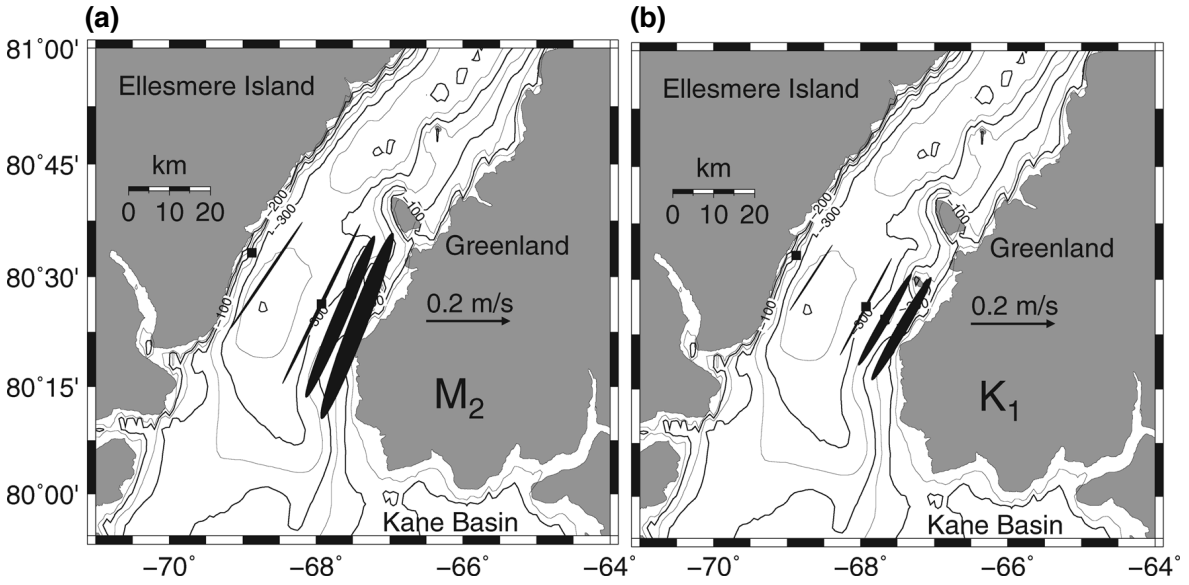

Figure 4.7: Figure from *Münchow and Melling* (2008) showing the shape of the depth-averaged tidal ellipses (see Section 4.3) for (a) the M2 and (b) the K1 tidal constituents. The tidal flow is aligned with the geographical orientation of Nares Strait, whilst the amplitude and the sense of clockwise rotation increases across the strait from Ellesmere Island to Greenland.

5.2. Overall, the semi-diurnal and diurnal bands were found to contain 66.4% and 26.3% of the tidal variance, respectively (Figure 4.8), and it was shown that the tidal flow in Nares Strait dominated the day-to-day variability, with the associated kinetic energy being an order of magnitude larger than that of the persistently southward subtidal flow (*Münchow et al.*, 2006; *Münchow and Melling*, 2008; *Rabe et al.*, 2012). In terms of the spatial variability, *Münchow and Melling* (2008) observed that the amplitude of all the major tidal constituents increased across Nares Strait from Ellesmere Island to Greenland, and they all exhibited a greater sense of rotation in a clockwise direction (Figure 4.7). The depth-averaged tidal flow is generally aligned with the along-strait direction, varying from 59° against Ellesmere Island to 66° against Greenland (note that this is not purely an observational result and is discussed in more detail in Section 4.3).

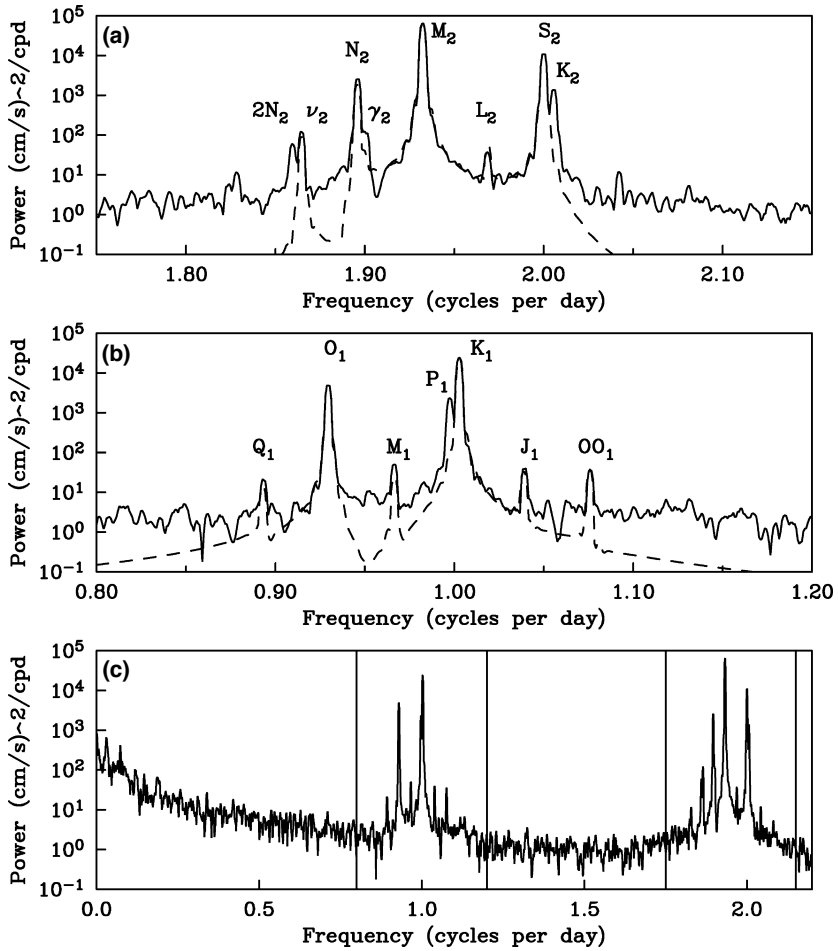

Figure 4.8: Figure from *Münchow and Melling* (2008) showing the power spectra of the depth-averaged along-strait current velocity through Nares Strait at a location ≈10 km from the coast of Greenland for (a) the semi-diurnal constituents, (b) the diurnal constituents, and (c) their context in a larger frequency range. The 7 major tidal constituents (M2, K1, S2, O1, N2, P1 and K2) clearly stand out as the dominant frequencies, and the dotted line indicates the spectra from a synthetic time series reconstructed using 11 tidal constituents.

4.3 Datasets and Data Analysis

4.3.1 Dataset: Acoustic Doppler Current Profilers

As part of the Arctic Sub-Arctic Ocean Flux program and the Canadian Arctic Through-Flow Study, ocean current observations in Nares Strait were made year-round between the summers of 2003 and 2006 using seabed mounted Acoustic Doppler Current Profilers (ADCPs). An array of 7 75-kHz Long Ranger Teledyne RD Instruments Inc. ADCPs was deployed across a 38 km wide section of section of Kennedy Channel (Figure 4.9 and black line in Figure 4.2), making measurements of the average current velocity over 8 meter bins every 30 minutes, between approximately 15 m above the seabed

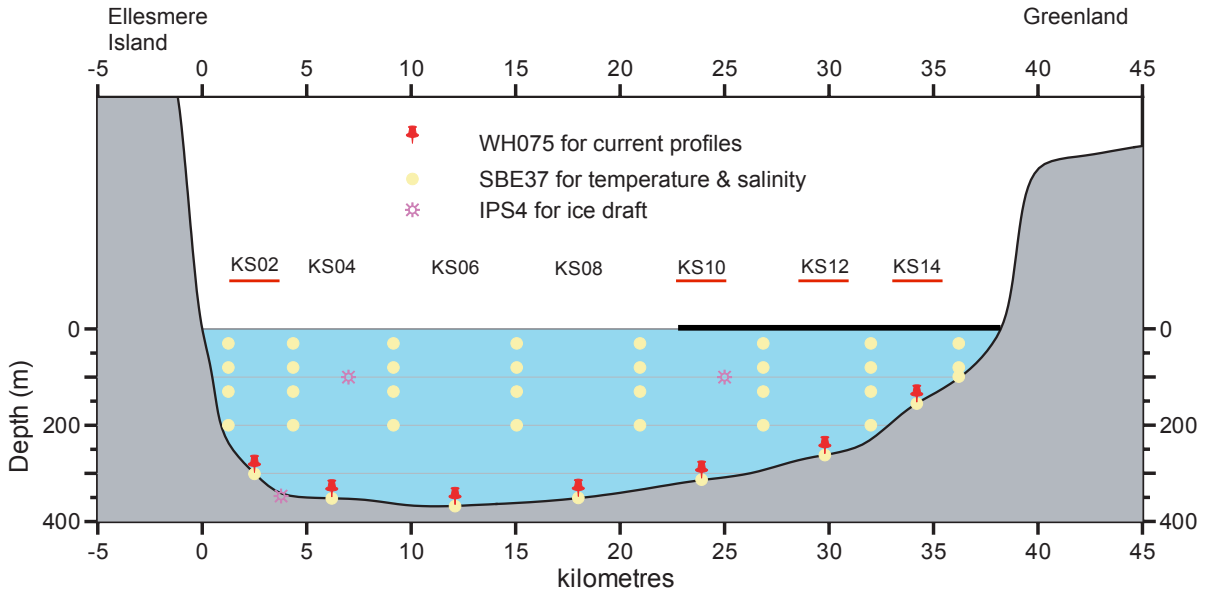

Figure 4.9: Schematic of the 2003 mooring array deployed across Kennedy Channel in Nares Strait. The locations of the ADCPs are donated by the red pins. Mooring numbers KS04, KS06 and KS08 were not retrieved in 2006. This chapter focuses on the data returned by KS02 against Ellesmere Island, and KS10, KS12 and KS14 against Greenland (the locations are underlined in red). The ADCPs will be referred to by their mooring names throughout this chapter. The black solid line at the sea surface against Greenland indicates the portion of the strait which is blocked by the constriction at Franklin Island, 30 km to the north-east. The yellow dots at the ADCP locations indicate the accompanying temperature and salinity sensors. A number of temperature and salinity sensors, as well as upward looking sonar (purple stars) were also deployed throughout the water column, but are not discussed in detail here. The figure was adapted from *Falkner* (2003).

and to within 35-40 m of the sea surface. Unfortunately, the second, third and fourth instruments in the array were not recovered, resulting in a 21 km gap in the centre of the strait. All four remaining ADCPs returned complete three-year data records, with mooring KS02 against the coast of Ellesmere Island, and moorings KS10, KS12 and KS14 against the coast of Greenland (Figure 4.9). Please note that throughout Chapters 4 and 5, the ADCPs will be primarily referred to by their mooring names.

ADCPs work by emitting "pings" of sound at a constant frequency into the water column. As the sound waves travel, zooplankton within the water column cause the sound waves to be reflected back to the instrument. The time delay between the transmission of the sound pulse and the detection of the echo gives an indication of the depth of the return, whilst the Doppler shift of the echo gives an indication of the current velocity. Each ADCP has four individual transducers inclined at an angle of ≈40 degrees to each other, to ensure that when the data from each transducer is combined, the dominant

orthogonal components of the velocity are resolved (i.e. the north-south and east-west velocities). As the echoes received by the ADCP originate from zooplankton within the water column, it is not possible to determine the current velocity during periods of low zooplankton abundance. These periods occurred primarily during the polar night, as well as for short periods each day due to the diel vertical migration. Velocity data were also not obtained during periods of significant ice motion (i.e. during summer and autumn), due to the high ambient noise levels drowning out the weaker echoes. Furthermore, due to the interference of surface echoes, no velocity data could be recovered within the upper 35-40 m of the water column (*Münchow and Melling*, 2008). Nevertheless, careful processing of the ADCP data does allow the ice velocity at the surface to be recovered. If it is assumed that the water just below the ice is moving at the same speed as the ice itself, then the ice velocity can be used as an estimate of the ocean velocity at the ice-ocean interface. Of course, during landfast ice seasons, the ice velocity is, by definition, equal to zero, and therefore the ocean velocity is assumed to be zero as well.

Due to the proximity of Nares Strait to the magnetic north pole, it is not possible to use a magnetic compass to determine the flow direction. Instead, each ADCP was mounted on a torsionally-rigid mooring to prevent it from rotating throughout the deployment (*Melling*, 2000; *Melling et al.*, 2008), and the true geographic heading of the flow was only determined after the velocity data were recovered at the end of the mooring deployment. To determine the true heading, observations of the tidal currents in Kennedy Channel over several tidal cycles in August 2003 (*Münchow et al.*, 2006) were compared with a barotropic tidal model of the Arctic with a 5 km resolution (*Padman and Erofeeva*, 2004), and both consistently showed that the depth-averaged tidal current was aligned with the geographic orientation of Nares Strait. Consequently, the unknown geographic heading of each ADCP was estimated through vector cross-correlation between the barotropic tidal model and the observed tidal current at the location of each mooring (*Münchow and Melling*, 2008). The correlation between the model and observations exceeds 0.94 for all four of the three-year velocity time series.

To obtain accurate estimates of the phase of the tide at each ADCP, it is necessary to know the exact time at which each velocity measurement was made. The nominal

sampling period was 1800 seconds, but an examination of each ADCP clock at the end of the deployment showed that all instruments were fast by varying degrees. This clock drift was accounted for by assuming it was equally distributed throughout the three-year deployment, and therefore a slight offset was added to the nominal sampling period for each ADCP, and a new set of sample times was generated.

In addition to each ADCP, each mooring also held one Sea-Bird Electronic SBE37 temperature salinity recorder. The nominal sampling period was 900 seconds, and clock drift was accounted for in a similar manner to the ocean current observations. Furthermore, a pressure sensor in each ADCP provided a concurrent measurement of the pressure field on the same time basis as the current measurements. Full deployment details for each of the moorings can be seen in *Falkner* (2003).

4.3.2 Datasets: Conductivity, Temperature and Depth Profiles

In conjunction with the deployment and recovery of the ADCP moorings, full Conductivity, Temperature and Depth (CTD) sections were taken across Nares Strait at the location of the mooring array during the summer of 2003, and on subsequent cruises in the summers of 2007 and 2009. Each profile sampled from the surface to the seabed, and the horizontal distance between profiles was typically between 2.5-5.0 km in order to fully resolve the internal Rossby deformation radius. The profiles were collected using a range of different instruments (for details see *Falkner*, 2003, *Melling*, 2007 and *Melling*, 2009). In 2003 the CTD salinities were calibrated against corresponding measurements from an Autosal, however, the corrections were not significant enough to warrant any alterations. In 2007 and 2009 no corresponding salinity samples were taken. Nevertheless, post-cruise calibration suggested conductivities were too low by a factor of 1.000288 and 1.000022, respectively. This corresponds to an additive correction to the salinity at 500 m of 0.011 and 0.001, respectively, and therefore only the 2007 data were corrected, as the change in 2009 is negligible (Melling, pers. comm.).

4.3.3 Data Analysis: Harmonic Analysis

Given a time series of u and v velocity components, which by convention are orientated eastward and northward, respectively, but can be in any orthogonal plane, a complete complex tidal vector $\mathbf{R}$ that contains a contribution from all tidal constituents as well as any residual flow can be constructed

$$\mathbf{R} = u + iv. \tag{4.3}$$

In this complex plane, each individual tidal constituent (k) that contributes to the full tidal response can be written as the sum of two counter-rotating components

$$\mathbf{R_k} = \mathbf{R_k^+} e^{i\omega_k t} + \mathbf{R_k^-} e^{-i\omega_k t}, \tag{4.4}$$

where $\mathbf{R_k}$ represents the total contribution to the complex tidal vector $\mathbf{R}$ from constituent k, ω_k is the radian frequency of the constituent, and t is time. The complex coefficients $\mathbf{R_k^+}$ and $\mathbf{R_k^-}$ in Equation 4.4 multiply the complex exponential rotating elements ($e^{i\omega_k t}$ and $e^{-i\omega_k t}$), which represent the anticlockwise (positive) and clockwise (negative) rotary components, respectively. Each rotary component has an associated positive real amplitude and phase given by

$$\begin{aligned} r_k^+ &= |\mathbf{R_k^+}| \\ r_k^- &= |\mathbf{R_k^-}|, \end{aligned} \tag{4.5}$$

and

$$\begin{aligned} \phi_k^+ &= \tan^{-1} \frac{\mathrm{Im}(\mathbf{R_k^+})}{\mathrm{Re}(\mathbf{R_k^+})} \\ \phi_k^- &= \tan^{-1} \frac{\mathrm{Im}(\mathbf{R_k^-})}{\mathrm{Re}(\mathbf{R_k^-})}, \end{aligned} \tag{4.6}$$

respectively, where Re and Im represent the real and imaginary parts, respectively. The vector addition of these two counter-rotating circular vectors defines the shape of the tidal ellipse for each individual tidal constituent (Figure 4.10). The tidal ellipse is the path traced by the velocity vector associated with each individual tidal constituent over a period of $t = 2\pi/\omega_k$. The ellipse parameters for each constituent: the semi-major axis (M), the semi-minor axis (m), the ellipse orientation (θ), and the phase (ϕ), can be written in terms of the real amplitudes and phases of the rotary components (the subscript k has been dropped for clarity but is assumed; Figure 4.10)

$$\begin{aligned} M &= (r^+ + r^-), \\ m &= (r^+ - r^-), \\ \theta &= \frac{\phi^+ + \phi^-}{2}, \\ \phi &= -\phi^+ + \theta. \end{aligned} \tag{4.7}$$

Given that the two rotary components are rotating at the same frequency but in opposite directions, then the semi-major axis (M) can be interpreted as the magnitude of the tidal current at the point in time when the two rotary vectors are aligned, and the semi-minor axis (m) as the magnitude of the tidal current when the vectors are opposed. Both the semi-major and semi-minor axes have the same units as u and v, but whilst the semi-major axis is always positive, the sign of the semi-minor axis varies depending on the sense of rotation of the tidal ellipse (positive for anticlockwise rotation in time and negative for clockwise rotation in time). The ellipse orientation (θ) is defined as the angle between the positive u axis and the semi-major axis that points in the direction of the positive v axis. The angle is defined as positive anticlockwise from the positive u axis and takes a range of 0 to π. The phase (ϕ) is interpreted as the time lag between an arbitrary reference time and the alignment of the velocity vector with the positive semi-major axis (i.e. the phase angle corresponds to the time lag between the reference time and the maximum velocity) and it takes a range of 0 to 2π. Although any arbitrary reference time can be used (such

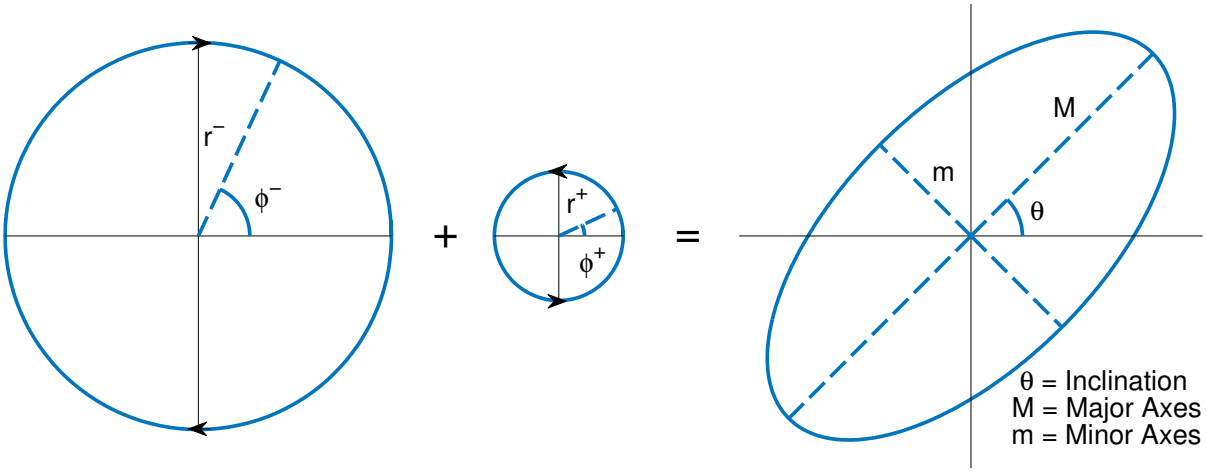

Figure 4.10: Schematic showing how the tidal ellipse for each tidal constituent with a semi-major axes (M), a semi-minor axes (m), an inclination angle (θ) and a phase (ϕ; not shown) can be represented as the vector sum of two counter-rotating circular components with real amplitudes r^+ and r^- and phases ϕ^+ and ϕ^-. The tidal ellipse represents the path traced by the velocity vector associated with each individual tidal constituent over a period of $t = 2\pi/\omega_k$.

as the start time or centre time of the dataset), here the astronomical argument correction is used in order to express the phase lags with respect to an absolute time origin. In this way, phase lags for different tidal constituents at different moorings which have different sample times can be directly compared (*Foreman and Henry*, 1989).

The astronomical argument correction assumes that each tidal constituent can be attributed to an artificial causal agent: in this case a fictitious star travelling around the equator at the same angular speed as the constituent of interest. Using this conceptual framework, the astronomical argument can be interpreted as the angular position of the fictitious star relative to any arbitrary longitude at time t. By setting the longitude to the Greenwich meridian, the astronomical argument becomes a function of only time and the frequency of each individual tidal constituent included in the model. Thus the phase lag (or more correctly the Greenwich phase lag) for each constituent at any ADCP can be interpreted as the time between the passage of its fictitious star over the Greenwich meridian and the time of maximum velocity.

A variety of different methods exist for finding the complex coefficients of the rotary components (i.e. $\mathbf{R}_\mathbf{k}^+$ and $\mathbf{R}_\mathbf{k}^-$ in Equation 4.4) and thus the ellipse parameters (i.e. M, m, θ and ϕ in Equation 4.7) for a specific tidal constituent. These include the simple "manual" fitting of sine and cosine waves or the use of Fourier transforms. However, in the case of tidal analysis where the frequencies of interest (i.e. the tidal constituents) are

well-defined, the simplest method is to use harmonic analysis. Here the complex tidal vector summed over all $k = 1, .., N$ constituents to be included in the analysis is modelled as

$$\mathbf{R^{mod}}(t) = \sum_{k=1,..,N} (\mathbf{R_k^+} e^{iV(t,\omega_k)} + \mathbf{R_k^-} e^{-iV(t,\omega_k)}) + \bar{\mathbf{R}} + \dot{\mathbf{R}}.t, \tag{4.8}$$

where $\bar{\mathbf{R}}$ represents the mean flow ($\bar{\mathbf{R}} = \bar{u} + i\bar{v}$), $\dot{\mathbf{R}}$ represents any trend in the data ($\dot{\mathbf{R}} = \dot{u} + i\dot{v}$), and $V(t, \omega_k)$ represents the astronomical argument correction. The benefit of harmonic analysis over Fourier methods is that the frequencies of interest can be directly specified, rather than being arbitrarily defined as a function of the record length and sampling interval. As a result, spectral leakage is minimised and the amplitude and phase estimates of the tidal constituents are at their most accurate.

The model is fitted to the data using an ordinary least-squares fit, which determines the complex coefficients $\mathbf{R_k^+}$ and $\mathbf{R_k^-}$ for all tidal constituents included in the analysis that minimise the following expression:

$$E = \sum_{t=1,..,n} |\mathbf{R^{ob}}(t) - \mathbf{R^{mod}}(t)|^2, \tag{4.9}$$

where $\mathbf{R^{ob}}(t)$ and $\mathbf{R^{mod}}(t)$ are the observed and modelled values of the complex tidal vector, respectively, at time $t = 1, .., n$. The harmonic analysis is carried out by the Matlab program UTide (*Codiga*, 2011).

Once the least-squares fit is complete, the residual between the modelled and the raw data is considered to be a signature of the subtidal flow and any other noise in the dataset. For long time series which are dominated by tidal signatures, the subtidal flow or noise are unlikely to have a significant effect on the estimates of the ellipse parameters. However, for shorter time series, they may have a noticeable impact and thus should be removed before the harmonic analysis is carried out. The simplest method is to compute a running average over the data with a window width of 48 hours, and then subtract the result from the original data. As a result, any variability with periods longer than 48 hours is removed, leaving just the tidal signature to be analysed. To quantify the effect of any remaining noise on the estimated ellipse parameters, 95% confidence intervals are calculated using Monte Carlo error propagation based on the variance/covariance statistics

of the estimated ellipse parameters. The presence of a substantial noise in the dataset will cause the width of the confidence intervals to increase.

Once the ellipse parameters and associated 95% confidence intervals for all of the constituents included in the analysis have been determined using UTide, the following inverse relationships can be used to calculate the real amplitudes and phases of the rotating components

$$\begin{aligned} r^+ &= \frac{1}{2}(m+M), \\ r^- &= -\frac{1}{2}(m-M), \\ \phi^+ &= \theta - \phi, \\ \phi^- &= 2\theta - \phi^+, \end{aligned} \tag{4.10}$$

and the corresponding 95% confidence intervals can be calculated from the standard error propagation formulae

$$\delta q = \sqrt{\left(\frac{\partial q}{\partial x_1}\delta x_1\right)^2 + ... + \left(\frac{\partial q}{\partial x_n}\delta x_n\right)^2}, \tag{4.11}$$

where x_1, $x_2 ... x_n$ are known with uncertainties δx_1, $\delta x_2 ... \delta x_n$, and $q = f(x_1, ..., x_n)$.

Whilst the method of harmonic analysis described above has been based on the analysis of a two-dimensional input (i.e. a complex tidal vector with both a u and a v velocity component), it is also possible to analyse any one-dimensional input, such as sea level, or a single velocity component. In the case of sea level, for example, the input is the real valued $\eta^{ob}(t)$, and in the above equations η should be substituted everywhere for u and v should be set to zero. Consequently, for any tidal constituent the real amplitude and phase of each of the rotary components are equal (the tidal ellipse is degenerate: m=0 and θ=0), and therefore the amplitude and phase of each tidal constituent that contributes to the observed sea level variability can be described with a single real amplitude and phase

lag (*Codiga*, 2011):

$$A = M = r^+ = r^-,$$

$$g = -\phi^+ = \phi^-. \tag{4.12}$$

4.3.4 Data Analysis: Phenomenological Analysis

Whilst the value of the ellipse parameters for each tidal constituent provide a statistical insight into the structure of the tides in Nares Strait, they can also be used to reconstruct synthetic time series of the velocity components associated with each tidal constituent. By reconstructing the along-strait velocity (positive northward) associated with a single tidal constituent over just three or four tidal cycles, and comparing it with, for example, the across-strait velocity (positive towards Greenland) or the pressure perturbation associated with the same tidal constituent, further insights can be gained into the structure and propagation of the tides in Nares Strait that are not provided by the results of a simple harmonic analysis.

4.4 Tidal Propagation in Nares Strait

Before investigating the dynamics behind the vertical and temporal structure of the tides in more detail, it is important to understand the nature of the tidal wave as it propagates through Nares Strait, and why the amplitude of the semi-diurnal tide is much greater in this region compared to the remainder of the Arctic (Figure 4.6). In shallow seas and narrow channels such as Nares Strait, the wave associated with each tidal constituent can propagate in a number of different forms. The most common form is a progressive wave, which is characterised by the steady geographic progression of the wave crest, often in the form of a Kelvin wave due to the effects of the Earth's rotation (e.g. the North Sea or the English Channel). In a progressive wave, the timing of the maximum velocity and the maximum perturbation in the sea surface height will occur at the same time (Figure 4.11), such that the phase difference at any given point between the maximum velocity

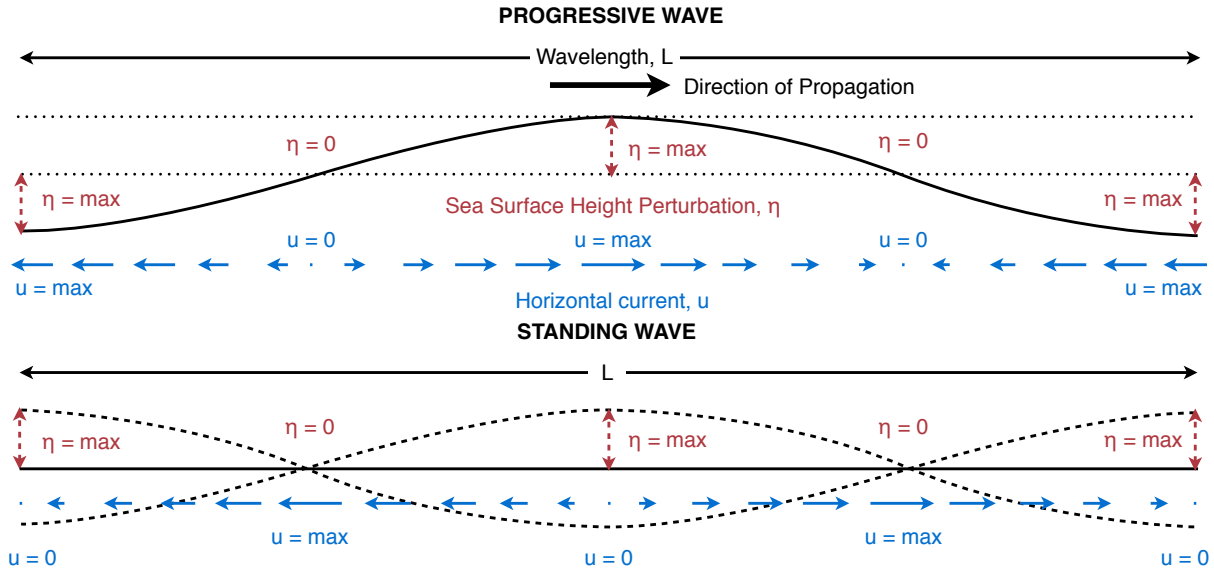

Figure 4.11: Schematic adapted from *Sverdrup et al.* (1942) of a progressive wave (top) and a standing wave (bottom) showing the relationship between the perturbation in the sea surface height (red) and the magnitude of the horizontal velocity (blue). For a progressive wave, the maximum horizontal velocity occurs at the time of the maximum perturbation in the sea surface height (phase difference = 0°), whilst for a standing wave, the maximum horizontal velocity occurs when the perturbation in the sea surface height is zero (phase difference = 90 °).

and the maximum sea surface height will be zero (*Segar*, 2012).

A second form the tidal wave can take is a standing wave. Here, a tidal wave entering a narrow channel or inlet whose length is approximately equal to a quarter of the wavelength of the incoming tide (e.g. the Bay of Fundy), interferes perfectly with the outgoing tidal wave from the previous tidal cycle that has been reflected off the landward end. The standing wave does not propagate in space, but rather oscillates in time around nodes and antinodes, where the constructive and destructive interference of the tidal waves result in the standing wave having a maximum amplitude (η = max) and zero amplitude ($\eta = 0$), respectively (Figure 4.11). In a standing wave, the timing of maximum velocity will occur when the perturbation in the sea surface height is zero, such that the phase difference between the maximum velocity and the maximum sea surface height at any given point will be 90 degrees (*Segar*, 2012).

Given these characteristic phase differences between the maximum velocity and sea surface height (i.e. 0° or 90°), the nature of the tidal wave associated with each of the major tidal constituents in Nares Strait can be determined by comparing the phase of the pressure perturbation to the phase of the depth-averaged along-strait tidal velocity. Reconstructed from the ellipse parameters estimated by a three-year harmonic analysis,

Figure 4.12 shows a two-day time series of the pressure perturbation and depth-averaged along-strait velocity associated with each tidal constituent at each ADCP. For the M2 and S2 tidal constituents, the phase difference is close to 90° for all ADCPs, suggesting that the tidal waves associated with these constituents have standing wave characteristics. Against the coast of Ellesmere Island (KS02) and Greenland (KS14; see Figure 4.9), the phase differences are slightly larger (≈+6° and +8°, respectively), suggesting that lateral friction may be affecting the propagation of the tidal wave. For the K1 tidal constituent, however, the phase difference is approximately 60° in the centre of the strait (KS10 and KS12), increasing to 70° at KS02 and decreasing to 46° at KS14. This suggests that the tidal wave associated with the K1 tidal constituent has neither purely progressive nor purely standing wave characteristics.

To understand why the M2 and S2 tidal constituents exhibit standing wave characteristics (especially given that Nares Strait is not closed at one end and thus an incoming tidal wave cannot be reflected off the landward end), it is important to examine how the tides propagate to the north in the central Arctic Ocean, and to the south in Baffin Bay. Using the results of the TPXO8 tidal model, Figure 4.13 shows that in both the central Arctic Ocean and Baffin Bay, the M2 and S2 tidal waves propagate as progressive waves anticlockwise from their source in the North Atlantic (*Kowalik and Proshutinsky*, 1994; *Egbert and Erofeeva*, 2002). As a result, two individual tidal waves of equal frequency propagate into Nares Strait: one from the north through Robeson Channel, and one from the south through Smith Sound. Figure 4.14 shows that the phase of each of these tidal waves as they enter Nares Strait are identical (≈110° and ≈150° for the M2 and S2 tidal constituents, respectively), and thus the standing wave characteristics exhibited by the M2 and S2 tidal constituents are generated through the interference of these waves as they propagate in opposite directions through Nares Strait. As the amplitude of a standing wave reflects the sum of the amplitudes of the two individual waves, it is the formation of this standing wave that is the reason behind the unusually strong M2 and S2 tides in Nares Strait.

In contrast, Figure 4.15a shows that there is a phase difference between the progressive K1 tidal wave to the north of Nares Strait in the Arctic Ocean (which is formed directly

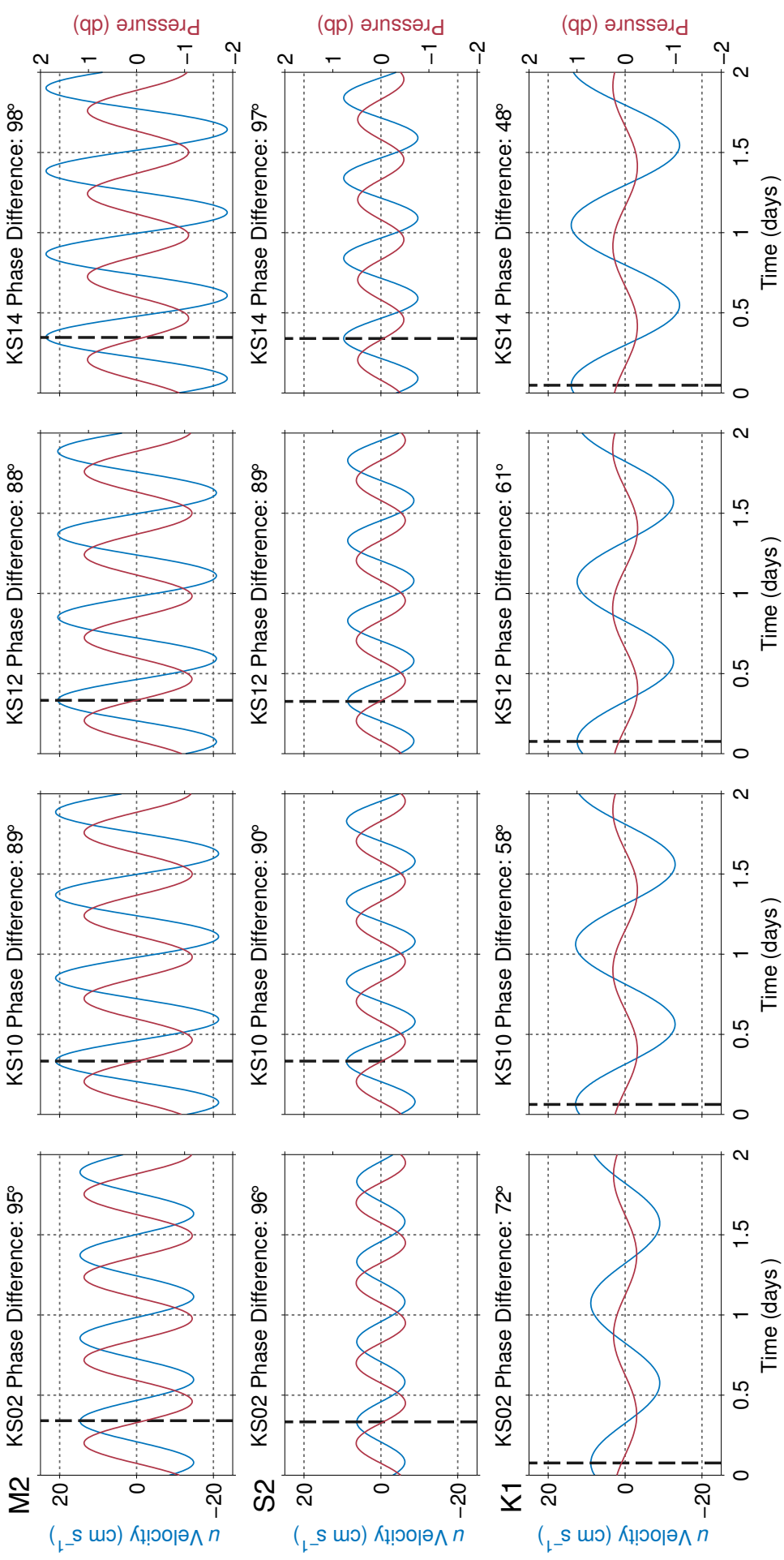

Figure 4.12: Reconstructed time series of the along-strait velocity (u; blue) and pressure perturbation (red) for the M2 (top), S2 (middle), and K1 (bottom) tidal constituents at KS02 (left), KS10 (middle-left), KS12 (middle-right), and KS14 (right). The black dashed lines indicate the timing of the first velocity maximum for each reconstructed tidal curve, and the phase difference represents the lag between the maximum along-strait velocity and the maximum pressure perturbation associated with each tidal constituent.

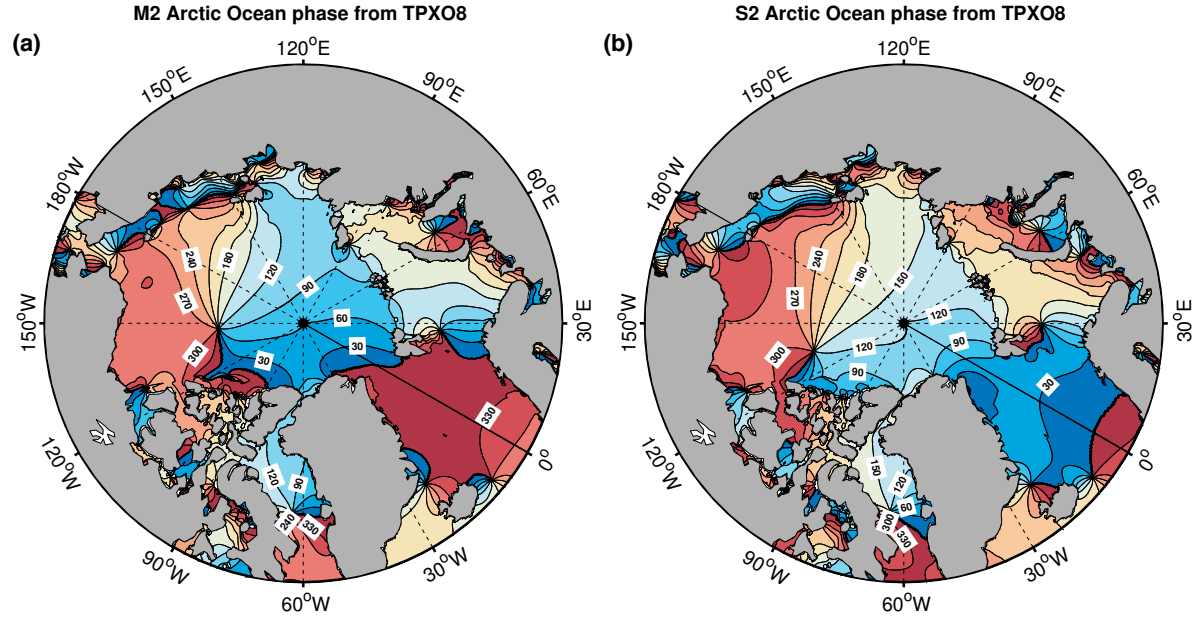

Figure 4.13: Phase in degrees of (a) the M2, and (b) S2 tidal constituents in the Arctic Ocean and Baffin Bay from the TPXO8 tidal model. The co-tidal or phase lines show that the tidal wave associated with each tidal constituent propagates as a progressive wave in an anticlockwise direction from their sources in the North Atlantic.

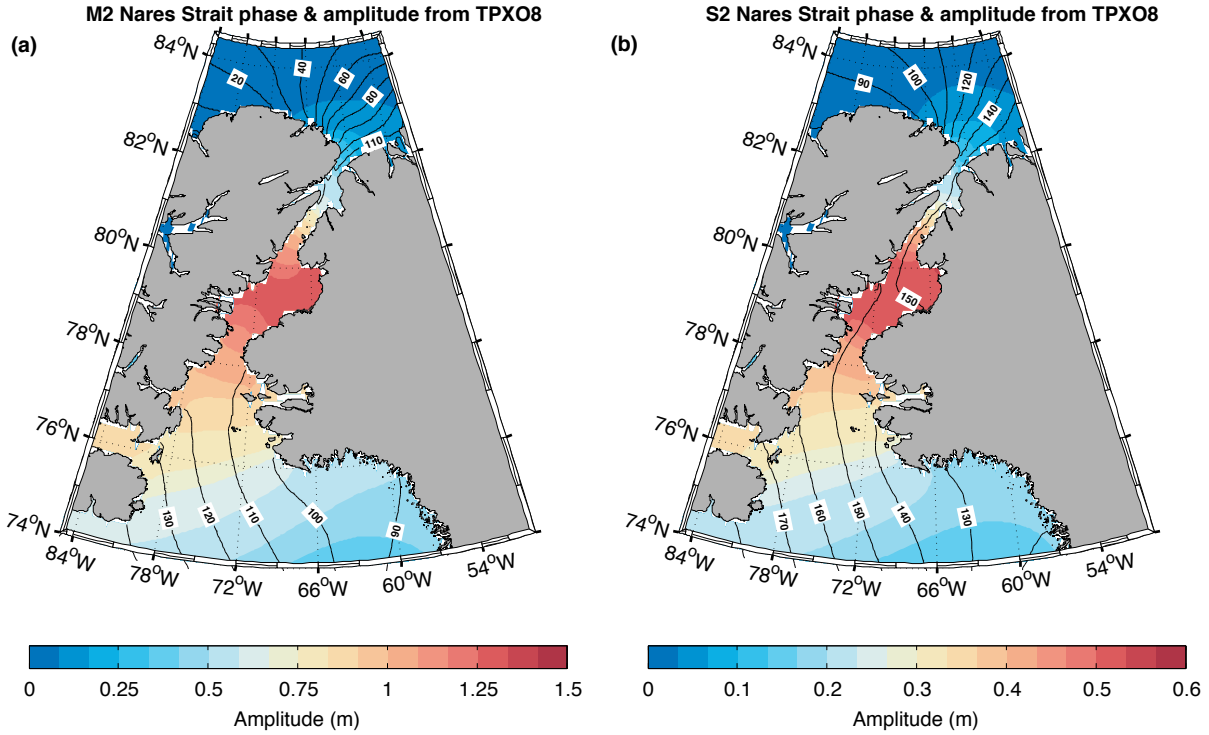

Figure 4.14: Amplitude in meters (coloured contours) and phase in degrees (black contours) of (a) the M2, and (b) S2 tidal constituents in Nares Strait from the TPXO8 tidal model. The co-tidal or phase lines show that the phase of the two tidal waves entering Nares Strait from either end are equal, resulting in the generation of a standing wave as they propagate through the strait. Note the different colour range for the amplitude.

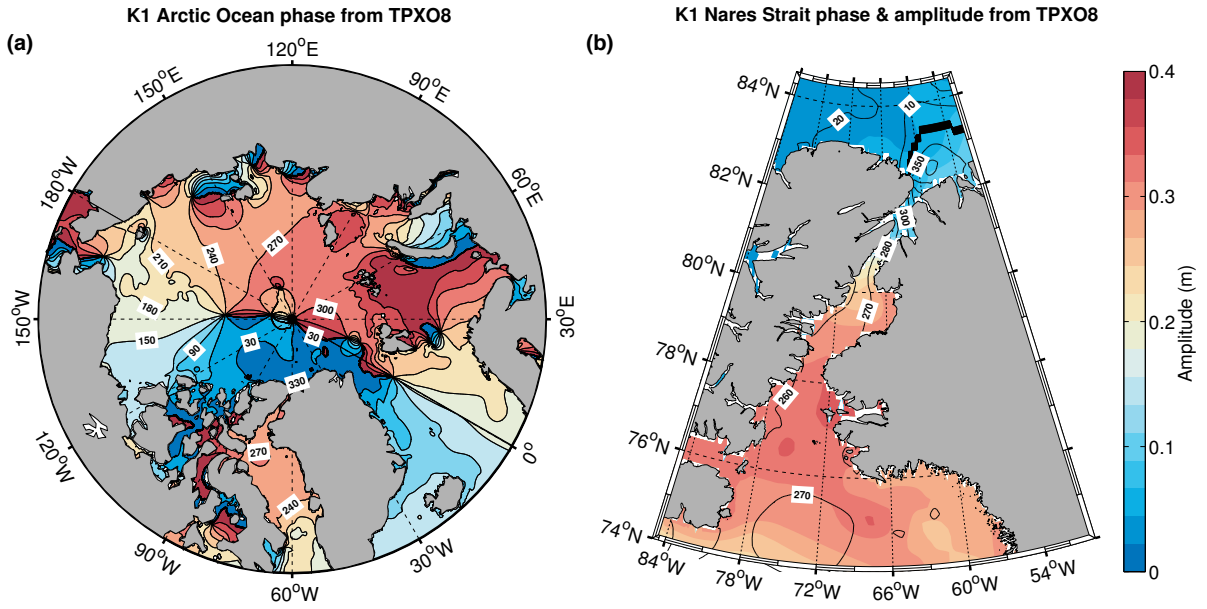

Figure 4.15: (a) Phase in degrees of the K1 tidal constituent in the Arctic Ocean and Baffin Bay from the TPXO8 tidal model. The co-tidal or phase lines show that the phase of the K1 wave at the northern end of Nares Strait is different to the phase of the wave at the southern end of Nares Strait. (b) Amplitude in meters (coloured contours) and phase in degrees (black contours) of the K1 tidal wave in Nares Strait. The co-tidal or phase lines shows that the wave propagates up Nares Strait from Baffin Bay to the Arctic Ocean (i.e. the phase increases with latitude). Note the different range on the amplitude axes compared to Figure 4.14.

in the Arctic Ocean by the astronomical forcing, rather than being sourced from the North Atlantic; *Proshutinsky*, 1991; *Kowalik and Proshutinsky*, 1993), and the K1 tidal wave to the south of Nares Strait in Baffin Bay. Consequently, the K1 tide in Nares Strait is characterised by the northward progression of a single tidal wave from Baffin Bay to the Arctic Ocean (Figure 4.15b; the phase or co-tidal lines consistently increases with latitude); thus a standing wave cannot form, and there is no amplification of the K1 tide in the middle of Nares Strait (as seen in the M2 and S2 tides). It is likely that the complex topography and bathymetry of the region are the reasons behind the non zero phase difference observed in Figure 4.12. It is interesting to observe, however, that there is a region of enhanced K1 amplitude (0.3 m to 0.4 m) to the south of Nares Strait where it meets Baffin Bay. This may be related to formation of shelf waves as the K1 tide interacts with the non-uniform bathymetry of the continental slope in this region (*Kowalik and Proshutinsky*, 1993).

To test the validity of using the barotropic TPXO8 tidal model to investigate the propagation of the tides through Nares Strait, Figure 4.16 shows the phase relationship

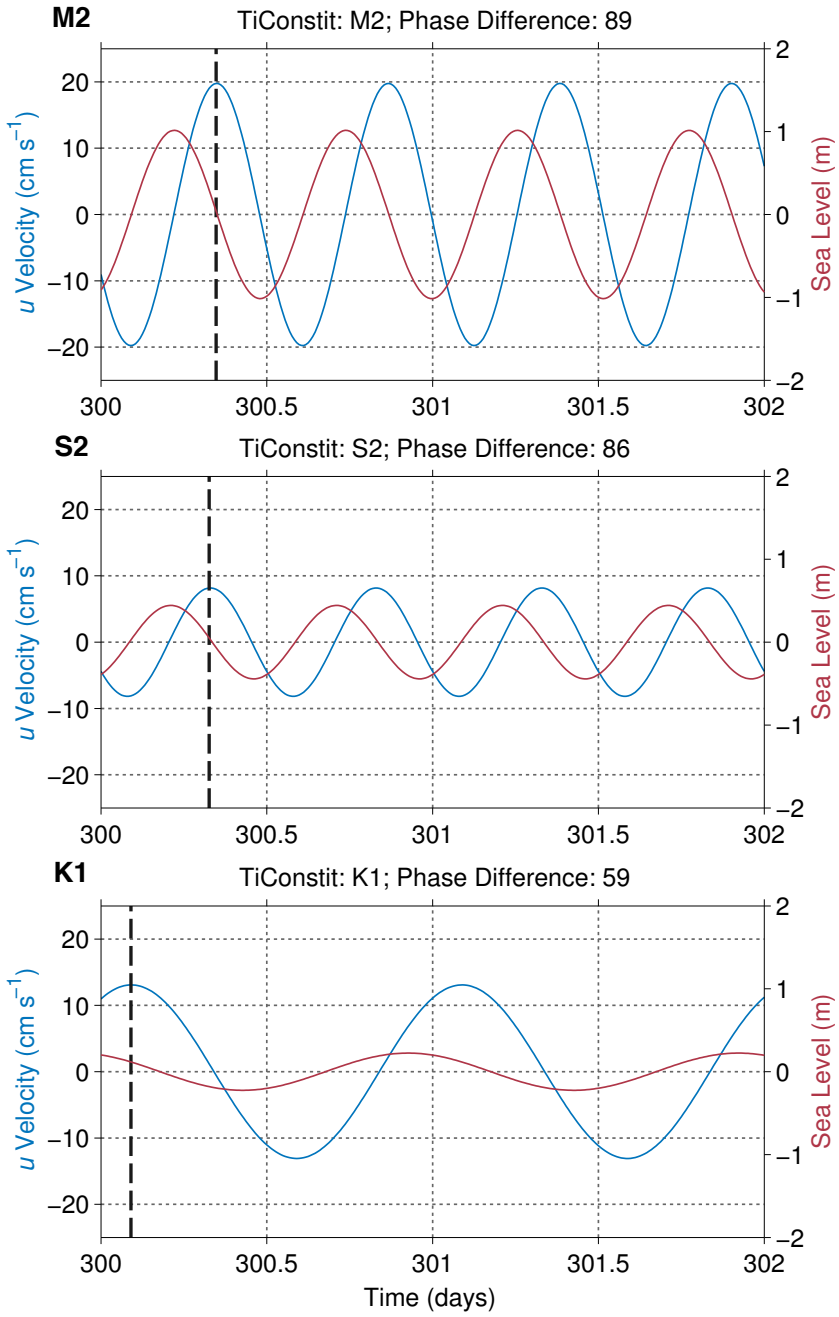

Figure 4.16: Reconstructed tidal curves from the TPXO8 barotropic tidal model for the along-strait velocity (u; blue) and sea level (red) for the M2 (top), S2 (middle), and K1 (bottom) tidal constituents at the location of the mooring array in Nares Strait. The black dashed lines indicate the timing of the first velocity maximum for each reconstructed tidal curve, and the phase difference represents the lag between the maximum along-strait velocity and the maximum sea level associated with each tidal constituent.

between the modelled sea level variation and the along-strait tidal velocity from TPXO8 at the location of the mooring array (nominally 80.5°N, 67.6°W). The phase difference for each tidal constituent is almost identical to those seen in Figure 4.12, which, along with the very high level of agreement between distribution of the co-tidal lines in Figures 4.14 and 4.15 and the observational results of *Greisman et al.* (1986), suggests that the

TPXO8 model is able to accurately reproduce the nature of the tides in Nares Strait. It is interesting to note, however, that the previous version of the TPXO model (TPXO7.2), which has a 1/4 degree resolution in the Arctic compared to the 1/30 degree resolution in TPXO8, cannot accurately reproduce the tides in Nares Strait. The phase differences between the maximum along-strait velocity and maximum sea level perturbation predicted by TPXO7.2 are 45°, 73° and 59° for the M2, S2 and K1 tidal constituents, respectively. This highlights the importance of using a high-resolution grid to resolve the complex bathymetry when modelling the tides in coastal areas such as Nares Strait.

The aim of this chapter was to provide an introduction to the tides and tidal propagation in the Nares Strait. In the following chapter, the depth and time variability of the tides in Nares Strait will be investigated, building upon the work of *Münchow and Melling* (2008) and taking the initial steps towards developing a fuller understanding of the role they may play in limiting the freshwater flux through this region.

Chapter 5

Vertical Structure of the Tides in Nares Strait

The aim of the previous chapter was to introduce the nature of the tides in Nares Strait, and to explore how the tidal wave associated with each of the major constituents propagates through the region. For the semi-diurnal tides (M2 and S2), it was shown that the tidal wave propagates as a standing wave, which explains why the amplitude of the M2 and S2 constituents in Nares Strait are unusually strong compared to their amplitude in the central Arctic Ocean. In contrast, the diurnal (K1) tidal wave propagates with a more progressive nature, and is strongly modified by the complex topography and bathymetry of the region.

5.1 Aims

With the intent of developing a dynamical understanding of the tides in Nares Strait that will help future studies in examining the role they may play in limiting the freshwater flux through this region, the aim here is to build upon the depth- and time-averaged analysis of *Münchow and Melling* (2008) by investigating the dynamical processes responsible for setting both the vertical and temporal variability in the structure of the dominant tidal constituents (i.e. M2, S2 and K1). In section 5.2 the time-averaged vertical structure of the tides in Nares Strait will be presented, along with a consideration of the across-strait component, and the results of some simple boundary layer models designed to determine

the important dynamical processes controlling the vertical structure. In Section 5.3 the temporal variability in the vertical structure of the tides will be explored, and the importance on the different ice regimes for the tidal dynamics in Nares Strait will be quantified. Broad estimates of the rate of tidal dissipation will be presented in section 5.4, and conclusions and avenues for further work from both this chapter, and Chapter 4, will be presented in Sections 5.5 and 5.6.

5.2 Time-Averaged Vertical Structure

To determine the vertical structure of the tides in Nares Strait, the full three-year velocity time series from each depth bin at each ADCP was harmonically analysed, and the ellipse parameters and associated 95% confidence intervals were extracted for the M2, S2 and K1 tidal constituents (which together account for approximately 90% of the total tidal variability). Due to the long length of the time series analysed, it was deemed unnecessary to carry out any pre-filtering to increase the signal-to-noise ratio, and this assumption is supported by the small size of the error bars seen in the results. Each data point represents the average ellipse parameters from both ice regimes in Nares Strait (mobile and landfast), except at the surface, where the data point is an average of only mobile ice seasons.

5.2.1 Ellipse Parameters

Figure 5.1 shows the vertical structure of the semi-major (M; red) and semi-minor (m; blue) axes of the tidal ellipse at each ADCP for the M2, S2 and K1 tidal constituents. There is significant variability both with depth and between the different tidal constituents and ADCPs. Against Greenland (KS14), the semi-major axes of the M2 and S2 tidal constituents exhibit smooth parabolic-like profiles with depth, decreasing in amplitude towards boundaries, due to friction at the seabed and the sea surface. As the surface data point represents the average amplitude from only mobile ice seasons, it appears that the integrated frictional effect of the various different boundary conditions that exist during these seasons (open sea, pack ice in free drift, and pack ice retarded by ice stress) has a

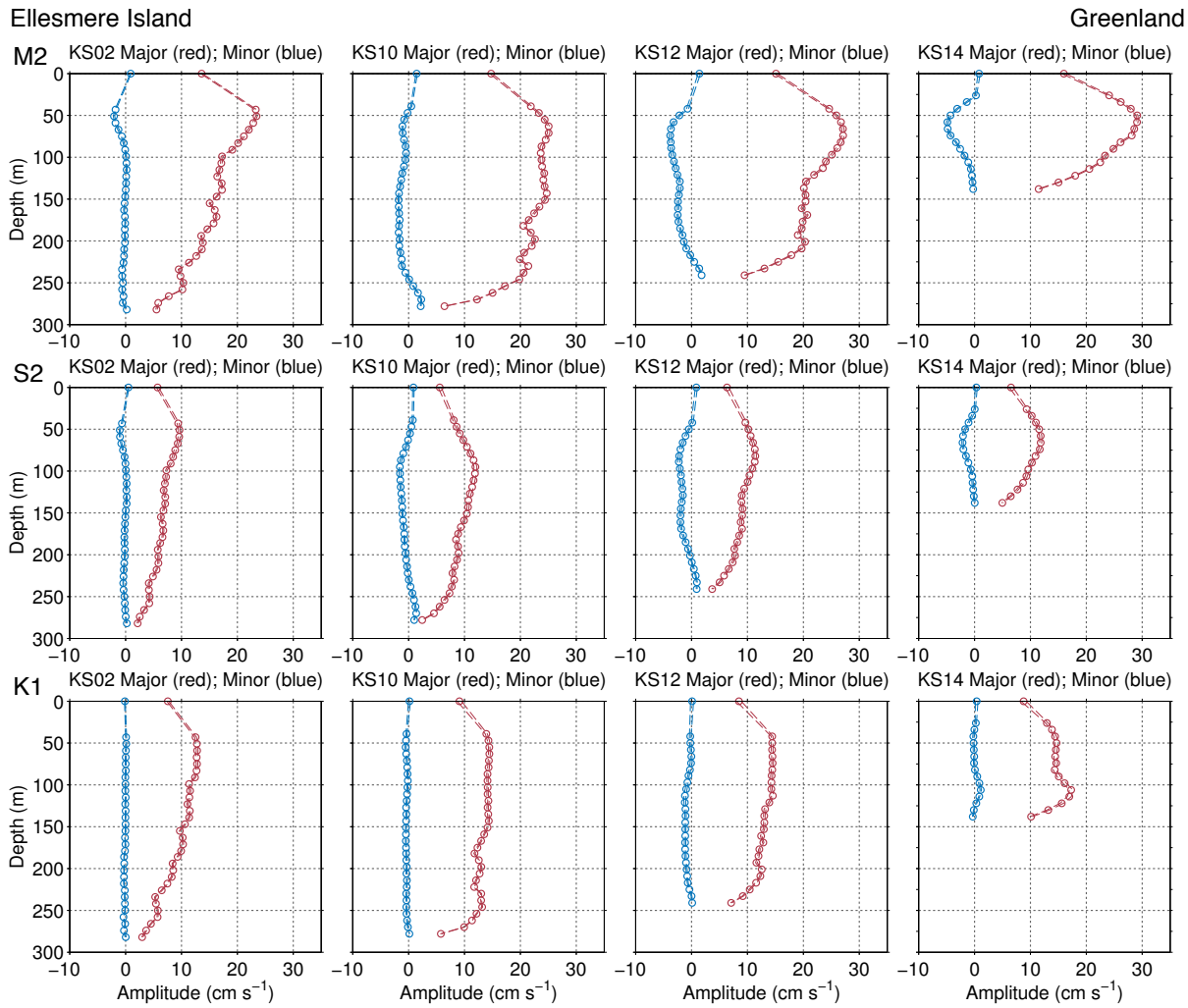

Figure 5.1: Vertical structure of the semi-major (M; red) and semi-minor (m; blue) axes of the tidal ellipse for the M2 (top), S2 (middle), and K1 (bottom) tidal constituents at KS02 (left), KS10 (middle-left), KS12 (middle-right), and KS14 (right). Each data point represents an average of both ice regimes in Nares Strait (mobile and landfast), except the surface point which is an average of only mobile ice periods. The dashed lines indicate the 95 percent confidence intervals for each data point.

substantial impact on the magnitude of the tidal current. A mid-water column maximum of ≈30 cm s^{-1} for the M2 constituent and ≈12 cm s^{-1} for the S2 constituent exists at a depth of ≈60-70 m. In contrast, the semi-major axis of the K1 constituent is relatively depth-invariant, except for a similar decrease near the boundaries and a maximum of ≈17 cm s^{-1} just above the seabed. As for the semi-minor axis, it is close to zero throughout the water column for the K1 tide, indicating a predominantly rectilinear tidal current. For the M2 and S2 constituents, it becomes increasingly negative with depth, indicating that the tidal velocity vector exhibits a greater sense of clockwise rotation. It is important to note, however, that for these constituents the semi-minor axes tend towards zero at the boundaries, indicating that the sense of clockwise rotation decreases.

In contrast to KS14, the semi-major axes of the M2, S2 and K1 constituents against Ellesmere Island (KS02) all show broadly the same vertical structure. The amplitude consistently increases with distance away from the seabed, reaching a maximum at 50 m of ≈13 cm s^{-1}, ≈5 cm s^{-1} and ≈7 cm s^{-1}, for M2, S2 and K1, respectively. Given the lack of data in the upper water column, the amplitude may continue to increase above 50 m, however, by examining the data from other ADCPs, it appears that this is unlikely. Compared to the remainder of the water column, there is a relative enhancement in the amplitude of the semi-major axis above 100 m for the M2 and S2 constituents, which is not seen in the K1 constituent. For all constituents, the semi-minor axis is essentially zero throughout the water column, except in the upper 100 m where there is a tendency towards greater clockwise rotation in the M2 and S2 tides.

For KS10 and KS12 (≈15 km and ≈10 km from the coast of Greenland, respectively), the amplitude of the semi-major axis associated with the K1 tide is broadly barotropic, reaching a maximum of ≈14-15 cm s^{-1} within 40-50 m of the seabed. In contrast, the amplitude of the M2 and S2 semi-major axes continue to increase away from the seabed up to a depth of at least 150 m. It is this thick shear layer that explains why, in a depth averaged sense, the amplitude of the S2 tide is weaker than that of the K1 tide (*Münchow and Melling*, 2008), despite the larger amplitude in terms of sea level perturbation seen in the TPXO8 model. Above 150 m, both M2 and S2 exhibit the same enhancement in the amplitude of the semi-major axis as that seen at KS02. When viewed in isolation, the structure in this region is very similar to the entire vertical structure of the M2 and S2 semi-major axes observed at KS14. Given that the total water depth at KS14 is equal to the depth over which the enhancement is observed at KS02, KS10 and KS12, this suggests that an enhancement in the semi-diurnal tidal constituents in the upper 150 m is a consistent feature across Nares Strait, and dominates the observed vertical structure at KS14. For M2 and S2, the semi-minor axis at KS10 and KS12 is generally negative throughout the water column, becoming positive in the region of the boundaries. For the K1 constituent, the semi-minor axis is not significantly different from zero throughout the water column at KS10, whilst at KS12, it becomes slightly negative below a depth of 100 m.

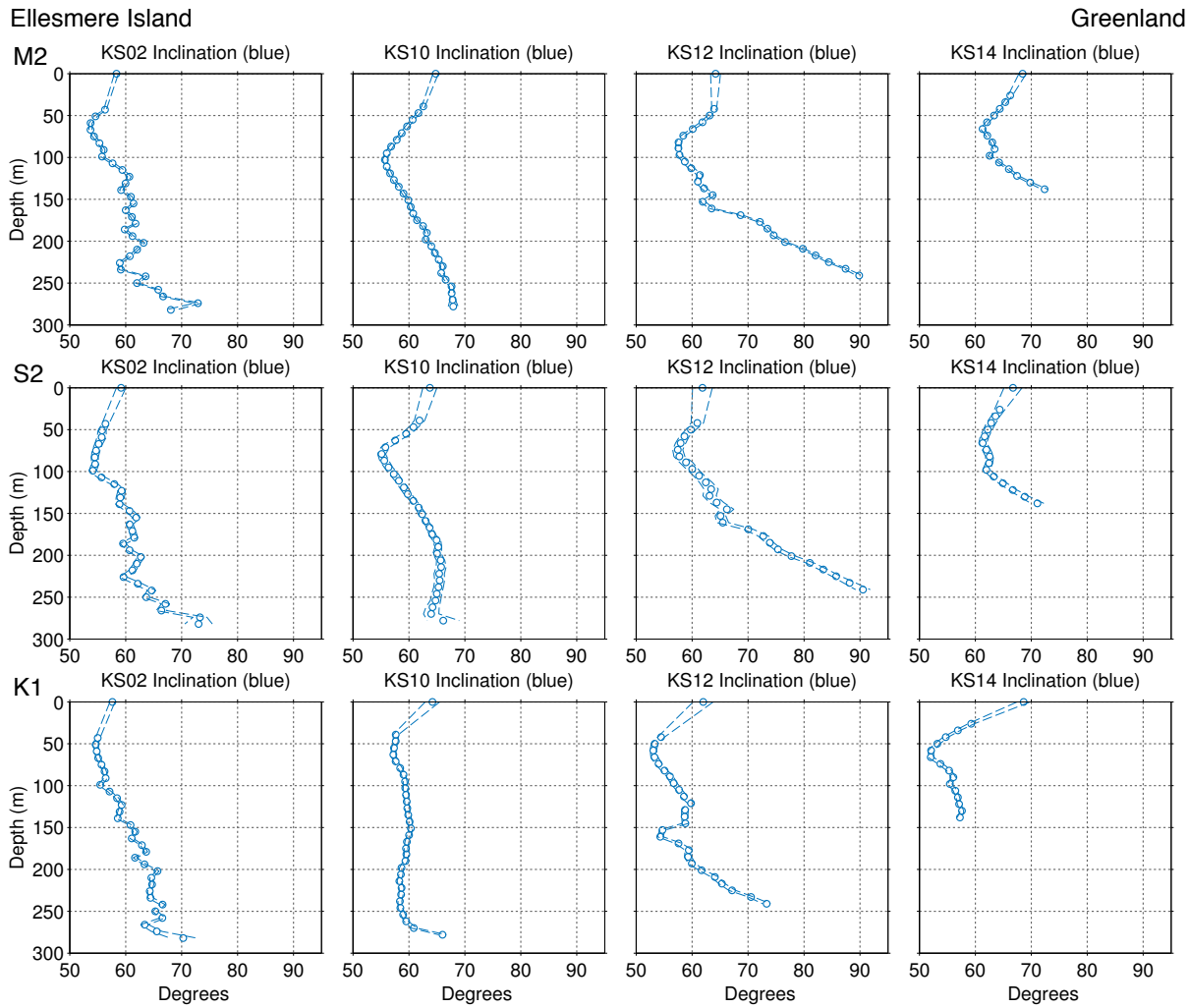

Figure 5.2: Vertical structure of the tidal ellipse inclination angle (θ) for the M2 (top), S2 (middle), and K1 (bottom) tidal constituents at KS02 (left), KS10 (middle-left), KS12 (middle-right), and KS14 (right). Each data point represents an average of both ice regimes in Nares Strait (mobile and landfast), except the surface point which is an average of only mobile ice periods. The dashed lines indicate the 95 percent confidence intervals for each data point.

For all constituents, there appears to be small scale vertical variability in the amplitude of the semi-major axis. Given that this appears in a three-year harmonic analysis, and that the data points have small error bars, this variability must be consistent in both time and space. Consequently, it is likely that it is due to some instrument error (Melling, pers. comm.), and will not be discussed in detail.

Figure 5.2 shows the vertical structure of the ellipse inclination angle at each ADCP for the M2, S2 and K1 tidal constituents. Although in a depth averaged sense the tidal flow is aligned with the along-strait direction (≈60°; *Münchow and Melling*, 2008), there is significant variability both in the vertical and between the different ADCPs. For most ADCPs and tidal constituents, the inclination angle is at a maximum at the boundaries,

and decreases to a minimum of ≈50-60° between 50 m and 150 m. At KS12, the inclination angle reaches an extreme maximum of ≈90° at the seabed. For all tidal constituents at KS02, there is less evidence of a minimum in the inclination angle between 50 m and 150 m, and instead the inclination angle consistently increases with depth. Furthermore, the inclination of the K1 tidal ellipse at KS10 appears to be relatively depth-invariant.

To summarise the results seen in Figures 5.1 and 5.2, Figure 5.3 shows section plots across Nares Strait of the semi-major and semi-minor axes of the tidal ellipse and the ellipse inclination angle for each tidal constituent. The washed out section indicates where no velocity data were recovered. Overall, there are a number of questions associated with the vertical structure of the tides in Nares Strait that motivate further investigation. These are:

1. Why is there an upper water column maximum in the amplitude of the semi-major axis associated with the semi-diurnal tides (M2 and S2), and why is this upper water column maximum not seen in the diurnal tides (K1)?

2. Why does the sense of clockwise rotation of the semi-diurnal tidal current vector increase across the strait (the semi-minor axis becomes progressively more negative), and therefore how is continuity maintained in the across-strait direction? Why is there is a trend towards anticlockwise rotation in the vicinity of the boundaries?

3. Why are the diurnal tides significantly more barotropic than the semi-diurnal tides, and why are they predominantly rectilinear across the strait?

4. Why against the coast of Ellesmere Island (KS02) do all tidal constituents exhibit the same vertical structure?

5.2.2 Across-Strait Component

As stated above, one interesting feature seen in Figure 5.1 is the observed spatial variability in the across-strait component of the tidal flow. Whilst at KS02 the semi-minor axis is close to zero, and thus the tidal flow is rectilinear (i.e. along-strait), at KS10, KS12 and KS14 there is a significant across-strait component associated with the

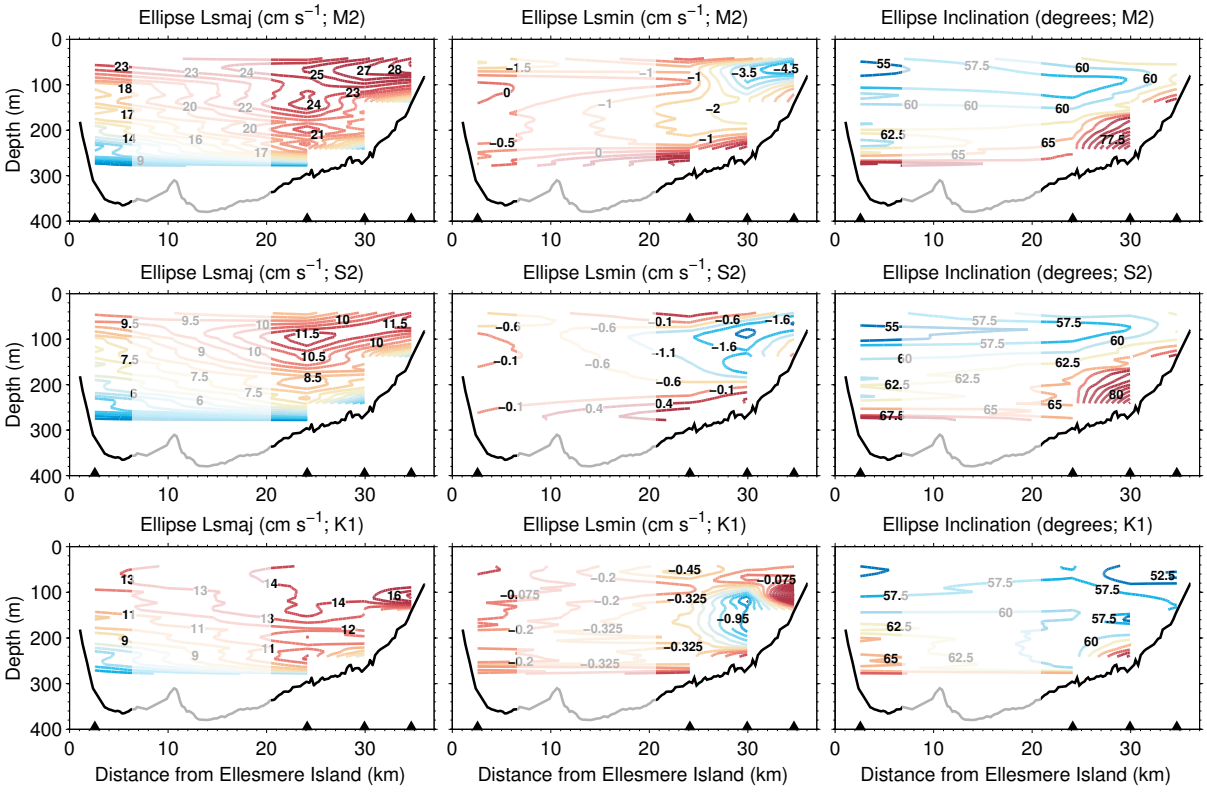

Figure 5.3: Section plots across Nares Strait as a function of depth and distance from Ellesmere Island of the semi-major axes (M; left), the semi-minor axes (m; middle), and the inclination angle (θ; right) associated with the tidal ellipse for the M2 (top), S2 (middle), and K1 (bottom) tidal constituents. The black triangles indicate the positions of the ADCPs. The washed out section indicates where no ADCPs were recovered, and therefore the vertical structure in this region should be treated with caution.

fattening of the semi-diurnal tidal ellipses. Given the requirement of continuity across the strait, how is the across-strait component of the flow facilitated at KS02, and is it of sufficient magnitude compared to the remainder of the strait?

Two mechanisms exist for facilitating an across-strait tidal flow: a fattening of the tidal ellipse (i.e. a large semi-minor axis), or a rotation of the tidal ellipse away from the along-strait direction (which is $\approx 60°$). The maximum across-strait flow associated with a fattening of the tidal ellipse will occur when the magnitude of the along-strait flow is at a minimum, and the maximum across-strait flow associated with a rotation of the tidal ellipse will occur when the magnitude of the along-strait flow is at a maximum. Consequently, by examining the phase difference between the maximum along-strait flow and the maximum across-strait flow, it is possible to determine which of these two mechanisms is dominant in facilitating the across-strait flow (it is important to note that both mechanisms can operate together, and although the phase difference will indicate which

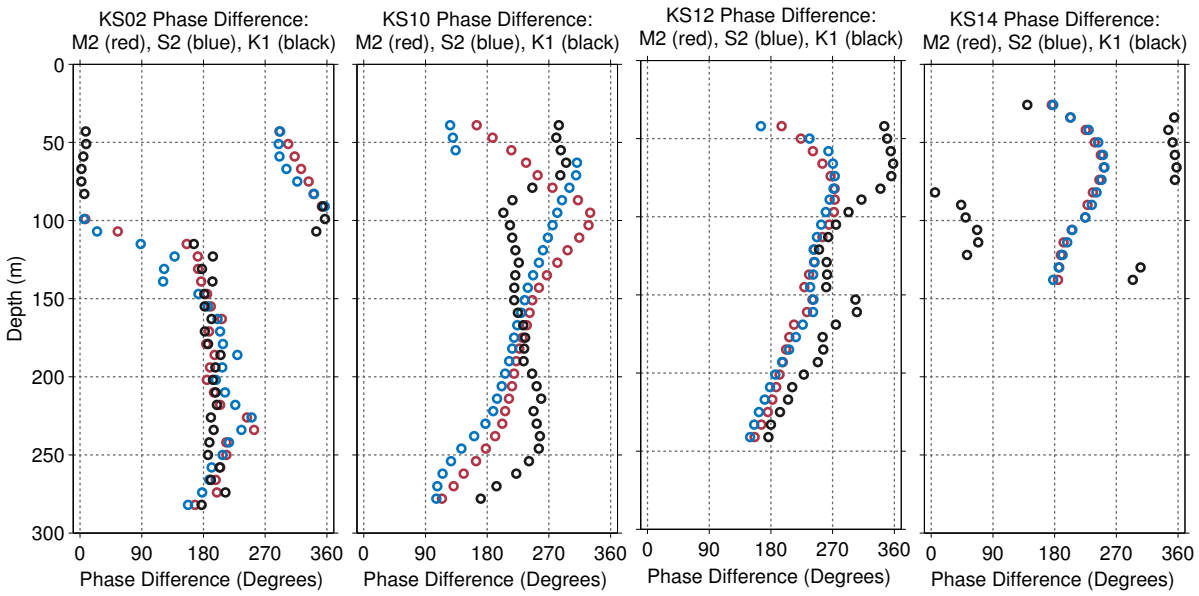

Figure 5.4: Phase difference between the maximum along-strait velocity and the maximum across-strait velocity wrapped to a range of 0-360° at KS02 (left), KS10 (middle-left), KS12 (middle-right), and KS14 (right), for the M2 (red), S2 (blue), and K1 (black) tidal constituents. A phase difference of 180° or 0° indicates that the maximum in the across-strait velocity is anti-phased with or in phase with the maximum along-strait velocity, respectively, and is associated with a rotation of the tidal ellipse facilitating the across-strait flow. A phase difference of 90° or 270° indicates that the maximum in the across-strait velocity leads or lags the maximum along-strait velocity by 90°, respectively, and the across-strait flow is facilitated by anticlockwise or clockwise rotation of the tidal current vector, respectively.

mechanism dominates, it does not indicate that the other mechanism has no effect).

Figure 5.4 shows the phase difference for all constituents at all ADCPs. At KS02, the phase difference is close to 180° below ≈100 m for all constituents. This indicates that the maximum across-strait flow coincides with the maximum along-strait flow, and therefore the across-strait flow is dominated by a rotation of the tidal ellipse towards Ellesmere Island (i.e. ellipse inclination angles >60°; Figure 5.2). The rotation of the ellipse and the anti-phasing between the velocity components is due to Ekman transport in the bottom boundary layer, whereby the maximum along-strait flow (i.e. towards the Arctic; defined as a positive), coincides with the maximum across-strait flow towards Ellesmere Island (defined as a negative). Above ≈100 m, the phase difference for the K1 constituent jumps to zero. In this case the across-strait flow is still dominated by a rotation of the tidal ellipse, however, the maximum along-strait flow now coincides with the maximum across-strait flow towards Greenland (i.e. ellipse inclination angles <60°; Figure 5.2). In contrast, for the M2 and S2 tidal constituents, the phase difference above ≈100 m tends towards 270°, and the across-strait flow is dominated by a fattening of

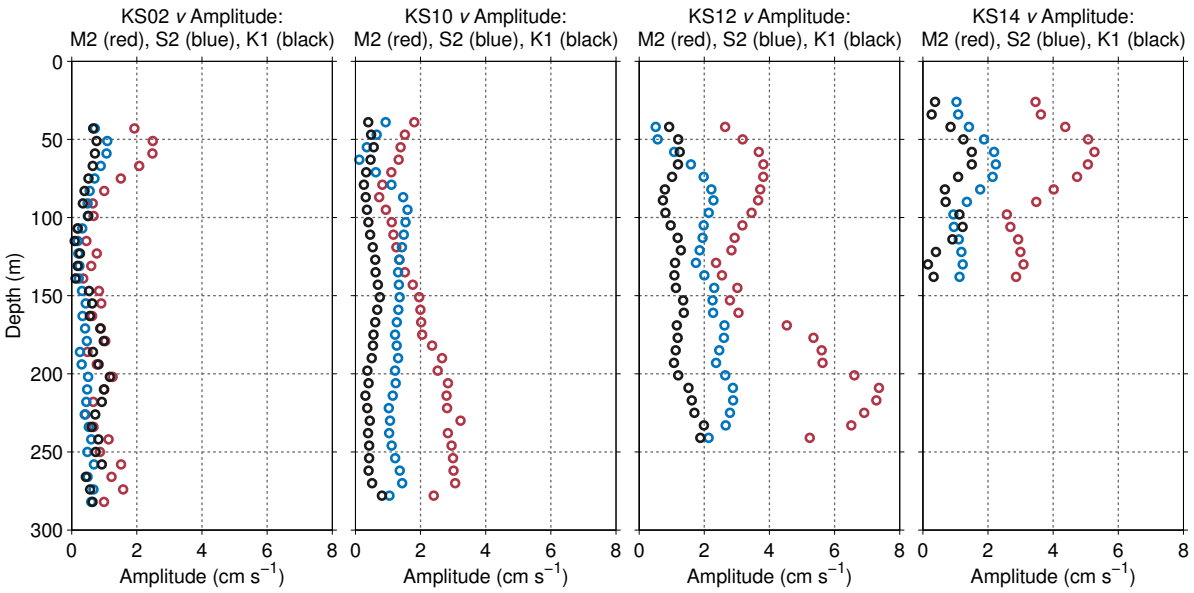

Figure 5.5: Amplitude of the across-strait velocity derived from a three-year harmonic analysis at KS02 (left), KS10 (middle-left), KS12 (middle-right), and KS14 (right) for the M2 (red), S2 (blue), and K1 (black) tidal constituents.

the tidal ellipse with clockwise rotation of the tidal current vector (the maximum positive across-strait flow lags the maximum positive along-strait flow by 90°; negative semi-minor axes in Figure 5.1).

As expected for the M2 and S2 constituents at all other ADCPs, the phase difference tends towards either 270° in the region of the upper water column maximum, or 90° at the boundaries, and indicates that the across-strait flow primarily occurs through a fattening of the tidal ellipse. The phase difference of 270° is consistent with the clockwise rotation seen in the upper water column maximum (negative semi-minor axes in Figure 5.1), whilst a phase difference of 90° corresponds with the trend towards anticlockwise rotation of the tidal current vector near the boundaries (the maximum positive across-strait flow leads the maximum positive along-strait flow; positive semi-minor axes in Figure 5.1). Two notable exceptions to this pattern are found near the seabed at KS12 and KS14, where the phase difference is close to 180°. At KS12, this due to the extreme inclination angles observed at the seabed dominating the across-strait flow (Figure 5.2).

Whilst Figure 5.4 indicates that the rotation of the tidal ellipse dominates the across-strait flow at KS02, it provides no information on the magnitude of the flow itself, and whether it can satisfy the requirement of continuity across the strait. Figure 5.5 shows the amplitude of the across-strait velocity obtained through a three-year harmonic analysis

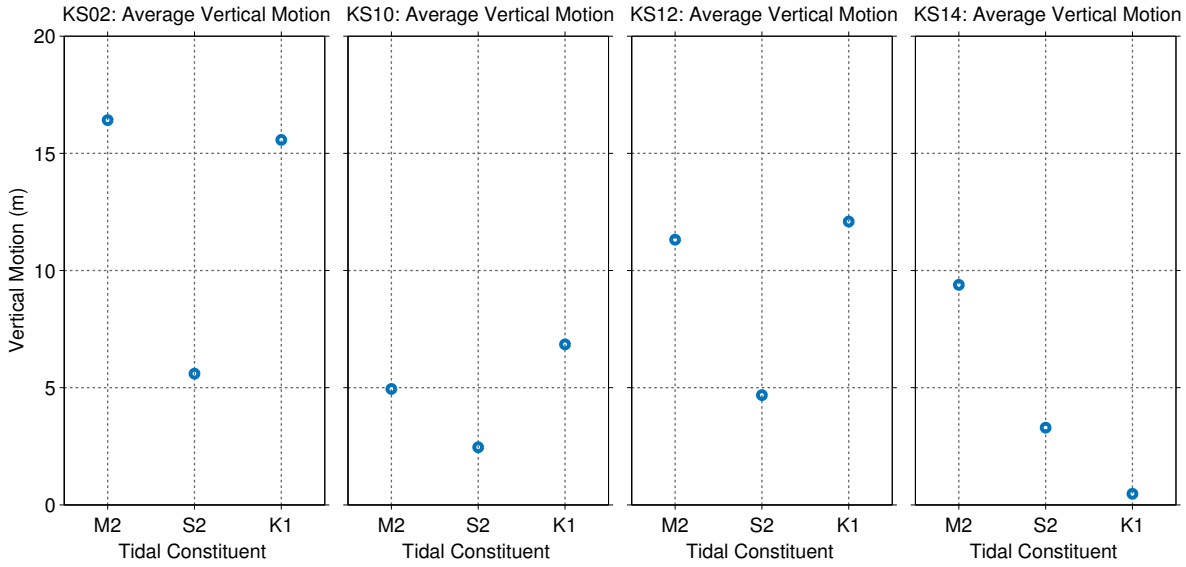

Figure 5.6: Average vertical motion over the period of each tidal constituent at KS02 (left), KS10 (middle-left), KS12 (middle-right), and KS14 (right). Note that the relatively large vertical motion associated with the K1 tidal constituent in comparison to its relatively weak across-strait velocity is due to the longer period of the diurnal tides.

at each ADCP depth bin. It is clear that the amplitude of the across-strait component at KS02 is smaller than that at all other ADCPs (especially for the semi-diurnal tidal constituents), and thus the requirement of continuity across the strait appears to be violated. However, if the three-year temperature and salinity time series recorded at each ADCP are harmonically analysed (where a running mean has been used to remove the subtidal variability prior to the analysis), and the resulting amplitudes are divided by the average vertical temperature and salinity gradients at the seabed derived from the summer CTD sections, then the average vertical motion at each ADCP over the period of each constituent can be determined (Figure 5.6). At KS02, the vertical motion associated with each tidal constituent is greater than the corresponding constituent at any other ADCP. If this motion is divided by half the tidal period of each constituent to give an average vertical velocity, and this vertical velocity is divided by the tangent of the slope of the bathymetry at KS02 (1.8°), then the amplitude of the horizontal velocity associated with this vertical motion can be calculated: 2.3 cm s^{-1}, 0.8 cm s^{-1} and 1.1 cm s^{-1} for the M2, S2 and K1 tidal constituents, respectively. If these velocities are added to the across-strait velocity at KS02 seen in Figure 5.5, then the disparity in the amplitude of the across-strait velocity between the different ADCPs is significantly reduced. Therefore, despite the rectilinear nature of the tidal current at KS02, it is the rotation of the tidal

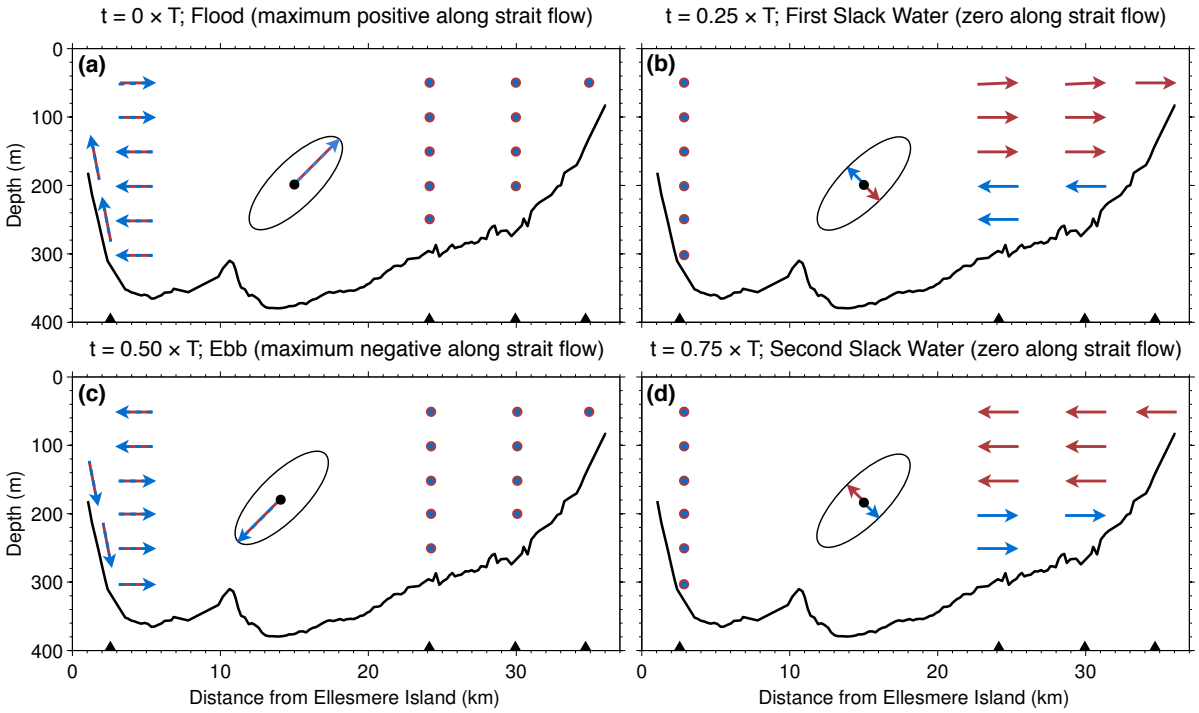

Figure 5.7: Schematic showing the dominant direction of the across-strait flow at each ADCP during the four major phases of each tidal cycle (where T is either the diurnal or semi-diurnal tidal period): (a) flood; t = 0 × T (maximum positive along-strait flow), (b) first slack water; t = 0.25 × T (zero along-strait flow), (c) ebb; 0.5 × T (maximum negative along-strait flow), and (d) second slack water; t = 0.75 × T. During each phase of the tidal cycle, blue arrows indicate the direction of the across-strait flow associated with anticlockwise rotation of the tidal current vector, whilst red arrows indicate the direction of the across-strait flow associated with clockwise rotation of the tidal current vector. Combined blue and red arrows/dots indicate that the dominant direction of the across-strait flow during that phase of the tidal cycle is identical for both clockwise and anticlockwise rotation of the tidal current vector.

current ellipse and the vertical motion associated with the steeply sloping bathymetry that combine to ensure that continuity is maintained across the strait.

To summarise the structure of the circulation within the cross-section of Nares Strait, the schematic in Figure 5.7 shows the dominant direction of the across-strait flow at each ADCP during the four major phases of each tidal cycle: flood (maximum positive along-strait flow), first slack water (zero along-strait flow), ebb (maximum negative along-strait flow), and second slack water. Overall, the across-strait flow shows a two layer structure with a phase lag of approximately a quarter of a tidal cycle across the strait. At $t = 0 \times T$ (where T is the period of either the diurnal or semi-diurnal tides), the tidal current vector is aligned with the positive semi-major axis of the tidal ellipse, and the tidal current velocity is at a maximum towards the Arctic (Figure 5.7a). At KS02, the across-strait flow is dominated by a rotation of the ellipse inclination angle, and thus the across-strait

flow is at a maximum. Water is moving towards Ellesmere Island below 100 m (ellipse inclinations angles >60°), and there is significant upwards vertical motion due to the steeply sloping bathymetry. Above this, the ellipse inclination angles are generally <60°, and water is moving towards Greenland. At KS10, KS12, and KS14, the across-strait flow is dominated by a fattening of the tidal ellipse, and therefore at this point in the tidal cycle the across-strait flow is small. A quarter of a tidal cycle later, however ($t = 0.25 \times T$; Figure 5.7b), the along-strait flow is close to zero and there is no across-strait flow at KS02 due to the rectilinear nature of the tidal currents. In contrast, the across-strait flow at KS10, KS12 and KS14 is at a maximum, and reflects the same pattern seen at KS02 a quarter of a cycle earlier. The clockwise rotation of the tidal current vector in the upper water column is moving water towards Greenland (red arrows), whilst below this the anticlockwise rotation near the boundaries is moving water towards Ellesmere Island. At the mid-point of the tidal cycle ($t = 0.50 \times T$; Figure 5.7c), the tidal current vector is now aligned with the negative semi-major axis of the tidal ellipse, and the tidal current velocity is at a maximum towards Baffin Bay. At KS02 the structure of the two layer flow reverses, with water moving towards Ellesmere Island above 100 m (driving a significant negative vertical motion down the steeply sloping bathymetry), and towards Greenland below this. Again, at this point of the tidal cycle, the across-strait flow at KS10, KS12, and KS14 is small. However, a quarter of a tidal cycle later at the second slack water ($t = 0.75 \times T$; Figure 5.7d), the clockwise rotation of the tidal current vector in the upper water column moves water towards Ellesmere Island, whilst the anticlockwise rotation of the tidal current vector in the lower water column moves water towards Greenland. Finally after a full tidal period, the tidal current vector is realigned with the positive semi-major axis of the tidal ellipse, and the cycle in the across-strait flow begins again.

5.2.3 Boundary Layer Models

To determine what the controlling processes are behind the vertical structure of the tides in Nares Strait (see Figures 5.1, 5.2 and 5.3), and to explore why, for example, the diurnal tides (K1) are significantly more barotropic than the semi-diurnal tides (M2 and S2), it is instructive to fit simple boundary layer models to the observed vertical structure

of the different tidal constituents at the different ADCPs (*Soulsby*, 1990).

Simple boundary layer models have been used to explain much of the observed vertical variation in the strength of tidal currents over continental shelf seas at both low (e.g. *Prandle*, 1982a and *Soulsby*, 1983) and high latitudes (e.g. *Prinsenberg and Bennett*, 1989 and *Makinson et al.*, 2006). The vertical structure in these models is governed by the extent to which turbulence generated by the strong frictional stresses exerted on the seabed can propagate upwards into the water column (*Howarth*, 1998). The frictional stresses at the seabed act to retard the tidal current within a region known as the benthic boundary layer. This layer consists of two regions: a thin high-shear layer at the seabed and a thicker low-shear region. Within the high-shear region, which is likely to be only a few meters thick, the current profile is logarithmic and the stress is approximately constant. In the low-shear region, which is tens of meters thick, the current profile can be described by a power law (*Howarth*, 1998). If the water column is deep enough, the tidal current speed will increase with height until it attains its frictionless free stream velocity. Above this depth the flow will be inviscid, the stress will be zero, and in the absence of any other baroclinic influences (e.g. internal tides), the flow will be independent of depth. However, if the water column is too shallow, the free stream region may not exist, and bottom-generated turbulence will extend throughout the water column (*Soulsby*, 1990). In a similar manner, if turbulence generated at an ice-ocean boundary layer propagates deep enough into the water column that it interacts with turbulence generated in the benthic boundary layer, then the entire water column may be affected by boundary layer dynamics.

Simple boundary layer models for the vertical structure of the tides in Nares Strait can be derived from the linearised equations of motion for a rotating fluid forced by sea surface slope pressure gradients and horizontal stresses both at the sea surface and the seabed (*Prandle*, 1982a,b; *Soulsby*, 1983; *Maas and van Haren*, 1987):

$$\frac{\partial u}{\partial t} - fv = -g\frac{\partial \eta}{\partial x} + \frac{1}{\rho}\frac{\partial \tau_{xz}}{\partial z}, \tag{5.1}$$

$$\frac{\partial v}{\partial t} + fu = -g\frac{\partial \eta}{\partial y} + \frac{1}{\rho}\frac{\partial \tau_{yz}}{\partial z}, \tag{5.2}$$

where u and v are the components of the horizontal tidal velocity in the x and y directions, respectively, τ_{xz} and τ_{yz} are the horizontal stresses similarly aligned, t is time, f is the Coriolis parameter, g is the acceleration due to gravity, η is the sea surface height, ρ is density, and z is depth. The vertical component of velocity has been ignored, along with the effects of advection and horizontal density gradients. Whilst periodic tidal solutions to Equations 5.1 and 5.2 are sought, the results in Section 5.2.1 show that the nature of the tidal flow varies across Nares Strait, with different dynamics and terms from Equations 5.1 and 5.2 dominating at different locations. Consequently, it is necessary to derive separate models for either side of the strait.

2D Eddy Viscosity Model Derivation

Against Greenland (i.e. at KS10, KS12 and KS14) the results in Figures 5.1, 5.2, and 5.3 show that the tides have both oscillatory and rotational aspects (i.e. the semi-minor axis is not zero and facilitates an across-strait flow; a 2D flow), and thus all terms in Equations 5.1 and 5.2 must be retained. In a manner similar to the harmonic analysis, both the two dimensional tidally-varying u and v velocity components and the $\partial\eta/\partial x$ and $\partial\eta/\partial y$ sea surface slope gradients can be combined into complex tidal vectors, and can thus be written as the sum of two independent counter-rotating components:

$$\mathbf{R} = u + iv = \mathbf{R}^{+}e^{i\omega t} + \mathbf{R}^{-}e^{-i\omega t}, \tag{5.3}$$

$$\mathbf{S} = \frac{\partial\eta}{\partial x} + i\frac{\partial\eta}{\partial y} = \mathbf{S}^{+}e^{i\omega t} + \mathbf{S}^{-}e^{-i\omega t}. \tag{5.4}$$

Multiplying Equation 5.2 by i and adopting the eddy viscosity stress model

$$\begin{aligned} \tau_{xz} &= \rho\nu_{xz}\frac{\partial u}{\partial z}, \\ \tau_{yz} &= \rho\nu_{yz}\frac{\partial v}{\partial z}, \end{aligned} \tag{5.5}$$

where ν is the eddy viscosity gives:

$$i\frac{\partial v}{\partial t} + ifu = \frac{\partial}{\partial z}\left(i\nu_{yz}\frac{\partial v}{\partial z}\right) - ig\frac{\partial \eta}{\partial y}. \tag{5.6}$$

The eddy viscosity stress model is a parameterisation of the vertical momentum transfer that occurs due to the turbulence generated by the frictional stresses exerted on the seabed (*Sverdrup et al.*, 1942). It is analogous to the transfer of momentum by the molecular viscosity in a laminar flow, but is orders of magnitude larger and takes place over a much greater depth scale. It assumes that the turbulence consists of many different eddies of many different sizes which are continuously forming and dissipating, and the associated Reynolds stresses are proportional to the mean velocity gradient. The combined effect of these turbulent eddies is responsible for the dispersive tendency of turbulence and its mixing of fluid properties, as well as the dissipation of energy as the kinetic energy in the smallest eddies is converted into heat (*Simpson and Sharples*, 2012).

Assuming that $\nu_{xz} = \nu_{yz} = \nu$ and adopting the decompositions given in Equation 5.3 and 5.4, Equation 5.1 can be added to Equation 5.6 to give:

$$\begin{aligned}
\left(i\frac{\partial v}{\partial t} + \frac{\partial u}{\partial t}\right) + (ifu - fv) &= \left(\frac{\partial}{\partial z}\left[i\nu\frac{\partial v}{\partial z}\right] + \frac{\partial}{\partial z}\left[\nu\frac{\partial u}{\partial z}\right]\right) - \left(ig\frac{\partial \eta}{\partial y} - g\frac{\partial \eta}{\partial x}\right), \\
\frac{\partial}{\partial t}(u+iv) + if(u+iv) &= \frac{\partial}{\partial z}\left(\nu\frac{\partial}{\partial z}[u+iv]\right) - g\left(\frac{\partial \eta}{\partial x} + i\frac{\partial \eta}{\partial y}\right), \\
\frac{\partial \mathbf{R}}{\partial t} + if\mathbf{R} &= \frac{\partial}{\partial z}\left(\nu\frac{\partial \mathbf{R}}{\partial z}\right) - g\mathbf{S}.
\end{aligned} \tag{5.7}$$

By expanding the complex tidal vectors $\mathbf{R}$ and $\mathbf{S}$ into their independent counter-rotating components (i.e. Equations 5.3 and 5.4), Equation 5.7 can be written as

$$\begin{aligned}
\frac{\partial}{\partial t}(\mathbf{R}^+e^{i\omega t} + \mathbf{R}^-e^{-i\omega t}) + if(\mathbf{R}^+e^{i\omega t} + \mathbf{R}^-e^{-i\omega t}) = \\
\frac{\partial}{\partial z}\left(\nu\frac{\partial}{\partial z}[\mathbf{R}^+e^{i\omega t} + \mathbf{R}^-e^{-i\omega t}]\right) - g(\mathbf{S}^+e^{i\omega t} + \mathbf{S}^-e^{-i\omega t}).
\end{aligned} \tag{5.8}$$

This expression can then be separated into two independent equations for the clockwise

and anticlockwise rotary components of the tidal current by evaluating the time derivative:

$$i\omega\mathbf{R}^{+}e^{i\omega t} - i\omega\mathbf{R}^{-}e^{-i\omega t} + if(\mathbf{R}^{+}e^{i\omega t} + \mathbf{R}^{-}e^{-i\omega t}) = \frac{\partial}{\partial z}\left(\nu\frac{\partial}{\partial z}[\mathbf{R}^{+}e^{i\omega t} + \mathbf{R}^{-}e^{-i\omega t}]\right) - g(\mathbf{S}^{+}e^{i\omega t} + \mathbf{S}^{-}e^{-i\omega t}), \quad (5.9)$$

and dividing by the complex exponential rotating elements to give:

$$\text{anticlockwise} : i(f+\omega)\boldsymbol{R}^{+} = \frac{\partial}{\partial z}\left(\nu\frac{\partial \boldsymbol{R}^{+}}{\partial z}\right) - g\boldsymbol{S}^{+}, \quad (5.10)$$

$$\text{clockwise} : i(f-\omega)\boldsymbol{R}^{-} = \frac{\partial}{\partial z}\left(\nu\frac{\partial \boldsymbol{R}^{-}}{\partial z}\right) - g\boldsymbol{S}^{-}. \quad (5.11)$$

By decomposing the rotary components into a contribution from an interior ($\mathbf{R}^{\pm}_{\mathbf{I}}$) and boundary layer ($\mathbf{R}^{\pm}_{\mathbf{BL}}$) part, such that $\mathbf{R}^{\pm} = \mathbf{R}^{\pm}_{\mathbf{I}} + \mathbf{R}^{\pm}_{\mathbf{BL}}$, and by defining the free stream interior velocity in the limit of no friction as:

$$\mathbf{R}^{\pm}_{\mathbf{I}} = \frac{ig\boldsymbol{S}^{\pm}}{(f \pm \omega)}, \quad (5.12)$$

then the sea surface slope gradient terms can be eliminated by substituting

$$-g\boldsymbol{S}^{\pm} = i(f \pm \omega)\mathbf{R}^{\pm}_{\mathbf{I}} \quad (5.13)$$

into Equations 5.10 and 5.11:

$$i(f \pm \omega)(\mathbf{R}^{\pm}_{\mathbf{I}} + \mathbf{R}^{\pm}_{\mathbf{BL}}) = \frac{\partial}{\partial z}\left(\nu\frac{\partial \mathbf{R}^{\pm}}{\partial z}\right) + i(f \pm \omega)\mathbf{R}^{\pm}_{\mathbf{I}}. \quad (5.14)$$

Finally, by subtracting $i(f \pm \omega)\mathbf{R}^{\pm}_{\mathbf{I}}$ from both sides of Equation 5.14, and by rewriting $\mathbf{R}^{\pm}_{\mathbf{BL}}$ as $\mathbf{R}^{\pm} - \mathbf{R}^{\pm}_{\mathbf{I}}$, a familiar Ekman problem second order differential equation for the magnitude of the positive and negative rotary components of the tidal ellipse at KS10, KS12, and KS14 can be formed:

$$\frac{\partial}{\partial z}\left(\nu\frac{\partial \mathbf{R}^{\pm}}{\partial z}\right) - i(f \pm \omega)(\mathbf{R}^{\pm} - \mathbf{R}^{\pm}_{\mathbf{I}}) = 0. \quad (5.15)$$

1D Eddy Viscosity Model Derivation

In contrast to the Greenland side of Nares Strait, Figures 5.1, 5.2 and 5.3 show that the tidal current against the coast of Ellesmere Island is highly rectilinear (due to the requirement of no normal flow through the coast of Ellesmere Island), and thus the flow is primarily oscillatory in nature (i.e. a 1D flow). There is little across-strait flow associated with a fattening of the tidal ellipse, and whilst there is an across-strait flow associated with the rotation of the tidal ellipse away from the along-strait direction, a significant proportion of this motion becomes vertically orientated due to the steeply sloping bathymetry. Therefore, if it is assumed that the u and v velocity components are aligned with the along-strait and across-strait directions, respectively, then compared to the Greenland side of Nares Strait, the v velocity component can essentially be set to zero, and Equations 5.1 and 5.2 reduce to

$$\frac{\partial u}{\partial t} = \frac{1}{\rho}\frac{\partial \tau_{xz}}{\partial z} - g\frac{\partial \eta}{\partial x}, \tag{5.16}$$

$$fu = -g\frac{\partial \eta}{\partial y}. \tag{5.17}$$

By adopting the eddy viscosity stress model (Equation 5.5), and by substituting the following expressions for a one-dimensionally varying tidal velocity and surface pressure gradient into Equation 5.16:

$$u = u_0 e^{i\omega t}, \tag{5.18}$$

$$\eta = \eta_0 e^{i\omega t}, \tag{5.19}$$

where u_0 and η_0 are the amplitudes of u and η, respectively, Equation 5.16 can be written as

$$i\omega u_0 = \frac{\partial}{\partial z}\left(\nu\frac{\partial u_0}{\partial z}\right) - g\frac{\partial \eta_0}{\partial x}, \tag{5.20}$$

where the time derivative has been evaluated and the result divided by $e^{i\omega t}$. Similar to the 2D derivation above, if u_0 is defined as the sum of an interior and boundary layer part

($u_0 = u_I + u_{BL}$), and in the limit of no friction u_I is set equal to

$$u_I = \frac{ig}{\omega}\frac{\partial \eta_0}{\partial x}, \tag{5.21}$$

then the sea surface slope term in Equation 5.20 can be eliminated, and an Ekman problem second order differential equation for the magnitude of the along stream tidal velocity at KS02 can be formed:

$$\frac{\partial}{\partial z}\left(\nu\frac{\partial u_0}{\partial z}\right) - i\omega(u_0 - u_I) = 0 \tag{5.22}$$

To make comparisons between Equations 5.22 and 5.15 easier, it can be assumed for a tidal current in Nares Strait that the amplitude of the along stream velocity (u_0) is analogous to the amplitude of the semi-major axis of the tidal ellipse, which for a rectilinear tidal current is itself equal to the sum of two equal counter-rotating circular components (i.e. $u_0 = |\mathbf{R}^+| + |\mathbf{R}^-|$ where $|\mathbf{R}^+| = |\mathbf{R}^-|$). In this sense, Equation 5.22 can also be separated into two independent equations for the clockwise and anticlockwise rotary components of the tidal current, and written as:

$$\frac{\partial}{\partial z}\left(\nu\frac{\partial \mathbf{R}^{\pm}}{\partial z}\right) - i\omega(\mathbf{R}^{\pm}_{\mathbf{BL}} - \mathbf{R}^{\pm}_{\mathbf{I}}) = 0. \tag{5.23}$$

Whilst the form of Equation 5.23 looks almost identical to that of Equation 5.15, it will be shown that the lack of an f term in Equation 5.23 results in the tides exhibiting a very different vertical structure against the coast of Ellesmere Island.

Eddy Viscosity Profile

In these simple boundary layer models, the vertical structure of the tides is dependent upon three unknowns. These are: (1) the prescribed vertical profile of the eddy viscosity (ν) that is consistent with the underlying physics, (2) the constant, "free stream" interior velocity for the clockwise rotary component ($\mathbf{R}^-$), and (3) the constant, "free stream" interior velocity for the anticlockwise ($\mathbf{R}^+$) rotary component. To determine these three unknowns, and to thus elucidate the important dynamics behind the vertical structure of the tides, the solutions to Equations 5.15 and 5.23 for a prescribed eddy viscosity profile

are iteratively fitted to the observed vertical structure of the major tidal constituents. The solutions are fitted using Matlab's Global Optimisation routines to minimise the combined root-mean-square error (RMSE) of both the clockwise and anticlockwise rotary components:

$$\text{RMSE} = \sqrt{\left[\sqrt{\frac{1}{n}\sum_{z=1}^{n}\left(\hat{\boldsymbol{R}}^{+}_{(z)} - \boldsymbol{R}^{+}_{(z)}\right)^2}\right]^2 + \left[\sqrt{\frac{1}{n}\sum_{z=1}^{n}\left(\hat{\boldsymbol{R}}^{-}_{(z)} - \boldsymbol{R}^{-}_{(z)}\right)^2}\right]^2} \tag{5.24}$$

where $\hat{\boldsymbol{R}}^{+}_{(z)}$ and $\boldsymbol{R}^{+}_{(z)}$ are the modelled and observed values of the anticlockwise rotary component at depths $z = 1, .., n$, respectively, and $\hat{\boldsymbol{R}}^{-}_{(z)}$ and $\boldsymbol{R}^{-}_{(z)}$ are the modelled and observed values of the clockwise rotary component, respectively, at the same depths. The Global Optimisation routine uses the algorithm described by *Ugray et al.* (2007) to ensure that a global minimum in the model solution is found.

Numerous different shapes for the prescribed eddy viscosity profile have been used in the literature to represent different physics and underlying water column structure. For example, *Maas and van Haren* (1987) and *Prandle* (1982a) used a constant eddy viscosity (i.e. $\nu_{(z)} = \nu_0$; Figure 5.8a) that is consistent with a homogeneous water column, and *Madsen* (1977) used a linearly-varying eddy viscosity ($\nu_{(z)} = \kappa u^* z$; where κ is the Von Kármán constant and u^* is the friction velocity; Figure 5.8b) that can represent a strengthening stratification towards the surface. *Shimizu* (2010) used a quadratic profile ($\nu_{(z)} = \kappa u^* z(1 - z/d)$; Figure 5.8c) to remain consistent with the physics associated with modification of the turbulent eddies near the boundaries, and *Howarth* (1998) used a variety of piecewise linear profiles (e.g. Figure 5.8d) to account for complex stratification profiles in the water column. Whilst an increasing level of complexity in the eddy viscosity profile can represent more complex physics, the increasing number of free parameters (Figure 5.8) can result in "over-fitting" between the model and the observed data. Consequently, when modelling the vertical structure of the tides in Nares Strait, the simplest possible eddy viscosity profiles that remain consistent with the underlying physics have been used. In addition, as the eddy viscosity is related to the turbulence generated by the frictional stresses exerted on the seabed by a tidal flow which varies in time and space, the magnitude of the eddy viscosity is also likely to be time- and space-

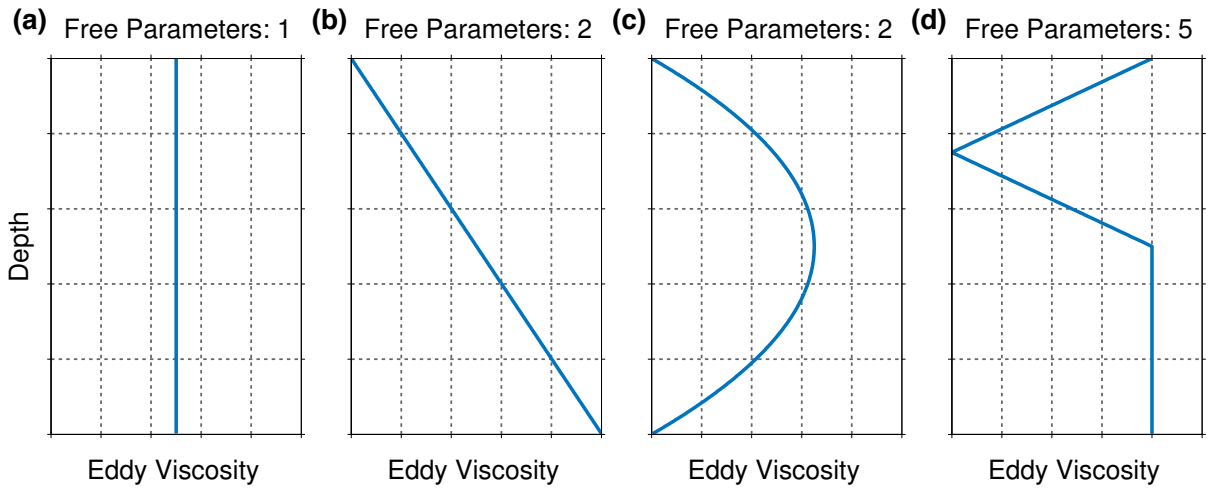

Figure 5.8: Schematic showing the structure of (a) a constant eddy viscosity profile, (b) a linear eddy viscosity profile, (c) a quadratic eddy viscosity profile, and (d) a piecewise linear eddy viscosity profile. All have been used to investigate the vertical structure of tidal currents over continental shelf seas. The number of free parameters required for each profile are indicated in the plot titles.

dependent. Due to the point nature of the models being considered here, however, spatial variations in the eddy viscosity (i.e. in the along-strait direction) have to be ignored, and as the aim of these models is to understand the dynamics behind the time-averaged vertical structure of the tides, it has been assumed that the eddy viscosity is independent of time. Although both *Howarth* (1998) and *Davies* (1990) conclude that the assumption of time independent viscosity does not introduce significant errors in the modelled vertical structure of the semi-diurnal tides at low latitudes, *Lavelle and Mofjeld* (1983) find that time-varying eddy viscosity is important for the generation of higher tidal harmonics (generated through the non-linear interactions of the major tidal constituents). If not accounted for, this can result in the maximum bed stress being underestimated by up to 60%, and the flow profile being distorted near the times of flow reversal. In Nares Strait, where the semi-diurnal tides are in near resonance with the inertial frequency, these effects could be significant and future work should aim to quantify the role they play.

In the following sections, the results of a variety of different solutions to Equations 5.15 and 5.23 that have been iteratively fitted to the average vertical structure of the tides in Nares Strait with various different vertical eddy viscosity profiles are discussed, along with the information they provide on the important dynamics.

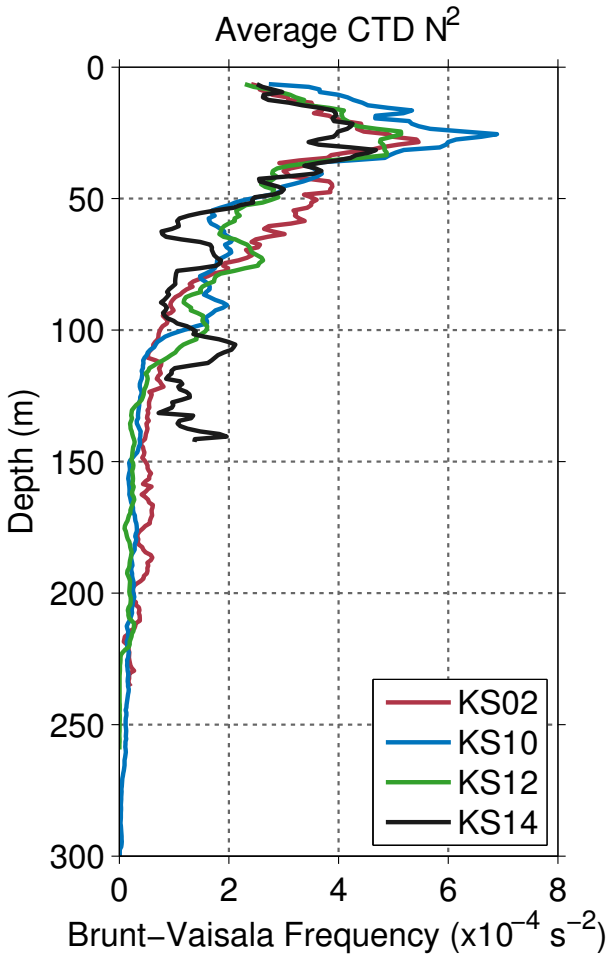

Figure 5.9: Average vertical profiles of the buoyancy frequency at KS02 (red), KS10 (blue), KS12 (green), and KS14 (black), derived from summer CTD casts taken across Nares Strait in 2003, 2007, and 2009. Note that during winter, the formation of sea ice at the surface mixes the water column down to 50-100 m, resulting in a near-zero buoyancy frequency in this region. The peak in maximum buoyancy frequency is therefore likely to be deeper during winter than during summer, and of a reduced magnitude.

Solution: 2D Constant Eddy Viscosity

Figure 5.9 shows the average buoyancy frequency at the locations of the four ADCP moorings derived from the summer CTD sections taken across Nares Strait in 2003, 2007, and 2009. The water column can be predominantly split into two regions: a homogeneous region below a depth of 150 m where there is little stratification, and a highly stratified region above 150 m which is due to the significant quantity of freshwater in the upper layers of Nares Strait. Consequently, the solutions to Equations 5.15 and 5.23 are initially fitted to the observed values of the rotary components from the seabed to a depth of 150 m using a constant eddy viscosity profile.

Focusing on the Greenland side of Nares Strait (i.e. at KS10, KS12 and KS14), the

general solution to Equation 5.15 is

$$\mathbf{R}^{\pm} = Ae^{\frac{(1\pm i)}{\delta^{\pm}}z} + Be^{-\frac{(1\pm i)}{\delta^{\pm}}z}, \tag{5.25}$$

where

$$\delta^{\pm} = \sqrt{\frac{2\nu}{(|f \pm \omega|)}} \tag{5.26}$$

represents the characteristic frictional boundary layer thickness for each of the rotary components, and A and B are determined from the boundary conditions and the prescribed eddy viscosity profile. Due to the total water depth at KS14 being shallower than 150 m, the model was only fitted to the observed data at KS10 and KS12. As there are no dynamical or physical constraints behind each model fit (i.e. the "best-fit" values of the unknown parameters are simply those that minimise the RMSE), each fit has to be carefully considered to ensure that it represents a realistic solution that is consistent with the underlying physics that are expected to be important.

Equations 5.12 and 5.26 show that for each tidal constituent at KS10 and KS12, the interior velocity ($\mathbf{R}_{\mathbf{I}}^{\pm}$) and characteristic frictional boundary layer thickness ($\delta^{\pm}$) for the clockwise and anticlockwise rotary components will scale with $|\omega - f|$ and $|\omega + f|$, respectively, where ω is the frequency of the tidal constituent and f is the Coriolis parameter. In Nares Strait, the average latitude of the mooring array (80°N) is close to the critical latitude of the major semi-diurnal tides (74° 28.30' N for the M2 tide and 85° 45.90' N for the S2 tide), where ω is equal to f. Consequently, $|\omega - f|$ will tend to zero, and the thickness of the boundary layer and interior velocity associated with the clockwise rotary component of the semi-diurnal tides should be at least an order of magnitude greater than that associated with the anticlockwise rotary component (*Furevik and Foldvik*, 1996; *Makinson*, 2002; *Makinson et al.*, 2006). For the diurnal tides in Nares Strait, f is nearly twice as large as ω, and thus there should be little difference in the interior velocity and boundary layer thickness between the clockwise and anticlockwise rotary components (*Robertson*, 2005). As the underlying physics suggests that the thickness of the anticlockwise boundary layer (δ^{+}) is always going to be equal to or less than the thickness of the clockwise boundary layer (δ^{-}), it is reasonable to assume that a combined boundary layer thickness

(i.e. the height at which the semi-major axis of the tidal ellipse reaches its free stream velocity), can be given by the depth of only the clockwise boundary layer. However, this assumption does not consider the relative sizes of $|\mathbf{R}^+|$ and $|\mathbf{R}^-|$, and instead *Soulsby* (1983) defines a combined boundary layer thickness given by:

$$\delta = \frac{(|\bar{\mathbf{R}}^+|\delta^+ + |\bar{\mathbf{R}}^-|\delta^-)}{(|\bar{\mathbf{R}}^+| + |\bar{\mathbf{R}}^-|)}, \tag{5.27}$$

where $|\bar{\mathbf{R}}^-|$ and $|\bar{\mathbf{R}}^+|$ are the depth averaged magnitudes of the clockwise and anticlockwise rotary components, respectively.

Figure 5.10 shows the results of fitting the solution to Equation 5.15 with a constant eddy viscosity profile to the observed vertical structure of the M2, S2, and K1 constituents between the seabed and a depth of 150 m at KS10 and KS12. At the seabed, a no-slip boundary condition is used, whilst the upper boundary condition is defined as the observed magnitude of the rotary components at a depth of 150 m. At each ADCP and for each tidal constituent, the solution was fitted using matrix inversion to determine the values of A and B in Equation 5.25. The uncertainty in each of the unknown parameters has been calculated by changing the depth range of the model fit by up to ± 24 m in 8 m increments (i.e. the depth of each ADCP velocity bin) and taking the standard deviation of the best fit parameters from each individual fit.

Across all ADCPs and tidal constituents, the maximum RMSE is only 0.7 ± 0.2 cm s^{-1}, and the uncertainty in the unknown parameters is small (except for $\mathbf{R_I^-}$ associated with the semi-diurnal constituents, which will be discussed in more detail later). In agreement with the underlying physics discussed above, the model has predicted nearly identical interior velocities for each of the rotary components associated with the diurnal constituent (K1), whereas for the semi-diurnal constituents (M2 and S2), the predicted interior velocity for the anticlockwise rotary component is an order of magnitude smaller than that of the clockwise rotary component (despite the greater uncertainty in the latter). Coupled with the fact that the eddy viscosity predicted by each of the model fits is essentially identical, this suggests that the best fit parameters represent realistic solutions for the vertical structure of the tides in Nares Strait.

Based on the average eddy viscosity of 0.06 m^2 s^{-1} at both KS10 and KS12, Table

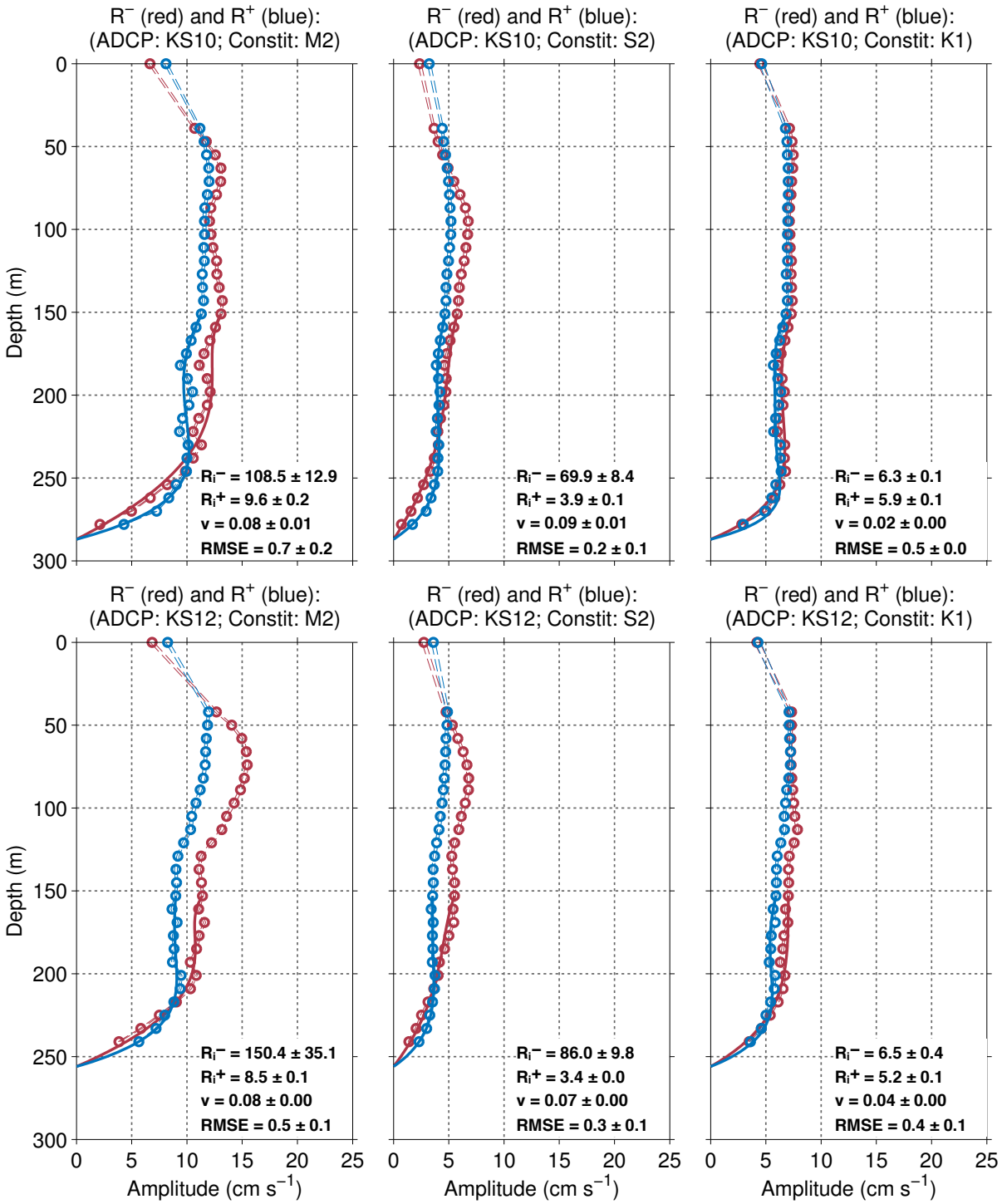

Figure 5.10: Modelled vertical structure of the clockwise ($\mathbf{R}^-$; red) and anticlockwise ($\mathbf{R}^+$; blue) rotary components predicted by using matrix inversion to fit the solution of Equation 5.15 with a constant eddy viscosity profile to the observed vertical structure of the M2 (left), S2 (middle), and K1 (right) constituents between the seabed and 150 m at KS10 (top) and KS12 (bottom). The solid lines are the model fit, whilst the hollow circles are the observed data. A no-slip boundary condition is used at the seabed, and the upper boundary condition is the observed magnitude of the rotary component at a depth of 150 m. The dashed lines indicate the 95 percent confidence interval for each data point. The best fit values of the unknown variables in the model fit are indicated in each plot, along with their uncertainties. An uncertainty of zero indicates that there is no uncertainty in the unknown variable to the reported precision. The units for the interior velocities ($\mathbf{R}_\mathbf{I}^-$ and $\mathbf{R}_\mathbf{I}^+$) and RMSE are cm s^{-1}, and the units for the eddy viscosity (ν) are m^2 s^{-1}.

	ADCP					
	KS10			KS12		
Tidal Constituent	δ^-	δ^+	δ	δ^-	δ^+	δ
M2	192	21	109	192	21	114
S2	268	20	149	268	20	159
K1	41	24	33	41	24	33

Table 5.1: Characteristic thickness in meters of the clockwise (δ^-), anticlockwise (δ^+), and combined (δ) frictional boundary layer associated with the M2, S2, and K1 tidal constituents at KS10 and KS12. The thickness of the clockwise and anticlockwise boundary layer was calculated through Equation 5.26 using the average eddy viscosity of 0.06 m^2 s^{-1} at both ADCPs. The combined boundary layer thickness was calculated through Equation 5.27.

5.1 shows the thickness of the boundary layer associated with the clockwise (δ^-) and anticlockwise (δ^+) rotary components of each tidal constituent at each ADCP, along with the combined boundary layer thickness (δ). For the K1 constituent at both KS10 and KS12, the thickness of the boundary layers associated with the clockwise and anticlockwise rotary components are ≈41 m and ≈24 m, respectively, resulting in a combined boundary layer thickness of ≈33 m. This suggests that the K1 tidal current reaches its free stream velocity within ≈33 m of the seabed, and the majority of the water column is unaffected by boundary layer dynamics. It is the existence of only these thin boundary layers that explains the observed barotropic nature of the K1 constituent at these ADCPs; even during landfast ice periods when a second under-ice boundary layer will extend downwards into the water column, it is unlikely that the boundary layer will extend deep enough to radically change the barotropic nature of the tidal current.

In contrast, for the M2 and S2 constituents, the proximity of the mooring array to the semi-diurnal critical latitude means that the boundary layer associated with the clockwise rotary component is an order of magnitude thicker than that associated with the anticlockwise rotary component. For example, for the M2 constituent at KS10, the boundary layer associated with the clockwise rotary component is ≈192 m thick, compared to only ≈21 m for the anticlockwise rotary component. The combined boundary layer thickness for the M2 and S2 tidal constituents at KS10 and KS12 ranges between 100 m and 160 m. As a result, a significant proportion of the water column at these ADCPs is affected by

the boundary layer, and this explains why the semi-diurnal tides are significantly less barotropic than the diurnal tides.

As the sense of rotation of the tidal current vector is determined by the difference in the amplitude of the positive and negative rotary components (i.e. Equation 4.7), it is the differing boundary layer thickness and interior velocity associated with each of the rotary components that explains the variability in the rotation of the tidal current vector between the different tidal constituents (Figure 5.1). For the K1 constituent, the boundary layer thickness and interior velocity associated with each of the rotary components are essentially identical, and thus the amplitude of the rotary components are equal throughout the water column. Consequently, the semi-minor axis is close to zero everywhere, and the tidal current is rectilinear. In contrast, for the M2 and S2 constituents, the much thicker clockwise boundary layer and greater interior velocity mean that the strength of the shear at the seabed associated with the clockwise rotary component (red line in Figure 5.10) is less than that associated with the anticlockwise rotary component (blue line in Figure 5.10), but extends higher into the water column. Therefore near the seabed, $|\mathbf{R}^+|$ is greater than $|\mathbf{R}^-|$, and the semi-diurnal tides exhibit anticlockwise rotation (positive semi-minor axis). However, higher in the water column, $|\mathbf{R}^-|$ becomes greater than $|\mathbf{R}^+|$, and the sense of rotation changes to clockwise (negative semi-minor axis).

As stated earlier, the uncertainty in the best fit parameters is small except for the interior velocity associated with the clockwise rotary component of the semi-diurnal tides. For example, when the depth below the surface to which the model is fitted is changed from 177 m to 129 m, the predicted interior velocity for the M2 clockwise rotary component at KS12 increases from 120.7 cm s^{-1} to 223.2 cm s^{-1}. As this uncertainty is not reflected in the positive rotary component, or in either of the rotary components associated with the K1 tide, it suggests that when the depth to which the model is fitted is less than the thickness of the boundary layer (the boundary layer associated with the semi-diurnal clockwise rotary component is ≈200 m thick at KS10 and KS12, whilst the model fits only cover the bottom 136 m at KS10 and the bottom 103 m at KS12), the clockwise interior velocity is sensitive to the boundary condition. To try to constrain the value of

the interior velocity further, Equation 5.12 can be used to calculate the value directly from the sea surface gradients (i.e. $\partial\eta/\partial x$ and $\partial\eta/\partial y$) in the TPXO8 tidal model. In this case, the value of the clockwise interior velocity is 172 ± 39 cm s^{-1} and 155 ± 36 cm s^{-1} for the M2 and S2 constituents, respectively, greater than that predicted by the model fits. However, there is still significant uncertainty associated with calculating the sea surface gradients over different spatial scales.

To confirm that the sensitivity of the clockwise interior velocity to the specified boundary condition has not affected the estimates of the eddy viscosity and the anticlockwise interior velocity, the solution to Equation 5.15 with a constant eddy viscosity profile was fitted to only the observed vertical structure of the anticlockwise rotary component. As Table 5.1 suggests that the anticlockwise component obtains its free stream velocity within ≈20-25 m of the sea bed, an analytical solution to Equation 5.15 with a zero stress upper boundary condition can be used (i.e. $\mathbf{R}^{\pm} \rightarrow \mathbf{R}_{\mathbf{I}}^{\pm}$ as $z \rightarrow \infty$):

$$\mathbf{R}^{\pm} = \mathbf{R}_{\mathbf{I}}^{\pm}(1 - e^{-A^{\pm}z}), \tag{5.28}$$

where

$$A^{\pm} = \frac{(1 \pm i)}{\delta^{\pm}}, \tag{5.29}$$

and $\delta^{\pm}$ is defined in Equation 5.26. Figure 5.11 shows that within the uncertainty, the best fit values of the eddy viscosity and the anticlockwise interior velocity are identical to those in Figure 5.10, and thus they appear to have been unaffected by the uncertainty in the clockwise interior velocity.

Solution: 1D Constant Eddy Viscosity

In comparison with the general solution of Equation 5.15 at KS10 and KS12 (i.e. Equation 5.25), the general solution to Equation 5.23 with a constant eddy viscosity profile that is applicable for the vertical structure of the tides at KS02 is almost identical:

$$\mathbf{R}^{\pm} = Ce^{\frac{(1\pm i)}{\delta^{\pm}}z} + De^{-\frac{(1\pm i)}{\delta^{\pm}}z}, \tag{5.30}$$

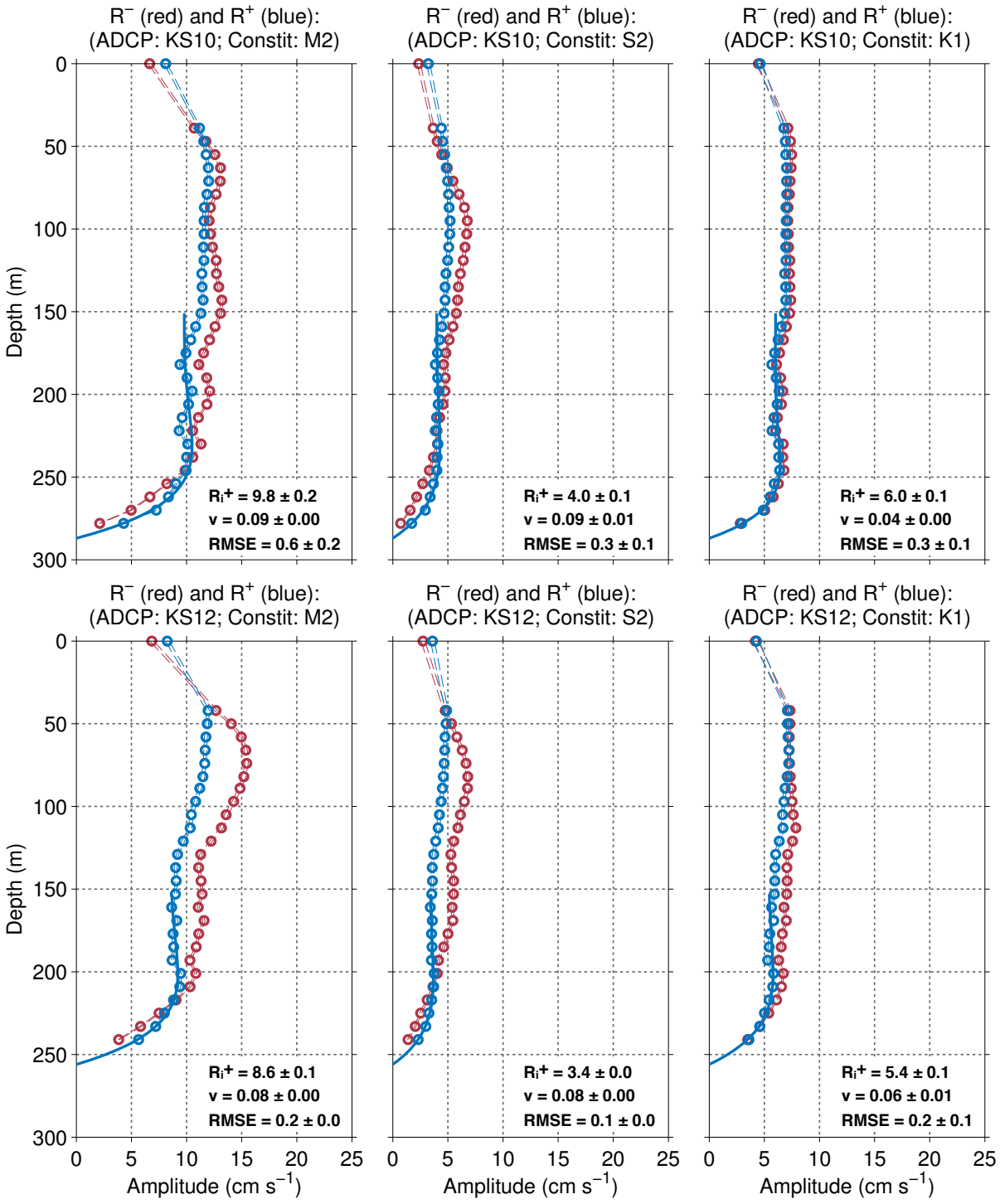

Figure 5.11: Modelled vertical structure of the anticlockwise ($\mathbf{R}^+$; blue) rotary component predicted by fitting an analytical solution to Equation 5.15 with a constant eddy viscosity profile and a free-slip upper boundary condition to the observed vertical structure of the M2 (left), S2 (middle), and K1 (right) constituents between the seabed and 150 m at KS10 (top) and KS12 (bottom). The solid line is the model fit, whilst the hollow circles are the observed data. A no-slip boundary condition is used at the seabed. The dashed lines indicate the 95 percent confidence interval for each data point. The best fit values of the unknown variables in the model fit are indicated in each plot, along with their uncertainties. An uncertainty of zero indicates that there is no uncertainty in the unknown variable to the reported precision. The units for the interior velocity ($\mathbf{R}_\mathbf{I}^+$) and RMSE are cm s^{-1}, and the units for the eddy viscosity (ν) are m^2 s^{-1}.

except that the characteristic frictional boundary layer thickness and interior velocity for each of the rotary components scale only with the tidal frequency rather than with the sum or difference between the tidal frequency and the Coriolis parameter (i.e. ω compared to $|\omega \pm f|$):

$$\delta^{\pm} = \sqrt{\frac{2\nu}{\omega}}, \qquad \text{and} \qquad u_I = \frac{ig}{\omega}\frac{\partial \eta_0}{\partial x}. \tag{5.31}$$

This suggests that the boundary layer thickness and interior velocity of the rotary components associated with each tidal constituent will be exactly equal, and it is the requirement of no normal flow through the coast of Ellesmere Island that is constraining the diurnal and semi-diurnal tides to exhibit the same vertical structure (albeit with different amplitudes).

To test whether this is the case, the solution to Equation 5.23 with a constant eddy viscosity profile was fitted to the observed vertical structure of the M2, S2 and K1 constituents between the seabed and a depth of 150 m at KS02. Similar to the 2D model fits described above, the solutions were fitted using matrix inversion to determine the values of C and D in Equation 5.30, and the two boundary conditions are no-slip at the bed and the observed value of the rotary components at a depth of 150 m. Again, the uncertainty in each of the unknown parameters was calculated by changing the depth range of the model fit by up to $\pm$24 m in 8 m increments.

As expected, Figure 5.12 shows that for all three tidal constituents, the amplitude of the interior velocity predicted by the model fit for both the clockwise and anticlockwise rotary components are identical to within the level of uncertainty. The maximum RMSE is 0.6 ± 0.1 cm s^{-1}, and the predicted eddy viscosities for each tidal constituent are similar. Overall this suggests that the model fits in Figure 5.12 do represent realistic solutions for the vertical structure of the tides at KS02, and, as stated above, it is the requirement of no normal flow through the coast of Ellesmere Island that dominates the dynamics, and constrains the tidal constituents to all exhibit the same vertical structure. It must be noted, however, that the uncertainty in the best fit parameters is slightly larger than that at KS10 and KS12, and the eddy viscosities are an order of magnitude greater. This lack of consistency in the eddy viscosities and the greater uncertainties do cast a little doubt upon the quality of the fit at KS02. On the other hand, it may simply reflect the proximity

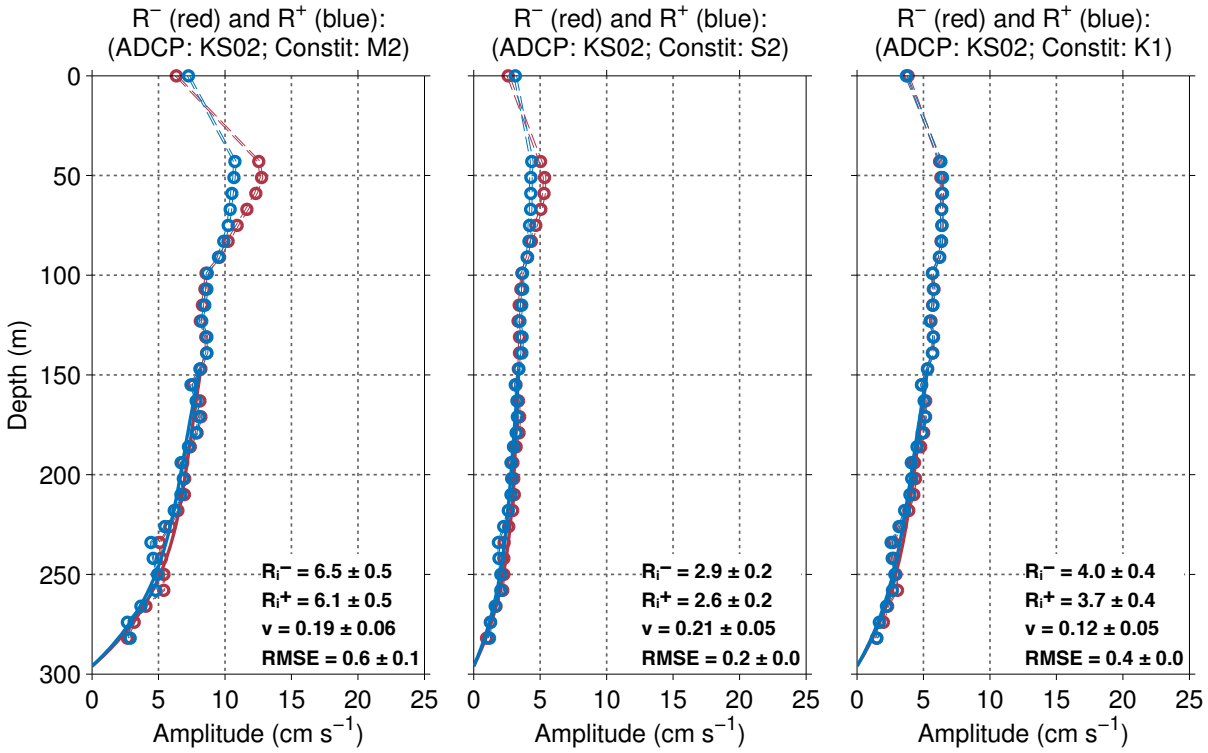

Figure 5.12: Modelled vertical structure of the clockwise ($\mathbf{R}^-$; red) and anticlockwise ($\mathbf{R}^+$; blue) rotary components predicted by using matrix inversion to fit the solution of Equation 5.22 with a constant eddy viscosity profile to the observed vertical structure of the M2 (left), S2 (middle), and K1 (right) constituents between the seabed and 150 m at KS02. The solid lines are the model fit, whilst the hollow circles are the observed data. A no-slip boundary condition is used at the seabed, and the upper boundary condition is the observed magnitude of the rotary component at a depth of 150 m. The dashed lines indicate the 95 percent confidence interval for each data point. The best fit values of the unknown variables in the model fit are indicated in each plot, along with their uncertainties. An uncertainty of zero indicates that there is no uncertainty in the unknown variable to the reported precision. The units for the interior velocities ($\mathbf{R}_\mathbf{I}^-$ and $\mathbf{R}_\mathbf{I}^+$) and RMSE are cm s^{-1}, and the units for the eddy viscosity (ν) are m^2 s^{-1}.

of the ADCP to the coast of Ellesmere Island, where the steeply sloping bathymetry is generating secondary dynamics that cannot be replicated in these simple boundary layer models (which assume the existence of a flat bottom). This is supported by the fact that the combined boundary layer thickness for each tidal constituent predicted by the model fits range between ≈50 m and ≈70 m (based on an average eddy viscosity of 0.17 m^2 s^{-1}), whereas by examining Figure 5.12 it is clear that there is shear present in the water column above these depths. It is possible that although the requirement of no normal flow through the coast of Ellesmere Island is the primary control on the vertical structure, the location of KS02 means that it sits within a lateral sidewall boundary layer, and the extra turbulence generated by the lateral shear is creating a thicker boundary layer than

that which would arise simply from bottom-generated turbulence. As the physics of lateral shear are not contained within the 1D model, the extra turbulence is manifested through larger eddy viscosities and greater uncertainty in the interior velocities.

Solution: Linear Eddy Viscosity

Up to this point, the use of a constant eddy viscosity profile has meant that the region of the water column over which the simple boundary layer models can be fitted has been restricted to the homogeneous region below 150 m. However, numerous studies have shown that the vertical structure of tidal currents are strongly effected by stratification, especially near the semi-diurnal critical latitude (e.g. *Prinsenberg and Bennett*, 1989; *Howarth*, 1998; *Makinson*, 2002; *Makinson et al.*, 2006). Given the region of strong stratification near the surface in Nares Strait, it is therefore important to fit the simple boundary layer models discussed above to the observed vertical structure of the tides over the entire water column to determine the role played by the stratification in the vertical structure of the tides.

Stratification acts to suppress the turbulent eddies generated by the frictional stresses exerted on the boundaries by the strong tidal flows, and thus inhibits the turbulent transfer of momentum into the interior. Consequently, the value of the eddy viscosity is reduced in regions of strong stratification, and boundary layers that extend into the stratification should therefore be thinner (*Souza and Simpson*, 1996). The solutions to Equations 5.25 and 5.30 with two different vertical eddy viscosity profiles that accounted for the strong stratification in the upper water column (i.e. a linearly decreasing profile and a piecewise linear profile; Figure 5.8) were fitted to the vertical structure of the major tidal constituents throughout the water column. Unfortunately, neither profile resulted in a realistic solution that could adequately reproduce the observed vertical structure. In the case of the linearly decreasing profile, the modelled vertical structure of the rotary components was significantly different compared to the observations, and the values of the best fit parameters predicted by the models were not consistent with the underlying physics (for example, for the M2 constituent at KS10, the amplitude of $\mathbf{R_I^-}$ was predicted to be nearly equal to the amplitude of $\mathbf{R_I^+}$). With the piecewise linear profile, the large

number of free parameters resulted in the "over-fitting" of an unrealistic solution. Taken together, this suggests that the vertical structure of the tides in the upper water column of Nares Strait are too complex for these simple boundary layer models, and instead a full turbulence closure model (such as those used by *Makinson et al.*, 2006 or *Simpson and Tinker*, 2009) will be needed to model the tides in this region. In these types of models, the vertical profile of the eddy viscosity is not defined a priori, but instead is calculated as a function of the flow properties themselves (e.g. the stratification, velocity shear etc.).

Despite being unable to model the vertical structure of the tides throughout the entire water column, it is still possible to speculate about the important role that stratification is playing in determining the vertical structure of the tides in Nares Strait. The amplification in the semi-major axis of the M2 and S2 tidal ellipses above 150 m in Figure 5.1 coincides with the depth range of maximum stratification (Figure 5.9), and appears to be associated primarily with an amplification in the clockwise rotary component (Figure 5.10). The amplification is consistent with the model and observational results of *Makinson* (2002) and *Makinson et al.* (2006), who show that the strong stratification beneath the Filchner-Ronne Ice Shelf in Antarctica during late summer results in a two- to threefold increase in the amplitude of the semi-diurnal tidal currents compared to mid-winter homogeneous conditions. Their results suggest that the strong stratification allows the water column in the region of the pycnocline to become decoupled from both the benthic and under-ice boundary layers, and thus the amplitude of the tidal current to increase significantly as it tends towards or obtains its free stream velocity. Furthermore, the fact that the amplification is restricted primarily to the clockwise rotary component is consistent with the boundary layer theory discussed above (i.e. Equation 5.26), which suggests that only the clockwise rotary component of the semi-diurnal tides should be affected by stratification, whilst the anticlockwise rotary component and all diurnal tides (e.g. K1) should remain unaffected (as is generally observed in Figures 5.1 and 5.3). Again, this is consistent with the results of *Makinson* (2002) and *Makinson et al.* (2006), who found that the two- to threefold amplification in the semi-diurnal tidal currents was restricted solely to the anticlockwise rotary component (note southern hemisphere).

Consequently, on the basis of the arguments presented above, there is strong evidence

to suggest that stratification in the upper water column and the proximity of the mooring array to the critical latitude is having a significant impact on the vertical structure of the tides in Nares Strait. The effect that the stratification has in decoupling the water column from the benthic and under-ice boundary layers can explain the upper water column maximum that is observed in the negative rotary component of the semi-diurnal tides, and the lack of amplification in both the K1 tide and the positive rotary component of the semi-diurnal tides is also consistent with this theory. On the other hand, it must be noted that the vertical motion associated with each tidal constituent (Figure 5.6) will result in modifications to the internal pressure field at tidal frequencies. Whilst this won't result in the formation of freely-propagating internal tides due to the proximity of the critical latitude (*Vlasenko et al.*, 2003), it will undoubtedly influence the velocity in the upper water column (where the density gradients are strongest), and may be partly responsible for the upper water column maximum in the tidal current strength.

Summary

In summary, the use of these simple boundary layer models has helped to answer a number of the questions regarding the vertical structure of the tides in Nares Strait that were posed at the end of Section 5.2.1. The observed difference between the broadly barotropic diurnal tides and the highly baroclinic semi-diurnal tides is due to the proximity of the mooring array to the semi-diurnal critical latitude, and thus the order of magnitude thicker semi-diurnal boundary layers (i.e. δ in Table 5.1). Similarly, the lack of rotation in the K1 tide is due to the broadly equal boundary layer thickness associated with each of the rotary components (i.e. $\delta^{\pm}$), whereas the effect of the critical latitude on the thickness of the M2 and S2 clockwise boundary layer (i.e. when $|\omega - f|$ tends to zero), explains the clockwise rotation observed in the mid-water column as well as the tendency towards more anticlockwise rotation at the bed. Against Ellesmere Island, the requirement of no normal flow through the coast is constraining each of the tidal constituents to exhibit the same vertical structure, although it appears that dynamics not included in the simple boundary layer models may also be important. At the surface, there is evidence to suggest that the strong stratification and the proximity of the mooring array to the critical latitude

can explain the upper water column maximum observed in the semi-diurnal tides, as well as why the same amplification is not observed in the diurnal tides (although more complicated turbulence closure models will be needed to test these theories).

5.3 Time-Dependent Vertical Structure

Whilst harmonically analysing the full three-year velocity time series from each depth bin at each ADCP allows the time-averaged vertical structure of the tides in Nares Strait to be determined, it provides no information on how the strength of an individual tidal constituent may change in time. The dynamics in Nares Strait are dominated by the quasi-annual cycle in ice regime (Section 4.1.2; *Rabe et al.*, 2012), that results in the presence of an under-ice no-slip boundary layer during landfast ice periods. To understand how this additional boundary layer, and other processes associated with the quasi-annual cycle in ice regime, may affect the vertical structure of the tides in Nares Strait, each three-year velocity time series from each ADCP depth bin was harmonically demodulated in order to track how the ellipse parameters of the major tidal constituents evolve in time.

5.3.1 Harmonic Demodulation and Inference Ratios

The process of harmonic demodulation involves splitting the original three-year velocity time series from each depth bin at each ADCP into shorter overlapping 31-day segments each separated by a day, and then harmonically analysing the individual segments in order to determine a time series of the ellipse parameters for the major tidal constituents (*Emery and Thomson*, 2004). Due to the shorter length of each individual velocity time series that is harmonically analysed, the subtidal variability was removed prior to the harmonic demodulation by subtracting a 48-hour running average of the data.

As with any frequency analysis method, the length of the time series being analysed determines the number of frequencies that can be resolved (Table 4.2). For example, in the case of harmonic analysis of the tides, a 182-day time series is required to distinguish the P1 constituent from the K1 constituent (the third largest and largest diurnal tidal constituents, respectively) and the K2 constituent from the S2 constituent (the fourth

and second largest semi-diurnal constituents, respectively; *Foreman and Henry*, 1989). As a result, a series of harmonic analyses over shorter periods of data (such as the 31-day segments being used here), would show spurious periodic behaviour in the amplitudes of the K1 and S2 tidal constituents due to the P1 and K2 tidal constituents, with a beat frequency (ω_B) given by

$$\omega_B = \frac{\omega_1 - \omega_2}{2}, \tag{5.32}$$

where ω_1 and ω_2 are the frequencies of the tidal constituents of interest. The effect of this beating between resolved and unresolved tidal constituents in the results of a harmonic demodulation are illustrated in Figure 5.13, which shows (a) the three-year pressure record from KS02, and (b) a time series of the magnitude of the M2 tide obtained through a 31-day harmonic demodulation of this pressure record. There is a clear annual modulation in the amplitude of the M2 tide, along with significant shorter-term variability. It would be easy to interpret the annual modulation as being associated with the quasi-annual cycle in ice conditions (grey line), or any other forcing with a seasonal cycle (red line), such that the amplitude of the M2 tide may appear to be greater during landfast ice periods. However, this is not the case. Instead, the annual modulation is associated with beating between the unresolved H1 and H2 tidal constituents, which have a frequency difference of 0.22816×10^{-3} cph and thus generate an annual cycle in the semi-diurnal tides with a beat period ($1/\omega_B$) of 365.25 days (red line).

In order to remove this spurious periodic behaviour without resorting to a longer time series (in this case at least 365 days), it is necessary to resort to inference ratios. These allow the constituents that cannot be resolved directly during the harmonic demodulation to be determined indirectly from known relationships with constituents which are resolved (*Foreman and Henry*, 1989). The effect of including inference ratios can be seen in Figure 5.13c. The annual modulation observed in the amplitude of the M2 tide has been removed, and as a result the non-physical relationship that appeared between the M2 tide and the changing ice regime has disappeared. Consequently, it is exceedingly important to use accurate inference ratios in a harmonic demodulation of the tides to ensure that any observed variability in the amplitude of a single tidal constituent can be confidently attributed to physical processes.

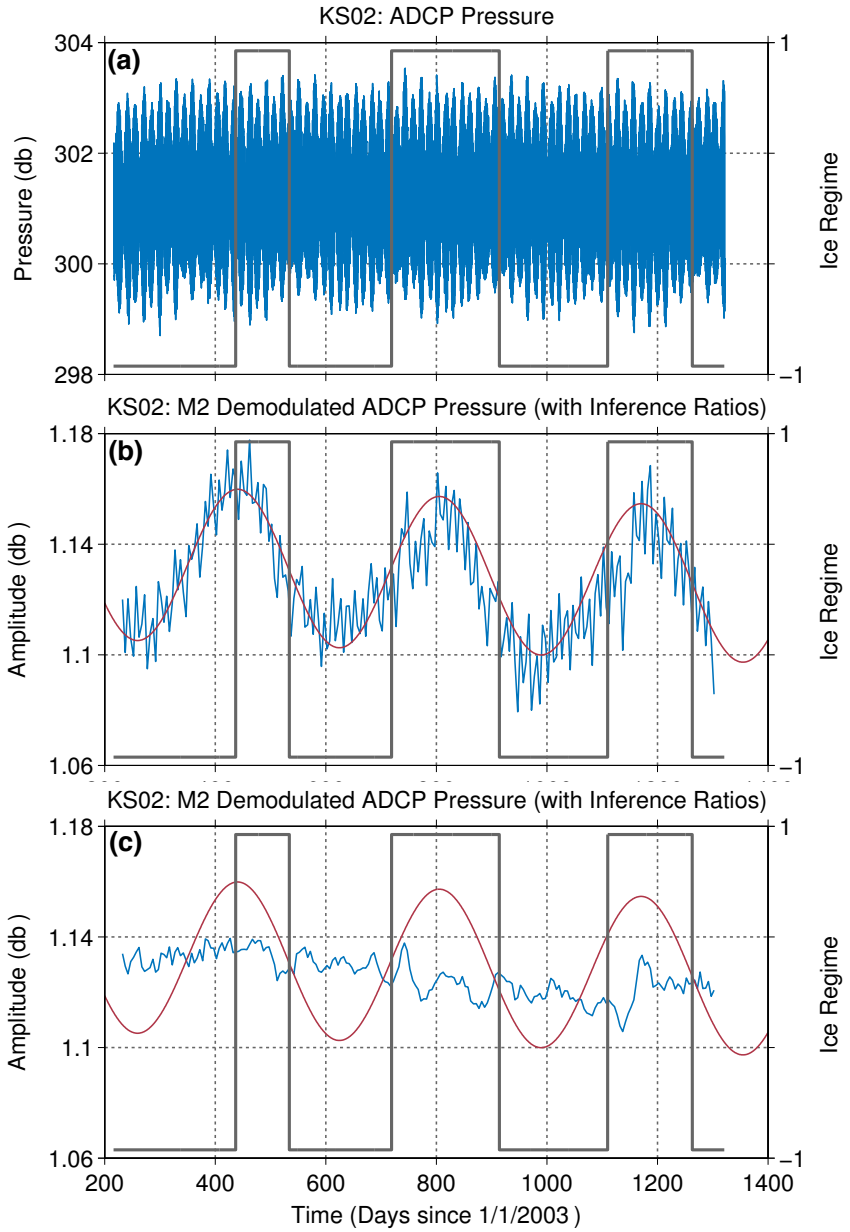

Figure 5.13: Time series of (a) the ADCP pressure at KS02, (b) the amplitude of the M2 tide at KS02 obtained through a 31-day harmonic demodulation of the pressure record, and (c) the amplitude of the M2 tide at KS02 obtained through a 31-day harmonic demodulation of the pressure record with inference ratios. The grey line in (a), (b) and (c) is the quasi-annual cycle in ice regime with positive values representing the landfast ice regime and negative values representing the mobile-ice regime. The red line in (b) and (c) is an annual sinusoid with a slight negative trend.

By definition, an inference ratio consists of an amplitude ratio (F) and phase offset (ζ) between an unresolved constituent and a reference constituent for both the clockwise:

$$F^- = r_I^-/r_R^- \qquad \text{and} \qquad \zeta^- = \phi_R^- - \phi_I^-, \tag{5.33}$$

Reference Constituent	Inferred Constituents
M2	MKS2, H1, H2, GAM2
S2	K2, T2, R2, L2, LDA2
N2	NU2, MU2, 2N2, EPS2
K1	P1, PHI1, S1, PS1

Table 5.2: Details of each tidal constituent that was inferred during the 31-day harmonic demodulation of the tides in Nares Strait, along with their corresponding reference constituent.

and anticlockwise rotary component of the tidal ellipse:

$$F^+ = r_I^+ / r_R^+ \qquad \text{and} \qquad \zeta^+ = \phi_R^+ - \phi_I^+, \tag{5.34}$$

where the subscript $_R$ represents the reference constituent, and the subscript $_I$ represents the inferred constituent. Table 5.2 shows which constituents were inferred during the 31-day harmonic demodulation, along with their corresponding reference constituent. Each inference ratio was calculated from the results of a full three-year harmonic analysis (where, due to the longer time series analysed, the inferred constituents can be included directly), and therefore it has to be assumed that irrespective of any temporal variability in the magnitude of the reference and inferred constituents, the ratio between them remain constant. Due to the highly baroclinic nature of the tides in Nares Strait, it was deemed that a set of inference ratios calculated from the depth-averaged tidal velocity at each ADCP was not able to consistently remove the effect of the unresolved constituents throughout the entire water column, and thus an independent set of inference ratios was calculated for each ADCP depth bin.

5.3.2 Ellipse Parameters

Figures 5.14 and 5.15 show average vertical profiles for each ice regime of the semi-major (red) and semi-minor (blue) axes of the tidal ellipse and the ellipse inclination angle for the major tidal constituents at each ADCP. During landfast ice seasons, the surface value of the major and minor axes of the tidal ellipse has been set to zero (i.e. a no-slip boundary condition at the ice-ocean interface), whilst the ellipse inclination angle

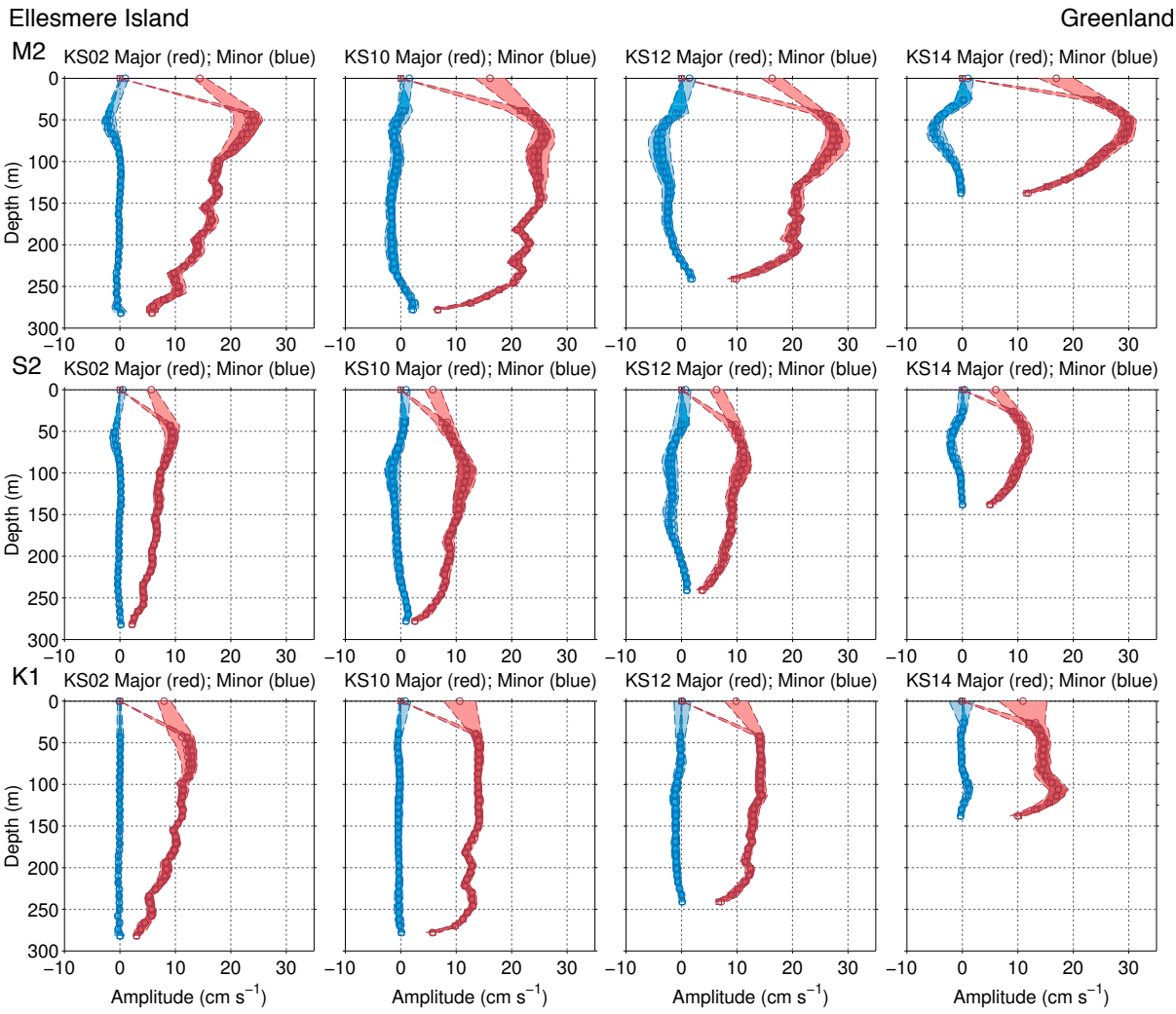

Figure 5.14: Vertical structure of the semi-major (M; red) and semi-minor (m; blue) axes of the tidal ellipse for the M2 (top), S2 (middle), and K1 (bottom) tidal constituents at KS02 (left), KS10 (middle-left), KS12 (middle-right), and KS14 (right) during the mobile (circles) and landfast (squares) ice regimes. The dashed lines represent plus or minus one standard deviation of all the data points included in each profile, and the darker shading indicates where the error bars from the two ice regimes overlap. The circles and squares are hard to distinguish from one another due to the lack of variability in the vertical structure between the two ice regimes.

is undefined. The width of the error bars indicate plus or minus one standard deviation of all the data points included in each average profile.

The results show that there is no difference within the uncertainty between the vertical structure of the tides during landfast and mobile ice seasons, and overall the majority of the water column is unaffected by the second no-slip under-ice boundary layer that exists during landfast ice seasons. Of course, within the upper 30 m, the magnitude of the semi-major axis will tend to zero during the landfast ice regime, but this is unobservable by the ADCPs. Furthermore, the width of the error bars for both the major and minor axes of the tidal ellipse are relatively narrow (Figure 5.14), suggesting that the major tidal

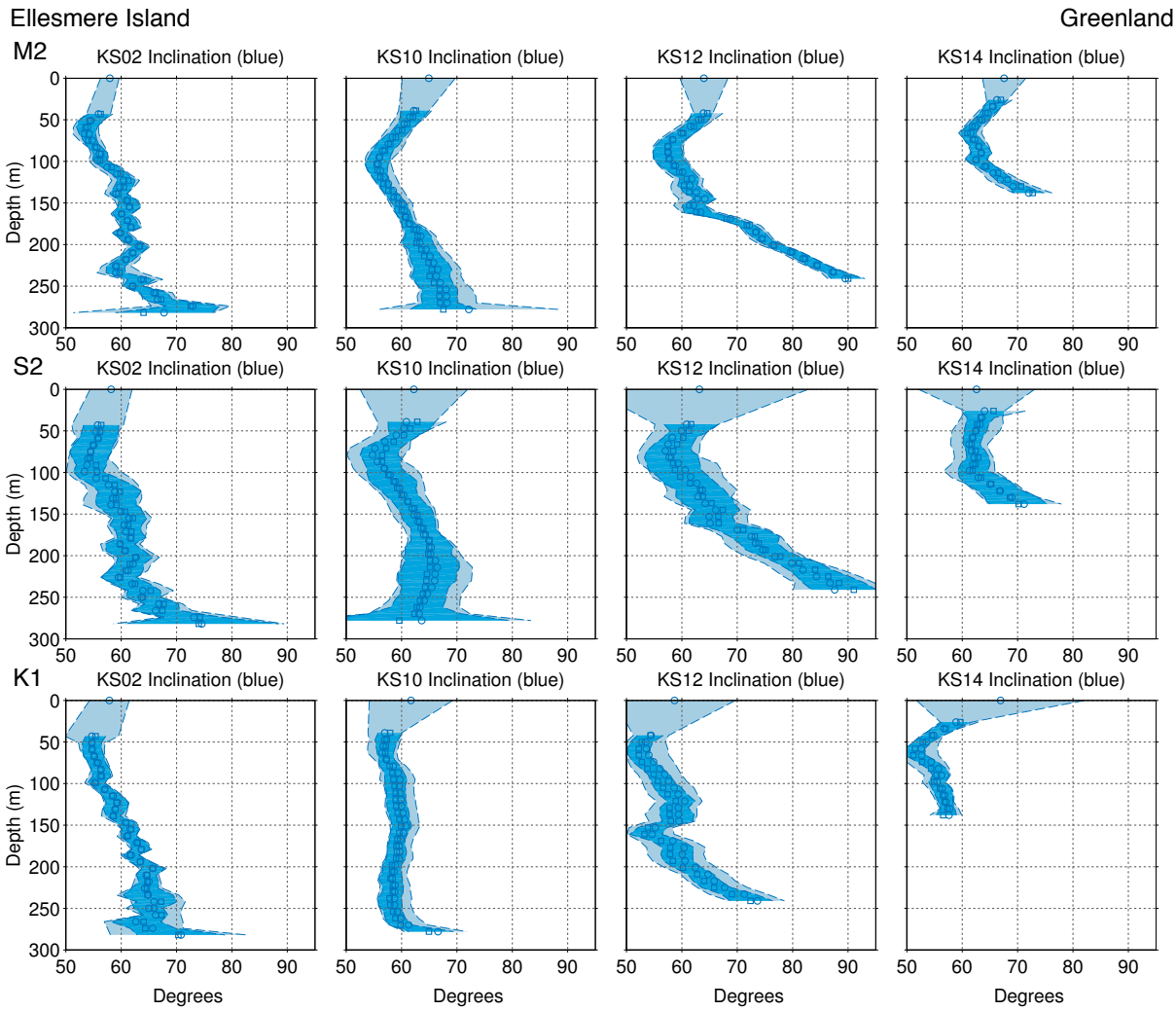

Figure 5.15: Vertical structure of the tidal ellipse inclination angle (θ) for the M2 (top), S2 (middle), and K1 (bottom) tidal constituents at KS02 (left), KS10 (middle-left), KS12 (middle-right), and KS14 (right) during the mobile (circles) and landfast (squares) ice regimes. The dashed lines represent plus or minus one standard deviation of the data points included in each profile, and the darker shading indicates where the error bars from the two ice regimes overlap. It is hard to distinguish the circles and squares from one another due to the lack of variability in the vertical structure between the two ice regimes.

constituents also exhibit little variability on timescales shorter than the quasi-annual cycle in ice regime. This result is somewhat counter-intuitive, and suggests that neither the change in water depth (*Kowalik and Proshutinsky*, 1994), nor the no-slip under-ice boundary layer present during the landfast ice regime have any impact on the vertical structure of the tides. Given the significant depths to which the boundary layer associated with the clockwise rotary component of the semi-diurnal tides should propagate into the water column (Table 5.1), this lends weight to the argument that the strong stratification at the surface is "decoupling" the under-ice boundary layer from the remainder of the water column (as suggested elsewhere in *Prinsenberg and Bennett*, 1989 and *Makinson*,

2002). On the other hand, it must be noted that an empirical orthogonal function analysis of the salinity field in Nares Strait by *Rabe et al.* (2010) has shown that during mobile ice seasons the salinity stratification near the surface is significantly stronger than that during landfast ice seasons. Consequently, if stratification is playing a leading role in determining the vertical structure in the upper water column, greater variation between the different ice regimes might be expected (unless the changes are restricted solely to the region of the water column that is unobservable by the ADCPs).

In terms of the ellipse inclination angle, and thus the dominant direction of the tidal stream, Figure 5.15 again shows that there is no significant difference within the uncertainty between the vertical structure associated with each of the ice regimes. However, as the width of the error bars can be up to 10° (and even greater near the surface), it appears as though the direction of the tidal stream exhibits significant high frequency variability. At the surface, this variability is likely to be associated with either the effect that the strong orographically channelled winds in Nares Strait have on the drift of the sea ice (*Samelson et al.*, 2006; *Samelson and Barbour*, 2008), which is used to determine the properties of the tidal flow at the surface during mobile ice conditions, or variability in the surface Ekman layer associated with the changing boundary condition (i.e. open sea, pack ice in free drift, and pack ice retarded by ice stress). In the interior and near the seabed, it is possible that short-term variations in the internal pressure field associated with upwelling and downwelling on either side of the strait (*Rabe et al.*, 2010), or a gradient in the inverse barometer effect along the strait, may also affect the tidal stream direction. Furthermore, the changing morphology of the sea ice cover may be affecting the tidal stream direction by dampening the tidally driven sea surface pressure gradients to a greater or lesser extent across the width of Nares Strait (although this effect should also be reflected in the magnitude of the tidal currents).

The lack of any significant variability in the vertical structure of the tides between the different ice regimes is further supported by the results in Table 5.3. Here, the best fit parameters obtained from fitting the simple boundary layer models derived in Section 5.2.3 with a constant eddy viscosity profile to the observed vertical structure of the tides between the seabed and a depth of 150 m during both mobile and landfast ice regimes,

are compared with the best fit parameters presented in Figures 5.10 and 5.12. The simple boundary layer models have not been fitted to the vertical structure at KS14 for the reasons discussed earlier. The maximum variability in the best fit parameters between the different ice regimes is only 10% of the value of the best fit parameters obtained from the three-year average vertical structure, and many of the best fit parameters are identical within the uncertainties. Subsequently, when the model fits are plotted together (Figure 5.16), there is no difference within the observational error bars in the predicted vertical structure of the tides during landfast and mobile ice regimes. Of course, these parameters and model fits relate only to the bottom boundary layer, and there is likely to be significant variability in the parameters associated with the presence of a no-slip under-ice boundary layer during the landfast ice regimes.

Table 5.3: Comparison between the best fit parameters predicted by fitting the simple boundary layer models described in Section 5.2.3 to the observed three-year averaged vertical structure of the major tidal constituents between the seabed and a depth of 150 m (i.e. Figures 5.10 and 5.12), and the best fit parameters predicted by fitting the simple boundary layer models to the observed vertical structure of the major tidal constituents during both mobile and landfast ice regimes (i.e. Figure 5.16). The units of the clockwise and anticlockwise interior velocities and the RMSE are cm s^{-1}, and the units of the eddy viscosity are m^2 s^{-1}. The uncertainties have been calculated by changing the depth of the model fit by up to $\pm$24 m, and taking the standard deviation of the best fit parameters from each individual fit. An uncertainty of zero indicates that there is no uncertainty in the best fit parameter to the reported precision

	M2			S2			K1		
	Mobile Ice	**Landfast Ice**	**Average**	**Mobile Ice**	**Landfast Ice**	**Average**	**Mobile Ice**	**Landfast Ice**	**Average**
KS02									
$\mathbf{R_I^-}$	6.7 ± 0.5	6.6 ± 0.5	6.5 ± 0.5	2.8 ± 0.1	2.8 ± 0.2	2.9 ± 0.2	4.0 ± 0.4	3.9 ± 0.3	4.0 ± 0.4
$\mathbf{R_I^+}$	6.3 ± 0.5	6.2 ± 0.5	6.1 ± 0.5	2.6 ± 0.1	2.6 ± 0.2	2.6 ± 0.2	3.7 ± 0.4	3.7 ± 0.3	3.7 ± 0.4
$\boldsymbol{\nu}$	0.18 ± 0.05	0.18 ± 0.06	0.19 ± 0.06	0.19 ± 0.04	0.21 ± 0.05	0.21 ± 0.05	0.12 ± 0.04	0.11 ± 0.03	0.12 ± 0.05
RMSE	0.7 ± 0.1	0.7 ± 0.1	0.6 ± 0.1	0.2 ± 0.0	0.3 ± 0.0	0.2 ± 0.0	0.4 ± 0.0	0.4 ± 0.0	0.4 ± 0.0
KS10									
$\mathbf{R_I^-}$	106.9 ± 13.2	118.7 ± 14.3	108.5 ± 12.9	66.8 ± 7.3	75.6 ± 10.1	69.9 ± 8.4	6.2 ± 0.1	6.3 ± 0.1	6.3 ± 0.1
$\mathbf{R_I^+}$	9.8 ± 0.1	9.8 ± 0.2	9.6 ± 0.2	3.9 ± 0.1	3.8 ± 0.1	3.9 ± 0.1	5.8 ± 0.1	5.9 ± 0.1	5.9 ± 0.1
$\boldsymbol{\nu}$	0.08 ± 0.01	0.09 ± 0.01	0.08 ± 0.01	0.08 ± 0.01	0.09 ± 0.01	0.09 ± 0.01	0.02 ± 0.00	0.02 ± 0.00	0.02 ± 0.00
RMSE	0.7 ± 0.2	0.8 ± 0.2	0.7 ± 0.2	0.2 ± 0.1	0.2 ± 0.1	0.2 ± 0.1	0.5 ± 0.0	0.5 ± 0.0	0.5 ± 0.0
KS12									
$\mathbf{R_I^-}$	152.4 ± 37.0	157.1 ± 35.3	150.4 ± 35.1	91.5 ± 11.7	72.5 ± 6.3	86.0 ± 9.8	6.4 ± 0.4	6.6 ± 0.4	6.5 ± 0.4
$\mathbf{R_I^+}$	8.9 ± 0.0	8.5 ± 0.1	8.5 ± 0.1	3.6 ± 0.0	3.2 ± 0.0	3.4 ± 0.0	5.3 ± 0.1	5.2 ± 0.1	5.2 ± 0.1
$\boldsymbol{\nu}$	0.07 ± 0.00	0.08 ± 0.00	0.08 ± 0.00	0.07 ± 0.00	0.07 ± 0.00	0.07 ± 0.00	0.04 ± 0.01	0.05 ± 0.00	0.04 ± 0.00
RMSE	0.5 ± 0.1	0.5 ± 0.1	0.5 ± 0.1	0.3 ± 0.1	0.2 ± 0.2	0.3 ± 0.1	0.4 ± 0.1	0.3 ± 0.1	0.4 ± 0.1

Table 5.3: *Caption on previous page*

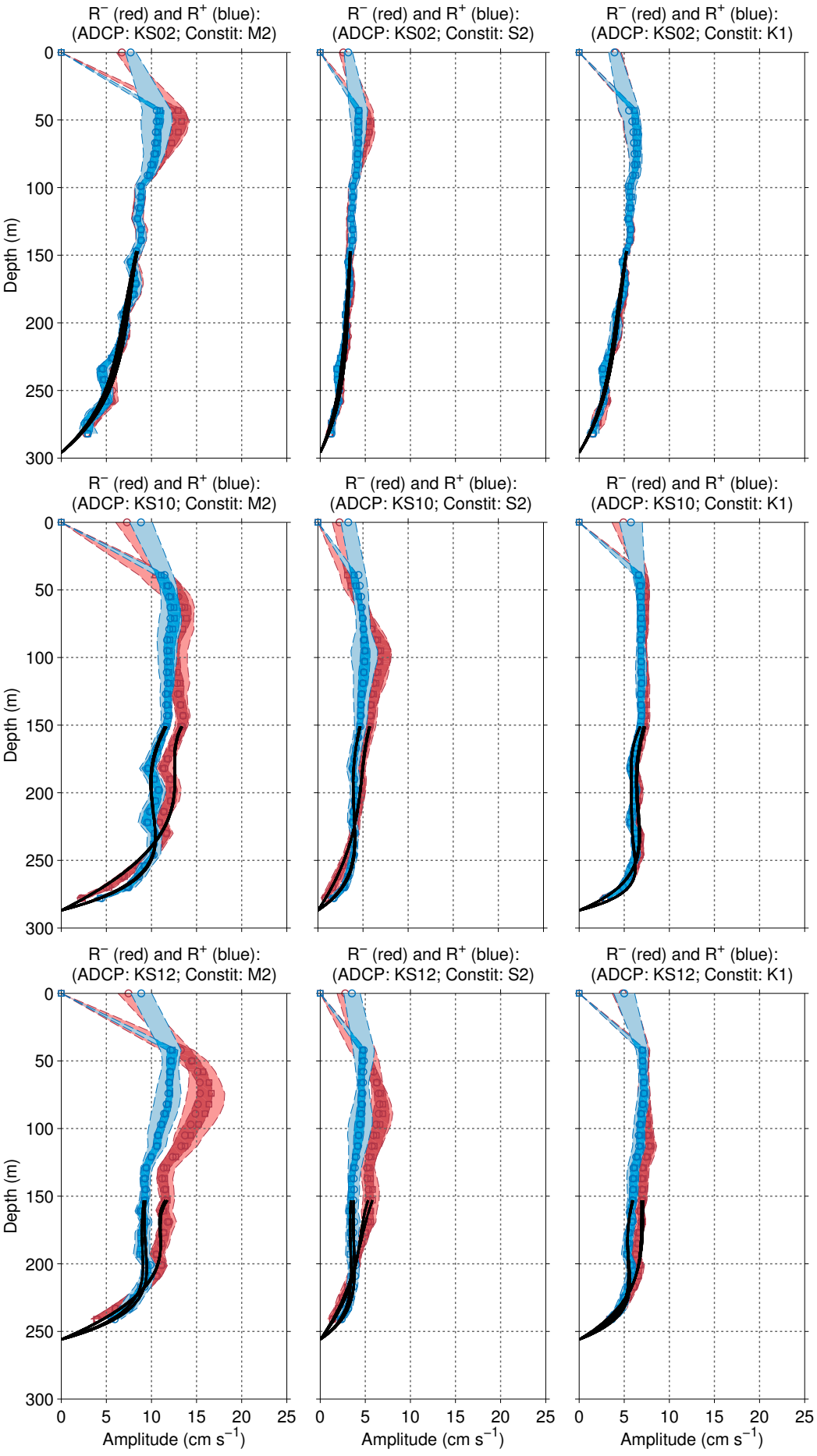

Figure 5.16: *Caption on following page*

Figure 5.16: Modelled vertical structure of the clockwise (red) and anticlockwise (blue) rotary components predicted by fitting the simple boundary layer models derived in Section 5.2.3 with a constant eddy viscosity profile to the observed vertical structure of the M2 (left), S2 (middle) and K1 (right) constituents between the seabed and 150 m at KS02 (top), KS10 (middle) and KS12 (bottom) during both mobile (solid black line) and landfast ice (dashed black line) regimes. The hollow circles and squares indicate the average vertical profile from the mobile and landfast ice regimes, respectively, and the thin dashed lines show plus or minus one standard deviation of all the data points included in each profile. The darker shading indicates where the error bars from the two ice regimes overlap. Note that it is hard to distinguish the circles and squares and model fits from one another due to the lack of variability in the vertical structure between the two ice regimes. The best fit parameters from each model fit are given in Table 5.3.

5.4 Tidal Dissipation

The turbulence generated at the seabed by the strong tidal flows will extract energy from the mean flow. This occurs as the kinetic energy associated with the turbulent motion is progressively cascaded to smaller and smaller scales, until eventually it reaches a point where molecular viscosity becomes important (typically on a length scale of a few millimetres), and the energy is dissipated into heat (*Simpson and Sharples*, 2012). Using the results of the simple boundary layer models presented in Section 5.2.3, it is possible to calculate the rate of tidal dissipation in Nares Strait over the region of the water column covered by the models (Polton, pers. comm.).

5.4.1 Derivation

An estimate of the tidal dissipation in Nares Strait can be derived by taking the scalar product of the momentum equation

$$\rho \frac{D\boldsymbol{u}}{Dt} + \rho f \boldsymbol{k} \times \boldsymbol{u} = -\rho g \nabla \eta + \frac{\partial \boldsymbol{\tau}}{\partial z}, \tag{5.35}$$

with the mean velocity (where bold symbols represent vector quantities), to give an equation for the kinetic energy of the mean flow (where $\rho f \boldsymbol{k} \times \boldsymbol{u} \cdot \boldsymbol{u}$ has been set to zero by definition):

$$\rho \frac{D}{Dt}\left(\frac{\boldsymbol{u} \cdot \boldsymbol{u}}{2}\right) = \boldsymbol{u} \cdot (-\rho g \nabla \eta) + \boldsymbol{u} \cdot \frac{\partial \boldsymbol{\tau}}{\partial z}. \tag{5.36}$$

At steady state (i.e. when Equation 5.36 is averaged over an integer number of tidal cycles) and when it is assumed that there is no advective flux of kinetic energy, the

material derivative can be set to zero. Integrating Equation 5.36 over the region of the water column to which the simple boundary layer models are fitted and substituting for the eddy viscosity stress model (Equation 5.5) gives:

$$0 = \int_0^h \overline{\boldsymbol{u} \cdot (-\rho g \nabla \eta)} \; dz + \rho \nu \overline{\boldsymbol{u} \cdot \frac{\partial \boldsymbol{u}}{\partial z}} \Bigg|_0^h - \rho \nu \int_0^h \overline{\frac{\partial \boldsymbol{u}}{\partial z} \cdot \frac{\partial \boldsymbol{u}}{\partial z}} \; dz, \tag{5.37}$$

where $z = 0$ is the seabed, $z = h$ is the depth to which the simple boundary layer models are fitted, ρ and ν are independent of depth, and the overbars indicate the average over an integer number of tidal cycles. The first term represents the integrated production of kinetic energy by the mean flow, the second term represents the work done at the boundaries of the integration region, and the third term which is positive definite, represents the integrated dissipation of kinetic energy through eddy viscous processes. Whether the work done at the boundaries of the integration region represents a production term or a dissipation term depends on the vertical structure of the velocity and the velocity shear in the water column. For example, if at $z = h$ the shear is zero (e.g. the tidal current has reached its free stream velocity), then there is no stress and the term can be set to zero (note that the term is always zero at the seabed due to the no slip condition). In this case, the depth-integrated production of kinetic energy is entirely balanced by the dissipation due to eddy viscous processes. On the other hand, if at $z = h$ the shear is positive and the water velocity continues to increase with depth above the integration region (e.g. the integration region does not cover the entire boundary layer), then the work done at the boundaries is positive and contributes to kinetic energy production. Conversely, if the shear is negative at $z = h$ and the water velocity decreases above the integration region (e.g. due to the effects of an under-ice boundary layer), then the work done at the boundaries is negative and results in the dissipation of kinetic energy.

By examining the vertical structure of the rotary components in Figures 5.10 and 5.12, it is clear that the shear is never negative at a depth of 150 m and thus the work done at the boundaries of the integration region does not represent a dissipation term. In this

case, the integrated tidal dissipation (ϵ) in W m^{-2} can be written as:

$$\epsilon = \rho\nu \int_0^h \frac{\partial \boldsymbol{u}}{\partial z} \cdot \frac{\partial \boldsymbol{u}}{\partial z} \, dz = \int_0^h \boldsymbol{\tau} \cdot \frac{\partial \boldsymbol{u}}{\partial z} \, dz, \tag{5.38}$$

where the overbars representing an average over an integer number of tidal cycles have been dropped for clarity, but are assumed. If the velocity vector $\boldsymbol{u}$ is decomposed into an interior and boundary layer part (such that $\boldsymbol{u} = \boldsymbol{u_I} + \boldsymbol{u_{BL}}$), and it is noted from Equation 5.35 that in steady state the vertical stress gradient can be written as a function of the boundary layer velocity:

$$\rho f \boldsymbol{k} \times \boldsymbol{u_{BL}} = \frac{\partial \boldsymbol{\tau}}{\partial z}, \tag{5.39}$$

then the expression for ϵ can be integrated by parts to give:

$$\epsilon = \boldsymbol{\tau} \cdot \boldsymbol{u}|_0^h - \int_0^h \frac{\partial \boldsymbol{\tau}}{\partial z} \cdot \boldsymbol{u} \, dz,$$

$$\epsilon = \boldsymbol{\tau} \cdot \boldsymbol{u}|_0^h - \int_0^h \rho f \boldsymbol{k} \times \boldsymbol{u_{BL}} \cdot (\boldsymbol{u_I} + \boldsymbol{u_{BL}}) \, dz. \tag{5.40}$$

Noting that $\rho f \boldsymbol{k} \times \boldsymbol{u_{BL}} \cdot \boldsymbol{u_{BL}}$ equals zero by definition, then

$$\epsilon = \boldsymbol{\tau} \cdot \boldsymbol{u}|_0^h - \int_0^h \rho f \boldsymbol{k} \times \boldsymbol{u_{BL}} \cdot \boldsymbol{u_I} \, dz,$$

$$\epsilon = \boldsymbol{\tau} \cdot \boldsymbol{u}|_0^h - \int_0^h \frac{\partial \boldsymbol{\tau}}{\partial z} \cdot \boldsymbol{u_I} \, dz. \tag{5.41}$$

Finally by evaluating the depth integral, and noting that $\boldsymbol{u_I}$ is independent of depth, then ϵ can be written as

$$\epsilon = \boldsymbol{\tau} \cdot (\boldsymbol{u} - \boldsymbol{u_I})|_0^h = \rho\nu \frac{\partial \boldsymbol{u}}{\partial z} \cdot (\boldsymbol{u} - \boldsymbol{u_I}) \Big|_0^h. \tag{5.42}$$

Alternatively, by substituting the complex tidal velocity vector (Equation 5.3)

$$\boldsymbol{u} = \mathbf{R}^+ e^{i\omega t} + \mathbf{R}^- e^{-i\omega t} \tag{5.43}$$

into Equation 5.42 and averaging over the period of a tidal cycle, Equation 5.42 can be written in terms of the rotary components of the tidal ellipse:

$$\epsilon = \rho\nu \,\mathrm{Re}\left\{ \frac{\partial \boldsymbol{R}^{+}}{\partial z}(\boldsymbol{R}^{+} - \boldsymbol{R}_{\boldsymbol{I}}^{+})^{*}\Big|_{0}^{h} + \frac{\partial \boldsymbol{R}^{-}}{\partial z}(\boldsymbol{R}^{-} - \boldsymbol{R}_{\boldsymbol{I}}^{-})^{*}\Big|_{0}^{h} \right\}, \tag{5.44}$$

where Re represents the real part and * indicates the complex conjugate. As the simple boundary layer models only cover the region of the water column between the seabed and a depth of 150 m, ϵ is likely to be biased low as it does not include the effect of dissipation associated with the under-ice boundary layer. Although this missing dissipation is likely to be small during mobile ice seasons, it could represent a significant proportion of the total dissipation during landfast ice seasons.

Whilst it is not possible to calculate an estimate of the dissipation associated with the under-ice boundary layer that is directly comparable to the integrated dissipation between the seabed and a depth of 150 m, it is still possible to estimate the importance of the under-ice boundary layer in terms of the difference in surface dissipation between the mobile and landfast ice regimes. As the eddy viscosity at the surface is unknown, the under-ice dissipation must be calculated directly from the ice-ocean stress, such that

$$\epsilon_{ice-ocean} = \int_{0}^{h} \frac{\partial \boldsymbol{u}}{\partial z} \cdot \boldsymbol{\tau_{ice-ocean}} \; dz, \tag{5.45}$$

where $z = 0$ is the depth of the first ADCP velocity measurement at ≈35-40 m, $z = h$ is the surface, and $\boldsymbol{\tau_{ice-ocean}}$ is the ice-ocean stress. The ice-ocean stress can be calculated from the bulk velocity difference between the surface ($\boldsymbol{u_{ice}}$) and the first ADCP velocity measurement ($\boldsymbol{u_{ocean}}$):

$$\boldsymbol{\tau_{ice-ocean}} = \rho C d_i |(\boldsymbol{u_{ice}} - \boldsymbol{u_{ocean}})|(\boldsymbol{u_{ice}} - \boldsymbol{u_{ocean}}), \tag{5.46}$$

where $Cd_i = 5 \times 10^{-3}$ is the ice-ocean drag coefficient (*Hibler*, 1979; *Yang*, 2006, 2009), and therefore the bulk under-ice dissipation between the surface and ≈35-40 m is given

by:

$$\epsilon_{ice-ocean} = \rho C d_i |(\boldsymbol{u_{ice}} - \boldsymbol{u_{ocean}})|(\boldsymbol{u_{ice}} - \boldsymbol{u_{ocean}}) \cdot (\boldsymbol{u_{ice}} - \boldsymbol{u_{ocean}}), \tag{5.47}$$

or alternatively in terms of the complex tidal vectors as:

$$\epsilon_{ice-ocean} = \rho C d_i \, \mathrm{Re}\left\{|(\boldsymbol{R_{ice}} - \boldsymbol{R_{ocean}})|(\boldsymbol{R_{ice}} - \boldsymbol{R_{ocean}})(\boldsymbol{R_{ice}} - \boldsymbol{R_{ocean}})^*\right\}, \tag{5.48}$$

where Re represents the real part, $*$ indicates the complex conjugate, and

$$\boldsymbol{R_{ice}} = R^+_{ice} e^{i\omega t} + R^-_{ice} e^{-i\omega t}, \tag{5.49}$$

and

$$\boldsymbol{R_{ocean}} = R^+_{ocean} e^{i\omega t} + R^-_{ocean} e^{-i\omega t}. \tag{5.50}$$

5.4.2 Results

Based on the three-year average vertical structure of the tides, the results in Table 5.4 show that the integrated tidal dissipation in Nares Strait between the seabed and a depth of 150 m is dominated by the M2 tide, due to the strong shear, thick boundary layers and large interior velocities associated with this constituent. Indeed, at all ADCPs the M2 tidal dissipation is nearly an order of magnitude greater than the dissipation associated with either the K1 or S2 constituents (e.g. at KS10 the M2 dissipation is 75.5 ± 6.3 mW m^{-2}, compared to 11.7 ± 1.5 mW m^{-2} and 9.7 ± 1.0 mW m^{-2} for the S2 and K1 constituents, respectively), and accounts for ≈70%, ≈78% and ≈76% of the total dissipation at KS02, KS10, and KS12, respectively. Fitting the simple boundary layer models to the observed vertical structure of the tides suggested that the interior velocity of the semi-diurnal clockwise rotary component is an order of magnitude greater than that of the semi-diurnal anticlockwise rotary component and both of the diurnal rotary components (Figure 5.10). Consequently, it might be expected that the dissipation associated with the semi-diurnal clockwise rotary component (i.e. $\epsilon\ \boldsymbol{R^-}$) would also be an order of magnitude greater than that of the semi-diurnal anticlockwise component (i.e.

	M2			S2			K1		
	Mobile Ice	**Landfast Ice**	**Average**	**Mobile Ice**	**Landfast Ice**	**Average**	**Mobile Ice**	**Landfast Ice**	**Average**
KS02									
$\epsilon\ \boldsymbol{R^-}$	17.0 ± 5.9	16.6 ± 6.1	16.3 ± 5.8	3.0 ± 0.8	3.1 ± 1.0	3.2 ± 1.0	3.6 ± 1.5	3.3 ± 1.2	3.7 ± 1.6
$\epsilon\ \boldsymbol{R^+}$	15.5 ± 5.4	15.0 ± 5.5	14.7 ± 5.2	2.6 ± 0.7	2.7 ± 0.8	2.8 ± 0.8	3.3 ± 1.4	3.0 ± 1.1	3.4 ± 1.5
ϵ **Total**	32.5 ± 11.2	31.7 ± 11.7	31.0 ± 11.0	5.6 ± 1.5	5.8 ± 1.8	6.0 ± 1.8	6.9 ± 2.9	6.3 ± 2.3	7.1 ± 3.1
KS10									
$\epsilon\ \boldsymbol{R^-}$	40.7 ± 1.5	46.9 ± 3.3	40.9 ± 2.2	5.5 ± 0.6	6.2 ± 0.6	5.7 ± 0.5	3.7 ± 0.3	3.9 ± 0.4	3.9 ± 0.4
$\epsilon\ \boldsymbol{R^+}$	35.2 ± 4.1	37.7 ± 5.3	34.6 ± 4.5	5.8 ± 0.9	6.1 ± 0.9	6.0 ± 0.9	5.7 ± 0.5	5.8 ± 0.6	5.9 ± 0.6
ϵ **Total**	75.9 ± 5.2	84.7 ± 8.1	75.5 ± 6.3	11.4 ± 1.5	12.3 ± 1.5	11.7 ± 1.4	9.4 ± 0.8	9.7 ± 0.9	9.7 ± 1.0
KS12									
$\epsilon\ \boldsymbol{R^-}$	41.2 ± 7.6	43.1 ± 6.8	39.7 ± 6.8	5.0 ± 0.4	4.2 ± 0.2	4.8 ± 0.4	5.5 ± 1.1	6.3 ± 0.9	5.7 ± 1.0
$\epsilon\ \boldsymbol{R^+}$	27.1 ± 1.2	25.7 ± 1.6	25.2 ± 1.2	4.3 ± 0.1	3.4 ± 0.1	3.9 ± 0.1	6.5 ± 0.7	6.7 ± 0.4	6.5 ± 0.6
ϵ **Total**	68.3 ± 7.8	68.8 ± 7.0	64.9 ± 7.0	9.3 ± 0.5	7.6 ± 0.3	8.7 ± 0.4	11.9 ± 1.8	12.9 ± 1.3	12.2 ± 1.6

Table 5.4: Estimates of depth-integrated tidal dissipation in mW m^{-2} between the seabed and a depth of 150 m associated with the M2 (left), S2 (middle), and K1 (right) tidal constituents for both ice regimes (mobile and landfast) and the three-year average vertical structure. $\epsilon\ \boldsymbol{R^-}$ is the dissipation associated with the clockwise rotary component, $\epsilon\ \boldsymbol{R^+}$ is the dissipation associated with the anticlockwise rotary component and ϵ **Total** is the total dissipation (i.e. Equation 5.44). The uncertainty in the dissipation is based on the uncertainty in the eddy viscosity and the interior velocities as discussed in Section 5.2.3.

$\epsilon\ \boldsymbol{R}^{+}$), and as the total dissipation is given by the sum of the two individual components (i.e. ϵ **Total**; Equation 5.44), then the total semi-diurnal dissipation will always be greater than the total diurnal dissipation. This is not the case, however, and the results in Table 5.4 show that the magnitude of the dissipation associated with each of the semi-diurnal rotary components are not significantly different from one another (especially for the S2 tide where they are essentially identical), and the total dissipation associated with the K1 tide is generally equal to or greater than the total dissipation associated with the S2 tide. For example at KS10 the dissipation associated with the S2 clockwise and anticlockwise rotary components is 5.7 $\pm$ 0.5 mW m^{-2} and 6.0 $\pm$ 0.9 mW m^{-2}, respectively, whilst at KS12 the total S2 dissipation is 8.7 $\pm$ 0.4 mW m^{-2} compared to 12.2 $\pm$ 1.6 mW m^{-2} for the K1 tide. In both of these cases, it appears that the stronger shear near the seabed associated with the semi-diurnal anticlockwise rotary component and both the diurnal rotary components is acting to offset the effect of the larger interior velocity associated with the semi-diurnal clockwise rotary component.

Figure 5.17 shows estimates of tidal dissipation in Nares strait from the TPXO8 tidal model. Here the rate of tidal dissipation (D) is calculated from the balance between the work done by the tide-generating force (W) and the divergence of tidal energy flux ($\boldsymbol{P}$; *Egbert and Ray*, 2000, 2001, 2003):

$$\begin{aligned} D &= W - \nabla \cdot \boldsymbol{P}, \\ D &= \rho g \left\langle \boldsymbol{U} \cdot \nabla(\zeta_{EQ} + \zeta_{SAL}) \right\rangle - \rho g \nabla \cdot \langle \boldsymbol{U}\zeta \rangle, \end{aligned} \tag{5.51}$$

where ζ and $\boldsymbol{U}$ are tidal elevations and volume transports, ζ_{EQ} is the equilibrium tide, ζ_{SAL} accounts for ocean self-attraction and loading, and $\langle\ \rangle$ indicate a time average. As this estimate of dissipation requires the calculation of second order gradients and is the small residual of two large numbers, any inaccuracies in the modelled tidal fields can result in highly inaccurate dissipation estimates. This might be especially true in Nares Strait, where the ice cover and its narrow cross section compared to the footprint of satellite altimeters might limit the quality of the altimeter data used in the inversion of the tidal fields. Nevertheless, despite these possible uncertainties in the modelled tidal fields, the

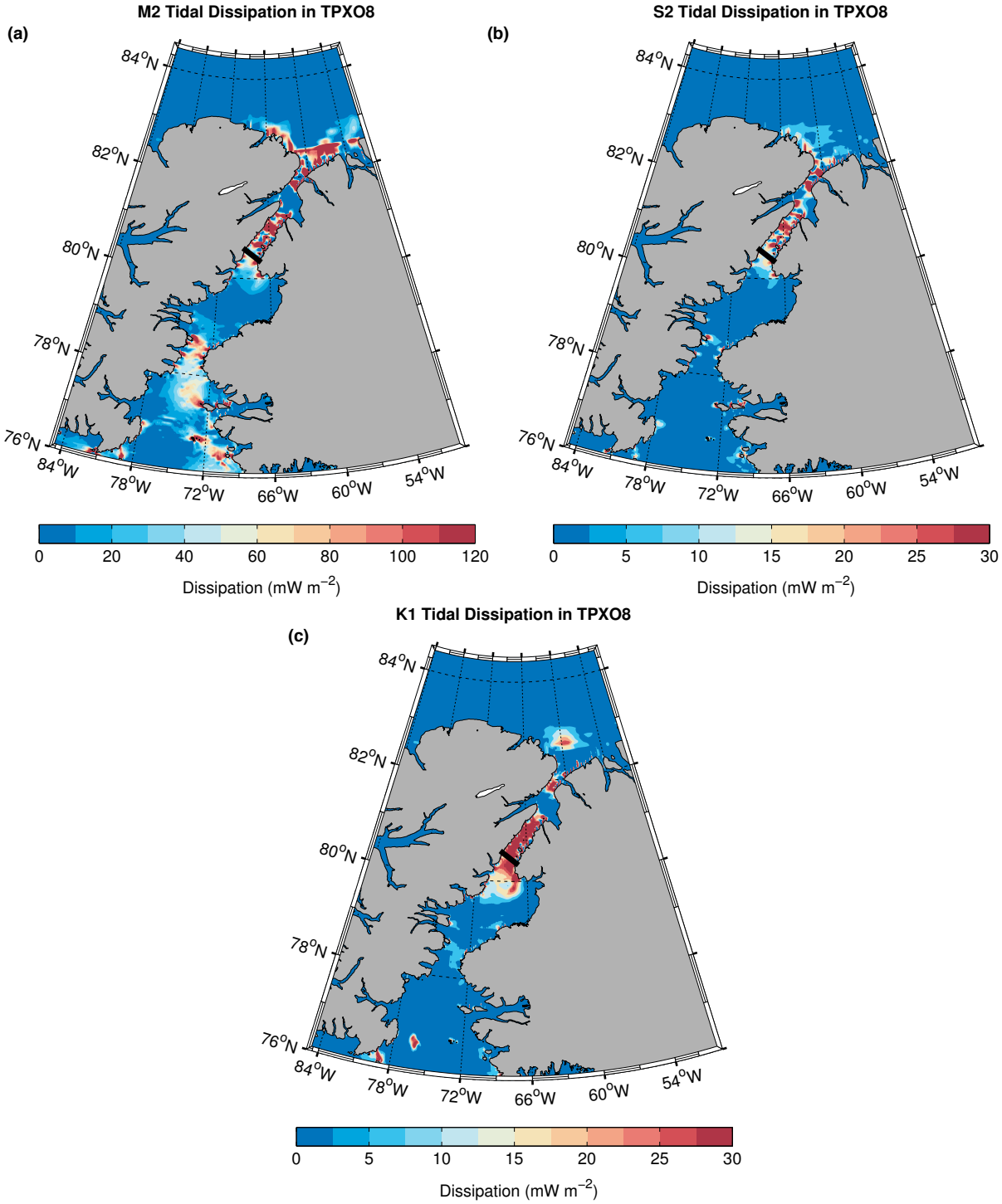

Figure 5.17: Estimates of the tidal dissipation in mW m^{-2} associated with (a) the M2, (b) the S2, and (c) the K1 tidal constituent in Nares Strait from the TPXO8 tidal model. The black line across Nares Strait in each of the figures indicates the position of the mooring array. Note the different colour range between each of the plots.

barotropic nature of the model, and the assumptions made regarding the quadratic drag at the seabed, the magnitude of the dissipation in TPXO8 is in very close agreement with the estimates presented in Table 5.4. The dissipation associated with the M2 tide is an order of magnitude greater than that associated with the S2 and K1 tides, and

at the location of the mooring array (black line in Figure 5.17), the average dissipation associated with each constituent (≈74 mW m^{-2}, ≈16 mW m^{-2}, and ≈44 mW m^{-2} for the M2, S2 and K1 constituents, respectively) is very similar to that calculated from the simple boundary layer models (especially given that the boundary layer models do not cover the entire water column). Furthermore, in TPXO8, the dissipation associated with the K1 tide is greater that that associated with the S2 tide (compare Figure 5.17b with Figure 5.17c), supporting the notion that the strength of the shear near the seabed is more important in determining the magnitude of the dissipation than either the depth of the boundary layer or the magnitude of the interior velocity. The similarity between the dissipation calculated from the ADCP data and that from the TPXO8 tidal model is an important result, and also appears to hold in other regions of the Arctic. For example the measurements of the average dissipation made by *Rippeth et al.*, 2015 along the continental shelf of the Eurasian Basin and in the central Canadian Basin also agree very well with the rate of tidal energy dissipation from the TPXO8 tidal model. Similar to the discussion in Section 4.4, this suggests that the significant increase in the resolution of the TPXO8 tidal model in the Arctic compared to previous iterations has greatly improved its ability to simulate the tides in the region. Overall, the magnitude of the tidal dissipation in Nares Strait is comparable in magnitude to that over the highly dissipative regions of, for example, Hudson Bay and the northwest European Shelf (*Egbert and Ray*, 2000, 2001; *Wilmes and Green*, 2014), but due to its limited size, is likely to be far less important than these latter two regions in a global sense.

In terms of the quasi-annual cycle in tidal dissipation caused by the changing ice regime, Table 5.4 shows that between the seabed and a depth of 150 m there is little difference in the dissipation between the mobile and landfast ice regimes, and for most tidal constituents at each ADCP, the dissipation is identical within the uncertainty. This is not unexpected, however, as the results of the harmonic demodulation in Figure 5.14 have already shown that over the region of the water column covered by the ADCPs, there is no change in the vertical structure of the tides between the different ice regimes. In contrast, Table 5.5 shows that when Equation 5.48 is averaged over the period of each tidal constituent, the effect of the quasi-annual cycle in ice regime on the magnitude

	M2		S2		K1	
	Mobile Ice	**Landfast Ice**	**Mobile Ice**	**Landfast Ice**	**Mobile Ice**	**Landfast Ice**
KS02						
ϵ **Total**	1.8	33.6	0.1	1.9	0.1	4.4
KS10						
ϵ **Total**	0.9	24.7	0.1	0.9	0.1	6.2
KS12						
ϵ **Total**	2.9	39.6	0.1	1.6	0.3	7.2

Table 5.5: Estimates of average under-ice dissipation (ϵ **Total**) in mW m^{-2} associated with the M2 (top), S2 (middle), and K1 (bottom) tidal constituents during both mobile and landfast ice regimes, calculated by averaging Equation 5.48 over the period of each tidal constituent.

of the under-ice dissipation is significantly more important. Whilst the magnitude of the under-ice tidal dissipation in Table 5.5 should not be directly compared with the magnitude of the dissipation in Table 5.4, the results show that the average dissipation in the under-ice boundary layer is one to two orders of magnitude greater during the landfast ice regime than that during the mobile ice regime for all constituents at all ADCPs. For example, for the M2 constituent at KS10, the average under-ice dissipation increases from 0.9 mW m^{-2} during the mobile ice regime to 24.7 mW m^{-2} during the landfast ice regime, whilst the average dissipation associated with the K1 tide increases from 0.1 mW m^{-2} to 6.2 mW m^{-2}. This suggests that the quasi-annual cycle in tidal dissipation associated with the changing ice regime will be driven solely by changes to the structure of the tides in the upper 35-40 m of the water column, which unfortunately cannot be observed by the ADCPs deployed in Nares Strait between 2003 and 2006.

5.5 Conclusions

Motivated by the need to understand and quantify the dominant frictional processes within Nares Strait, and with the aim of providing the first steps towards developing a fuller understanding of the role that the tides may play in limiting the freshwater flux through this region, the overall aim of Chapters 4 and 5 was to build upon the work of

Münchow and Melling (2008) by investigating the important dynamical processes behind the vertical and temporal variability in the major tidal constituents across Nares Strait. Using data collected between 2003 and 2006 as part of the Arctic Sub-Arctic Ocean Flux program and the Canadian Arctic Through-Flow study, along with data from Version 8 of the Oregon State University TOPEX/Poseidon Global Inverse Solution (TPXO8) barotropic tidal model, a number of key findings/conclusions can be drawn.

1: Tidal Propagation

The findings in Chapter 4 show that by comparing the phase difference between the maximum depth-averaged along channel tidal velocity and the maximum pressure perturbation associated with each tidal constituent at each ADCP, the tidal wave associated with both the M2 and S2 constituents in Nares Strait exhibits standing wave characteristics, whilst the K1 tidal wave is more progressive in nature (Figure 4.12). The semi-diurnal standing waves arise through the interaction of two tidal waves with equal frequency and phase propagating in opposite directions through Nares Strait from their sources in the Arctic Ocean and Baffin Bay (Figures 4.13 and 4.14). In contrast, the K1 tide is primarily progressive as only a single K1 tidal wave propagates through Nares Strait from the south towards the Arctic Ocean (Figure 4.15). Overall, the standing wave nature of the semi-diurnal tides explains the unusually strong tidal currents that are observed in Nares Strait, compared to the remainder of the Arctic Ocean (Figure 4.6).

2: Time-Averaged Vertical Structure

A harmonic analysis of each three-year velocity time series at each ADCP depth bin shows that there is significant variability in the vertical structure of the tides between the different ADCPs and tidal constituents. Across the majority of Nares Strait the major diurnal tide (K1) is primarily barotropic, whilst the major semi-diurnal tides (M2 and S2) are significantly more baroclinic (semi-major axis in Figure 5.1). In contrast, against the coast of Ellesmere Island, all three major tidal constituents exhibit the same vertical structure, albeit with different amplitudes. Across Nares Strait a consistent amplification in the strength of the both the M2 and S2 tides is observed in the upper water column,

but the same amplification is not observed in the K1 tide. The K1 tide is predominantly rectilinear at all depths, whereas the M2 and S2 tides exhibit clockwise rotation in the mid-water column and anticlockwise rotation near the seabed (semi-minor axis in Figure 5.1). In contrast, against the coast of Ellesmere Island, both the M2 and S2 tides are predominantly rectilinear, and an examination of the phase difference between the maximum along-strait velocity and maximum across-strait velocity (Figure 5.4), shows that continuity in the across-strait direction is maintained through a rotation of the tidal ellipse inclination angle (Figure 5.2) and the vertical motion associated with the steeply sloping bathymetry.

Much of the variability in the tides can be explained by the dynamics contained in simple boundary layer models that are fitted to the observed vertical structure of the two independent counter-rotating components associated with each of the major tidal constituents at each ADCP. Against the coast of Ellesmere Island, all constituents exhibit the same vertical structure and are predominantly rectilinear due to the requirement of no normal flow through the coast (Figure 5.12). Throughout the remainder of the strait, the proximity of the mooring array to the semi-diurnal critical latitude means that the benthic boundary layers associated with the M2 and S2 tides are an order of magnitude thicker than the benthic boundary layer associated with the K1 tide (Table 5.1); thus the semi-diurnal tides are significantly more baroclinic than the diurnal tides. The lack of rotation in the K1 tide across the strait is due to the broadly equal interior velocities and boundary layer thicknesses associated with each of the rotary components (Figure 5.10), whereas the effect of the semi-diurnal critical latitude on the M2 and S2 clockwise rotary component (Equations 5.12 and 5.26) explains the clockwise rotation observed in the mid-water column and the anticlockwise rotation near the bed. Although the simple boundary layer models can only be fitted to the observed vertical structure of the tides between the seabed and a depth of 150 m, there is strong evidence to suggest that the upper water column maximum in the M2 and S2 tides is due to the effect that stratification has in decoupling the water column from the benthic and under-ice semi-diurnal boundary layers (*Makinson*, 2002; *Makinson et al.*, 2006). On the other hand, it is possible that vertical motion at tidal frequencies is modifying the internal pressure gradients in the upper water

column and contributing to the upper water column maximum.

3: Temporal Variability

A 31-day harmonic demodulation of each velocity time series from each ADCP depth bin shows that within the observational uncertainty, there is no difference in the vertical structure of the tides between the landfast and mobile ice regimes (Figures 5.14 and 5.15). Of course within the upper 10s of meters of the water column the tidal current will tend to zero during landfast ice seasons due to the no-slip under-ice boundary layer, but this region of the water column cannot be observed by the ADCPs. The lack of variability in the upper water column and the absence of a thick semi-diurnal boundary layer penetrating down from the ice surface lends weight to the argument that the strong stratification near the surface is decoupling the under-ice boundary layer from the remainder of the water column.

4: Tidal Dissipation

Between the seabed and a depth of 150 m, the tidal dissipation in Nares Strait is dominated by that associated with the M2 tide (Table 5.4), which accounts for ≈70%, ≈78% and ≈76% of the total dissipation at KS02, KS10, and KS12, respectively. The strength of the shear near the seabed is the most important factor in determining the magnitude of the dissipation, and thus the dissipation associated with the K1 tide is generally equal to or greater than the dissipation associated with the S2 tide, despite the thicker boundary layer and interior velocity associated with the clockwise rotary component of the latter. The magnitude of the dissipation in the TPXO8 tidal model (Figure 5.17) agrees well with the estimates derived from the simple boundary layer models, especially considering the limitations of calculating dissipation from the modelled tidal fields in TPXO8. The quasi-annual cycle in ice regime has no effect on the magnitude of the dissipation between the seabed and 150 m, but, at the surface, the dissipation during the landfast ice regime can be up to two orders of magnitude greater (Table 5.5). This suggests that changes to the vertical structure of the tides in the upper 35-40 m of the water column will be solely responsible for driving a quasi-annual cycle in tidal dissipation,

but are unfortunately unobservable by the ADCPs. Overall, the magnitude of the tidal dissipation in Nares Strait is comparable to that over the highly dissipative regions of Hudson Bay and the northwest European Shelf, but in a global sense is less important due to its limited size.

5.6 Future Work

The work in this chapter has built substantially upon that of *Münchow and Melling* (2008), and has considerably increased our knowledge of the dynamical processes that are important for setting the vertical structure of the tides in Nares Strait. However, there are a number of key outstanding questions that could not be addressed here that motivate further study.

Due to the complex nature of the tidal currents in the upper water column, and the use of only simple point eddy viscosity boundary layer models, it was not possible to fully model the vertical structure of the tides above a depth of 150 m. Although there is robust evidence to suggest that it is the strong stratification in this region that is the controlling dynamic behind the observed structure, it would be instructive to develop more complex 1D turbulence closure models that could confirm this hypothesis directly. Instead of relying on the eddy viscosity profile being defined a priori, turbulence closure models determine the value of the eddy viscosity directly from the amount of turbulence in the water column (*Simpson and Sharples*, 2012). The turbulence closure schemes range in complexity from those that prescribe the eddy viscosity as a simple function of the gradient Richardson number, through to those such as the Mellor–Yamada and $\kappa - \epsilon$ schemes which involve the use of one, two, or more equations for the turbulent quantities (*Burchard et al.*, 1998). In these models the profile of the eddy viscosity can directly reflect the underlying complexity of the water column (e.g. regions of strong stratification) without the concern of over-fitting that is present when equally complex profiles are used in the models described in this chapter. Examples of 1D turbulence closure models that have been used to investigate tidal/mixing dynamics in shallow shelf seas include those of *Simpson et al.* (1996), *Simpson et al.* (2002), and *Makinson* (2002).

In addition to determining the role played by stratification in the upper water column,

the use of these more complex turbulent closure models will also allow the depth-integrated tidal dissipation in Nares Strait to be calculated in a consistent manner throughout the water column (including the effect of the under-ice boundary layer), and therefore the exact change in the magnitude of the dissipation between the mobile and landfast ice regimes could be quantified.

Beyond the development of a 1D turbulence closure model, the results presented in this chapter could be further corroborated by analysing the more recent observational data collected in Nares Strait during the periods 2007-2009 and 2009-2012 (*Melling*, 2007, 2009, 2012). In addition, during 2009, the ice conditions in the strait were significantly different from the mean climatology, as the lack of formation of an ice bridge across Smith Sound during the winter of 2008 meant that the ice in the strait never became landfast, and was free to drift from the Arctic Ocean to Baffin Bay all winter long. It would be interesting to explore whether these abnormal conditions had any effect on the structure of the tides.

Finally, future studies should principally aim to understand the role that both the unusually strong tidal flows in Nares Strait, as well as other important frictional processes such as lateral friction/eddies, hydraulic control over the shallow sill in Kane Basin, and internal wave drag, may play in limiting the flux of freshwater through Nares Strait. In light of the rate at which the Arctic Ocean is changing, and the effect that this is expected to have on the export of freshwater through the region, there is significant motivation to use the observational data discussed in Chapters 4 and 5, as well as 1D and 3D models of the flow through the strait, to develop a full understanding of each of these processes.

Chapter 6

Summary and Implications

Over the past few decades, the Arctic Ocean has experienced a period of unprecedented change. Atmospheric temperatures have been increasing faster than at any other location on the planet (*Hassol*, 2004), September sea ice extent has been declining at such a rate that an ice-free summer is almost certain to occur some time between the middle and the end of the century (e.g. *Wang and Overland*, 2009; *Stroeve et al.*, 2012a), and the sources, sinks and distribution of freshwater in the ocean have been changing radically (e.g. *Giles et al.*, 2012; *Morison et al.*, 2012). These changes, along with many others, are all expected to have significant impacts at both local and global scales by, for example, altering the dynamics of the global atmospheric and oceanic circulation (e.g. *Jahn and Holland*, 2013), affecting the stability of methane hydrates contained within permafrost and under the sea floor (*Kerr*, 2010; *Whiteman et al.*, 2013), and disturbing the state of fragile ecosystems (e.g. *Wassmann et al.*, 2011). Motivated by these impacts, the aim of this thesis was to examine and understand how a number of different aspects of the Arctic Ocean's circulation and dynamics are being affected by the changing environment. In this chapter, a summary of the work in this thesis is presented, and a number of implications of the results for the wider Arctic Ocean and scientific community are discussed.

6.1 Summary

In Chapter 2, the changing dynamics behind the accumulation of freshwater in the Beaufort Gyre were considered. To date, variability in the freshwater content of the

Beaufort Gyre has primarily been considered to be a function of only the wind, with *Proshutinsky and Johnson* (1997) and *Proshutinsky et al.* (2002) identifying two wind regimes in the Arctic Ocean associated with the Arctic Oscillation. During the anticyclonic regime, freshwater is generally accumulated in the Beaufort Gyre over several years due to a strengthened atmospheric Beaufort High (i.e. Figure 1.5c), whereas during the cyclonic regime (i.e. Figure 1.5b), a weaker Beaufort High leads to a release of freshwater. The work in this thesis, however, considers how a change in the boundary conditions (i.e. a decline in the sea ice cover at the surface) and an increase in the efficiency by which wind energy is transferred into the upper ocean, may affect these dynamics. In particular, a simple reduced gravity model of the Canadian Basin was used to explore whether sea ice decline could explain the accelerated accumulation of freshwater in the region that has recently been observed by, for example, *McPhee et al.* (2009) and *Giles et al.* (2012). By idealistically perturbing the annual cycle in ocean surface stress (i.e. the total wind energy transmitted through the sea ice), an increase in the annual mean momentum flux lead to a linear accumulation of freshwater in the Beaufort Gyre (thus providing an explanation for the accelerated accumulation), whilst a change in the seasonality (i.e. an asymmetrical annual cycle) had no effect on the annual mean freshwater content. In the model, both the timescale over which the Arctic Ocean adjusted to a change in forcing (approximately 14 years), and the total quantity of freshwater accumulated are determined by the balance between Ekman pumping and an eddy-induced bolus transport towards the boundary. This highlights the important role that will be played by eddies in the adjustment of the Arctic Ocean to the changing environment.

An acceleration in the accumulation of freshwater in the surface layer of the Arctic Ocean will also play a significant role in the sea ice budget at the surface by increasing the strength of the stratification associated with the cold halocline, and limiting the extent to which the heat contained within the Atlantic layer can be entrained through surface-generated mixing (*Aagaard et al.*, 1981). At the same time, however, stronger wind forcing of the upper ocean is also expected to drive periodic increases in vertical mixing that may enhance the vertical diffusive heat flux from the Atlantic layer (*Rainville et al.*, 2011). By perturbing the magnitude of the vertical mixing and the freshwater input through a wide

parameter space in a 1D model of the Arctic Ocean water column, Chapter 3 showed that an enhanced diffusive heat flux from the Atlantic layer driven by the elevated vertical mixing initially warms the mixed layer in both the Eurasian and Canadian basins, but the change in mixed layer temperature is insufficient to adversely affect the sea ice cover at the surface (similar to the results of *Nummelin et al.*, 2015). Furthermore, a decrease in the diffusive heat flux in the Eurasian Basin causes the mixed layer to cool after about a decade. In contrast, in the case of strongly elevated vertical mixing, the cold halocline in the Eurasian Basin can be fully eroded within 10 years. Once this has occurred, processes at the surface such as wind-forced overturning, storm-driven mixing, and convective static instability can entrain enough heat from the Atlantic layer to melt half a meter of sea ice in 6 months, which is comparable in magnitude to the other major oceanic processes responsible for the ongoing melting of Arctic sea ice. In the Canadian Basin, the cold halocline is never fully eroded due to the stronger stratification, and if the Beaufort Gyre continues to accumulate freshwater in the future due to the processes discussed in Chapter 2, this result is unlikely to change.

Along with the expected intensification of the Arctic hydrological cycle (*Held and Soden*, 2006) and the projected increase in the freshwater input from river runoff and excess precipitation over evaporation (e.g. *Vavrus et al.*, 2012), the changing dynamics and stratification of the wind-driven surface freshwater layer discussed in Chapters 2 and 3 are also likely to modify the quantity of freshwater that is exported through Fram Strait and the Canadian Arctic Archipelago (CAA; e.g. *Holland et al.*, 2007; *Stewart and Haine*, 2013). However, local dynamics in these regions will also be important in controlling the export of freshwater from the Arctic Ocean, and in particular, the turbulence generated by the especially strong tidal flows in Nares Strait to the west of Greenland may represent an important frictional constraint on the subtidal flow through this region. Accordingly, Chapters 4 and 5 investigated the important dynamics behind the vertical and temporal variability in the tides in Nares Strait, thus taking the initial steps towards a fuller understanding of the role they may play in limiting the freshwater flux through this region. By using output from the TPXO8 tidal model, and by comparing the observed phase difference between the maximum along-strait velocity and the maximum pressure pertur-

bation associated with each of the major tidal constituents in Nares Strait, it was shown that the semi-diurnal tides (M2 and S2) propagate through the strait with standing wave characteristics (thus explaining the unusually strong tidal currents in this region), whilst the diurnal tides (K1) propagate with a more progressive nature. Significant variability in the vertical structure of the tides was observed across the strait and between the different tidal constituents, although surprisingly little temporal variability was observed due to the quasi-annual cycle in ice regime. The dynamics behind the vertical structure appear to be associated with the proximity of the mooring array to the semi-diurnal critical latitude (which results in order of magnitude thicker boundary layers for the M2 and S2 tides compared to the K1 tide), the restriction of no normal flow through the coast of Ellesmere Island, and the effect of the strong stratification in the upper water column. Estimates of tidal dissipation in Nares Strait calculated from the results of simple boundary layer models are consistent with those predicted by the TPXO8 tidal model, and are comparable in magnitude to that over the lower latitude, highly dissipative region of the northwest European Shelf.

6.2 Implications and Discussion

6.2.1 Modelling the Arctic

The results in Chapters 2 and 3 have a number of implications for large-scale modelling of the Arctic Ocean that should be considered by the wider scientific community. For example, Chapter 2 showed that an asymmetrical annual cycle in ocean surface stress does not affect the annual mean freshwater content of the Beaufort Gyre, due to the fact that the timescale over which the Arctic Ocean adjusts to a change in forcing is considerably longer than seasonal (~decadal). This long adjustment timescale is also seen in the results of *Lique et al.* (2015), who used a 3D yet idealised general circulation model to explore the interactions that exist between the wind-driven surface layer and the Atlantic layer in the Canadian Basin. The wind forcing used in their model was based on that in Chapter 2 of this thesis. The decadal length adjustment timescale is set by the length of time required for the isopycnal slope to steepen sufficiently such

that the eddy bolus flux towards the boundary can balance the Ekman transport. This highlights the important role played by eddies in the adjustment of the Arctic Ocean to a change in forcing, and it is important for the wider scientific community to investigate and quantify their effects on the changing Arctic Ocean more rigorously. Indeed, the work in Chapter 2 is reminiscent of the early dynamical studies of the Antarctic Circumpolar Current (ACC), which showed that enhanced southern hemisphere westerly winds result in an intensification of the ACC due to a steeper isopycnal slope (e.g. *Fyfe and Saenko*, 2006). However, when eddy resolving/eddy permitting models are used in place of models that require the effect of eddies to be parameterised (such as in Chapter 2), the ACC exhibits behaviour known as *eddy saturation* and *eddy compensation*. *Eddy saturation* is a phenomena whereby the zonal transport associated with the ACC exhibits a limited sensitivity to increasing wind stress, as the increased momentum input is transferred to the bottom via enhanced interfacial form stress, rather than acting to accelerate the zonal transport. Similarly, *eddy compensation* is a phenomena whereby steepening of the ACC isopycnals driven by elevated Southern Ocean winds and stronger Ekman transport is opposed by a strengthening of the mesoscale eddy field, such that sum of the eddy and Ekman-induced transport velocities (i.e. $T = T_{Ek} - T_{Eddies}$ from Chapter 2) increases substantially less than the Ekman transport (*Morrison and Hogg*, 2013; *Munday et al.*, 2013). If such phenomena were to be important in the Arctic, the response of the Beaufort Gyre to the changing efficiency of momentum transfer into the upper ocean could be significantly different. The quantity of freshwater accumulated in the Beaufort Gyre might be noticeably smaller for the same change in the ocean surface stress, as the elevated Ekman transport towards the centre of the gyre will be offset by a stronger eddy-induced bolus transport towards the boundary, and an acceleration of the circulation associated with the Beaufort Gyre under stronger momentum transfer may not be observed. As the nature of the response will have important implications for the large-scale Arctic freshwater budget, and the export of freshwater through, for example, Nares Strait (where the local dynamics discussed in Chapters 4 and 5 will become important), exploring the response of the Beaufort Gyre to increased momentum transfer in a high resolution model should be a priority.

Throughout Chapters 2 and 3, the effects of the changing sea ice cover on momentum transfer and turbulent mixing in the Arctic were not included explicitly in the simple process models, and instead were represented through the idealised perturbations made to the annual cycle in ocean surface stress and the vertical structure of the velocity shear, respectively. However, as sea ice continues to decline, and the Arctic transitions from a generally quiescent ocean that is dominated by thermohaline forcing to one that is increasingly turbulent and wind-driven, both enhanced momentum transfer and elevated turbulent mixing are likely to have profound effects on the Arctic's large-scale properties and mean circulation. For example, *Rainville et al.* (2011) surmise that a change in the extent to which the Arctic Ocean is wind-forced might lead to an overall spin-up of the Arctic Ocean, affecting the dynamics of the Atlantic water circulation, the freshwater budget, and the quantity of freshwater exported to either side of Greenland. It would also modify the distribution and extent of coastal and slope upwelling regions (e.g. *Pickart et al.*, 2009), with implications for slope currents, water mass transformations, and biology. At the same time, elevated turbulent mixing will likely alter mixed layer properties and the distribution of freshwater throughout large swathes of the Arctic Ocean, and might erode the double diffusive staircases found in the Arctic Ocean (e.g. *Timmermans et al.*, 2008). These staircases play an important role in the ventilation of Atlantic water in the interior basins (*McLaughlin et al.*, 2009), and are currently responsible for a significant proportion of the present-day heat flux from the Atlantic layer (indeed, their erosion may lead to a temporary reduction in the vertical heat flux over the near future). Consequently, there is a pressing need for the wider community to understand and incorporate the relevant physics associated with Arctic sea ice decline and its effect on turbulent mixing and the transfer of momentum into the upper ocean into state-of-the-art coupled atmosphere-ice-ocean models, and to perform similar experiments to those discussed in Chapters 2 and 3 in more realistic high-resolution pan-Arctic settings.

In terms of the momentum transfer through sea ice, promising progress is being made by, for example, *Flocco et al.* (2010) and *Tsamados et al.* (2014), who have incorporated the physics of melt ponds and form drag associated with the changing shape of the ice pack into the Los Alamos sea ice model (CICE), and such physics may be noticeably improving

our ability to predict summer sea ice extent (e.g. *Schröder et al.*, 2014). In contrast, more progress must be made regarding the representation of turbulent mixing in pan-Arctic models. In designing the model experiments discussed in Chapter 3, it was discovered that the standard K-Profile Parameterisation (KPP) that is used in most large-scale global models (*Large et al.*, 1994) was not appropriate for modelling the Arctic. Indeed, when the KPP scheme was initialised with diffusivity constants appropriate for the Arctic Ocean (for example with a background mixing of 10^{-6} m^2 s^{-1} rather than 10^{-5} m^2 s^{-1}), it produced spuriously large changes in the magnitude of the vertical diffusivity for only small changes in the magnitude of the shear (perhaps unsurprising given that the KPP scheme is tuned for mixing in the thermocline at low latitudes). However, as *Zhang and Steele* (2007) highlight how sensitive simulations of the Arctic Ocean are to the magnitude of the vertical mixing (for example mixing that is too strong can reverse the circulation of Atlantic water in the Canadian Basin), it is important that future studies work to improve the parameterisations of turbulence mixing that are used in pan-Arctic models, and one avenue that could be explored is the development of spatially-varying diffusivity constants that scale with the strength of the internal wave field. Such an approach is similar to the work done in developing a spatially-varying eddy diffusivity constant that reflects the changing strength of the mesoscale eddy field, and this has been shown to reduce the drift in climate models (for example see *Ferrari and Polzin*, 2005 and *Danabasoglu and Marshall*, 2007).

Furthermore, until relatively recently, many state-of-the-art general circulation models did not resolve the complex and narrow passageways of the CAA due their coarse resolution (e.g. *Holland et al.*, 2007), and this has been shown to have noticeable impacts on their simulation of freshwater storage and export from the Arctic Ocean (*Jahn et al.*, 2010). Although recent improvement in the resolution of these models now allows for multiple channels in the CAA to be opened (e.g. see *Jahn et al.*, 2012), many still do not include the effects of the strong tidal currents seen in this region (Chapters 4 and 5), or are capable of simulating other important local dynamics such as hydraulic control over shallow sills and lateral boundary layer/eddy processes. The effect on these missing mechanisms on the simulated Arctic freshwater budget could be significant, and their

inclusion in high-resolution pan-Arctic or regional models should be a priority. Indeed, *Holloway and Proshutinsky* (2007) have shown that by including tidal effects in a pan-Arctic model, the loss of heat from the Atlantic layer is enhanced, and local impacts on the sea ice budget can be significant.

Beyond the use of pan-Arctic models, recent progress has also been made in reconstructing the fields of sea surface height and dynamic ocean topography in the ice-covered Arctic from satellite radar altimeters (e.g. *Peacock and Laxon*, 2004; *Kwok and Morison*, 2011), directly revealing the nature of the large-scale circulation. As a spin-up of the Arctic Ocean or the effect of elevated turbulent mixing on the circulation will be directly reflected in these observations, there is a strong argument for examining whether any trends in the circulation that are related to the changing annual cycle in sea ice extent can as yet be detected, and to use these observations as validation for model experiments.

6.2.2 Elevated Mixing at the Basin Margins

Whilst the analysis and model runs discussed in Chapter 3 were based on climatological temperature and salinity profiles from the interior of the Eurasian and Canadian basins, closer to the basin margins, where it has been proposed that the dominant mixing in the Arctic Ocean occurs (e.g. *Timmermans et al.*, 2008; *Rippeth et al.*, 2015), the effect of periodic increases in vertical mixing and enhanced freshwater input may be markedly different. For example, near the Atlantic water inflow in the Nansen Basin, the salinity stratification is significantly weaker, the Atlantic layer is considerably warmer, and the Atlantic water temperature gradient extends much closer to the surface due to the less well-developed cold halocline. In this region, it is likely that irrespective of any future increase in the freshwater input, the warmer Atlantic layer and more extensive temperature gradient will result in an elevated vertical heat flux driving significantly more heat into the mixed layer than that seen in the results of Chapter 3, and the weaker stratification will culminate in the cold halocline being eroded on much shorter timescales. In addition, the pulses of warm Atlantic water that have been seen to enter the Arctic with temperature anomalies of up to 2°C (*Polyakov et al.*, 2004, 2010) may also periodically facilitate a larger diffusive heat flux out of the Atlantic layer. As a result, it is highly

probable that the quantity of sea ice that can be melted by elevated vertical mixing near the Atlantic water inflow will be significantly greater than that in the interior. As this loss of sea ice might impact the dynamics of Atlantic water subduction and the formation of the Arctic Ocean cold halocline (e.g. *Rudels et al.*, 1996), elevated mixing in this region may have Arctic-wide implications by, for example, altering the temperature of the Atlantic layer, changing the depth range over which it is found, and perhaps leading to an overall weakening of the stratification associated with the cold halocline throughout the interior basins. As even our current knowledge of the key mechanisms responsible for the formation of the cold halocline and the subduction of Atlantic water remains uncertain, a detailed study of this region that aims to understand the important dynamics for both the present-day and the future Arctic Ocean will be worthwhile.

Away from the Atlantic water inflow, the shallow shelf areas found around the periphery of the deep Eurasian and Canadian basins may also respond very differently to a future increase in vertical mixing, and their response is equally likely to have Arctic-wide implications. These regions play an immensely important role in receiving the freshwater that enters the Arctic through river runoff, and redistributing it throughout the remainder of the Arctic Ocean. As discussed by *Steele and Boyd* (1998), *Dmitrenko et al.* (2008), and *Morison et al.* (2012), variability in the movement of freshwater between the shelves and the deep central basins can affect the freshwater content throughout the Arctic Ocean, and can fundamentally alter the distribution of Pacific and Atlantic waters at the surface, as well as the orientation and strength of the Transpolar Drift. Consequently, a change in the circulation triggered by elevated vertical mixing in these regions (for example see *Rainville and Woodgate*, 2009), may affect the Arctic-wide freshwater budget, the circulation and export of sea ice from the Arctic Ocean, and the export of liquid freshwater through, for example, Nares Strait (Chapters 4 and 5). Furthermore, primary productivity over the Arctic shelves is affected by the strong couplings that exist between light availability, ice and snow cover, the timing of under-ice and open water algal blooms, sea water temperatures, and nutrient availability (*Leu et al.*, 2011). Elevated vertical mixing in the future may strongly influence the nature of these couplings by enhancing the nutrient supply to the photic zone (perhaps through the re-suspension of bottom sediments,

e.g. *Rainville et al.*, 2011), modifying the stratification in the water column, and changing the nature of the sea ice cover at the surface. Therefore, elevated vertical mixing may play a leading role in determining the future timing and magnitude of phytoplankton blooms within the Arctic, with important implications for the Arctic carbon budget and the transfer of energy to higher trophic levels.

6.2.3 Arctic Freshwater Pathways

In addition to understanding how the dynamics of freshwater accumulation in the Beaufort Gyre may be affected by sea ice decline and the changing Arctic Ocean, the work in Chapter 2 also has implications for how variability in the Beaufort Gyre may impact variability in the export of freshwater to either side of Greenland. Although in the suite of experiments examined in Chapter 2 it was concluded that variability in the Beaufort Gyre cannot at present be the main driver behind the annual variability seen at Davis Strait and Fram Strait, it is possible that should the decline in Arctic sea ice cover continue to amplify the annual cycle in ocean surface stress, and thus the quantity of freshwater that is seasonally retained and released from the Beaufort Gyre increases, it may begin to play a noticeably more important role in the future. It must be noted, however, that it is unlikely that the variability at Davis Strait and Fram Strait will ever directly reflect the variability seen in the Beaufort Gyre, especially at short timescales. Indeed, the local dynamics important for controlling the export of freshwater to either side of Greenland (such as the strong tidal currents in Nares Strait discussed in Chapters 4 and 5) will likely have a leading order affect. In addition, the variability and timescales associated with the complex pathways and mechanisms by which freshwater released from the Beaufort Gyre is advected towards Fram Strait and the Canadian Arctic Archipelago will also be important. As the details of these pathways remain uncertain (e.g. *Lique et al.*, 2010), but are likely to include complex eddy interactions and narrow currents such as the Western Arctic Shelfbreak Current (e.g. *Spall et al.*, 2008; *Watanabe*, 2011; *Zhao et al.*, 2014), future studies should focus on understanding these processes and their associated timescales through both high-resolution model studies and targeted observational campaigns. In addition, it is probable that the effects of future increases in

turbulent mixing (Chapter 3) will also play a significant role in determining exactly how variability in the Beaufort Gyre is reflected downstream, highlighting the need to explore the interactions and feedbacks that exist between the different dynamics explored in this thesis in high-resolution pan-Arctic models.

6.2.4 The Changing Canadian Basin

Due to the stronger stratification and ever-present halocline found in the Canadian Basin, the results in Chapter 3 highlight that over the parameter space explored in the idealised 1D model of the Arctic Ocean water column, the sea ice cover in this region always remains isolated from the heat contained within the Atlantic layer, and a change in the stratification over the much shallower summer Pacific water does not allow a significant amount of heat to be entrained through surface-generated mixing (in agreement with *Toole et al.*, 2010). Consequently, this suggests that whilst the majority of sea ice retreat to date in the Arctic Ocean has occurred in the Canadian Basin, in future decades, elevated vertical mixing will play a more important role in the ongoing melting of Arctic sea ice in the Eurasian Basin, where the stratification is weaker and the cold halocline is more easily eroded. This is perhaps particularly pertinent in the light of the results in Chapter 2, and the accelerated accumulation of freshwater in the Beaufort Gyre. Indeed, if freshwater accumulation in the Beaufort Gyre was to continue as the upper Arctic Ocean becomes increasingly forced by the winds, the decrease in the surface salinity in the Canadian Basin would continue to strengthen the stratification, and further isolate the sea ice cover from the heat contained within the Atlantic layer and the summer Pacific water. At the same time, however, the corresponding removal of freshwater from the Eurasian Basin (e.g. *McPhee et al.*, 2009 and *Rabe et al.*, 2011) would result in a weakening of the stratification, making it even easier for elevated vertical mixing in the Eurasian Basin to drive an enhanced diffusive heat flux or erode the cold halocline in the future.

In spite of this, the Canadian Basin is also the region of the Arctic that is responding fastest to the changing Arctic environment. A number of recent studies have highlighted how the upper layers of the Canadian Basin have changed rapidly over recent years, with a significant warming in many of the different water masses that make up the surface layer

in this region. For example, *Jackson et al.* (2011) show that the near-surface temperature maximum has warmed by 0.5-1.5°C between 1993 and 2009, and between 2006 and 2012, the maximum temperature of Alaskan Coastal Water (a constituent of summer Pacific water) increased from ≈-1.3°C to ≈0.2°C (*Timmermans et al.*, 2014). If these warming trends were to continue over the coming decades, the quantity of heat that might be fluxed out of these layers and into the mixed layer, through both vertical mixing and convection, might become much greater than that observed in Chapter 3. Thus the sea ice cover in the Canadian Basin may well become significantly more susceptible to elevated vertical mixing than it is at present. If this were the case, it would undoubtedly feed back onto the circulation of the Beaufort Gyre by altering the momentum transfer into the upper ocean, and would likely have significant impacts on the export of freshwater through the CAA and Nares Strait.

6.2.5 Palaeoclimatic Dynamics

The results of Chapter 3 also have implications for palaeo ocean dynamics. Dansgaard-Oeschger (D-O) cycles are visible in many different palaeoclimatic records and proxies (e.g. Greenland ice cores and ocean sediment cores; *Bond et al.*, 1993; *Dansgaard et al.*, 1993), and are characterised by millennial length cold periods (stadials) terminated by an abrupt jump to warmer conditions (warming of 10 ± 5°C in <10 years; interstadials). These warmer conditions exist for 200-400 years, before a general cooling trend over the following 50-200 years returns the system to the preceding cold conditions (e.g. *Huber et al.*, 2006). A recent paper by *Dokken et al.* (2013) has suggested that the mechanism behind these D-O cycles is related to the stratification and stability of the palaeo Nordic Seas. During the cold stadial phases, the water column structure looked similar to that in the Arctic today, with an extensive sea ice cover and fresh surface layer isolated from the warm Atlantic layer beneath by a cold halocline. As the heat contained within the Atlantic layer was isolated from the surface and the atmosphere by the sea ice cover, the temperature of the Atlantic water slowly increased and became progressively lighter over time due to the continued inflow of warm Atlantic water across the Greenland-Scotland Ridge. Eventually this eroded the strong density gradient associated with the cold halocline, and the heat

contained within the Atlantic layer could be directly vented to the surface, melting the sea ice cover, warming the atmosphere, and triggering the transition to the warm interstadial conditions. Whilst *Dokken et al.* (2013) constructed this dynamical argument through the analysis of a high-resolution multiproxy marine sediment core, the results in Chapter 3 confirm that in the absence of a cold halocline, venting of heat from the Atlantic layer is sufficient to melt a significant quantity of sea ice at the surface, and thus the proposed dynamical mechanism is indeed realistic. However, as density is primarily determined by salinity at high latitudes, and the mechanism outlined by *Dokken et al.* (2013) suggests that it is the increasing temperature of the Atlantic layer that erodes the density gradient associated with the cold halocline, it would be interesting to examine how quickly the Atlantic layer would have to warm over the period of a D-O cycle such that temperature begins to dominate in the equation of state.

6.3 Outlook

Through the use of small scale observations and idealised process models that are not often applied to the understanding of Arctic Ocean dynamics, the work in this thesis has provided new insight into how the changing environment is affecting the Arctic Ocean's circulation, sea ice cover, and freshwater budget. The dynamical processes investigated in this thesis, however, will not operate in isolation, and the complex two-way couplings and feedbacks that will arise between the ice and the ocean and many other aspects of the Arctic's climate system will all be of critical importance in determining the integrated response of the Arctic Ocean to the changing environment. Consequently, in light of the rate at which the Arctic environment is changing (*Jeffries et al.*, 2013), and the significant feedback processes that will almost certainly drive further environmental change over the coming decades (*Overland et al.*, 2013), future studies using idealised process models, large-scale high-resolution pan-Arctic circulation models, and targeted and high quality observational campaigns that aim to make further progress in understanding the dynamics of the changing Arctic Ocean should be a priority.

Bibliography

Aagaard, K. (1981), On the deep circulation in the Arctic Ocean, *Deep Sea Research Part A. Oceanographic Research Papers*, **28**, 251–268, doi:10.1016/0198-0149(81)90066-2.

Aagaard, K., and E. C. Carmack (1989), The role of sea ice and other fresh water in the Arctic circulation, *Journal of Geophysical Research*, **94**, 14,485–14,498, doi:10.1029/JC094IC10P14485.

Aagaard, K., and E. C. Carmack (1994), The Arctic Ocean and Climate: A Perspective, in *The Polar Oceans and Their Role in Shaping the Global Environment*, *Geophysical Monograph Series*, vol. 85, edited by O. M. Johannessen, R. D. Muench, and J. E. Overland, pp. 5–20, American Geophysical Union, Washington D.C., doi:10.1029/GM085.

Aagaard, K., L. K. Coachman, and E. Carmack (1981), On the halocline of the Arctic Ocean, *Deep Sea Research Part A. Oceanographic Research Papers*, **28**, 529–545, doi:10.1016/0198-0149(81)90115-1.

Aksenov, Y., V. I. Ivanov, A. J. G. Nurser, S. Bacon, I. V. Polyakov, A. C. Coward, A. C. Naveria-Garabato, and A. Beszczynska-Möller (2011), The Arctic Circumpolar Boundary Current, *Journal of Geophysical Research*, **116**, C09017, doi:10.1029/2010JC006637.

Alkire, M. B., J. Morison, and R. Andersen (2015), Variability in the meteoric water, sea-ice melt, and Pacific water contributions to the central Arctic Ocean, 2000-2014, *Journal of Geophysical Research*, **120**, 1573–1598, doi:10.1002/2014JC010023.

Alley, R. B., and A. M. Ágústsdóttir (2005), The 8k event: Cause and consequences of a major Holocene abrupt climate change, *Quaternary Science Reviews*, **24**, 1123–1149, doi:10.1016/j.quascirev.2004.12.004.

Allison, L. C., H. L. Johnson, and D. P. Marshall (2011), Spin-up and adjustment of the Antarctic Circumpolar Current and global pycnocline, *Journal of Marine Research*, **69**, 167–189, doi:10.1357/002224011798765330.

Amante, C., and B. W. Eakins (2009), ETOPO1 1 Arc-Minute Global Relief Model: Procedures, data sources and analysis, *NOAA Tech. Memo. NESDIS NGDC 24*, doi:10.7289/V5C8276M.

Andreas, E. L., T. W. Horst, A. A. Grachev, P. O. G. Persson, C. W. Fairall, P. S. Guest, and R. E. Jordan (2010), Parametrizing turbulent exchange over summer sea ice and the marginal ice zone, *Quarterly Journal of the Royal Meteorological Society*, **136**, 927–943, doi:10.1002/qj.618.

Ardyna, M., M. Babin, M. Gosselin, E. Devred, L. Rainville, and J. Tremblay (2014), Recent Arctic Ocean sea-ice loss triggers novel fall phytoplankton blooms, *Geophysical Research Letters*, **41**, 6207–6212, doi:10.1002/2014GL061047.

Arrigo, K. R., G. van Dijken, and S. Pabi (2008), Impact of a shrinking Arctic ice cover on marine primary production, *Geophysical Research Letters*, **35**, L19603, doi:10.1029/2008GL035028.

Bamber, J., M. Van Den Broeke, J. Ettema, J. Lenaerts, and E. Rignot (2012), Recent large increases in freshwater fluxes from Greenland into the North Atlantic, *Geophysical Research Letters*, **39**, L19501, doi:10.1029/2012GL052552.

Barnes, E. A. (2013), Revisiting the evidence linking Arctic amplification to extreme weather in midlatitudes, *Geophysical Research Letters*, **40**, 4734–4739, doi:10.1002/grl.50880.

Barnes, E. A., and J. A. Screen (2015), The impact of Arctic warming on the midlatitude jet-stream: Can it? Has it? Will it?, *WIREs: Climate Change*, **6**, 277–286, doi:10.1002/wcc.337.

Barry, R., M. Serreze, and J. Maslanik (1993), The Arctic Sea-Ice Climate System: Observations and Modeling, *Review of Geophysics*, **31**, 397–422, doi:10.1029/93rg01998.

Barthélemy, A., T. Fichefet, H. Goosse, and G. Madec (2015), Modeling the interplay between sea ice formation and the oceanic mixed layer: Limitations of simple brine rejection parameterizations, *Ocean Modelling*, **86**, 141–152, doi:10.1016/j.ocemod.2014.12.009.

Bates, N. R., S. B. Moran, D. A. Hansell, and J. T. Mathis (2006), An increasing CO_2 sink in the Arctic Ocean due to sea-ice loss, *Geophysical Research Letters*, **33**, L23609, doi:10.1029/2006GL027028.

Becker, J. J., D. T. Sandwell, W. H. F. Smith, J. Braud, B. Binder, J. Depner, D. Fabre, J. Factor, S. Ingalls, S.-H. Kim, R. Ladner, K. Marks, S. Nelson, A. Pharaoh, R. Trimmer, J. Von Rosenberg, G. Wallace, and P. Weatherall (2009), Global Bathymetry and Elevation Data at 30 Arc Seconds Resolution: SRTM30_PLUS, *Marine Geodesy*, **32**, 355–371, doi:10.1080/01490410903297766.

Belkin, I. M. (2004), Propagation of the "Great Salinity Anomaly" of the 1990s around the northern North Atlantic, *Geophysical Research Letters*, **31**, L08306, doi:10.1029/2003GL019334.

Belkin, I. M., S. Levitus, J. Antonov, and S.-A. Malmberg (1998), "Great Salinity Anomalies" in the North Atlantic, *Progress in Oceanography*, **41**, 1–68, doi:10.1016/S0079-6611(98)00015-9.

Beszczynska-Möller, A., R. Woodgate, C. Lee, H. Melling, and M. Karcher (2011), A Synthesis of Exchanges Through the Main Oceanic Gateways to the Arctic Ocean, *Oceanography*, **24**, 82–99, doi:10.5670/oceanog.2011.59.

Beszczynska-Möller, A., E. Fahrbach, U. Schauer, and E. Hansen (2012), Variability in Atlantic water temperature and transport at the entrance to the Arctic Ocean, 1997-2010, *ICES Journal of Marine Science*, **69**, 852–863, doi:10.1093/icesjms/fss056.

Bintanja, R., and F. M. Selten (2014), Future increases in Arctic precipitation linked to local evaporation and sea-ice retreat, *Nature*, **509**(7501), 479–482, doi:10.1038/nature13259.

Bjork, G. (1989), A One-Dimensional Time-Dependent Model for the Vertical Stratification of the Upper Arctic Ocean, *Journal of Physical Oceanography*, **19**, 52–76, doi:10.1175/1520-0485(1989)019<0052:AODTDM>2.0.CO;2.

Bond, G., W. Broecker, S. Johnsen, J. McManus, L. Labeyrie, J. Jouzel, and G. Bonani (1993), Correlations between climate records from North Atlantic sediments and Greenland ice, *Nature*, **365**, 143–147, doi:10.1038/365143a0.

Bourgain, P., and J. C. Gascard (2011), The Arctic Ocean halocline and its interannual variability from 1997 to 2008, *Deep Sea Research Part I: Oceanographic Research Papers*, **58**, 745–756, doi:10.1016/j.dsr.2011.05.001.

Budikova, D. (2009), Role of Arctic sea ice in global atmospheric circulation: A review, *Global and Planetary Change*, **68**, 149–163, doi:10.1016/j.gloplacha.2009.04.001.

Burchard, H., O. Petersen, and T. P. Rippeth (1998), Comparing the performance of the Mellor-Yamada and the κ-ϵ two-equation turbulence models, *Journal of Geophysical Research*, **103**, 10,543–10,554, doi:10.1029/98JC00261.

Burchard, H., K. Bolding, and M. R. Villarreal (1999), GOTM, a general ocean turbulence model. Theory, implementation and test cases, *Technical Report EUR 18745*, European Commission.

Campbell, A. R., J. H. Simpson, and G. L. Allen (1998), The Dynamical Balance of Flow in the Menai Strait, *Estuarine, Coastal and Shelf Science*, **46**, 449–455, doi:10.1006/ecss.1997.0244.

Carmack, E., and F. McLaughlin (2011), Towards recognition of physical and geochemical change in Subarctic and Arctic Seas, *Progress in Oceanography*, **90**, 90–104, doi:10.1016/j.pocean.2011.02.007.

Carton, J. A., Y. Ding, and K. R. Arrigo (2015), The seasonal cycle of the Arctic Ocean under climate change, *Geophysical Research Letters*, **42**, doi:10.1002/2015GL064514.

Cavalieri, D. J., and C. L. Parkinson (2012), Arctic sea ice variability and trends, 1979–2010, *The Cryosphere*, **6**, 881–889, doi:10.5194/tc-6-881-2012.

Coachman, L. K., and C. A. Barnes (1963), The Movement of Atlantic Water in the Arctic Ocean, *Arctic*, **16**, 8–16, doi:10.14430/arctic3517.

Codiga, D. L. (2011), Unified Tidal Analysis and Prediction Using the UTide Matlab Functions, *Technical report 2011-01*, Graduate School of Oceanography, University of Rhode Island, Narragansett, RI.

Comiso, J. C. (2012), Large Decadal Decline of the Arctic Multiyear Ice Cover, *Journal of Climate*, **25**, 1176–1193, doi:10.1175/JCLI-D-11-00113.1.

Condron, A., P. Winsor, C. Hill, and D. Menemenlis (2009), Simulated Response of the Arctic Freshwater Budget to Extreme NAO Wind Forcing, *Journal of Climate*, **22**, 2422–2437, doi:10.1175/2008JCLI2626.1.

Curry, B., C. M. Lee, B. Petrie, R. E. Moritz, and R. Kwok (2014), Multiyear Volume, Liquid Freshwater, and Sea Ice Transports through Davis Strait, 2004–10, *Journal of Physical Oceanography*, **44**, 1244–1266, doi:10.1175/JPO-D-13-0177.1.

Curry, J. A., J. L. Schramm, and E. E. Ebert (1995), Sea Ice-Albedo Climate Feedback Mechanism, *Journal of Climate*, **8**, 240–247, doi:10.1175/1520-0442(1995)008<0240:SIACFM>2.0.CO;2.

Danabasoglu, G., and J. Marshall (2007), Effects of vertical variations of thickness diffusivity in an ocean general circulation model, *Ocean Modelling*, **18**, 122–141, doi:10.1016/j.ocemod.2007.03.006.

Dansgaard, W., S. J. Johnsen, H. B. Clausen, D. Dahl-Jensen, N. S. Gundestrup, C. U. Hammer, C. S. Hvidberg, J. P. Steffensen, A. E. Sveinbjörnsdottir, J. Jouzel, and G. Bond (1993), Evidence for general instability of past climate from a 250-kyr ice-core record, *Nature*, **364**, 218–220, doi:10.1038/364218a0.

D'Asaro, E. A., and M. D. Morehead (1991), Internal waves and velocity fine structure in the Arctic Ocean, *Journal of Geophysical Research*, **96**, 12,725–12,738, doi:10.1029/91JC01071.

D'Asaro, E. A., and J. H. Morison (1992), Internal waves and mixing in the Arctic Ocean, *Deep Sea Research Part A. Oceanographic Research Papers*, **39**, S459–S484, doi:10.1016/S0198-0149(06)80016-6.

Davies, A. M. (1990), On the importance of time varying eddy viscosity in generating higher tidal harmonics, *Journal of Geophysical Research*, **95**, 20,287–20,312, doi:10.1029/JC095iC11p20287.

Davis, P. E. D., C. Lique, and H. L. Johnson (2014), On the Link between Arctic Sea Ice Decline and the Freshwater Content of the Beaufort Gyre : Insights from a Simple Process Model, *Journal of Climate*, **27**, 8170–8184, doi:10.1175/JCLI-D-14-00090.1.

de Boisséson, E., V. Thierry, H. Mercier, and G. Caniaux (2010), Mixed layer heat budget in the Iceland Basin from Argo, *Journal of Geophysical Research*, **115**, C10055, doi:10.1029/2010JC006283.

de Steur, L., E. Hansen, R. Gerdes, M. Karcher, E. Fahrbach, and J. Holfort (2009), Freshwater fluxes in the East Greenland Current: A decade of observations, *Geophysical Research Letters*, **36**, L23611, doi:10.1029/2009GL041278.

de Steur, L., E. Hansen, C. Mauritzen, A. Beszczynska-Möller, and E. Fahrbach (2014), Impact of recirculation on the East Greenland Current in Fram Strait: Results from moored current meter measurements between 1997 and 2009, *Deep Sea Research Part I: Oceanographic Research Papers*, **92**, 26–40, doi:10.1016/j.dsr.2014.05.018.

de Steur, L., R. S. Pickart, D. J. Torres, and H. Valdimarsson (2015), Recent changes in the freshwater composition east of Greenland, *Geophysical Research Letters*, **42**, 2326–2332, doi:10.1002/2014GL062759.

Dee, D. P., S. M. Uppala, A. J. Simmons, P. Berrisford, P. Poli, S. Kobayashi, U. Andrae, M. A. Balmaseda, G. Balsamo, P. Bauer, P. Bechtold, A. C. M. Beljaars, L. van de Berg, J. Bidlot, N. Bormann, C. Delsol, R. Dragani, M. Fuentes, A. J. Geer, L. Haimberger, S. B. Healy, H. Hersbach, E. V. Hólm, L. Isaksen, P. Kå llberg, M. Köhler, M. Matricardi, A. P. McNally, B. M. Monge-Sanz, J. J. Morcrette, B. K. Park, C. Peubey, P. de Rosnay, C. Tavolato, J. N. Thépaut, and F. Vitart (2011), The ERA-Interim reanalysis: configuration and performance of the data assimilation system, *Quarterly Journal of the Royal Meteorological Society*, **137**, 553–597, doi:10.1002/qj.828.

Deser, C., and H. Teng (2008), Recent Trends in Arctic Sea ice and the Evolving Role of Atmospheric Circulation Forcing, 1979–2007, in *Arctic Sea Ice Decline: Observations, Projections, Mechanisms, and Implications*, *Geophysical Monograph Series*, vol. 180, edited by E. T. DeWeaver, C. M. Bitz, and L. B. Tremblay, AGU, Washington D.C., USA, doi:10.1029/180GM03.

Deser, C., R. A. Tomas, and L. Sun (2015), The Role of Ocean-Atmosphere Coupling in the Zonal-Mean Atmospheric Response to Arctic Sea Ice Loss, *Journal of Climate*, **28**, 2168–2186, doi:10.1175/JCLI-D-14-00325.1.

Dickson, B., I. Yashayaev, J. Meincke, B. Turrell, S. Dye, and J. Holfort (2002), Rapid freshening of the deep North Atlantic Ocean over the past four decades, *Nature*, **416**, 832–837, doi:10.1038/416832a.

Dickson, R., B. Rudels, S. Dye, M. Karcher, J. Meincke, and I. Yashayaev (2007), Current estimates of freshwater flux through Arctic and subarctic seas, *Progress in Oceanography*, **73**, 210–230, doi:10.1016/j.pocean.2006.12.003.

Dickson, R. R., J. Meincke, S.-A. Malmberg, and A. J. Lee (1988), The "Great Salinity Anomaly" in the Northern North Atlantic 1968-1982, *Progress in Oceanography*, **20**, 103–151, doi:10.1016/0079-6611(88)90049-3.

Dickson, R. R., T. J. Osborn, J. W. Hurrell, J. Meincke, J. Blindheim, B. Adlandsvik, T. Vinje, G. Alekseev, and W. Maslowski (2000), The Arctic Ocean Response to the North Atlantic Oscillation, *Journal of Climate*, **13**, 2671–2696, doi:10.1175/1520-0442(2000)013<2671:TAORTT>2.0.CO;2.

Dmitrenko, I. A., S. A. Kirillov, and L. B. Tremblay (2008), The long-term and interannual variability of summer fresh water storage over the eastern Siberian shelf: Implication for climatic change, *Journal of Geophysical Research*, **113**, C03007, doi:10.1029/2007JC004304.

Dodd, P. A., B. Rabe, E. Hansen, E. Falck, A. MacKensen, E. Rohling, C. Stedmon, and S. Kristiansen (2012), The freshwater composition of the Fram Strait outflow derived from a decade of tracer measurements, *Journal of Geophysical Research*, **117**, C11005, doi:10.1029/2012JC008011.

Dokken, T. M., K. H. Nisancioglu, C. Li, D. S. Battisti, and C. Kissel (2013), Dansgaard-Oeschger cycles: Interactions between ocean and sea ice intrinsic to the Nordic seas, *Paleoceanography*, **28**, 491–502, doi:10.1002/palo.20042.

Dong, B., and R. T. Sutton (2002), Variability in North Atlantic heat content and heat transport in a coupled ocean-atmosphere GCM, *Climate Dynamics*, **19**, 485–497, doi:10.1007/s00382-002-0239-7.

Dosser, H. V., L. Rainville, and J. M. Toole (2014), Near-Inertial Internal Wave Field in the Canada Basin from Ice-Tethered Profilers, *Journal of Physical Oceanography*, **44**, 413–426, doi:10.1175/JPO-D-13-0117.1.

Dumont, D., Y. Gratton, and T. E. Arbetter (2009), Modeling the Dynamics of the North Water Polynya Ice Bridge, *Journal of Physical Oceanography*, **39**, 1448–1461, doi:10.1175/2008JPO3965.1.

Eady, E. T. (1949), Long Waves and Cyclone Waves, *Tellus A*, **1**, 33–52, doi:10.3402/tellusa.v1i3.8507.

Egbert, G. D., and S. Y. Erofeeva (2002), Efficient Inverse Modeling of Barotropic Ocean Tides, *Journal of Climate*, **19**, 183–204, doi:10.1175/1520-0426(2002)019<0183:EIMOBO>2.0.CO;2.

Egbert, G. D., and R. D. Ray (2000), Significant dissipation of tidal energy in the deep ocean inferred from satellite altimeter data, *Nature*, **405**, 775–778, doi:10.1038/35015531.

Egbert, G. D., and R. D. Ray (2001), Estimates of M2 tidal energy dissipation from TOPEX/Poseidon altimeter data, *Journal of Geophysical Research*, **106**, 22,475–22,502, doi:10.1029/2000JC000699.

Egbert, G. D., and R. D. Ray (2003), Semi-diurnal and diurnal tidal dissipation from TOPEX/Poseidon altimetry, *Geophysical Research Letters*, **30**, 1907, doi:10.1029/2003GL017676.

Emery, W. J., and R. E. Thomson (2004), *Data Analysis Methods in Physical Oceanography*, 2^{nd} ed., Elsevier, Amsterdam.

Fahrbach, E., J. Meincke, S. Ø sterhus, G. Rohardt, U. Schauer, V. Tverberg, and J. Verduin (2001), Direct measurements of volume transports through Fram Strait, *Polar Research*, **20**, 217–224, doi:10.1111/j.1751-8369.2001.tb00059.x.

Falkner, K. K. (2003), Variability and Forcing of Fluxes through Nares Strait and Jones Sound: A Freshwater Emphasis, *Research cruise report: Mission HLY031*, Oregon State University.

Fer, I. (2009), Weak vertical diffusion allows maintenance of cold halocline in the central Arctic, *Atmospheric and Oceanic Science Letters*, **2**, 148–152.

Fer, I. (2014), Near-Inertial Mixing in the Central Arctic Ocean, *Journal of Physical Oceanography*, **44**, 2031–2049, doi:10.1175/JPO-D-13-0133.1.

Ferrari, R., and K. Polzin (2005), Finescale Structure of the *T*-*S* Relation in the Eastern North Atlantic, *Journal of Physical Oceanography*, **38**, 1437–1454, doi:10.1175/JPO2763.1.

Fichot, C. G., K. Kaiser, S. B. Hooker, R. M. W. Amon, M. Babin, S. Bélanger, S. A. Walker, and R. Benner (2013), Pan-Arctic distributions of continental runoff in the Arctic Ocean, *Scientific reports*, **3**, 1053, doi:10.1038/srep01053.

Flocco, D., D. L. Feltham, and A. K. Turner (2010), Incorporation of a physically based melt pond scheme into the sea ice component of a climate model, *Journal of Geophysical Research*, **115**, C08012, doi:10.1029/2009JC005568.

Flocco, D., D. Schroeder, D. L. Feltham, and E. C. Hunke (2012), Impact of melt ponds on Arctic sea ice simulations from 1990 to 2007, *Journal of Geophysical Research*, **117**, C09032, doi:10.1029/2012jc008195.

Foreman, M. G. G., and R. F. Henry (1989), The harmonic analysis of tidal model time series, *Advances in Water Resources*, **12**, 109–120, doi:10.1016/0309-1708(89)90017-1.

Fowler, C., W. Emery, and M. Tschudi (2013), Polar Pathfinder Daily 25 km EASE-Grid Sea Ice Motion Vectors. Version 2, *Tech. rep.*, National Snow and Ice Data Center, Boulder, Colorado, USA.

Francis, J. A., and S. J. Vavrus (2012), Evidence linking Arctic amplification to extreme weather in mid-latitudes, *Geophysical Research Letters*, **39**, L06801, doi:10.1029/2012GL051000.

Furevik, T., and A. Foldvik (1996), Stability at M_2 critical latitude in the Barents Sea, *Journal of Geophysical Research*, **101**, 8823–8837, doi:10.1029/96JC00081.

Fyfe, J. C., and O. A. Saenko (2006), Simulated changes in the extratropical Southern Hemisphere winds and currents, *Geophysical Research Letters*, **33**, L06701, doi:10.1029/2005GL025332.

Garrett, C., and W. Munk (1975), Space-Time Scales of Internal Waves: A Progress Report, *Journal of Geophysical Research*, **80**, 291–297, doi:10.1029/JC080i003p00291.

Gelderloos, R., F. Straneo, and C. A. Katsman (2012), Mechanisms behind the Temporary Shutdown of Deep Convection in the Labrador Sea: Lessons from the Great Salinity Anomaly Years 1968–71, *Journal of Climate*, **25**, 6743–6755, doi:10.1175/JCLI-D-11-00549.1.

Gent, P. R. (2011), The Gent–McWilliams parameterization: 20/20 hindsight, *Ocean Modelling*, **39**, 2–9, doi:10.1016/j.ocemod.2010.08.002.

Giles, K. A., S. W. Laxon, A. L. Ridout, D. J. Wingham, and S. Bacon (2012), Western Arctic Ocean freshwater storage increased by wind-driven spin-up of the Beaufort Gyre, *Nature Geoscience*, **5**, 194–197, doi:10.1038/ngeo1379.

Gill, A. E. (1982), *Atmopshere-Ocean Dynamics*, 662 pp., Academic Press, San Diego, USA and London, UK.

Godin, G., and J. Candela (1987), Tides and currents in Fury and Hecla Strait, *Estuarine, Coastal and Shelf Science*, **24**, 513–525, doi:10.1016/0272-7714(87)90131-4.

Goldenberg, S. B., C. W. Landsea, A. M. Mestas-Nuñez, and W. M. Gray (2001), The Recent Increase in Atlantic Hurricane Activity: Causes and Implications, *Science*, **293**, 474–479, doi:10.1126/science.1060040.

Gornitz, V., and I. Fung (1994), Potential distribution of methane hydrates in the world's oceans, *Global Biogeochemical Cycles*, **8**, 335–347, doi:10.1029/94GB00766.

Gregg, M. C. (1989), Scaling turbulent dissipation in the thermocline, *Journal of Geophysical Research*, **94**, 9686–9698, doi:10.1029/JC094iC07p09686.

Greisman, P., S. Grant, A. Blaskovich, and B. van Hardenburg (1986), Tidal Propagation Measurements in Baffin Bay, Lancaster Sound, and Nares Strait, *Canadian Contractor Report of Hydrography and Ocean Sciences No. 25*, Bedford Institute of Oceanography.

Guthrie, J. D., J. H. Morison, and I. Fer (2013), Revisiting internal waves and mixing in the Arctic Ocean, *Journal of Geophysical Research*, **118**, 3966–3977, doi:10.1002/jgrc.20294.

Haine, T. W. N., B. Curry, R. Gerdes, E. Hansen, M. Karcher, C. Lee, B. Rudels, G. Spreen, L. de Steur, K. D. Stewart, and R. Woodgate (2015), Arctic freshwater export: Status, mechanisms, and prospects, *Global and Planetary Change*, **125**, 13–35, doi:10.1016/j.gloplacha.2014.11.013.

Häkkinen, S., and A. Proshutinsky (2004), Freshwater content variability in the Arctic Ocean, *Journal of Geophysical Research*, **109**, C03051, doi:10.1029/2003JC001940.

Halle, C., and R. Pinkel (2003), Internal wave variability in the Beaufort Sea during the winter of 1993/1994, *Journal of Geophysical Research*, **108**, 3210, doi:10.1029/2000JC000703.

Hansen, B., S. Østerhus, W. R. Turrell, S. Jónsson, H. Valdimarsson, H. Hátún, and S. M. Olsen (2008), The Inflow of Atlantic Water, Heat, and Salt to the Nordic Seas Across the Greenland–Scotland Ridge, in *Arctic-Subarctic Ocean Fluxes: Defining the Role of the Northern Seas in Climate*, edited by R. R. Dickson, J. Meincke, and P. Rhines, pp. 15–43, Springer-Verlag, doi:10.1007/978-1-4020-6774-7_2.

Hassol, S. J. (2004), *Impacts of a Warming Arctic: Arctic Climate Impact Assessment*, Cambridge University Press, Cambridge, United Kingdom and New York, NY, USA.

Held, I. M., and B. J. Soden (2006), Robust Responses of the Hydrological Cycle to Global Warming, *Journal of Climate*, **19**, 5686–5699, doi:10.1175/JCLI3990.1.

Henyey, F. S., J. Wright, and S. M. Flatté (1986), Energy and action flow through the internal wave field: An eikonal approach, *Journal of Geophysical Research*, **91**, 8487–8495, doi:10.1029/JC091iC07p08487.

Hibler, W. D. (1979), A Dynamic Thermodynamic Sea Ice Model, *Journal of Physical Oceanography*, **9**, 815–846, doi:10.1175/1520-0485(1979)009<0815:ADTSIM>2.0.CO;2.

Holland, M. M., J. Finnis, A. P. Barrett, and M. Serreze (2007), Projected changes in Arctic Ocean freshwater budgets, *Journal of Geophysical Research*, **112**, G04S55, doi:10.1029/2006JG000354.

Holloway, G. (1992), Representing Topographic Stress for Large-Scale Ocean Models, *Journal of Physical Oceanography*, **22**, 1033–1046, doi:10.1175/1520-0485(1992)022<1033:RTSFLS>2.0.CO;2.

Holloway, G., and A. Proshutinsky (2007), Role of tides in Arctic ocean/ice climate, *Journal of Geophysical Research*, **112**, C04S06, doi:10.1029/2006JC003643.

Holloway, G., F. Dupont, E. Golubeva, S. Häkkinen, E. Hunke, M. Jin, M. Karcher, F. Kauker, M. Maltrud, M. A. Morales Maqueda, W. Maslowski, G. Platov, D. Stark, M. Steele, T. Suzuki, J. Wang, and J. Zhang (2007), Water properties and circulation in Arctic Ocean models, *Journal of Geophysical Research*, **112**, C04S03, doi:10.1029/2006JC003642.

Howarth, M. J. (1998), The effect of stratification on tidal current profiles, *Continental Shelf Research*, **18**, 1235–1254, doi:10.1016/S0278-4343(98)00042-9.

Huber, C., M. Leuenberger, R. Spahni, J. Flückiger, J. Schwander, T. F. Stocker, S. Johnsen, A. Landais, and J. Jouzel (2006), Isotope calibrated Greenland temperature record over Marine Isotope Stage 3 and its relation to CH_4, *Earth and Planetary Science Letters*, **243**, 504–519, doi:10.1016/j.epsl.2006.01.002.

Huntington, H. P. (2001), *Arctic Flora and Fauna. Status and Conservation*, Arctic Council: Conservation of Arctic Flora and Fauna Working Group (CAFF).

Jackson, J. M., E. C. Carmack, F. A. McLaughlin, S. E. Allen, and R. G. Ingram (2010), Identification, characterization, and change of the near-surface temperature maximum in the Canada Basin, 1993–2008, *Journal of Geophysical Research*, **115**, C05021, doi:10.1029/2009JC005265.

Jackson, J. M., S. E. Allen, F. A. McLaughlin, R. A. Woodgate, and E. C. Carmack (2011), Changes to the near-surface waters in the Canada Basin, Arctic Ocean from 1993–2009: A basin in transition, *Journal of Geophysical Research*, **116**, C10008, doi:10.1029/2011JC007069.

Jackson, L. C., R. Kahana, T. Graham, M. A. Ringer, T. Woollings, J. V. Mecking, and R. A. Wood (2015), Global and European climate impacts of a slowdown of the AMOC in a high resolution GCM, *Climate Dynamics*, doi:10.1007/s00382-015-2540-2.

Jahn, A., and M. M. Holland (2013), Implications of Arctic sea ice changes for North Atlantic deep convection and the meridional overturning circulation in CCSM4-CMIP5 simulations, *Geophysical Research Letters*, **40**, 1206–1211, doi:10.1002/grl.50183.

Jahn, A., B. Tremblay, L. A. Mysak, and R. Newton (2010), Effect of the large-scale atmospheric circulation on the variability of the Arctic Ocean freshwater export, *Climate Dynamics*, **34**, 201–222, doi:10.1007/s00382-009-0558-z.

Jahn, A., Y. Aksenov, B. A. de Cuevas, L. de Steur, S. Häkkinen, E. Hansen, C. Herbaut, M. N. Houssais, M. Karcher, F. Kauker, C. Lique, A. Nguyen, P. Pemberton, D. Worthen, and J. Zhang (2012), Arctic Ocean freshwater: How robust are model simulations?, *Journal of Geophysical Research*, **117**, C00D16, doi:10.1029/2012JC007907.

Jaiser, R., K. Dethloff, D. Handorf, A. Rinke, and J. Cohen (2012), Impact of sea ice cover changes on the Northern Hemisphere atmospheric winter circulation, *Tellus, Series A: Dynamic Meteorology and Oceanography*, **64**, 11595, doi:10.3402/tellusa.v64i0.11595.

Jakobsson, M., A. Grantz, Y. Kristoffersen, and R. Macnab (2004), Bathymetry and physiography of the arctic ocean and its constituent seas, in *The Organic Carbon Cycle in the Arctic Ocean*, pp. 1–6, Springer, Heidelberg, doi:10.1007/978-3-642-18912-8.

Jakobsson, M., R. Macnab, L. Mayer, R. Anderson, M. Edwards, J. Hatzky, H. W. Schenke, and P. Johnson (2008), An improved bathymetric portrayal of the Arctic Ocean: Implications for ocean modeling and geological, geophysical and oceanographic analyses, *Geophysical Research Letters*, **35**, L07602, doi:10.1029/2008GL033520.

Jakobsson, M., L. Mayer, B. Coakley, J. A. Dowdeswell, S. Forbes, B. Fridman, H. Hodnesdal, R. Noormets, R. Pedersen, M. Rebesco, H. W. Schenke, Y. Zarayskaya, D. Accettella, A. Armstrong, R. M. Anderson, P. Bienhoff, A. Camerlenghi, I. Church, M. Edwards, J. V. Gardner, J. K. Hall, B. Hell, O. Hestvik, Y. Kristoffersen, C. Marcussen, R. Mohammad, D. Mosher, S. V. Nghiem, M. T. Pedrosa, P. G. Travaglini, and P. Weatherall (2012), The International Bathymetric Chart of the Arctic Ocean (IBCAO) Version 3.0, *Geophysical Research Letters*, **39**, L12609, doi:10.1029/2012GL052219.

Jeffries, M. O., J. E. Overland, and D. K. Perovich (2013), The Arctic shifts to a new normal, *Physics Today*, **66**, 35–40, doi:10.1063/PT.3.2147.

Johns, W. E., M. O. Baringer, L. M. Beal, S. A. Cunningham, T. Kanzow, H. L. Bryden, J. J. M. Hirschi, J. Marotzke, C. S. Meinen, B. Shaw, and R. Curry (2011), Continuous, Array-Based Estimates of Atlantic Ocean Heat Transport at 26.5 °N, *Journal of Climate*, **24**, 2429–2449, doi:10.1175/2010JCLI3997.1.

Johnson, H. L., and D. P. Marshall (2002), A Theory for the Surface Atlantic Response to Thermohaline Variability, *Journal of Physical Oceanography*, **32**, 1121–1132, doi:10.1175/1520-0485(2002)032<1121:ATFTSA>2.0.CO;2.

Johnson, M., S. Gaffigan, E. Hunke, and R. Gerdes (2007), A comparison of Arctic Ocean sea ice concentration among the coordinated AOMIP model experiments, *Journal of Geophysical Research*, **112**, C04S11, doi:10.1029/2006JC003690.

Jones, E. P. (2001), Circulation in the Arctic Ocean, *Polar Research*, **20**, 139–146, doi:10.1111/j.1751-8369.2001.tb00049.x.

Jones, E. P., L. G. Anderson, and J. H. Swift (1998), Distribution of Atlantic and Pacific waters in the upper Arctic Ocean: Implications for circulation, *Geophysical Research Letters*, **25**, 765–768, doi:10.1029/98GL00464.

Jones, E. P., J. H. Swift, L. G. Anderson, M. Lipizer, G. Civitarese, K. K. Falkner, G. Kattner, and F. McLaughlin (2003), Tracing Pacific water in the North Atlantic Ocean, *Journal of Geophysical Research*, **108**, 3116, doi:10.1029/2001JC001141.

Karcher, M., F. Kauker, R. Gerdes, E. Hunke, and J. Zhang (2007), On the dynamics of Atlantic Water circulation in the Arctic Ocean, *Journal of Geophysical Research*, **112**, C04S02, doi:10.1029/2006JC003630.

Karcher, M., J. N. Smith, F. Kauker, R. Gerdes, and W. M. Smethie (2012), Recent changes in Arctic Ocean circulation revealed by iodine-129 observations and modeling, *Journal of Geophysical Research*, **117**, C08007, doi:10.1029/2011JC007513.

Karcher, M. J., and J. M. Oberhuber (2002), Pathways and modification of the upper and intermediate waters of the Arctic Ocean, *Journal of Geophysical Research*, **107**, 3049, doi:10.1029/2000JC000530.

Kattsov, V. M., J. E. Walsh, W. L. Chapman, V. A. Govorkova, T. V. Pavlova, and X. Zhang (2007), Simulation and Projection of Arctic Freshwater Budget Components by the IPCC AR4 Global Climate Models, *Journal of Hydrometeorology*, **8**, 571–589, doi:10.1175/JHM575.1.

Kawaguchi, Y., S. Nishino, and J. Inoue (2015), Fixed-Point Observation of Mixed Layer Evolution in the Seasonally Ice-Free Chukchi Sea: Turbulent Mixing due to Gale Winds and Internal Gravity Waves, *Journal of Physical Oceanography*, **45**, 836–853, doi:10.1175/JPO-D-14-0149.1.

Kerr, R. A. (2010), Climate change. 'Arctic Armageddon' Needs More Science, Less Hype, *Science*, **329**, 620–621, doi:10.1126/science.329.5992.620.

Killworth, P. D., and J. M. Smith (1984), A one-and-a-half dimensional model for the Arctic halocline, *Deep Sea Research Part A. Oceanographic Research Papers*, **31**, 271–293, doi:10.1016/0198-0149(84)90105-5.

Koch-Larrouy, A., G. Madec, P. Bouruet-Aubertot, T. Gerkema, L. Bessières, and R. Molcard (2007), On the transformation of Pacific Water into Indonesian Throughflow Water by internal tidal mixing, *Geophysical Research Letters*, **34**, L04604, doi:10.1029/2006GL028405.

Koenigk, T., U. Mikolajewicz, H. Haak, and J. Jungclaus (2007), Arctic freshwater export in the 20th and 21st centuries, *Journal of Geophysical Research*, **112**, G04S41, doi:10.1029/2006JG000274.

Kowalik, Z., and A. Y. Proshutinsky (1993), Diurnal tides in the Arctic Ocean, *Journal of Geophysical Research*, **98**, 16,449–16,468, doi:10.1029/93JC01363.

Kowalik, Z., and A. Y. Proshutinsky (1994), The Arctic Ocean Tides, in *The Polar Oceans and Their Role in Shaping the Global Environment*, *Geophysical Monograph Series*, vol. 85, edited by O. M. Johannessen, R. D. Muench, and J. E. Overland, pp. 137–158, American Geophysical Union, Washington D.C., doi:10.1029/GM085.

Krishfield, R. A., A. Proshutinsky, K. Tateyama, W. J. Williams, E. C. Carmack, F. A. McLaughlin, and M.-L. Timmermans (2014), Deterioration of perennial sea ice in the Beaufort Gyre from 2003 to 2012 and its impact on the oceanic freshwater cycle, *Journal of Geophysical Research*, **119**, 1271–1305, doi:10.1002/2013JC008999.

Kwok, R., and J. Morison (2011), Dynamic topography of the ice-covered Arctic Ocean from ICESat, *Geophysical Research Letters*, **38**, L02501, doi:10.1029/2010GL046063.

Kwok, R., and D. A. Rothrock (2009), Decline in Arctic sea ice thickness from submarine and ICESat records: 1958-2008, *Geophysical Research Letters*, **36**, L15501, doi:10.1029/2009GL039035.

Kwok, R., G. F. Cunningham, M. Wensnahan, I. Rigor, H. J. Zwally, and D. Yi (2009), Thinning and volume loss of the Arctic Ocean sea ice cover: 2003–2008, *Journal of Geophysical Research*, **114**, C07005, doi:10.1029/2009JC005312.

Large, W. G., J. C. Mcwilliams, and S. C. Doney (1994), Oceanic vertical mixing: A review and a model with a nonlocal boundary layer parameterization, *Review of Geophysics*, **32**, 363–403, doi:10.1029/94RG01872.

Lavelle, J. W., and H. O. Mofjeld (1983), Effects of time-varying viscosity on oscillatory turbulent channel flow, *Journal of Geophysical Research*, **88**, 7607–7616, doi:10.1029/JC088iC12p07607.

Laxon, S. W., K. A. Giles, A. L. Ridout, D. J. Wingham, R. Willatt, R. Cullen, R. Kwok, A. Schweiger, J. Zhang, C. Haas, S. Hendricks, R. Krishfield, N. Kurtz, S. Farrell, and M. Davidson (2013), CryoSat-2 estimates of Arctic sea ice thickness and volume, *Geophysical Research Letters*, **40**, 732–737, doi:10.1002/grl.50193.

Leu, E., J. E. Søreide, D. O. Hessen, S. Falk-Petersen, and J. Berge (2011), Consequences of changing sea-ice cover for primary and secondary producers in the European Arctic shelf seas: Timing, quantity, and quality, *Progress in Oceanography*, **90**, 18–32, doi:10.1016/j.pocean.2011.02.004.

Levine, M. D., C. A. Paulson, and J. H. Morison (1985), Internal Waves in the Arctic Ocean: Comparisons with Lower-Latitude Observations, *Journal of Physical Oceanography*, **15**, 800–809, doi:10.1175/1520-0485(1985)015<0800:iwitao>2.0.co;2.

Levine, M. D., C. A. Paulson, and J. H. Morison (1987), Observations of internal gravity waves under the Arctic pack ice, *Journal of Geophysical Research*, **92**, 779–782, doi:10.1029/JC092iC01p00779.

Lewis, E. L., E. P. Jones, P. Lemke, T. D. Prowse, and P. Wadhams (2000), *The Freshwater Budget of the Arctic Ocean*, Kluwer Academic Publishers, Dordrecht, The Netherlands.

Lien, V. S., F. B. Vikebø, and Ø. Skagseth (2013), One mechanism contributing to covariability of the Atlantic inflow branches to the Arctic, *Nature communications*, **4**, 1488, doi:10.1038/ncomms2505.

Linders, J., and G. Björk (2013), The melt-freeze cycle of the Arctic Ocean ice cover and its dependence on ocean stratification, *Journal of Geophysical Research*, **118**, 5963–5976, doi:10.1002/jgrc.20409.

Lindsay, R. W., and J. Zhang (2005), The Thinning of Arctic Sea Ice, 1988–2003: Have We Passed a Tipping Point?, *Journal of Climate*, **18**, 4879–4894, doi:10.1175/JCLI3587.1.

Lique, C., and M. Steele (2012), Where can we find a seasonal cycle of the Atlantic water temperature within the Arctic Basin?, *Journal of Geophysical Research*, **117**, C03026, doi:10.1029/2011JC007612.

Lique, C., A. M. Treguier, M. Scheinert, and T. Penduff (2009), A model-based study of ice and freshwater transport variability along both sides of Greenland, *Climate Dynamics*, **33**, 685–705, doi:10.1007/s00382-008-0510-7.

Lique, C., A. M. Treguier, B. Blanke, and N. Grima (2010), On the origins of water masses exported along both sides of Greenland: A Lagrangian model analysis, *Journal of Geophysical Research*, **115**, C05019, doi:10.1029/2009JC005316.

Lique, C., J. D. Guthrie, M. Steele, A. Proshutinsky, J. H. Morison, and R. Krishfield (2014), Diffusive vertical heat flux in the Canada Basin of the Arctic Ocean inferred from moored instruments, *Journal of Geophysical Research*, **119**, 496–508, doi:10.1002/2013JC009346.

Lique, C., H. L. Johnson, and P. E. D. Davis (2015), On the interplay between the circulation in the surface and the intermediate layers of the Arctic Ocean, *Journal of Physical Oceanography*, doi:10.1175/JPO-D-14-0183.1.

Liu, J., J. A. Curry, H. Wang, M. Song, and R. M. Horton (2012), Impact of declining Arctic sea ice on winter snowfall, *Proceedings of the National Academy of Sciences*, **109**, 4074–4079, doi:10.1073/pnas.1114910109.

Maas, L. R. M., and J. J. M. van Haren (1987), Observations on the vertical structure of tidal and inertial currents in the central North Sea, *Journal of Marine Research*, **45**, 293–318, doi:10.1357/002224087788401106.

MacGilchrist, G. A., A. C. Naveira Garabato, T. Tsubouchi, S. Bacon, S. Torres-Valdés, and K. Azetsu-Scott (2014), The Arctic Ocean carbon sink, *Deep Sea Research Part I: Oceanographic Research Papers*, **86**, 39–55, doi:10.1016/j.dsr.2014.01.002.

Madsen, O. S. (1977), A Realistic Model of the Wind-Induced Ekman Boundary Layer, *Journal of Physical Oceanography*, **7**, 248–255, doi:10.1175/1520-0485(1977)007<0248:ARMOTW>2.0.CO;2.

Makinson, K. (2002), Modeling Tidal Current Profiles and Vertical Mixing Beneath Filchner–Ronne Ice Shelf, Antarctica, *Journal of Physical Oceanography*, **32**, 202–215, doi:10.1175/1520-0485(2002)032<0202:MTCPAV>2.0.CO;2.

Makinson, K., M. Schröder, and S. Østerhus (2006), Effect of critical latitude and seasonal stratification on tidal current profiles along Ronne Ice Front, Antarctica, *Journal of Geophysical Research*, **111**, C03022, doi:10.1029/2005JC003062.

Markus, T., J. C. Stroeve, and J. Miller (2009), Recent changes in Arctic sea ice melt onset, freezeup, and melt season length, *Journal of Geophysical Research*, **114**, C12024, doi:10.1029/2009JC005436.

Marshall, J., H. Jones, K. R, and W. R (2002), Can Eddies Set Ocean Stratification?, *Journal of Physical Oceanography*, **32**, 26–38, doi:10.1175/1520-0485(2002)032<0026:CESOS>2.0.CO;2.

Martin, T., and R. Gerdes (2007), Sea ice drift variability in Arctic Ocean Model Intercomparison Project models and observations, *Journal of Geophysical Research*, **112**, C04S10, doi:10.1029/2006JC003617.

Martin, T., M. Steele, and J. Zhang (2014), Seasonality and long-term trend of Arctic Ocean surface stress in a model, *Journal of Geophysical Research*, **119**, 1723–1738, doi:10.1002/2013JC009425.

Martinson, D. G. (1990), Evolution of the southern ocean winter mixed layer and sea ice: Open ocean deepwater formation and ventilation, *Journal of Geophysical Research*, **95**, 11,641–11,654, doi:10.1029/JC095iC07p11641.

Martinson, D. G., and R. A. Iannuzzi (1998), Antarctic Ocean-Ice Interactions: Implications from Ocean Bulk Property Distributions in the Weddell Gyre, in *Antarctic Research Series Volume on Antarctic Sea Ice Physical Properties and Processes*, *Antarctic Research Series*, vol. 74, edited by M. O. Jeffries, pp. 243–271, American Geophysical Union, Washington, D. C.

Martinson, D. G., and M. Steele (2001), Future of the Arctic sea ice cover: Implications of an Antarctic analog, *Geophysical Research Letters*, **28**, 307–310, doi:10.1029/2000GL011549.

Maslanik, J., and J. Stroeve (1999), updated daily, *Near-Real-Time DMSP SSM/I-SSMIS Daily Polar Gridded Sea Ice Concentrations*, pp. Boulder, Colorado USA: NASA DAAC at the National Snow and Ice Data Center.

Maslanik, J., J. Stroeve, C. Fowler, and W. Emery (2011), Distribution and trends in Arctic sea ice age through spring 2011, *Geophysical Research Letters*, **38**, L13502, doi:10.1029/2011GL047735.

Maslanik, J. A., C. Fowler, J. Stroeve, S. Drobot, J. Zwally, D. Yi, and W. Emery (2007), A younger, thinner Arctic ice cover: Increased potential for rapid, extensive sea-ice loss, *Geophysical Research Letters*, **34**, L24501, doi:10.1029/2007GL032043.

Mauritzen, C. (2012), Oceanography: Arctic freshwater, *Nature Geoscience*, **5**, 162–164, doi:10.1038/ngeo1409.

Maykut, G. A., and N. Untersteiner (1971), Some results from a time-dependent thermodynamic model of sea ice, *Journal of Geophysical Research*, **76**, 1550–1575, doi:10.1029/JC076i006p01550.

McGeehan, T., and W. Maslowski (2012), Evaluation and control mechanisms of volume and freshwater export through the Canadian Arctic Archipelago in a high-resolution pan-Arctic ice-ocean model, *Journal of Geophysical Research*, **117**, C00D14, doi:10.1029/2011JC007261.

McLaughlin, F., E. Carmack, R. Macdonald, A. J. Weaver, and J. Smith (2002), The Canada Basin, 1989–1995: Upstream events and far-field effects of the Barents Sea, *Journal of Geophysical Research*, **107**, 3082, doi:10.1029/2001JC000904.

McLaughlin, F. A., E. C. Carmack, W. J. Williams, S. Zimmermann, K. Shimada, and M. Itoh (2009), Joint effects of boundary currents and thermohaline intrusions on the warming of Atlantic water in the Canada Basin, 1993-2007, *Journal of Geophysical Research*, **114**, C00A12, doi:10.1029/2008JC005001.

McPhee, M. G. (2012), Advances in understanding ice–ocean stress during and since AIDJEX, *Cold Regions Science and Technology*, **76-77**, 24–36, doi:10.1016/j.coldregions.2011.05.001.

McPhee, M. G. (2013), Intensification of Geostrophic Currents in the Canada Basin, Arctic Ocean, *Journal of Climate*, **26**, 3,130–3,138, doi:10.1175/JCLI-D-12-00289.1.

McPhee, M. G., A. Proshutinsky, J. H. Morison, M. Steele, and M. B. Alkire (2009), Rapid change in freshwater content of the Arctic Ocean, *Geophysical Research Letters*, **36**, L10602, doi:10.1029/2009GL037525.

Melling, H. (2000), Exchanges of Freshwater Through the Shallow Straits of the North American Arctic, in *The Freshwater Budget of the Arctic Ocean*, edited by E. L. Lewis, E. P. Jones, P. Lemke, T. D. Prowse, and P. Wadhams, NATO Science Series, pp. 479–502, Springer Netherlands.

Melling, H. (2002), Sea ice of the northern Canadian Arctic Archipelago, *Journal of Geophysical Research*, **107**, 3181, doi:10.1029/2001JC001102.

Melling, H. (2004), Fluxes Through the Northern Canadian Arctic Archipelago, *ASOF Newsletter*, **2**, 3–7.

Melling, H. (2006), CCGS Henry Larsen, 9th August - 1st September 2006. Canadian Arctic Through-Flow 2006 Cruise to Nares Strait, *Cruise Report 2006-28*, Institute of Ocean Sciences.

Melling, H. (2007), CCGS Henry Larsen, 9th August - 1st September 2007. Canadian Arctic Through-Flow 2007 Cruise to Nares Strait, *Cruise Report 2007-52*, Institute of Ocean Sciences.

Melling, H. (2009), CCGS Henry Larsen, 8th August - 1st September 2009. Canadian Arctic Through Flow 2009 Cruise to Nares Cardigan & Penny Straits, *Cruise Report 2009-05*, Institute of Ocean Sciences.

Melling, H. (2012), CCGS Henry Larsen, 2nd August - 17th August 2012. Canadian Arctic Through-Flow 2012 Cruise to Nares Strait, *Cruise Report 2012-20*, Institute of Ocean Sciences.

Melling, H., Y. Gratton, and G. Ingram (2001), Ocean circulation within the North Water polynya of Baffin Bay, *Atmosphere-Ocean*, **39**, 301–325, doi:10.1080/07055900.2001.9649683.

Melling, H., T. A. Agnew, K. K. Falkner, D. A. Greenberg, C. M. Lee, A. Münchow, B. Petrie, S. J. Prinsenberg, R. M. Samelson, and R. A. Woodgate (2008), Fresh-Water Fluxes via Pacific and Arctic Outflows across the Canadian Polar Shelf, in *Arctic-Subarctic Ocean Fluxes: Defining the Role of the Northern Seas in Climate*, edited by R. R. Dickson, J. Meincke, and P. Rhines, pp. 193–247, Springer-Verlag, doi:10.1007/978-1-4020-6774-7_10.

Morison, J., R. Kwok, C. Peralta-Ferriz, M. Alkire, I. Rigor, R. Andersen, and M. Steele (2012), Changing Arctic Ocean freshwater pathways, *Nature*, **481**, 66–70, doi:10.1038/nature10705.

Morison, J. H., C. E. Long, and M. D. Levine (1985), Internal wave dissipation under sea ice, *Journal of Geophysical Research*, **90**, 11,959–11,966, doi:10.1029/JC090iC06p11959.

Morrison, A. K., and A. M. Hogg (2013), On the Relationship between Southern Ocean Overturning and ACC Transport, *Journal of Physical Oceanography*, **43**, 140–148, doi:10.1175/JPO-D-12-057.1.

Münchow, A., and H. Melling (2008), Ocean current observations from Nares Strait to the west of Greenland : Interannual to tidal variability and forcing, *Journal of Marine Research*, **66**, 801–833, doi:10.1357/002224008788064612.

Münchow, A., H. Melling, and K. K. Falkner (2006), An Observational Estimate of Volume and Freshwater Flux Leaving the Arctic Ocean through Nares Strait, *Journal of Physical Oceanography*, **36**, 2025–2041, doi:10.1175/JPO2962.1.

Münchow, A., K. K. Falkner, and H. Melling (2007), Spatial continuity of measured seawater and tracer fluxes through Nares Strait, a dynamically wide channel bordering the Canadian Archipelago, *Journal of Marine Research*, **65**, 759–788, doi:10.1357/002224007784219048.

Munday, D. R., H. L. Johnson, and D. P. Marshall (2013), Eddy Saturation of Equilibrated Circumpolar Currents, *Journal of Physical Oceanography*, **43**, 507–532, doi:10.1175/JPO-D-12-095.1.

Munk, W., and C. Wunsch (1998), Abyssal recipes II: energetics of tidal and wind mixing, *Deep-Sea Research Part I: Oceanographic Research Papers*, **45**, 1977–2010, doi:10.1016/S0967-0637(98)00070-3.

Munk, W. H. (1966), Abyssal recipes, *Deep Sea Research and Oceanographic Abstracts*, **13**, 707–730, doi:10.1016/0011-7471(66)90602-4.

Nazarenko, L., G. Holloway, and N. Tausnev (1998), Dynamics of transport of "Atlantic signature" in the Arctic Ocean, *Journal of Geophysical Research*, **103**, 31,003–31,015, doi:10.1029/1998JC900017.

Nishino, S., Y. Kawaguchi, J. Inoue, T. Hirawake, A. Fujiwara, R. Futsuki, J. Onodera, and M. Aoyama (2015), Nutrient supply and biological response to wind-induced mixing, inertial motion, internal waves, and currents in the northern Chukchi Sea, *Journal of Geophysical Research*, **120**, 1975–1992, doi:10.1002/2014JC010407.

Nummelin, A., C. Li, and L. H. Smedsrud (2015), Response of Arctic Ocean stratification to changing river runoff in a column model, *Journal of Geophysical Research*, **120**, doi:10.1002/2014JC010571.

Ogi, M., and J. M. Wallace (2012), The role of summer surface wind anomalies in the summer Arctic sea ice extent in 2010 and 2011, *Geophysical Research Letters*, **39**, L09704, doi:10.1029/2012GL051330.

Overland, J. E., and M. Wang (2010), Large-scale atmospheric circulation changes are associated with the recent loss of Arctic sea ice, *Tellus, Series A: Dynamic Meteorology and Oceanography*, **62**, doi:10.1111/j.1600-0870.2009.00421.x.

Overland, J. E., and M. Wang (2013), When will the summer Arctic be nearly sea ice free?, *Geophysical Research Letters*, **40**, 2097–2101, doi:10.1002/grl.50316.

Overland, J. E., J. M. Adams, and N. A. Bond (1997), Regional Variation of Winter Temperatures in the Arctic, *Journal of Climate*, **10**, 821–837, doi:10.1175/1520-0442(1997)010<0821:rvowti>2.0.co;2.

Overland, J. E., J. A. Francis, E. Hanna, and M. Wang (2012), The recent shift in early summer Arctic atmospheric circulation, *Geophysical Research Letters*, **39**, L19804, doi:10.1029/2012GL053268.

Overland, J. E., M. Wang, J. E. Walsh, and J. C. Stroeve (2013), Future Arctic climate changes : Adaptation and mitigation time scales, *Earth's Future*, **2**, 68–74, doi:10.1002/2013EF000162.

Pacanowski, R. C., and G. H. Philander (1981), Paramterization of Vertical Mixing in Numerical Models of Tropical Oceans, *Journal of Physical Oceanography*, **11**, 1443–1451, doi:10.1175/1520-0485(1981)011<1443:povmin>2.0.co;2.

Padman, L., and S. Erofeeva (2004), A barotropic inverse tidal model for the Arctic Ocean, *Geophysical Research Letters*, **31**, L02303, doi:10.1029/2003GL019003.

Parkinson, C. L., and J. C. Comiso (2013), On the 2012 record low Arctic sea ice cover: Combined impact of preconditioning and an August storm, *Geophysical Research Letters*, **40**, 1356–1361, doi:10.1002/grl.50349.

Peacock, N. R., and S. W. Laxon (2004), Sea surface height determination in the Arctic Ocean from ERS altimetry, *Journal of Geophysical Research*, **109**, C07001, doi:10.1029/2001JC001026.

Peralta-Ferriz, C., and R. A. Woodgate (2015a), Seasonal and interannual variability of pan-Arctic surface mixed layer properties from 1979 to 2012 from hydrographic data, and the dominance of stratification for multiyear mixed layer depth shoaling, *Progress in Oceanography*, doi:10.1016/j.pocean.2014.12.005.

Peralta-Ferriz, C., and R. A. Woodgate (2015b), Seasonal and interannual variability of pan-Arctic surface mixed layer properties from 1979 to 2012 from hydrographic data, and the dominance of stratification for multiyear mixed layer depth shoaling, *Progress in Oceanography*, doi:10.1016/j.pocean.2014.12.005.

Peralta-Ferriz, C., J. H. Morison, J. M. Wallace, and J. Zhang (2011), A basin-coherent mode of sub-monthly variability in Arctic Ocean bottom pressure, *Geophysical Research Letters*, **38**, L14606, doi:10.1029/2011GL048142.

Peralta-Ferriz, C., J. H. Morison, J. M. Wallace, J. A. Bonin, and J. Zhang (2014), Arctic Ocean Circulation Patterns Revealed by GRACE, *Journal of Climate*, **27**, 1445–1468, doi:10.1175/JCLI-D-13-00013.1.

Perovich, D. K., T. C. Grenfell, B. Light, and P. V. Hobbs (2002), Seasonal evolution of the albedo of multiyear Arctic sea ice, *Journal of Geophysical Research*, **107**, 8044, doi:10.1029/2000JC000438.

Perovich, D. K., B. Light, H. Eicken, K. F. Jones, K. Runciman, and S. V. Nghiem (2007), Increasing solar heating of the Arctic Ocean and adjacent seas, 1979–2005: Attribution and role in the ice-albedo feedback, *Geophysical Research Letters*, **34**, L19505, doi:10.1029/2007GL031480.

Perovich, D. K., J. A. Richter-Menge, K. F. Jones, and B. Light (2008), Sunlight, water, and ice: Extreme Arctic sea ice melt during the summer of 2007, *Geophysical Research Letters*, **35**, L11501, doi:10.1029/2008GL034007.

Peterson, B. J., R. M. Holmes, J. W. McClelland, C. J. Vörösmarty, R. B. Lammers, A. I. Shiklomanov, I. A. Shiklomanov, and S. Rahmstorf (2002), Increasing River Discharge to the Arctic Ocean, *Science*, **298**, 2171–2173, doi:10.1126/science.1077445.

Peterson, I., J. Hamilton, S. Prinsenberg, and R. Pettipas (2012), Wind-forcing of volume transport through Lancaster Sound, *Journal of Geophysical Research*, **117**, C11018, doi:10.1029/2012JC008140.

Pickart, R. S., G. W. K. Moore, D. J. Torres, P. S. Fratantoni, R. A. Goldsmith, and J. Yang (2009), Upwelling on the continental slope of the Alaskan Beaufort Sea: Storms, ice, and oceanographic response, *Journal of Geophysical Research*, **114**, C00A13, doi:10.1029/2008JC005009.

Pinkel, R. (2005), Near-Inertial Wave Propagation in the Western Arctic, *Journal of Physical Oceanography*, **35**, 645–665, doi:10.1175/JPO2715.1.

Pinker, R. T., X. Niu, and Y. Ma (2014), Solar heating of the Arctic Ocean in the context of ice-albedo feedback, *Journal of Geophysical Research*, **119**, 8395–8409, doi:10.1002/2014JC010232.

Plueddemann, A. J. (1992), Internal wave observations from the Arctic environmental drifting buoy, *Journal of Geophysical Research*, **97**, 12,619–12,638, doi:10.1029/92JC01098.

Polyakov, I. V., G. V. Alekseev, L. A. Timokhov, U. S. Bhatt, R. L. Colony, H. L. Simmons, D. Walsh, J. E. Walsh, and V. F. Zakharov (2004), Variability of the Intermediate Atlantic Water of the Arctic Ocean over the Last 100 Years, *Journal of Climate*, **17**, 4485–4497, doi:10.1175/JCLI-3224.1.

Polyakov, I. V., A. Beszczynska, E. C. Carmack, I. A. Dmitrenko, E. Fahrbach, I. E. Frolov, R. Gerdes, E. Hansen, J. Holfort, V. V. Ivanov, M. A. Johnson, M. Karcher, F. Kauker, J. Morison, K. A. Orvik, U. Schauer, H. L. Simmons, O. Skagseth, V. T. Sokolov, M. Steele, L. A. Timokhov, D. Walsh, and J. E. Walsh (2005), One more step toward a warmer Arctic, *Geophysical Research Letters*, **32**, L17605, doi:10.1029/2005GL023740.

Polyakov, I. V., L. A. Timokhov, V. A. Alexeev, S. Bacon, I. A. Dmitrenko, L. Fortier, I. E. Frolov, J.-C. Gascard, E. Hansen, V. V. Ivanov, S. Laxon, C. Mauritzen, D. Perovich, K. Shimada, H. L. Simmons, V. T. Sokolov, M. Steele, and J. Toole (2010), Arctic Ocean Warming Contributes to Reduced Polar Ice Cap, *Journal of Physical Oceanography*, **40**, 2743–2756, doi:10.1175/2010JPO4339.1.

Polyakov, I. V., A. V. Pnyushkov, and L. A. Timokhov (2012), Warming of the Intermediate Atlantic Water of the Arctic Ocean in the 2000s, *Journal of Climate*, **25**, 8362–8370, doi:10.1175/JCLI-D-12-00266.1.

Polzin, K. L., A. C. Naveira Garabato, T. N. Huussen, B. M. Sloyan, and S. Waterman (2014), Finescale parameterizations of turbulent dissipation, *Journal of Geophysical Research*, **119**, 1383–1419, doi:10.1002/2013JC008979.

Popova, E. E., A. Yool, A. C. Coward, Y. K. Aksenov, S. G. Alderson, B. A. de Cuevas, and T. R. Anderson (2010), Control of primary production in the Arctic by nutrients and light: Insights from a high resolution ocean general circulation model, *Biogeosciences*, **7**, 3569–3591, doi:10.5194/bg-7-3569-2010.

Prandle, D. (1982a), The vertical strcuture of tidal currents, *Geophysical & Astrophysical Fluid Dynamics*, **22**, 29–49, doi:10.1080/03091928208221735.

Prandle, D. (1982b), The vertical structure of tidal currents and other oscillatory flows, *Continental Shelf Research*, **1**, 191–207, doi:10.1016/0278-4343(82)90004-8.

Prinsenberg, S., J. Hamilton, I. Peterson, and R. Pettipas (2009), Observing and interpreting the seasonal variability of the oceanographic fluxes passing through Lancaster Sound of the Canadian Arctic Archipelago, in *Influence of Climate Change on the Changing Arctic and Sub-Arctic Conditions*, edited by J. C. J. Nihoul and A. G. Kostianoy, pp. 125–142, Springer, Dordrecht, The Netherlands.

Prinsenberg, S. J., and E. B. Bennett (1989), Vertical Variations of Tidal Current Profiles in Shallow Land Fast Ice-Covered Regions, *Journal of Physical Oceanography*, **19**, 1268–1278, doi:10.1175/1520-0485(1989)019<1268:VVOTCI>2.0.CO;2.

Prinsenberg, S. J., and J. Hamilton (2005), Monitoring the volume, freshwater and heat fluxes passing through Lancaster Sound in the Canadian Arctic Archipelago, *Atmosphere Ocean*, **43**, 1–22, doi:10.3137/ao.430101.

Proshutinsky, A., R. H. Bourke, and F. A. McLaughlin (2002), The role of the Beaufort Gyre in Arctic climate variability: Seasonal to decadal climate scales, *Geophysical Research Letters*, **29**, 2100, doi:10.1029/2002GL015847.

Proshutinsky, A., R. Krishfield, M.-L. Timmermans, J. Toole, E. Carmack, F. McLaughlin, W. J. Williams, S. Zimmermann, M. Itoh, and K. Shimada (2009), Beaufort Gyre freshwater reservoir: State and variability from observations, *Journal of Geophysical Research*, **114**, C00A10, doi:10.1029/2008JC005104.

Proshutinsky, A. Y. (1991), Tidal water and ice dynamics in the Arctic Ocean, in *Proceedings of the International Conference on the Role of the Polar Regions in Global Change*, vol. 1, pp. 296–303, Geophysical Institute, University of Alaska Press, Fairbanks, USA.

Proshutinsky, A. Y., and M. A. Johnson (1997), Two circulation regimes of the wind-driven Arctic Ocean, *Journal of Geophysical Research*, **102**, 12,493–12,514, doi:10.1029/97JC00738.

Rabe, B., A. Münchow, H. L. Johnson, and H. Melling (2010), Nares Strait hydrography and salinity field from a 3-year moored array, *Journal of Geophysical Research*, **115**, C07010, doi:10.1029/2009JC005966.

Rabe, B., M. Karcher, U. Schauer, J. M. Toole, R. A. Krishfield, S. Pisarev, F. Kauker, R. Gerdes, and T. Kikuchi (2011), An assessment of Arctic Ocean freshwater content changes from the 1990s to the 2006-2008 period, *Deep-Sea Research Part I: Oceanographic Research Papers*, **58**, 173–185, doi:10.1016/j.dsr.2010.12.002.

Rabe, B., H. L. Johnson, A. Münchow, and H. Melling (2012), Geostrophic ocean currents and freshwater fluxes across the Canadian polar shelf via Nares Strait, *Journal of Marine Research*, **70**, 603–640, doi:10.1357/002224012805262725.

Rabe, B., M. Karcher, F. Kauker, U. Schauer, J. M. Toole, R. A. Krishfield, S. Pisarev, T. Kikuchi, and J. Su (2014), Arctic Ocean basin liquid freshwater storage trend 1992 - 2012, *Geophysical Research Letters*, **41**, 961–968, doi:10.1002/2013GL058121.

Rainville, L., and P. Winsor (2008), Mixing across the Arctic Ocean: Microstructure observations during the Beringia 2005 Expedition, *Geophysical Research Letters*, **35**, L08606, doi:10.1029/2008GL033532.

Rainville, L., and R. A. Woodgate (2009), Observations of internal wave generation in the seasonally ice-free Arctic, *Geophysical Research Letters*, **36**, L23604, doi:10.1029/2009GL041291.

Rainville, L., C. M. Lee, and R. A. Woodgate (2011), Impact of Wind-Driven Mixing in the Arctic Ocean, *Oceanography*, **24**, 136–145, doi:10.5670/oceanog.2011.65.

Rawlins, M. A., M. Steele, M. M. Holland, J. C. Adam, J. E. Cherry, J. A. Francis, P. Y. Groisman, L. D. Hinzman, T. G. Huntington, D. L. Kane, J. S. Kimball, R. Kwok, R. B. Lammers, C. M. Lee, D. P. Lettenmaier, K. C. Mcdonald, E. Podest, J. W. Pundsack, B. Rudels, M. C. Serreze, A. Shiklomanov, O. Skagseth, T. J. Troy, C. J. Vörösmarty, M. Wensnahan, E. F. Wood, R. Woodgate, D. Yang, K. Zhang, and T. Zhang (2010), Analysis of the Arctic System for Freshwater Cycle Intensification: Observations and Expectations, *Journal of Climate*, **23**, 5715–5737, doi:10.1175/2010JCLI3421.1.

Rey, L. (1982), The Arctic Ocean: A Polar Mediterranean, in *The Arctic Ocean: The Hydrographic Environment and the Fate of Pollutants*, pp. 29–41, Wiley, New York.

Rigor, I. G., and J. M. Wallace (2004), Variations in the age of Arctic sea-ice and summer sea-ice extent, *Geophysical Research Letters*, **31**, L09401, doi:10.1029/2004GL019492.

Rippeth, T. P., B. J. Lincoln, Y.-D. Lenn, J. A. M. Green, A. Sundfjord, and S. Bacon (2015), Tide-mediated warming of Arctic halocline by Atlantic heat fluxes over rough topography, *Nature Geoscience*, **8**, 191–194, doi:10.1038/ngeo2350.

Robertson, R. (2005), Baroclinic and barotropic tides in the Weddell Sea, *Antarctic Science*, **17**, 461–474, doi:10.1017/S0954102005002890.

Rudels, B. (2015), Arctic Ocean circulation, processes and water masses: A description of observations and ideas with focus on the period prior to the International Polar Year 2007-2009, *Progress in Oceanography*, **123**, 22–67, doi:10.1016/j.pocean.2013.11.006.

Rudels, B., L. G. Anderson, and E. P. Jones (1996), Formation and evolution of the surface mixed layer and halocline of the Arctic Ocean, *Journal of Geophysical Research*, **101**, 8807–8821, doi:10.1029/96JC00143.

Rudels, B., R. Meyer, E. Fahrbach, V. V. Ivanov, S. Ø sterhus, D. Quadfasel, U. Schauer, V. Tverberg, and R. A. Woodgate (2000), Water mass distribution in Fram Strait and over the Yermak Plateau in summer 1997, *Annales Geophysicae*, **18**, 687–705, doi:10.1007/s005850000216.

Rudels, B., E. P. Jones, U. Schauer, and P. Eriksson (2004), Atlantic sources of the Arctic Ocean surface and halocline waters, *Polar Research*, **23**, 181–208, doi:10.1111/j.1751-8369.2004.tb00007.x.

Sadler, H. E. (1976), Water, Heat, and Salt Transports through Nares Strait, Ellesmere Island, *Journal of the Fisheries Research Board of Canada*, **33**, 2286–2295, doi:10.1139/f76-275.

Samelson, R. M., and P. L. Barbour (2008), Low-Level Jets, Orographic Effects, and Extreme Events in Nares Strait: A Model-Based Mesoscale Climatology, *Monthly Weather Review*, **136**, 4746–4759, doi:10.1175/2007MWR2326.1.

Samelson, R. M., T. Agnew, H. Melling, and A. Münchow (2006), Evidence for atmospheric control of sea-ice motion through Nares Strait, *Geophysical Research Letters*, **33**, L02506, doi:10.1029/2005GL025016.

Schauer, U., H. Loeng, B. Rudels, V. K. Ozhigin, and W. Dieck (2002a), Atlantic Water flow through the Barents and Kara Seas, *Deep-Sea Research Part I: Oceanographic Research Papers*, **49**, 2281–2298, doi:10.1016/S0967-0637(02)00125-5.

Schauer, U., B. Rudels, E. P. Jones, L. G. Anderson, R. D. Muench, G. Björk, J. H. Swift, V. Ivanov, and A. M. Larsson (2002b), Confluence and redistribution of Atlantic water in the Nansen, Amundsen and Makarov basins, *Annales Geophysicae*, **20**, 257–273, doi:10.5194/angeo-20-257-2002.

Schauer, U., E. Fahrbach, and S. Østerhus (2004), Arctic warming through the Fram Strait: Oceanic heat transport from 3 years of measurements, *Journal of Geophysical Research*, **109**, C06026, doi:10.1029/2003JC001823.

Schlosser, P., G. Bönisch, M. Rhein, and R. Bayer (1991), Reduction of Deepwater Formation in the Greenland Sea During the 1980s: Evidence from Tracer Data., *Science*, **251**, 1054–1056, doi:10.1126/science.251.4997.1054.

Schmidtko, S., G. C. Johnson, and J. M. Lyman (2013), MIMOC: A global monthly isopycnal upper-ocean climatology with mixed layers, *Journal of Geophysical Research*, **118**, 1658–1672, doi:10.1002/jgrc.20122.

Schröder, D., D. L. Feltham, D. Flocco, and M. Tsamados (2014), September Arctic sea-ice minimum predicted by spring melt-pond fraction, *Nature Climate Change*, **4**, 353–357, doi:10.1038/NCLIMATE2203.

Schuur, E. A. G., J. G. Vogel, K. G. Crummer, H. Lee, J. O. Sickman, and T. E. Osterkamp (2009), The effect of permafrost thaw on old carbon release and net carbon exchange from tundra, *Nature*, **459**, 556–559, doi:10.1038/nature08031.

Schweiger, A., R. Lindsay, J. Zhang, M. Steele, H. Stern, and R. Kwok (2011), Uncertainty in modeled Arctic sea ice volume, *Journal of Geophysical Research*, **116**, C00D06, doi:10.1029/2011JC007084.

Screen, J. A., and I. Simmonds (2010), The central role of diminishing sea ice in recent Arctic temperature amplification, *Nature*, **464**, 1334–1337, doi:10.1038/nature09051.

Screen, J. A., C. Deser, I. Simmonds, and R. Tomas (2014a), Atmospheric impacts of Arctic sea-ice loss, 1979-2009: separating forced change from atmospheric internal variability, *Climate Dynamics*, **43**, 333–344, doi:10.1007/s00382-013-1830-9.

Screen, J. A., C. Deser, and L. Sun (2014b), Reduced Risk of North American Cold Extremes due to Continued Arctic Sea Ice Loss, *Bulletin of the American Meteorological Society*, doi:10.1175/BAMS-D-14-00185.1.

Segar, D. A. (2012), *Introduction to Ocean Sciences*, 3^{rd} ed., 522 pp.

Serreze, M., A. P. Barrett, A. G. Slater, M. Steele, J. Zhang, and K. E. Trenberth (2007), The large-scale energy budget of the Arctic, *Journal of Geophysical Research*, **112**, D11122, doi:10.1029/2006JD008230.

Serreze, M. C., and A. P. Barrett (2011), Characteristics of the Beaufort Sea High, *Journal of Climate*, **24**, 159–182, doi:10.1175/2010JCLI3636.1.

Serreze, M. C., A. P. Barrett, A. G. Slater, R. A. Woodgate, K. Aagaard, R. B. Lammers, M. Steele, R. Moritz, M. Meredith, and C. M. Lee (2006), The large-scale freshwater cycle of the Arctic, *Journal of Geophysical Research*, **111**, C11010, doi:10.1029/2005JC003424.

Serreze, M. C., A. P. Barrett, J. C. Stroeve, D. N. Kindig, and M. M. Holland (2009), The emergence of surface-based Arctic amplification, *The Cryosphere*, **3**, 11–19, doi:10.5194/tc-3-11-2009.

Shaw, W. J., and T. P. Stanton (2014), Vertical diffusivity of the Western Arctic Ocean halocline, *Journal of Geophysical Research*, **119**, 5017–5038, doi:10.1002/2013JC009598.

Shiklomanov, A. (2010), River discharge, in *Arctic Report Card 2010*, edited by J. Richter-Menge and J. E. Overland, pp. 38–40, NOAA.

Shimizu, K. (2010), An analytical model of capped turbulent oscillatory bottom boundary layers, *Journal of Geophysical Research*, **115**, C03011, doi:10.1029/2009JC005548.

Simmonds, I., and K. Keay (2009), Extraordinary September Arctic sea ice reductions and their relationships with storm behavior over 1979–2008, *Geophysical Research Letters*, **36**, L19715, doi:10.1029/2009GL039810.

Simmonds, I., and I. Rudeva (2012), The great Arctic cyclone of August 2012, *Geophysical Research Letters*, **39**, L23709, doi:10.1029/2012GL054259.

Simmons, H. L., R. W. Hallberg, and B. K. Arbic (2004), Internal wave generation in a global baroclinic tide model, *Deep-Sea Research Part II: Topical Studies in Oceanography*, **51**, 3043–3068, doi:10.1016/j.dsr2.2004.09.015.

Simpson, J. H., and J. Sharples (2012), *Introduction to the Physical and Biological Oceanography of Shelf Seas*, 424 pp., Cambridge University Press.

Simpson, J. H., and J. P. Tinker (2009), A test of the influence of tidal stream polarity on the structure of turbulent dissipation, *Continental Shelf Research*, **29**, 320–332, doi:10.1016/j.csr.2007.05.013.

Simpson, J. H., W. R. Crawford, T. P. Rippeth, A. R. Campbell, and J. V. S. Cheok (1996), The Vertical Structure of Turbulent Dissipation in Shelf Seas, *Journal of Physical Oceanography*, **26**, 1579–1590, doi:10.1175/1520-0485(1996)026<1579:tvsotd>2.0.co;2.

Simpson, J. H., H. Burchard, N. R. Fisher, and T. P. Rippeth (2002), The semi-diurnal cycle of dissipation in a ROFI: model-measurement comparisons, *Continental Shelf Research*, **22**, 1615–1628, doi:10.1016/S0278-4343(02)00025-0.

Sirevaag, A., and I. Fer (2012), Vertical heat transfer in the Arctic Ocean: The role of double-diffusive mixing, *Journal of Geophysical Research*, **117**, C07010, doi:10.1029/2012JC007910.

Smedsrud, L. H., R. Ingvaldsen, J. E. O. Nilsen, and O. Skagseth (2010), Heat in the Barents Sea: transport, storage, and surface fluxes, *Ocean Science*, **6**, 219–234, doi:10.5194/os-6-219-2010.

Smith, W. H. F., and D. T. Sandwell (1997), Global Sea Floor Topography from Satellite Altimetry and Ship Depth Soundings, *Science*, **26**, 1956–1962, doi:10.1126/science.277.5334.1956.

Soulsby, R. L. (1983), The bottom boundary layer of shelf seas, in *Physical Oceanography of Coastal and Shelf Seas*, edited by B. Johns, pp. 189–266, Elsevier, Amsterdam.

Soulsby, R. L. (1990), Tidal-current boundary layers, in *The Sea, vol. 9A, Ocean Engineering Science*, edited by B. Le Méhauté and D. M. Hanes, pp. 523–566, Wiley-Interscience, New York.

Souza, A. J., and J. H. Simpson (1996), The modification of tidal ellipses by stratification in the Rhine ROFI, *Continental Shelf Research*, **16**, 997–1007, doi:10.1016/0278-4343(95)00042-9.

Spall, M. A. (2003), On the thermohaline circulation in flat bottom marginal seas, *Journal of Marine Research*, **61**, 1–25, doi:10.1357/002224003321586390.

Spall, M. A. (2004), Boundary Currents and Watermass Transformation in Marginal Seas, *Journal of Physical Oceanography*, **34**, 1197–1213, doi:10.1175/1520-0485(2004)034<1197:BCAWTI>2.0.CO;2.

Spall, M. A. (2013), On the Circulation of Atlantic Water in the Arctic Ocean, *Journal of Physical Oceanography*, **43**, 2352–2371, doi:10.1175/JPO-D-13-079.1.

Spall, M. A., R. S. Pickart, P. S. Fratantoni, and A. J. Plueddemann (2008), Western Arctic Shelfbreak Eddies: Formation and Transport, *Journal of Physical Oceanography*, **38**, 1644–1668, doi:10.1175/2007JPO3829.1.

Spreen, G., S. Kern, D. Stammer, and E. Hansen (2009), Fram Strait sea ice volume export estimated between 2003 and 2008 from satellite data, *Geophysical Research Letters*, **36**, L19,502, doi:10.1029/2009GL039591.

Sprintall, J., A. L. Gordon, A. Koch-Larrouy, T. Lee, J. T. Potemra, K. Pujiana, and S. E. Wijffels (2014), The Indonesian seas and their role in the coupled ocean–climate system, *Nature Geoscience*, **7**, 487–492, doi:10.1038/ngeo2188.

Steele, M., and T. Boyd (1998), Retreat of the cold halocline layer in the Arctic Ocean, *Journal of Geophysical Research*, **103**, 10,419–10,435, doi:10.1029/98JC00580.

Steele, M., and W. Ermold (2007), Steric sea level change in the Northern Seas, *Journal of Climate*, **20**, 403–417, doi:10.1175/JCLI4022.1.

Steele, M., R. Morley, and W. Ermold (2001), PHC: A Global Ocean Hydrography with a High-Quality Arctic Ocean, *Journal of Climate*, **14**, 2,079–2,087, doi:10.1175/1520-0442(2001)014<2079:PAGOHW>2.0.CO;2.

Steele, M., J. Morison, W. Ermold, I. Rigor, M. Ortmeyer, and K. Shimada (2004), Circulation of summer Pacific halocline water in the Arctic Ocean, *Journal of Geophysical Research*, **109**, C02027, doi:10.1029/2003JC002009.

Steele, M., W. Ermold, and J. Zhang (2008), Arctic Ocean surface warming trends over the past 100 years, *Geophysical Research Letters*, **35**, L02614, doi:10.1029/2007GL031651.

Steele, M., W. Ermold, and J. Zhang (2011), Modeling the formation and fate of the near-surface temperature maximum in the Canadian Basin of the Arctic Ocean, *Journal of Geophysical Research*, **116**, C11015, doi:10.1029/2010JC006803.

Steiner, N., G. Holloway, R. Gerdes, S. Häkkinen, D. Holland, M. Karcher, F. Kauker, W. Maslowski, A. Proshutinsky, M. Steele, and J. Zhang (2004), Comparing modeled streamfunction, heat and freshwater content in the Arctic Ocean, *Ocean Modelling*, **6**, 265–284, doi:10.1016/S1463-5003(03)00013-1.

Stewart, K. D., and T. W. N. Haine (2013), Wind-driven Arctic freshwater anomalies, *Geophysical Research Letters*, **40**, 6196–6201, doi:10.1002/2013GL058247.

Stouffer, R. J., J. Yin, J. M. Gregory, K. W. Dixon, M. J. Spelman, W. Hurlin, A. J. Weaver, M. Eby, G. M. Flato, H. Hasumi, A. Hu, J. H. Jungclaus, I. V. Kamenkovich, A. Levermann, M. Montoya, S. Murakami, S. Nawrath, A. Oka, W. R. Peltier, D. Y. Robitaille, A. Sokolov, G. Vettoretti, and S. L. Weber (2006), Investigating the Causes of the Response of the Thermohaline Circulation to Past and Future Climate Changes, *Journal of Climate*, **19**, 1365–1387, doi:10.1175/JCLI3689.1.

Straneo, F., and F. J. Saucier (2008), The Arctic–subarctic exchange through Hudson Strait, in *Arctic-Subarctic Ocean Fluxes: Defining the Role of the Northern Seas in Climate*, edited by R. R. Dickson, J. Meincke, and P. Rhines, pp. 249–261, Springer-Verlag, doi:10.1007/978-1-4020-6774-7_11.

Stroeve, J., M. M. Holland, W. Meier, T. Scambos, and M. Serreze (2007), Arctic sea ice decline: Faster than forecast, *Geophysical Research Letters*, **34**, L09501, doi:10.1029/2007gl029703.

Stroeve, J. C., V. Kattsov, A. Barrett, M. Serreze, T. Pavlova, M. Holland, and W. N. Meier (2012a), Trends in Arctic sea ice extent from CMIP5, CMIP3 and observations, *Geophysical Research Letters*, **39**, L16502, doi:10.1029/2012GL052676.

Stroeve, J. C., M. C. Serreze, M. M. Holland, J. E. Kay, J. Malanik, and A. P. Barrett (2012b), The Arctic's rapidly shrinking sea ice cover: a research synthesis, *Climate Change*, **110**, 1005–1027, doi:10.1007/s10584-011-0101-1.

Sverdrup, H. L., M. W. Johnson, and R. H. Fleming (1942), Waves and Tides, in *The Oceans: Their Physics, Chemistry, and General Biology*, pp. 516–604, Prentice-Hall, New York.

Takahashi, T., S. C. Sutherland, C. Sweeney, A. Poisson, N. Metzl, B. Tilbrook, N. Bates, R. Wanninkhof, R. A. Feely, C. Sabine, J. Olafsson, and Y. Nojiri (2002), Global sea-air CO_2 flux based on climatological surface ocean pCO_2, and seasonal biological and temperature effects, *Deep-Sea Research Part II: Topical Studies in Oceanography*, **49**, 1601–1622, doi:10.1016/S0967-0645(02)00003-6.

Tamocai, C., J. G. Canadell, E. A. G. Schuur, P. Kuhry, G. Mazhitova, and S. Zimov (2009), Soil organic carbon pools in the northern circumpolar permafrost region, *Global Biogeochemical Cycles*, **23**, GB2023, doi:10.1029/2008GB003327.

Teller, J. T., D. W. Leverington, and J. D. Mann (2002), Freshwater outbursts to the oceans from glacial Lake Agassiz and their role in climate change during the last deglaciation, *Quaternary Science Reviews*, **21**, 879–887, doi:10.1016/S0277-3791(01)00145-7.

Thompson, D. W. J., and J. M. Wallace (1998), The Arctic oscillation signature in the wintertime geopotential height and temperature fields, *Geophysical Research Letters*, **25**, 1297–1300, doi:10.1029/98GL00950.

Timmermann, A., Y. Okumura, S. I. An, A. Clement, B. Dong, E. Guilyardi, A. Hu, J. H. Jungclaus, M. Renold, T. F. Stocker, R. J. Stouffer, R. Sutton, S. P. Xie, and J. Yin (2007), The Influence of a Weakening of the Atlantic Meridional Overturning Circulation on ENSO, *Journal of Climate*, **20**, 4899–4919, doi:10.1175/JCLI4283.1.

Timmermann, R., H. Goosse, G. Madec, T. Fichefet, C. Ethe, and V. Dulière (2005), On the representation of high latitude processes in the ORCA-LIM global coupled sea ice–ocean model, *Ocean Modelling*, **8**, 175–201, doi:10.1016/j.ocemod.2003.12.009.

Timmermans, M.-L. (2015), The impact of stored solar heat on Arctic sea ice growth, *Geophysical Research Letters*, **42**, 6399–6406, doi:10.1002/2015GL064541.

Timmermans, M.-L., J. Toole, R. Krishfield, and P. Winsor (2008), Ice-Tethered Profiler observations of the double-diffusive staircase in the Canada Basin thermocline, *Journal of Geophysical Research*, **113**, C00A02, doi:10.1029/2008JC004829.

Timmermans, M.-L., A. Proshutinsky, E. Golubeva, J. M. Jackson, R. Krishfield, M. McCall, G. Platov, J. Toole, and W. Williams (2014), Mechanisms of Pacific Summer Water Variability in the Arctic's Central Canada Basin, *Journal of Geophysical Research*, **119**, 7523–7548, doi:10.1002/2014JC010273.

Tomczak, M., and J. S. Godfrey (2003), Arctic oceanography; the path of North Atlantic Deep Water, in *Regional Oceanography: an Introduction*, 2^{nd} ed., pp. 83–104, Daya Publishing House, Delhi.

Toole, J. M., M.-L. Timmermans, D. K. Perovich, R. A. Krishfield, A. Proshutinsky, and J. A. Richter-Menge (2010), Influences of the ocean surface mixed layer and thermohaline stratification on Arctic Sea ice in the central Canada Basin, *Journal of Geophysical Research*, **115**, C10018, doi:10.1029/2009JC005660.

Travers, C. S. (2012), Quantifying Sea-Ice Volume Flux using Moored Instrumentation in the Bering Strait, Master's thesis, University of Washington.

Tsamados, M., D. L. Feltham, D. Schroeder, D. Flocco, S. L. Farrell, N. T. Kurtz, S. W. Laxon, and S. Bacon (2014), Impact of variable atmospheric and oceanic form drag on simulations of Arctic sea ice, *Journal of Physical Oceanography*, **44**, 1329–1353, doi:10.1175/JPO-D-13-0215.1.

Tsukernik, M., C. Deser, M. Alexander, and R. Tomas (2010), Atmospheric forcing of Fram Strait sea ice export: A closer look, *Climate Dynamics*, **35**, 1349–1360, doi:10.1007/s00382-009-0647-z.

Turner, J. S. (2010), The Melting of Ice in the Arctic Ocean: The Influence of Double-Diffusive Transport of Heat from Below, *Journal of Physical Oceanography*, **40**, 249–256, doi:10.1175/2009JPO4279.1.

Ugray, Z., L. Lasdon, J. Plummer, F. Glover, J. Kelly, and R. Martí (2007), Scatter Search and Local NLP Solvers: A Multistart Framework for Global Optimization, *INFORMS Journal on Computing*, **19**, 328–340, doi:10.1287/ijoc.1060.0175.

Vancoppenolle, M., T. Fichefet, and H. Goosse (2009a), Simulating the mass balance and salinity of Arctic and Antarctic sea ice. 2. Importance of sea ice salinity variations, *Ocean Modelling*, **27**, 54–69, doi:10.1016/j.ocemod.2008.11.003.

Vancoppenolle, M., T. Fichefet, H. Goosse, S. Bouillon, G. Madec, and M. A. M. Maqueda (2009b), Simulating the mass balance and salinity of Arctic and Antarctic sea ice. 1. Model description and validation, *Ocean Modelling*, **27**, 33–53, doi:10.1016/j.ocemod.2008.10.005.

Vaughan, D. G., J. C. Comiso, I. Allison, J. Carrasco, G. Kaser, R. Kwok, P. Mote, T. Murray, F. Paul, J. Ren, E. Rignot, O. Solomina, K. Steffen, and T. Zhang (2013), Observations: Cryosphere, in *Climate Change 2013: The Physical Science Basis. Contribution of Working Group I to the Fifth Assessment Report of the Intergovernmental Panel on Climate Change*, edited by T. F. Stocker, D. Qin, G. K. Plattner, M. Tignor, S. K. Allen, J. Boschung, A. Nauels, Y. Xia, V. Bex, and P. M. Midgley, pp. 317–382, Cambridge University Press, Cambridge, United Kingdom and New York, NY, USA.

Vavrus, S. J., M. M. Holland, A. Jahn, D. A. Bailey, and B. A. Blazey (2012), Twenty-First-Century Arctic Climate Change in CCSM4, *Journal of Climate*, **25**, 2696–2710, doi:10.1175/JCLI-D-11-00220.1.

Vellinga, M., and R. A. Wood (2002), Global Climatic Impacts of a Collapse of the Atlantic Thermohaline Circulation, *Climatic Change*, **54**, 251–267, doi:10.1023/A:1016168827653.

Vellinga, M., and R. A. Wood (2008), Impacts of thermohaline circulation shutdown in the twenty-first century, *Climatic Change*, **91**, 43–63, doi:10.1007/s10584-006-9146-y.

Vihma, T. (2014), Effects of Arctic Sea Ice Decline on Weather and Climate: A Review, *Surveys in Geophysics*, **35**, 1175–1214, doi:10.1007/s10712-014-9284-0.

Vlasenko, V., N. Stashchuk, K. Hutter, and K. Sabinin (2003), Nonlinear internal waves forced by tides near the critical latitude, *Deep-Sea Research Part I: Oceanographic Research Papers*, **50**, 317–338, doi:10.1016/S0967-0637(03)00018-9.

Wang, J., J. Zhang, E. Watanabe, M. Ikeda, K. Mizobata, J. E. Walsh, X. Bai, and B. Wu (2009), Is the Dipole Anomaly a major driver to record lows in Arctic summer sea ice extent?, *Geophysical Research Letters*, **36**, L05706, doi:10.1029/2008GL036706.

Wang, M., and J. E. Overland (2009), A sea ice free summer Arctic within 30 years?, *Geophysical Research Letters*, **36**, L07502, doi:10.1029/2009GL037820.

Wang, M., and J. E. Overland (2012), A sea ice free summer Arctic within 30 years: An update from CMIP5 models, *Geophysical Research Letters*, **39**, L18501, doi:10.1029/2012GL052868.

Wang, M., and J. E. Overland (2015), Projected Future Duration of the Sea-Ice-Free Season in the Alaskan Arctic, *Progress in Oceanography*, doi:10.1016/j.pocean.2015.01.001.

Wassmann, P., C. M. Duarte, S. Agustí, and M. K. Sejr (2011), Footprints of climate change in the Arctic marine ecosystem, *Global Change Biology*, **17**, 1235–1249, doi:10.1111/j.1365-2486.2010.02311.x.

Watanabe, E. (2011), Beaufort shelf break eddies and shelf-basin exchange of Pacific summer water in the western Arctic Ocean detected by satellite and modeling analyses, *Journal of Geophysical Research*, **116**, C08034, doi:10.1029/2010JC006259.

White, D., L. Hinzman, L. Alessa, J. Cassano, M. Chambers, K. K. Falkner, J. Francis, W. J. Gutowski, M. Holland, R. M. Holmes, H. Huntington, D. Kane, A. Kliskey, C. Lee, J. McClelland, B. Peterson, T. S. Rupp, F. Straneo, M. Steele, R. A. Woodgate, D. Yang, K. Yoshikawa, and T. Zhang (2007), The arctic freshwater system: Changes and impacts, *Journal of Geophysical Research*, **112**, G04S54, doi:10.1029/2006JG000353.

Whiteman, G., C. Hope, and P. Wadhams (2013), Climate Science: Vast costs of Arctic change, *Nature*, **499**, 401–403, doi:10.1038/499401a.

Wilmes, S.-B., and J. A. M. Green (2014), The evolution of tides and tidal dissipation over the past 21,000 years, *Journal of Geophysical Research*, **119**, 4083–4100, doi:10.1002/2013JC009605.

Woodgate, R. A., and K. Aagaard (2005), Revising the Bering Strait freshwater flux into the Arctic Ocean, *Geophysical Research Letters*, **32**, L02602, doi:10.1029/2004GL021747.

Woodgate, R. A., K. Aagaard, and T. J. Weingartner (2006), Interannual changes in the Bering Strait fluxes of volume, heat and freshwater between 1991 and 2004, *Geophysical Research Letters*, **33**, L15609, doi:10.1029/2006GL026931.

Woodgate, R. A., T. Weingartner, and R. Lindsay (2010), The 2007 Bering Strait oceanic heat flux and anomalous Arctic sea-ice retreat, *Geophysical Research Letters*, **37**, L01602, doi:10.1029/2009GL041621.

Woodgate, R. A., T. J. Weingartner, and R. Lindsay (2012), Observed increases in Bering Strait oceanic fluxes from the Pacific to the Arctic from 2001 to 2011 and their impacts on the Arctic Ocean water column, *Geophysical Research Letters*, **39**, L24603, doi:10.1029/2012GL054092.

Woollings, T., J. Gregory, J. G. Pinto, M. Reyers, and D. Brayshaw (2012), Response of the North Atlantic storm track to climate change shaped by ocean–atmosphere coupling, *Nature Geoscience*, **5**, 313–317, doi:10.1038/ngeo1438.

Wunsch, C. (2005), The Total Meridional Heat Flux and Its Oceanic and Atmospheric Partition, *Journal of Climate*, **18**, 4374–4380, doi:10.1175/JCLI3539.1.

Yang, J. (2005), The Arctic and Subarctic Ocean Flux of Potential Vorticity and the Arctic Ocean Circulation, *Journal of Physical Oceanography*, **35**, 2387–2407, doi:10.1175/JPO2819.1.

Yang, J. (2006), The Seasonal Variability of the Arctic Ocean Ekman Transport and Its Role in the Mixed Layer Heat and Salt Fluxes, *Journal of Climate*, **19**, 5366–5387, doi:10.1175/JCLI3892.1.

Yang, J. (2009), Seasonal and interannual variability of downwelling in the Beaufort Sea, *Journal of Geophysical Research*, **114**, C00A14, doi:10.1029/2008JC005084.

Zhang, J., and D. A. Rothrock (2003), Modeling Global Sea Ice with a Thickness and Enthalpy Distribution Model in Generalized Curvilinear Coordinates, *Monthly Weather Review*, **131**, 845–861, doi:10.1175/1520-0493(2003)131<0845:MGSIWA>2.0.CO;2.

Zhang, J., and M. Steele (2007), Effect of vertical mixing on the Atlantic Water layer circulation in the Arctic Ocean, *Journal of Geophysical Research*, **112**, C04S04, doi:10.1029/2006JC003732.

Zhang, J., R. Lindsay, M. Steele, and A. Schweiger (2008), What drove the dramatic retreat of arctic sea ice during summer 2007?, *Geophysical Research Letters*, **35**, L11505, doi:10.1029/2008GL034005.

Zhang, J., R. Lindsay, A. Schweiger, and I. Rigor (2012), Recent changes in the dynamic properties of declining Arctic sea ice: A model study, *Geophysical Research Letters*, **39**, L20503, doi:10.1029/2012gl053545.

Zhang, J., R. Lindsay, A. Schweiger, and M. Steele (2013), The impact of an intense summer cyclone on 2012 Arctic sea ice retreat, *Geophysical Research Letters*, **40**, 720–726, doi:10.1002/grl.50190.

Zhang, R., and T. L. Delworth (2005), Simulated Tropical Response to a Substantial Weakening of the Atlantic Thermohaline Circulation, *Journal of Climate*, **18**, 1853–1860, doi:10.1175/JCLI3460.1.

Zhang, R., and T. L. Delworth (2006), Impact of Atlantic multidecadal oscillations on India/Sahel rainfall and Atlantic hurricanes, *Geophysical Research Letters*, **33**, L17712, doi:10.1029/2006GL026267.

Zhao, M., M.-L. Timmermans, S. Cole, R. Krishfield, A. Proshutinsky, and J. Toole (2014), Characterizing the eddy field in the Arctic Ocean halocline, *Journal of Geophysical Research*, **119**, 8800–8817, doi:10.1002/2014JC010488.